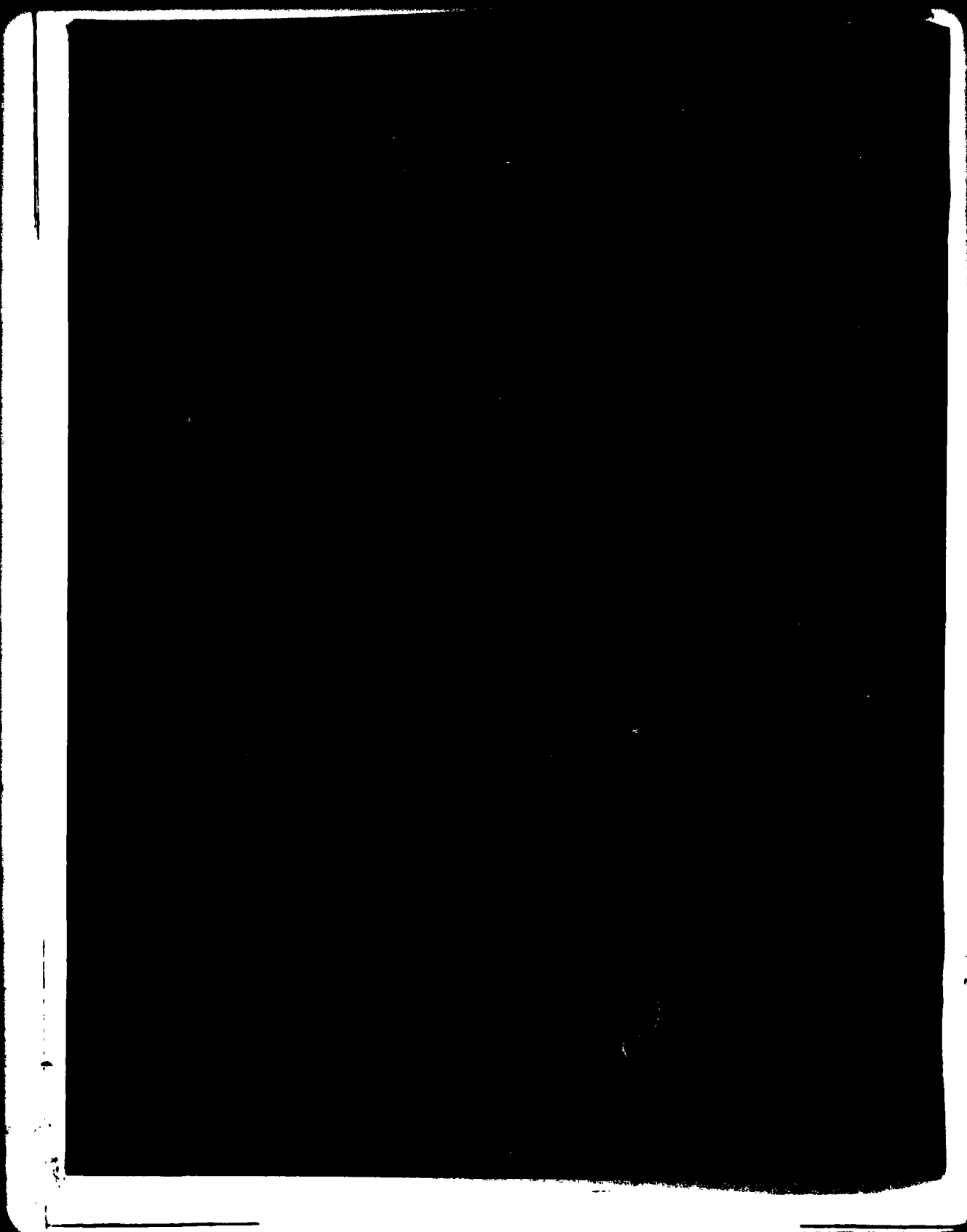




ADA 07991



UNCLASSIFIED

SECURITY CLASSIFICATION OF THIS PAGE (When Data Entered)

REPORT DOCUMENTATION PAGE		READ INSTRUCTIONS BEFORE COMPLETING FORM
1. REPORT NUMBER NSWC TR 79-378 ✓	2. GOVT ACCESSION NO.	3. RECIPIENT'S CATALOG NUMBER 9 Rept. for
4. TITLE (and Subtitle) 6 BURNING VELOCITIES OF A SOLID PROPELLANT, VIA A MICROWAVE TECHNIQUE, AT ELEVATED PRESSURES AND PRESSURIZATION RATES.		5. TYPE OF REPORT OR REPORT COVERED 1976-1978
7. AUTHOR(s) 10 L. H. Russell		8. CONTRACT OR GRANT NUMBER(s)
9. PERFORMING ORGANIZATION NAME AND ADDRESS Naval Surface Weapons Center (G33) ✓ Dahlgren, Virginia 22448		10. PROGRAM ELEMENT PROJECT, TASK AREA & WORK UNIT NUMBERS 16 17 61152N ZR00001 ZR02402 G01AA210/BA250
11. CONTROLLING OFFICE NAME AND ADDRESS		12. REPORT DATE 11 October 1979
14. MONITORING AGENCY NAME & ADDRESS (if different from Controlling Office) 12 269		13. NUMBER OF PAGES 262
		15. SECURITY CLASS. (of this report) UNCLASSIFIED
		15a. DECLASSIFICATION/DOWNGRADING SCHEDULE
16. DISTRIBUTION STATEMENT (of this Report) Approved for public release; distribution unlimited.		
17. DISTRIBUTION STATEMENT (of the abstract entered in Block 20, if different from Report) 14 NSWC/TR-79-378		
18. SUPPLEMENTARY NOTES		
19. KEY WORDS (Continue on reverse side if necessary and identify by block number) solid propellants phase angle combustion chambers microwaves burning rates high pressure tests Doppler shifts waveguides		
20. ABSTRACT (Continue on reverse side if necessary and identify by block number) Presented are the results of a research effort to directly measure, via a microwave Doppler/phase shift technique, the burning rate of solid propellant in both steady and dynamic elevated pressure environments. The recession velocity of the propellant when it burned planarly within a small rectangular waveguide was directly proportional to the time rate of change of a measured relative phase angle. This relative phase angle was based upon the phase relationship between guided microwave reflections from two		

DD FORM 1473 1 JAN 73

EDITION OF 1 NOV 65 IS OBSOLETE  
S/N 0102-014-6601

UNCLASSIFIED

SECURITY CLASSIFICATION OF THIS PAGE (When Data Entered)

391 598 2W

UNCLASSIFIED

SECURITY CLASSIFICATION OF THIS PAGE(When Data Entered)

20. ABSTRACT (Continued)

surfaces, one a reference plane and the other an effective plane created by the dielectric discontinuity at the burning propellant surface. In the pressure range from 500 to 10,000 psig, steady-state burning rate tests with a single base nitrocellulose gun propellant, M6, were successfully conducted in a large volume combustion fixture which incorporated a coaxial-to-waveguide adapter having unique pressure sealing microwave feedthroughs. In addition to yielding burning rate values intermediate to those from conventional closed chamber and strand burner tests, the experiments established the uncertainty in the proportionality constant linking M6 burning rate and the time derivative of relative phase angle. A one-dimensional theoretical model was formulated and, with the aid of appropriately chosen constants, yielded predictions which agreed very well with the experimentally observed behavior of a solid propellant undergoing planar burning within a waveguide. In conjunction with a nonlinear parameter estimation technique, utilization of the model allowed apparent instantaneous burning rates to be corrected for biases which had been caused by the presence of significant fixed microwave reflections.

In the attempt to extend the microwave technique to rapid pressurizations, a twin propellant strand differential system was constructed to help isolate the propellant combustion response from its mechanical response. In this approach, changes in relative phase angle were intended to be associated with only that motion of the microwave reflecting plane caused by propellant burning. The ability of the technique to cancel propellant mechanical responses was evaluated in a series of vibration or non-burning dynamic tests conducted at two distinctly different pressurization rates, slow and fast. Within the volume of interest, typical pressure changes were from 1450 to 7000 psig and were created by a controlled influx of nitrogen gas; characteristic pressurization rates were  $50 \times 10^3$  and  $1 \times 10^6$  psi/sec. Dynamic experiments which included propellant combustion were also conducted under similar pressurization conditions. Results from the transient burning tests and the vibration experiments indicated that major problems must still be overcome before accurate, direct dynamic burning rate measurements can be made via the microwave/Doppler phase shift technique.

UNCLASSIFIED

SECURITY CLASSIFICATION OF THIS PAGE(When Data Entered)

## FOREWORD

During fiscal years 1976 through 1978, financial support for this investigation was provided by the Naval Surface Weapons Center (NSWC) Independent Research Program. The research effort described in this report also comprised a Doctoral Dissertation submitted by the author to the University of Pittsburgh, Pittsburgh, Pennsylvania, in April 1979.

The author gratefully acknowledges the support of NSWC, Dahlgren, Virginia. Particular appreciation is expressed to the following NSWC personnel for their technical assistance: J. M. Boyle, R. C. Hooper, D. R. McClure, K. R. Nichols, E. J. Shuler, J. D. Terrel, R. C. Viets, and M. S. Wieland.

This report was reviewed and approved by K. G. Thorsted, Head, Propulsion Branch and C. L. Dettinger, Acting Head, Gun Systems and Munitions Division.

Released by:



CDR. R. P. FUSCALDO  
Assistant for Weapons Systems  
Weapons Systems Department

Accession For	
NTIS GRA&I	<input checked="" type="checkbox"/>
DDC TAB	<input type="checkbox"/>
Unannounced Justification	<input type="checkbox"/>
By _____	
Distribution/ _____	
Availability Codes	
Dist	Avail and/or special
A	

**TABLE OF CONTENTS**

	<u>Page</u>
FOREWORD . . . . .	iii
LIST OF FIGURES . . . . .	vii
LIST OF TABLES . . . . .	xv
NOMENCLATURE . . . . .	xvi
1.0 INTRODUCTION . . . . .	1
2.0 DESIGN RATIONALE . . . . .	5
3.0 THEORETICAL MODEL . . . . .	9
4.0 NONLINEAR PARAMETER ESTIMATION . . . . .	15
5.0 EXPERIMENTAL APPARATUS AND TEST PROCEDURES . . . . .	20
6.0 RESULTS AND ANALYSIS . . . . .	31
6.1 Phase Angle Resolution . . . . .	31
6.2 Steady-State Burning Rate Tests . . . . .	33
6.3 Dynamic Experiments . . . . .	47
6.31 Vibration Tests . . . . .	47
6.32 Transient Burning Tests . . . . .	53
7.0 CONCLUSIONS . . . . .	57
APPENDIX A FIGURES . . . . .	61
APPENDIX B TABLES . . . . .	184
APPENDIX C GAS DYNAMIC MODEL . . . . .	193
APPENDIX D FINITE ELEMENT ANALYSIS . . . . .	202
APPENDIX E PHASE ANGLE DERIVATIVE RELATIONSHIPS . . . . .	207
APPENDIX F EQUIPMENT LIST . . . . .	210
APPENDIX G DIGITAL SIGNAL ANALYSIS . . . . .	217
BIBLIOGRAPHY . . . . .	228

LIST OF FIGURES

<u>Figure</u>		<u>Page</u>
1	Comparison of the Prediction of the Gas Dynamic Model with Experimental Data from a Typical Slow Pressurization . . . . .	62
2	Comparison of the Prediction of the Gas Dynamic Model with Experimental Data from a Typical Fast Pressurization . . . . .	63
3	Structural Idealization of Dielectric Material Epoxy-Bonded within a Waveguide . . . . .	64
4	Mechanical Response Velocity Caused by a Theoretical Pressurization and Relevant to Node Number One in the Structural Idealization . . . . .	65
5	Mechanical Response Velocity Caused by a Theoretical Pressurization and Relevant to Node Number One in the Structural Idealization . . . . .	66
6	Mechanical Response Velocity Caused by a Theoretical Pressurization and Relevant to Node Number One in the Structural Idealization . . . . .	67
7	Mechanical Response Velocity Caused by a Theoretical Pressurization and Relevant to Node Number One in the Structural Idealization . . . . .	68
8	Mechanical Response Velocity Caused by a Theoretical Pressurization and Relevant to Node Number One in a Less Rigid Form of the Structural Idealization . . . . .	69
9	Schematic of the Twin Strand Differential System . . . . .	70
10	Phasor Diagram Applicable to the Twin Strand Differential System . . . . .	71
11	Phasor Diagram Applicable to a Single Propellant Strand and a Spatially Fixed Reference Plane . . . . .	72
12	Governing Equation as a Function of Actual Phase Angle . . . . .	73

<u>Figure</u>	<u>Page</u>
13 Schematic of the Overall Experimental System . . . . .	74
14 Electrical Schematic of Simple Highpass Filter . . . . .	75
15 Electrical Schematic of Filter-Amplifier . . . . .	76
16 Electrical Schematic of Time Delay Sequencer . . . . .	77
17 Electrical Schematic of Capacitive Discharge Circuit . . . . .	78
18 Combustion Fixture Section View . . . . .	79
19 Combustion Fixture Offset Partial Section View . . . . .	80
20 Section View of Pressure Sealing Microwave Feedthrough . . . . .	81
21 Front Face of Dielectric Transition Window with Two Adjacent Microwave Feedthroughs . . . . .	82
22 Sections of Semi-Rigid Coaxial Cable Which Connect the Dielectric Transition Window to the X-Band Waveguide . . . . .	83
23 Section View of Twin Load . . . . .	84
24 Twin Load Sitting Upon the Dielectric Transition Window . . . . .	85
25 Voltage Standing Wave Ratio (VSWR) for the Dielectric Transition Window . . . . .	86
26 Waveguide-to-Waveguide Version of the Dielectric Transition Window . . . . .	87
27 Schematic of Pressurizing System . . . . .	88
28 Overview of Experimental Facility . . . . .	89
29 Closeup View of Waveguide Circuitry . . . . .	90
30 View Inside of the Protective Shelter . . . . .	91
31 Dual Propellant Waveguide and Two M6 Propellant Strands . . . . .	92

<u>Figure</u>	<u>Page</u>
32 Phase Noise versus Phase Angle . . . . .	93
33 Maximum RMS Phase Noise versus Nominal System Bandwidth . . . . .	94
34 Minimum RMS Phase Noise versus Nominal System Bandwidth . . . . .	95
35 Minimum RMS Phase Noise versus Test Signal Power . . . . .	96
36 Maximum RMS Phase Noise versus Test Signal Power . . . . .	97
37 Measured Phase Angle on the 11 <sup>th</sup> Steady-State Test . . . . .	98
38 Test Chamber Pressure on the 11 <sup>th</sup> Steady-State Test . . . . .	99
39 Measured Phase Angle on the 8 <sup>th</sup> Steady-State Test . . . . .	100
40 Unfolded Measured Phase Angle on the 8 <sup>th</sup> Steady-State Test . . . . .	101
41 Change in Relative Amplitude of the Test Signal on the 8 <sup>th</sup> Steady-State Test . . . . .	102
42 Test Chamber Pressure on the 8 <sup>th</sup> Steady-State Test . . . . .	103
43 Test Signal Amplitude on the 8 <sup>th</sup> Steady-State Test . . . . .	104
44 Apparent or Uncorrected Burning Rate on the 8 <sup>th</sup> Steady-State Test; Determined by the Use of Central Differences Applied to Raw Data . . . . .	105
45 Real Symmetric Transfer Function Used in Lowpass Digital Filtering . . . . .	106
46 Hybrid Amplitude Spectrum in dB for the Unfolded Measured Phase Angle on the 8 <sup>th</sup> Steady-State Test . . . . .	107
47 Accumulative Energy Spectrum for the Unfolded Measured Phase Angle on the 8 <sup>th</sup> Steady-State Test . . . . .	108
48 Hybrid Amplitude Spectrum in dB for the Test Signal Amplitude on the 8 <sup>th</sup> Steady-State Test . . . . .	109
49 Accumulative Energy Spectrum for the Test Signal Amplitude on the 8 <sup>th</sup> Steady-State Test . . . . .	110

<u>Figure</u>	<u>Page</u>
50 Filtered Unfolded Measured Phase Angle on the 8 <sup>th</sup> Steady-State Test . . . . .	111
51 Filtered Test Chamber Pressure on the 8 <sup>th</sup> Steady-State Test . . . . .	112
52 Filtered Test Signal Amplitude on the 8 <sup>th</sup> Steady-State Test . . . . .	113
53 Apparent or Uncorrected Burning Rate on the 8 <sup>th</sup> Steady-State Test: Determined by the Use of the Differentiating Digital Filter . . . . .	114
54 Test Signal Amplitude versus Unfolded Measured Phase Angle for the 8 <sup>th</sup> Steady-State Test: Optimized Theory Compared to Filtered Experimental Data . . . . .	115
55 Nondimensional Phasor Plot of the Tip of Vector $\vec{C}$ for the 8 <sup>th</sup> Steady-State Test: Optimized Theory Compared to Filtered Experimental Data . . . . .	116
56 Theoretically Adjusted Burning Rate for the 8 <sup>th</sup> Steady-State Test . . . . .	117
57 Apparent or Uncorrected Burning Rate on the 5 <sup>th</sup> Steady-State Test: Determined by the Use of the Differentiating Digital Filter . . . . .	118
58 Theoretically Adjusted Burning Rate for the 5 <sup>th</sup> Steady-State Test . . . . .	119
59 Actual Phase Angle for the 8 <sup>th</sup> Steady-State Test . . . . .	120
60 Unfolded Measured Phase Angle on the 6 <sup>th</sup> Steady-State Test . . . . .	121
61 Test Signal Amplitude versus Unfolded Measured Phase Angle for the 6 <sup>th</sup> Steady-State Test (Raw Data) . . . . .	122
62 Burning Rate versus Pressure for M6 Propellant . . . . .	123
63 Test Chamber Pressure on Vibration Test 1VT . . . . .	124
64 Test Chamber Pressurization Rate on Vibration Test 1VT . . . . .	125

<u>Figure</u>	<u>Page</u>
65 Change in Relative Amplitude Between the Test and Reference Signals on Vibration Test 1VT . . . . .	126
66 Measured, Theoretical, and Combined Phase Angles for Vibration Test 1VT . . . . .	127
67 Theoretical and Pseudo-Experimental Velocities for Vibration Test 1VT . . . . .	128
68 Test Chamber Pressure on Vibration Test 4VT . . . . .	129
69 Test Chamber Pressurization Rate on Vibration Test 4VT . . . . .	130
70 Change in Relative Amplitude Between the Test and Reference Signals on Vibration Test 4VT . . . . .	131
71 Measured, Theoretical, and Combined Phase Angles for Vibration Test 4VT . . . . .	132
72 Theoretical and Pseudo-Experimental Velocities for Vibration Test 4VT . . . . .	133
73 Test Chamber Pressure on Vibration Test 5VT . . . . .	134
74 Test Chamber Pressurization Rate on Vibration Test 5VT . . . . .	135
75 Change in Relative Amplitude Between the Test and Reference Signals on Vibration Test 5VT . . . . .	136
76 Measured, Theoretical, and Combined Phase Angles for Vibration Test 5VT . . . . .	137
77 Theoretical and Pseudo-Experimental Velocities for Vibration Test 5VT . . . . .	138
78 Test Chamber Pressure on Vibration Test 12VT . . . . .	139
79 Test Chamber Pressurization Rate on Vibration Test 12VT . . . . .	140
80 Change in Relative Amplitude Between the Test and Reference Signals on Vibration Test 12VT . . . . .	141

<u>Figure</u>		<u>Page</u>
81	Measured, Theoretical, and Combined Phase Angles for Vibration Test 12VT . . . . .	142
82	Theoretical and Pseudo-Experimental Velocities for Vibration Test 12VT . . . . .	143
83	Test Chamber Pressure on Vibration Test 10VT . . . . .	144
84	Test Chamber Pressurization Rate on Vibration Test 10VT . . . . .	145
85	Change in Relative Amplitude Between the Test and Reference Signals on Vibration Test 10VT . . . . .	146
86	Measured, Theoretical, and Combined Phase Angles for Vibration Test 10VT . . . . .	147
87	Theoretical and Pseudo-Experimental Velocities for Vibration Test 10VT . . . . .	148
88	Test Chamber Pressure on Vibration Test 11VT . . . . .	149
89	Test Chamber Pressurization Rate on Vibration Test 11VT . . . . .	150
90	Change in Relative Amplitude Between the Test and Reference Signals on Vibration Test 11VT . . . . .	151
91	Measured, Theoretical, and Combined Phase Angles for Vibration Test 11VT . . . . .	152
92	Theoretical and Pseudo-Experimental Velocities for Vibration Test 11VT . . . . .	153
93	Test Chamber Pressure on Vibration Test 6VT . . . . .	154
94	Test Chamber Pressurization Rate on Vibration Test 6VT . . . . .	155
95	Change in Relative Amplitude Between the Test and Reference Signals on Vibration Test 6VT . . . . .	156
96	Measured, Theoretical, and Combined Phase Angles for Vibration Test 6VT . . . . .	157

<u>Figure</u>		<u>Page</u>
97	Theoretical and Pseudo-Experimental Velocities for Vibration Test 6VT . . . . .	158
98	Test Chamber Pressure on Vibration Test 7VT . . . . .	159
99	Test Chamber Pressurization Rate on Vibration Test 7VT . . . . .	160
100	Change in Relative Amplitude Between the Test and Reference Signals on Vibration Test 7VT . . . . .	161
101	Measured, Theoretical, and Combined Phase Angles for Vibration Test 7VT . . . . .	162
102	Theoretical and Pseudo-Experimental Velocities for Vibration Test 7VT . . . . .	163
103	Test Chamber Pressure on Vibration Test 8VT . . . . .	164
104	Test Chamber Pressurization Rate on Vibration Test 8VT . . . . .	165
105	Change in Relative Amplitude Between the Test and Reference Signals on Vibration Test 8VT . . . . .	166
106	Measured, Theoretical, and Combined Phase Angles for Vibration Test 8VT . . . . .	167
107	Theoretical and Pseudo-Experimental Velocities for Vibration Test 8VT . . . . .	168
108	Test Chamber Pressure on Vibration Test 9VT . . . . .	169
109	Test Chamber Pressurization Rate on Vibration Test 9VT . . . . .	170
110	Change in Relative Amplitude Between the Test and Reference Signals on Vibration Test 9VT . . . . .	171
111	Measured, Theoretical, and Combined Phase Angles for Vibration Test 9VT . . . . .	172
112	Theoretical and Pseudo-Experimental Velocities for Vibration Test 9VT . . . . .	173

<u>Figure</u>		<u>Page</u>
113	Test Chamber Pressure on Transient Burning Test 1TBT . . . . .	174
114	Test Chamber Pressurization Rate on Transient Burning Test 1TBT . . . . .	175
115	Change in Relative Amplitude Between the Test and Reference Signals on Transient Burning Test 1TBT . . . . .	176
116	Measured Phase Angle on Transient Burning Test 1TBT . . . . .	177
117	Theoretical and Apparent Experimental Burning Rates for Transient Burning Test 1TBT . . . . .	178
118	Test Chamber Pressure on Transient Burning Test 2TBT . . . . .	179
119	Test Chamber Pressurization Rate on Transient Burning Test 2TBT . . . . .	180
120	Change in Relative Amplitude Between the Test and Reference Signals on Transient Burning Test 2TBT . . . . .	181
121	Measured Phase Angle on Transient Burning Test 2TBT . . . . .	182
122	Theoretical and Apparent Experimental Burning Rates for Transient Burning Test 2TBT . . . . .	183

## LIST OF TABLES

<u>Table</u>	<u>Page</u>
1 Characteristics of Theoretical Pressurizations Used in Finite Element Analysis . . . . .	185
2 Composition of M6 Propellant Used in Microwave Tests . . . . .	185
3 Composition of Pyrotechnic Paste Used in Microwave Tests . . . . .	185
4 Relationships Among Inhibiting Techniques, Pressure, and Non-Planar Burning . . . . .	186
5 Digital Filter Parameters Applicable to All Discrete Data Acquired on a Given Steady-State Burning Test . . . . .	187
6 Digital Filter Parameters Applicable to All Discrete Data Acquired on a Given Dynamic Test . . . . .	187
7 Experimentally Determined Microwave Parameters . . . . .	188
8 Attenuation Constants and Loss Tangents Based Upon Theory and the Total Change in Test Signal Amplitude . . . . .	188
9 Constants from Optimization Solutions . . . . .	189
10 Comparison of Mean Steady-State Burning Rates and Standard Deviations for Raw, Filtered, and Theoretically Adjusted Data . . . . .	189
11 Summary of Results for Steady-State Burning Tests . . . . .	190
12 Propellant Ignition Delays . . . . .	191
13 Physical Circumstances for Dynamic Tests . . . . .	191
14 Pressurization Rate Parameters for Dynamic Tests . . . . .	192
15 Digital Lowpass Cutoff Frequencies for Physical Quantities Relevant to Dynamic Tests . . . . .	192

## NOMENCLATURE

- $A$  = magnitude of a vector representing a microwave fixed reflection
- $A$  = cross sectional area of one rectangular opening in the dual propellant waveguide
- $A_m$  = *relative amplitude* based on the DFT amplitude of a given physical quantity; used in spectral analysis of experimental data
- $A_p$  = cross sectional area of the solid propellant strand
- $A_{rel}$  = change in decibels between the test and reference RF voltage amplitudes on a dynamic test
- $A_t$  = throat area in a flow nozzle
- $a$  = exponent for pressure as used in a steady burning rate correlation
- $a$  = dimension of the longest side in the cross section of a rectangular waveguide; used in defining cutoff wavelength
- $a$  = length of X-band waveguide as per Figure 9
- $B$  = magnitude of a vector representing the microwave reflection from a moving surface which is perpendicular to the incident wave train
- $B$  = coefficient in a steady burning rate correlation

- $B_0$  = constant associated with the initial magnitude of vector  $\vec{B}$
- $b$  = length of X-band waveguide as per Figure 9
- $b_n^d$  = discrete filter weights for differentiating
- $b_n^s$  = discrete filter weights for smoothing
- $C$  = magnitude of a vector resulting from the sum of vector  $\vec{A}$  and vector  $\vec{B}$ ; on steady burning tests  $C$  is the test signal magnitude as measured by the microwave technique
- $C_d$  = discharge coefficient
- $C_{m,i}$  = any one of a set of discrete measured test signal magnitudes
- $C_{t,i}$  = any one of a set of theoretically predicted test signal amplitudes
- $c$  = length of X-band waveguide as per Figure 9
- $c$  = speed of light
- $c_p$  = specific heat at constant pressure
- $c_v$  = specific heat at constant volume
- $D$  = flexural rigidity
- $D$  = diameter
- $d_t$  = flow nozzle throat diameter

- $E$  = total effective energy available from a unit mass of propellant
- $E$  = elastic modulus
- $E_m$  = accumulative energy based on the DFT energy of a given experimental quantity; used in spectral analysis of experimental data
- $e$  = specified tolerance or relative error
- $e$  = internal energy per unit mass
- $\bar{F}_m$  = independent values of the discrete Fourier transform or DFT
- $f$  = frequency
- $f_c$  = cutoff frequency for the  $TE_{10}$  wave in a dielectric filled rectangular waveguide
- $f_i$  = any frequency within the range of nominal system bandwidths
- $f_{REF}$  = reference frequency in the range of nominal system bandwidths
- $f_s$  = sampling frequency of the A/D system
- $f_s$  = shear force
- $f_1$  = end of the pass band for digital filtering
- $f_2$  = beginning of the rejection band for digital filtering
- $G$  = shear modulus

- $g_c$  = Newton's proportionality constant
- $g_m^d$  = individual members of the differentiated output set
- $g_m^s$  = individual members of the smoothed output set
- $H(z)$  = Heaviside unit function; equal to 1 for positive argument and 0 for negative argument
- $H(\omega)$  = real symmetric transfer function associated with an infinite number of filter weights
- $\bar{H}(\omega)$  = real symmetric transfer function associated with a finite number of filter weights
- $h$  = plate thickness
- $h$  = enthalpy
- $K_F$  = force or force constant of propellant
- $k$  = wave number
- $k$  = constant used in defining the size of the transition band for the digital filter
- $\bar{k}$  = effective spring constant
- $k_1$  = spring constant based on  $EA/h$
- $k_2$  = spring constant based on the deflection of a circular flat plate

- $l$  = instantaneous length of a propellant strand affixed within a rectangular waveguide
- $\dot{l}$  =  $dl/dt$ ; instantaneous velocity of the microwave reflecting plane associated with the exposed surface of a solid propellant strand affixed within a rectangular waveguide
- $l_0$  = initial length of propellant strand
- $m$  = mass
- $\dot{m}_p$  = efflux of propellant combustion products in mass per unit time
- $N$  = number of discrete samples of data
- $N$  = associated with the number of filter weights; total number of filter weights equals  $2N + 1$
- $n$  = number of moles
- $P$  = power
- $p$  = pressure
- $q$  = uniformly distributed force per unit area
- $R$  = universal gas constant
- $R_0$  = radius of a circular flat plate
- $\bar{R}$  = gas constant for a particular gas

- $r$  = propellant burning rate
- $r$  = pressure ratio; outlet or low divided by inlet or high static pressure
- $r$  = radius
- $r_{crit}$  = the ratio between the outlet and inlet static pressures at throat sonic velocity
- $T$  = time interval between samples
- $T$  = temperature
- $T_o$  = isochoric adiabatic flame temperature
- $T_{ref}$  = reference temperature
- $t$  = time
- $t$  = transformation variable
- $V$  = volume
- $V$  = voltage
- $V_r$  = magnitude of the vector representing the microwave reflection from the reference plane on a steady-state burning test
- $v_{mr}$  = mechanical response velocity of the surface of the reference propellant strand

- $v_{m t}$  = mechanical response velocity of the surface of the test propellant strand
- $W$  = mass rate of flow through a nozzle
- $w$  = local deflection of a circular flat plate
- $\bar{w}$  = mean deflection of a circular flat plate
- $X$  = dial setting of the digital test channel gain control on the network analyzer
- $X_{null}$  = test channel gain in dB which if internally imposed by the network analyzer would make the output from the relative gain indicator equal to zero volts
- $x$  = mass fraction
- $x_{b,i}^{NEW}$  = individual values of the components in the new base vector  $\{x_b^{NEW}\}$ ; each component relates to an  $x_i$  coordinate axis
- $x_{b,i}^{OLD}$  = individual values of the components in the old base vector  $\{x_b^{OLD}\}$ ; each component relates to an  $x_i$  coordinate axis
- $x_{p,i}$  = individual values of the components in the vector  $\{x_p\}$  which evolves from a pattern move; each component relates to an  $x_i$  coordinate axis
- $x_i$  = coordinate axis; there are  $n$  coordinate axes or dimensions
- $Y$  = instantaneous relative amplitude based on output from the relative gain indicator

- $Y$  = expansion factor
- $Y_o$  = initial relative amplitude based on output from the relative gain indicator
- $Z$  = input impedance of the harmonic frequency converter
- $\alpha$  = angle between a vector representing a microwave fixed reflection and the real axis in a phasor plot
- $\alpha_d$  = attenuation constant for the one-way loss of a  $TE_{10}$  wave in a dielectric filled rectangular waveguide
- $\beta_p$  = phase constant for a propellant filled rectangular waveguide
- $\beta_w$  = phase constant for standard X-band waveguide
- $\gamma$  = ratio of specific heats
- $\gamma_o$  = ratio of specific heats at the isochoric adiabatic flame temperature
- $\Delta\ell_T$  = instantaneous change in length of the test propellant strand
- $\Delta Y$  = instantaneous change in the relative amplitude based on output from the relative gain indicator
- $\Delta\psi_a$  = total change in actual phase angle during complete combustion of the test propellant strand

- $\Delta\psi_m$  = total change in measured phase angle during complete combustion of the test propellant strand
- $\delta$  = loss angle
- $\delta_i$  = fixed exploratory increment parallel to the  $x_i$  coordinate axis
- $\epsilon$  = permittivity
- $\epsilon'$  = real permittivity
- $\epsilon''$  = complex permittivity
- $\epsilon_0$  = permittivity of free space
- $\epsilon_r$  = relative permittivity, commonly called the dielectric constant
- $\eta$  = multivariable objective function
- $\eta_0$  = covolume in Noble-Abel equation of state
- $\lambda$  = nondimensional radian frequency
- $\lambda_c$  = nondimensional end of the radian frequency pass band in the digital filter
- $\lambda_c$  = cutoff wavelength for the  $TE_{10}$  wave in a dielectric filled rectangular waveguide
- $\lambda_{pg}$  = phase wavelength of the  $TE_{10}$  wave in a dielectric filled rectangular waveguide

- $\lambda_R$  = nondimensional sharpness of the radian frequency roll-off after the end of the digital filter pass band
- $\lambda'_R$  = nondimensional parameter which specifies the size of the radian frequency region within which errors between  $H(\omega)$  and  $\bar{H}(\omega)$  are of a specific magnitude
- $\mu$  = attenuation constant based on actual phase angle and relevant to the two-way loss of a  $TE_{10}$  wave in a dielectric filled waveguide
- $\mu'$  = attenuation constant based on propellant test strand length and relevant to the two-way loss of a  $TE_{10}$  wave in a dielectric filled waveguide
- $\mu_0$  = permeability of free space
- $\nu$  = Poisson's ratio
- $\nu$  = frequency
- $\rho$  = density
- $\rho_p$  = density of solid propellant
- $\sigma$  = standard deviation
- $\tau$  = shear stress
- $\tau$  = time

- $\phi_i$  = phase noise at any frequency within the range of nominal system bandwidths
- $\phi_{REF}$  = reference phase noise value in the range of nominal system bandwidths
- $\psi_a$  = actual phase angle; defined in Figures 10 and 11
- $\dot{\psi}_a$  =  $d\psi_a/dt$ ; time rate of change of actual phase angle
- $\psi_{a,f}$  = value of actual phase angle at propellant burnout
- $\psi_{a,i}$  = value of actual phase angle at the start of propellant burning
- $\psi_{a,R}$  = angle between the vector  $\vec{B}_R$  and the real axis in the phasor plot of Figure 10
- $\psi_{a,T}$  = angle between the vector  $\vec{B}_T$  and the real axis in the phasor plot of Figure 10
- $\psi_m$  = measured phase angle; defined in Figures 10 and 11
- $\dot{\psi}_m$  =  $d\psi_m/dt$ ; time rate of change of measured phase angle
- $\psi_{m,i}$  = value of measured phase angle at  $t = 0$  on a vibration test
- $\psi_{m,R}$  = angle between the vector  $\vec{C}_R$  and the real axis in the phasor plot of Figure 10
- $\psi_{m,T}$  = angle between the vector  $\vec{C}_T$  and the real axis in the phasor plot of Figure 10

$\psi_{SR}$  = phase shift caused by a jump in wave impedance at the non-burning propellant surface

$\psi_{ST}$  = phase shift caused by a jump in wave impedance at the burning propellant surface

$\psi_{sum}$  = phase angle constructed from the sum of measured phase angle and the change in theoretical phase angle; relevant only to vibration tests

$\psi_{th}$  = theoretical phase angle defined in equation (35); relevant only to vibration tests

$\omega$  = radian frequency

$\omega_D$  = Doppler angular frequency

$\omega_s$  = radian sampling frequency of the A/D system

$\omega_1$  = radian frequency at the end of the pass band for the digital filter

$\omega_2$  = radian frequency at the start of the rejection band for the digital filter

### Subscripts

a = actual

FL = flow onset from a chamber

- fa = filter-amplifier; 3 dB amplitude point
- h = high pressure side of nozzle
- IG = ignition of propellant
- i = index which takes on the values 1 and 2 in order to identify parameters relevant to the driver and test chambers, respectively
- ℓ = low pressure side of nozzle
- m = measured
- na = network analyzer; 3 dB amplitude point
- pm = phasemeter; 3 dB amplitude point
- R = reference
- sys = nominal system; 3 dB amplitude point
- T = test
- 1 = driver chamber
- 2 = test chamber

**Double Subscripts**

- $i, N_2$  = nitrogen in the driver and test chambers for  $i = 1$  and  $2$ , respectively

$i,p$  = propellant combustion products in the driver and test chambers  
for  $i = 1$  and  $2$ , respectively

$R, dB_m$  = reference, decibels referred to 1 mW

$T, dB_m$  = test, decibels referred to 1 mW

## SI CONVERSION

<u>Multiply</u>	<u>By</u>	<u>To Obtain</u>
BTU/lbm-°R	$4.1868 \times 10^3$	J/kg-K
deg	$1.7453 \times 10^{-2}$	rad
in.	$2.5400 \times 10^{-2}$	m
in. <sup>2</sup>	$6.4516 \times 10^{-4}$	m <sup>2</sup>
in. <sup>3</sup>	$1.6387 \times 10^{-5}$	m <sup>3</sup>
in.-blf	$1.1298 \times 10^{-1}$	J
lbf/in. <sup>2</sup>	$6.8948 \times 10^3$	Pa
lbm/in. <sup>3</sup>	$2.7680 \times 10^4$	kg/m <sup>3</sup>
°R	$5.5556 \times 10^{-1}$	K

## 1.0 INTRODUCTION

The immediate objectives of this research effort were twofold: first, to measure the burning velocity of a solid propellant responding within a steady high pressure environment via a microwave Doppler/phase shift technique similar to that employed by other researchers<sup>(1-5)</sup>\* but in relatively low pressure investigations; and secondly, to further modify this microwave approach and evaluate the ability of the new system to distinguish the combustion response from the combined combustion/mechanical response of a solid propellant surface when burning within a highly transient pressure environment. The primary reason for implementing a microwave technique was the potential for acquiring the one-dimensional motion of a steady or dynamically burning propellant strand via essentially continuous, direct measurement.

In the case of transient burning rate determination, the current primary tool is the closed bomb or closed chamber test<sup>(6,7)</sup> which is inherently indirect since it relates the experimentally observed pressure-time data to the burning rate by an interactive framework of assumed theoretical expressions for the thermodynamic and thermochemical processes taking place in a closed volume. In a recent publication,<sup>(8)</sup> a comparison was made of the theory, data reduction techniques, and overall methodology utilized by researchers active in closed bomb work. The beauty of a direct technique for determining solid propellant burning rates in rapidly varying pressure environments is that the acquired data would show the deviation from steady-state predictions of burning behavior and could be used to evaluate and improve theoretical models of the instantaneous regression rate of solid propellant under rapid pressure transient. Such models of dynamic burning have been numerically compared<sup>(9-11)</sup> for a given imposed pressure variation at the edge of

---

\*Parenthetical references placed superior to the line of text refer to the bibliography.

the flame zone. Although strong differences in the dynamic burning rate predictions were observed, no attempt could be made to identify which was even qualitatively correct because of a lack of existing experimental data.

An excellent review article on the theory of dynamic burning of solid propellants has recently been published.<sup>(12)</sup> The dynamic burning effect is simply the departure of the instantaneous burning rate from the steady-state value corresponding to the instantaneous pressure. This effect is physically caused by the finite time interval required for the temperature profiles inside the condensed phase, and possibly the reaction zone, to adapt to the transient gas phase pressure. When the characteristic time of the pressure transient is of the same order or less than the characteristic time of the unburned solid phase, dynamic burning behavior becomes important.

A variety of direct measurement techniques have been utilized for the acquisition of solid propellant burning rates. Some of these approaches were reviewed in detail in reference 2 and are briefly noted in the following list.

1. Probes are embedded in the propellant at given distances and detect the arrival time of the burning surface. The sensing elements can be thermocouples, fuse wires, conducting bridges, or anything which detects the passage of the burning plane.
2. A positioning servomechanism feeds a propellant strand into a combustion chamber at the same rate at which it is consumed. Various sensing systems can be used to locate the burning surface and supply an accurate feedback signal for the servomotor.
3. After leaving a source and passing through a test rocket motor in which a solid propellant grain is burning, a beam of x-rays impinge

upon a fluorescent screen of an image intensifier. The fluoroscopic x-ray images are then photographed by a movie camera.

4. A propellant strand is used as the dielectric material in a capacitor which is part of the total capacitance of a tuned L-C circuit in an electronic oscillator. The variation in capacitance caused by burning is proportional to the change in strand length.
5. In the ultrasonic pulse-echo technique, a high frequency sound pulse is transmitted through an acoustic spacer and a mating propellant sample, reflects from the fixed and moving interfaces, and returns to the original source where time dependent electrical signals are produced and displayed on a CRT. High speed photography of the screen coupled with a linear relationship between the distance traveled by the two displayed signals allows the determination of the actual propellant length burned.
6. In the microwave interferometric or CW radar approach, a microwave signal at a fixed source frequency is passed through a propellant strand and reflects from the burning surface. The Doppler shifted reflected signal is mixed with a portion of the original signal to produce a traveling wave with amplitude maxima which occur at a frequency proportional to burning rate.

All of the above mentioned direct measurement techniques give satisfactory burning rate results for steady and near steady-state conditions. In fact, the classical method of determining steady-state propellant burning rates is approach number one, better known as the strand burner technique. However, none of these approaches has the extremely small propellant length resolution and rapid response time required to obtain regression rate data under highly transient pressure conditions. To gain

some appreciation of the order of magnitude of such stringent length resolution and response time requirements, consider the burning response of a typical gun propellant during a pressurization from 1500 psig to 7500 psig over the course of 6 msec. The average pressurization rate is  $1 \times 10^6$  psi/sec and the propellant will regress 0.0055 in. if it burns according to a steady-state correlation and the instantaneous pressure. If knowledge of the strand length at 14 spatial locations would satisfactorily define the combustion response during the pressurization, then the required length resolution must be  $3.93 \times 10^{-4}$  in. ( $\cong 10 \mu\text{m}$ ) or less. The strand length data must be acquired at a rate of 2.33 kHz or higher. Only the microwave Doppler/phase shift technique exhibits the apparent potential for meeting the rigorously exacting response time and length resolution requirements fundamental to direct burning rate determination during a rapid pressure transient.

## 2.0 DESIGN RATIONALE

To meet the objective of acquiring high pressure steady-state burning rates of solid propellant via the microwave technique, the primary obstacle to overcome was the requirement of containing high pressure gas inside the combustion fixture while simultaneously introducing the guided microwaves into the non-burning base end of the propellant strand. In the case of transient burning rate determination, however, the problems transcend those associated with sealing a large volume pressure vessel. The motion of a burning propellant surface subjected to a pressure transient will be the result of both a combustion response and a purely mechanical response. The magnitude of this mechanical response depends upon the geometry and rheological properties of the propellant strand, the sample confinement characteristics, and the pressurization or depressurization rate. Hence, the primary obstacle to progress in transient burning rate measurements was initially identified as the inability of the previously utilized microwave techniques to observe only the combustion response.

In the approach taken to rectify this deficiency, two guided microwave signals oscillating at the same source frequency are simultaneously passed through the base ends of two identical propellant strands and allowed to reflect from the opposite end of each strand. In one strand the signal is reflected from a burning surface and becomes the test signal. In the other strand the signal is reflected from the non-burning surface and becomes the reference signal. If the reflecting surfaces of each propellant strand are exposed to the same pressure environment and if each strand has identical confinement geometry, then the reflecting surfaces should ideally undergo the same mechanical response to the transient pressure force. It is, however, only the burning surface which should experience the additional motion caused by the combustion response. By continuously comparing the phase angle of the test signal with the phase angle of the reference signal, a relative phase angle is

obtained. The rate of change of this relative phase angle is directly proportional to the burning rate of the propellant.

The pressure transient affecting the microwave reflecting surfaces of the propellant samples was to be predominantly the result of a precise external mass addition of inert gas rather than a pressure rise caused by the deflagration of a propellant strand. This approach insures that the complete pressure history is the result of an imposed, experimentally controllable action. Consequently, the test vehicle was envisaged as a combustion fixture having two independently pressurizable chambers connected by a controllable flow path. The larger chamber was identified as the driver chamber while the microwave reflecting propellant surfaces were to be within a small volume test chamber.

To assist in establishing the final geometric configuration of the dual-chambered combustion fixture, a gas dynamic model was formulated and utilized to predict combustion fixture performance. This theoretical model is described in Appendix C. Use of the model allowed parametric investigations of all important system parameters; for example, consideration was given to initial temperatures and pressures and gaseous compositions in the two chambers, the size of the connecting flow nozzle, chamber initial volumes, propellant sample burning rate and cross sectional area, and ignition and flow onset times.

One of the more important outputs from the gas dynamic model was the pressure history in the test chamber. As shown in Figures 1 and 2, there was reasonable agreement between such theoretical predictions and experimental data. With respect to these figures, the pressurization of the test chamber was accomplished by an influx of nitrogen gas which began coming from the driver chamber at 1.57 msec. In the actual vibration tests no propellant was burning. However, if an M6 propellant strand of cross sectional area  $0.1186 \text{ in.}^2$  had been ignited at  $t = 1.57 \text{ msec}$  and had burned planarly in accordance with a conventional

burning rate law ( $r = Bp_2^a$ ), the theoretically predicted transient test chamber pressures would have been only very slightly higher than those predicted pressures indicated in Figures 1 and 2.

In order to gain some semi-quantitative and qualitative information about the one-dimensional mechanical response velocity of the exposed surface of a propellant strand when subjected to forces caused by transient gas pressure, a finite element analysis was applied to the structural idealization presented in Figure 3. A detailed description of this structural idealization can be found in Appendix D. Two aspects of the schematic in Figure 3 should, however, be reiterated here. First, interconnection nodes 52 through 101 in conjunction with the attached springs were intended to simulate the rigidizing effect upon the dielectric material caused when it is bonded over its entire perimeter area to the inside waveguide walls. Secondly, the transient force  $F(t)$  applied to interconnection node number one was calculated by taking the product of cross sectional waveguide area and a time dependent test chamber pressure predicted by the gas dynamic model.

Shown in Figures 4-7 are the velocities of interconnection node number one when subjected to four increasingly severe theoretical test chamber pressurizations. Each of these pressurizations was a prediction from the gas dynamic model in which the following parameters or expressions had been fixed: propellant ignition and flow onset times (both at  $t = 0$ ), test and driver chamber initial volumes (2.11 in.<sup>3</sup> and 88.00 in.<sup>3</sup>, respectively), initial chamber temperatures (both 540°R), initial chamber gaseous compositions (both 100% nitrogen), the explicit dependence of propellant burning rate on test chamber pressure, and strand cross sectional area (0.1186 in.<sup>2</sup>). Those parameters which were varied in order to create the different pressurizations were the flow nozzle throat area and the initial pressures in the test and driver chambers. Presented in Table 1 are the identifying characteristics of the four pressurizations utilized in calculating the predictions shown in Figures 4-7.

Although intuitively obvious, the results in Figures 4-7 emphasize that the magnitude of the mechanical response velocity of the first interconnection node will become increasingly large as the severity of the transient loading increases. Even for the extremely rigid structural idealization shown in Figure 3 and discussed in Appendix B, the theoretically predicted mechanical response velocity becomes roughly the same as the propellant burning rate when the magnitude of the pressurization rate approaches that relevant to gun interior ballistics. Further insight into propellant strand mechanical response can be gained by examining a highly compliant, though not very realistic, structural idealization of the propellant in the waveguide. This idealization was constructed by eliminating those springs shown in Figure 3 which were within segments 51 through 87. Application of the same transient loading associated with Figure 4 to this soft system yielded the mechanical response velocity shown in Figure 8. The maximum velocity indicated in Figure 8 is 167 times larger than the maximum velocity shown in Figure 4. The information in Figure 8, as well as that in the preceding four figures, is based upon an undamped response.

Use of the finite element model in conjunction with the gas dynamic model gave considerable insight into the magnitude of the mechanical response of a solid propellant strand when subjected to a transient loading. This investigation clearly demonstrated that the mechanical response velocity is highly sensitive to strand confinement geometry. Thus, it was apparent that it would be a very difficult task to insure the sameness of mechanical response in the twin strand differential system. As based upon the theoretical investigation, the physical situation thought to give the best chance for realizing the desired mechanical response similarity was that wherein the complete perimeter area of each of the two propellant strands was epoxy-bonded to the inside waveguide walls.

### 3.0 THEORETICAL MODEL

A schematic of the twin strand differential system along with the relevant voltage waveforms is shown in Figure 9. In expressing the voltages of the reflected test and reference signals at the monitoring points, all wave impedance mismatches within each arm except those at the burning and non-burning surfaces were assumed to be of negligible magnitude. As depicted in this simplified figure, standard X-band waveguides lead to and go from the propellant samples while the strands themselves fill rectangular waveguides of special cross sectional dimension. Hence, two separate phase constants,  $\beta_w$  and  $\beta_p$ , should be used in accounting for the accumulative phase angle differences between the source signal and the two reflected signals. The difference in phase angle between the reflected signals is

$$\psi_a = \beta_w(b_T - b_R) + \beta_w(c_T - c_R) + (\psi_{ST} - \psi_{SR}) + 2\beta_p(\ell_T - \ell_R) \quad (1)$$

where  $\psi_{ST}$  and  $\psi_{SR}$  are the phase shifts caused by a jump in wave impedance at the burning and non-burning surfaces, respectively.

If the lengths  $b_T$ ,  $b_R$ ,  $c_T$ , and  $c_R$  are constant and if  $\psi_{ST}$  and  $\psi_{SR}$  do not change with time, then taking (d/dt) of equation (1) yields

$$\dot{\psi}_a = 2\beta_p(\dot{\ell}_T - \dot{\ell}_R) \quad (2)$$

Assume that motion of the burning surface results from both a propellant deflagration and a mechanical or vibratory response. Let the non-burning surface undergo motion caused by only a mechanical response. Thus,

$$\dot{\ell}_T = -r_a + v_{mT} \quad (3)$$

$$\dot{\ell}_R = v_{mR} \quad (4)$$

where the burning rate  $r_a$  is considered positive if  $\ell_T$  decreases during combustion. If  $v_{mR} = v_{mT}$  or if both mechanical responses are zero, then

$$\dot{\psi}_a = -2\beta_p r_a \quad (5)$$

The phase constant is given by

$$\beta_p = \frac{2\pi}{\lambda_{pg}} \quad (6)$$

where  $\lambda_{pg}$  is the wavelength of the microwave signal in the propellant filled waveguide. Rearranging equations (5) and (6) allows the burning rate to be expressed as

$$r_a = -\frac{\lambda_{pg}}{720^\circ} \frac{d\psi_a}{dt} \quad (7)$$

Assume that  $v_{mR}$  and  $v_{mT}$  are both zero and let  $\ell_T = \ell_o$  at the start of burning while  $\ell_T = 0$  at sample burnout. Then integrating equation (2) over the course of a complete test strand burn allows the total change in relative phase angle to be expressed as

$$\Delta\psi_a = (\psi_{a,i} - \psi_{a,r}) = 2\beta_p \ell_o \quad (8)$$

The phase wavelength can now be written as

$$\lambda_{pg} = \frac{4\pi\ell_o}{\Delta\psi_a} \quad (9)$$

Based upon microwave theory,<sup>(28)</sup> the phase wavelength can be expressed as

$$\lambda_{pg} = \frac{c}{f} (\epsilon_r)^{-1/2} \left[ 1 - \left( \frac{f_c}{f} \right)^2 \right]^{-1/2} \quad (10)$$

For the dominant  $TE_{10}$  wave in a dielectric filled rectangular waveguide, the cutoff frequency is

$$f_c = \frac{c}{\lambda_c} = \frac{c}{2a} (\epsilon_r)^{-1/2} \quad (11)$$

If the non-burning surface is at rest, then the previous development reduces to a statement of the Doppler effect which is the basis of CW radar.<sup>(29)</sup> The Doppler angular frequency is given by

$$\omega_D = 2\pi(f_R - f_T) = \frac{d\psi_a}{dt} = \frac{4\pi}{\lambda_{pg}} \frac{d\ell_T}{dt} \quad (12)$$

where  $(f_R - f_T)$  is known as the beat frequency. In using the conventional CW radar approach, the velocity of the moving reflecting surface is determined by the measurement of the beat frequency. However, the time interval required to determine the beat frequency is much too long to have any practical utility in measuring solid propellant burning velocity in a dynamic pressure environment. For example, if the wavelength of the microwave signal in the propellant filled waveguide was 1 in. and if the propellant burning rate was 1 in./sec, then these typical values would produce a beat frequency of only 2 Hz.

Shown in Figure 10 is a phasor diagram relevant to the schematic presented in Figure 9. However, the situation depicted in Figure 10 is more general since the previously neglected wave impedance mismatches within each branch of the system are now assumed to cause fixed reflections of significant magnitude. Because of the presence of  $\vec{A}_T$  and  $\vec{A}_R$ , the test and reference signals are no longer composed of only the microwave reflections from the moving surfaces,  $\vec{B}_T$  and  $\vec{B}_R$ . Rather, the test and reference signals,  $\vec{C}_T$  and  $\vec{C}_R$ , respectively, must be considered as resultant phasors. The phase angle difference between the test and reference signals is  $\psi_m = (\psi_{m,T} - \psi_{m,R})$ . If it is assumed that the fixed reflections are very small compared to the magnitudes of  $\vec{B}_T$  and  $\vec{B}_R$ , then  $\psi_m$  can be equated to  $\psi_a = (\psi_{a,T} - \psi_{a,R})$ . It was precisely this assumption which was used in arriving at equation (7). Since the experimental technique was intended to exploit equation (7) but could only measure  $\psi_m$ , it was very important to try to minimize the magnitude of the undesirable fixed reflections.

Shown in Figure 11 is a less complicated phasor diagram representing the microwave process when a single solid propellant strand burns planarly within a waveguide. For simplicity, this phasor has been constructed by considering that the reference signal was of constant magnitude and that it was rotating at the source radian frequency. Such a reference signal could easily be achieved if the reference strand in Figure 9 was replaced with a fixed waveguide short that was subject to

no mechanical excitation. In Figure 11 the test and reference signals are represented by  $\vec{C}$  and  $\vec{V}_r$ , respectively. Assuming that the mechanical response of the propellant strand is negligible when compared to its combustion response, the governing equations relevant to this phasor diagram can be expressed as follows:

$$A \sin \alpha + B \sin \psi_a = C \sin \psi_m \quad (13)$$

$$A \cos \alpha + B \cos \psi_a = C \cos \psi_m \quad (14)$$

$$B = B_0 \exp(\mu \psi_a) \quad (15)$$

In phasor notation these equations reduce to

$$Ae^{i\alpha} + B_0 e^{\mu \psi_a} e^{i\psi_a} = C e^{i\psi_m} \quad (16)$$

As before, the measured test microwave signal is the resultant of the fixed background field and the instantaneous microwave field returning from the moving reflective surface. The magnitude of this latter reflected wave depends upon the following three parameters:  $\mu$  the attenuation constant for the microwaves in the propellant fixed waveguide,  $\psi_a$  the instantaneous value of the relative phase angle, and  $B_0$  a constant associated with the initial conditions. The constant magnitude  $A$  and the constant phase angle  $\alpha$  define the fixed microwave reflection.

To determine the actual propellant regression rate, equation (7) ought to be applied but only  $\dot{\psi}_m$  can be measured in the actual test circumstance. The apparent or measured burning rate is

$$r_m = - \frac{\lambda_{pE}}{720^\circ} \frac{d\psi_m}{dt} \quad (17)$$

However, as derived in Appendix E, there is a relationship between  $\dot{\psi}_a$  and  $\dot{\psi}_m$  which is

$$\dot{\psi}_a = \frac{\dot{\psi}_m}{\left[ 1 - \frac{A}{C} \cos(\psi_m - \alpha) + \frac{\mu A}{C} \sin(\psi_m - \alpha) \right]} \quad (18)$$

This equation clearly shows that the measured burning rate,  $r_m$ , exactly agrees with the actual burning rate,  $r_a$ , only when  $A = 0$ .

#### 4.0 NONLINEAR PARAMETER ESTIMATION

Interpreting the measured instantaneous burning rate,  $r_m$ , in the presence of significant fixed reflections can be quite difficult. For the physical situation represented by the phasor diagram in Figure 11, a technique for extracting the actual burning rate,  $r_a$ , can be derived. Eliminating C from equations (13-15) yields

$$B_o \exp(\mu\psi_a)[\sin(\psi_m - \psi_a)] + A[\sin(\psi_m - \alpha)] = 0 \quad (19)$$

If  $\mu$ , A,  $B_o$ , and  $\alpha$  are at constant values for a given test, then for any specific  $\psi_m$  value equation (19) becomes a function of only  $\psi_a$ ; that is,

$$F(\psi_a) = 0 \quad (20)$$

Hence, for each measured phase angle,  $\psi_m$ , when all other parameters have values, there is some actual phase angle,  $\psi_a$ , which satisfies equation (20). As shown clearly in Figure 12, equation (20) has multiple  $\psi_a$  roots. Also indicated in this figure is the fact that for some input parameters  $F(\psi_a)$  exhibits no zero crossings in certain portions of the domain of  $\psi_a$ .

Newton's method<sup>(30)</sup> can be used to approximate the root to within a small uncertainty. The algorithm terminates when the absolute value of the change in the root approximation from one iteration to the next falls below a small specified tolerance  $\epsilon$ . To find the correct root of equation (20) for a given  $\psi_m$  and a specific four constant parameter set, the root finding procedure should be started

with a good first approximation. For regions close to or at the propellant burnout stage, a reasonable assumption is that  $\psi_a \cong \psi_m$ , and this should be the first guess. Each correct root must allow the following physical constraints to be upheld:

$$C \geq 0 \quad (21)$$

$$\left. \begin{array}{l} \sin(\psi_a - \psi_m) \\ \sin(\psi_m - \alpha) \\ \sin(\psi_a - \alpha) \end{array} \right\} = \text{same sign} \quad (22)$$

Note that relation (21) is dominant in the constraint hierarchy. When applying equations (22), which are based upon the Law of Sines for a plane triangle, it is presupposed that A, B, and C are positive magnitudes. When any of the angle differences in equations (22) are small (say less than  $\epsilon$ ), then certain knowledge that equations (22) are upheld becomes lacking. When this particular situation occurs, the  $\psi_a$  root is fixed until new values of  $\psi_m$  allow increases in the relevant angle differences.

With the  $\psi_a$  root established for the given  $\psi_m$ , a theoretical value of C can be calculated. However, there is also a measured value of C for each  $\psi_m$ . These facts form the basis for the optimization process to be described. Define the objective function to be minimized as

$$\eta = \sum_i (C_{t,i} - C_{m,i})^2 \quad (23)$$

The nonlinear parameter estimation of the constants  $\mu$ ,  $A$ ,  $B_0$ , and  $\alpha$  is achieved by minimizing the degree of disparity between a set of discrete measured  $C$  values and the corresponding theoretical  $C$  values. When all  $\psi_m$  in the set monotonically increase or decrease, the objective function depends only upon the four parameters  $\mu$ ,  $A$ ,  $B_0$ , and  $\alpha$ . Hence,  $\eta$  is a multivariable objective function amenable to minimization by direct search techniques. One such numerical scheme is the Hooke and Jeeves<sup>(31,32)</sup> pattern search; it is this approach which is described briefly below.

A direct search method (the term "direct search" having been coined by Hooke and Jeeves) requires only the evaluation of the objective function at a particular location. This is in contrast to the gradient techniques which require both function and gradient values to be found at any position. In utilizing the Hooke and Jeeves pattern search to locate the optimum of  $\eta$ , both the objective function and the system variables are, for practical purposes, considered unrestricted even though each of the four independent variables is constrained to be within a given search interval. Since the function  $\eta$  is very well behaved and the inequality restrictions are set to be very far from the expected local optimum, the numerical optimization can be considered essentially unrestricted in the primary search space.

A generalized sequential procedure for implementing the Hooke and Jeeves search is given by the following four items.

1. Select from within the  $n$ -dimensional search space a set of feasible values for the independent variables. Although this is the initial base vector, it is also an old base vector  $\{x_b^{OLD}\}$ .
2. Sequentially explore along each of the  $x_i$  direction the locations which are defined by

$$x_{b,i}^{OLD} \pm \delta_i \quad (24)$$

Temporarily move the new base vector to each position for which the objective function is improved. Once this local search is performed for all n-dimensions in turn, the exploratory part of any stage is complete and a new base vector  $\{x_b^{NEW}\}$  will have been established. If, after an exploratory stage, it is found that  $\{x_b^{NEW}\} = \{x_b^{OLD}\}$ , the fixed step sizes  $\delta_i$  relevant to each  $x_i$  should be reduced and step 2 should be repeated.

3. If  $\{x_b^{NEW}\} \neq \{x_b^{OLD}\}$ , then make the pattern or extrapolative move given by

$$\{x_p\} = 2\{x_b^{NEW}\} - \{x_b^{OLD}\} \quad (25)$$

Two cases arise after such a move:

- a. If the objective function shows an improvement at  $\{x_p\}$ , then redesignate the last  $\{x_b^{NEW}\}$  as  $\{x_b^{OLD}\}$  and go back to step 2 after noting that now  $x_{p,i}$  must be substituted for  $x_{b,i}^{OLD}$  in equation (24).
  - b. If there is no improvement in the objective function, then return to step 2 after noting that the next local exploration will begin from the last  $\{x_b^{NEW}\}$  which is the best point yet found. Hence, when back at step 2, the current  $x_{b,i}^{NEW}$  must be used in place of  $x_{b,i}^{OLD}$  in equation (24). Essentially, all past successes and failures are forgotten and a fresh start of the algorithm begins.
4. The search sequence terminates after the fixed step sizes  $\delta_i$  have been reduced to some acceptably small values and the local explorations have failed to find an enhancement of the objective function.

The acceleration in distance, which is the prime advantage of the Hooke and Jeeves pattern search, is apparent in item three above. Thus, although the technique starts cautiously with relatively short pattern moves, the extrapolated length rapidly increases with repeated successes.

After the Hooke and Jeeves pattern search has been used to determine the optimized constants applicable to a given situation, the denominator of the right-hand-side of equation (18) can be computed. In this computation, let the  $C$  value relevant to each  $\psi_m$  be considered the theoretical prediction. With  $\dot{\psi}_m$  experimentally measured,  $\dot{\psi}_a$  can be calculated from equation (18) and used in equation (7) to find  $r_a$ . Hence, for the physical situation represented by Figure 11, a method has been derived for extracting the actual burning rate from experimental data biased by the presence of unwanted, microwave fixed reflections.

## 5.0 EXPERIMENTAL APPARATUS AND TEST PROCEDURES

A schematic of the overall experimental system is shown in Figure 13. The microwave source was an amplitude-leveled, backward-wave oscillator (BWO) set to operate at 10 GHz and stabilized by a phase-locked synchronizer to 1 part in  $10^8$  per second. All equipment relevant to the experiments is identified in detail in Appendix F. An RF power meter and a digital frequency meter were used to give visual verification of the stabilized frequency and output power constancy of the microwave source. A traveling-wave-tube microwave amplifier (TWT), delivering 1 watt output for an input of 1 mW or less, was incorporated in the system to insure that sufficient RF power was always available to conduct an experiment. As indicated in Figure 13, the amplified microwave source signal was equally split by a 3 dB directional coupler and passed into the test and reference arms. On the source side of this coupler, RG-9A/U coaxial cable was used to connect the components. Within each main arm of the microwave circuit, the microwave signal was transmitted via standard X-band waveguide except for a 4.5 in. segment of semi-rigid coaxial cable linking the E-H tuner and the combustion fixture.

With the exception of a variable phase shifter located in the first part of the test arm, the two sides of the microwave circuit are identical. As the microwave signal progresses through an arm of the circuit, 10% of its power is diverted via a 10 dB directional coupler into a cancellation loop containing a variable attenuator and a variable phase shifter. Before being fed back into the main arm via a 3 dB reversed directional coupler, both the amplitude and phase of this diverted signal can be adjusted. At the 3-port circulator, the main signal is directed through an E-H tuner and on to the combustion fixture where it is reflected and begins the return trip to the circulator. After redirection by the 3-port circulator, the reflected signal picks up the signal from the cancellation loop and passes through a variable attenuator which was used to establish the initial input power to the harmonic frequency converter. Ferrite isolators, which permit microwaves to pass in only one

direction, were used in both main arms to reduce the effect of undesirable reflections upon the RF signals of interest. The isolator located just downstream from the microwave source prevented the entry of potentially damaging reflections into the BWO.

The reflected test and reference RF signals are first processed by two Hewlett-Packard instruments, the Model 8411A harmonic frequency converter and the Model 8410A network analyzer. These two devices working in combination have a nominal bandwidth of 10 kHz and convert the RF signals being measured into two 278 kHz sine waves which carry the same relative amplitude and phase information as the original RF signals. The amplitude relationship between the 278 kHz IF signals was determined by a Hewlett-Packard model 8413A phase-gain indicator, a plug-in to the network analyzer which also has a 10 kHz nominal bandwidth. The voltage output from this relative gain indicator was proportional to the ratio of the input RF voltages at the test and reference sides of the harmonic frequency converter. The dc output signal from this instrument has a scale factor of 50 mV/dB where the number of decibels is given by  $20 \log_{10}(V_T/V_R)$ . The relative gain indicator yields positive analog voltage and clockwise meter deflection for ratios of 0 to +30 dB and negative voltage and counterclockwise meter deflection for ratios of 0 to -30 dB.

The reference channel output from the network analyzer is a 278 kHz sine wave with amplitude fixed at about 2 volts peak-to-peak. The 278 kHz IF signal coming from the test channel output of the network analyzer has an amplitude which can vary between 0 and 3.5 volts RMS; the specific amplitude value depends upon the test channel RF input and a preselected test channel gain. This test channel gain is relative to the reference channel and is established by the use of precision digital control dials located on the network analyzer front panel; they have a 69 dB range and a 1 dB resolution. For the particular network analyzer used in the experiments, a digital gain control setting of 25 dB was needed to make the

meter on the relative gain indicator read about 0 dB when test and reference signals of equal RF power entered the harmonic frequency converter.

The phase angle relationship between the two 278 kHz IF signals which came from the network analyzer was measured by a Dranetz Engineering Labs, Inc., phasemeter. This unit was specially modified by the manufacturer to have a bandwidth of 7.32 kHz. The analog output of this phasemeter is related to phase angle by the scale factor 10 mV/deg while the RMS phase noise on the output signal is about 4 millidegrees when operating at full bandwidth. At 278 kHz the reference input to the phasemeter can vary from 1.8 to 2.6 volts peak-to-peak. During this condition of the reference input, the 278 kHz test input to the phasemeter should be between 17 and 177 millivolts RMS for best results. To realize this amplitude window on the test channel input to the phasemeter, it was necessary to amplify the 278 kHz IF input signal. Two means of amplification were available; either the digital test channel gain control integral to the network analyzer could be used or external amplification of the test IF signal could be utilized. As indicated by Figure 13, the latter approach was taken. Use of an external 20 dB amplifier allowed the tracking of a much larger increase in test signal RF amplitude by the relative gain indicator than was possible when the internal gain control was utilized. Before entering the test channel of the phasemeter, the output from the 20 dB amplifier was conditioned by the simple passive highpass filter shown in Figure 14.

The phasemeter analog output ranges were  $\pm 1.8$  volts dc or 0 to 3.6 volts dc depending upon manual selection. Output from the phasemeter was conditioned by a filter-amplifier having 16 selectable lowpass settings. This device was fabricated in-house and its electrical schematic is shown in Figure 15. The filter bandwidth was selected to be compatible with the chosen sampling frequency of the analog-to-digital (A/D) data acquisition system. This system was built in-house and was used to record the transient voltage outputs from the phasemeter, the relative gain indicator,

and the two piezoelectric quartz pressure transducers mounted in the combustion fixture. Major components of the A/D data acquisition system are identified in Appendix F. On the 12-bit A/D channels the minimum time between samples was 30  $\mu$ sec while on the 15-bit channel it was 10  $\mu$ sec. This corresponds to maximum through-put rates of 33.3 kHz and 100 kHz, respectively. The intervals between sampling by the A/D system were selectable as follows: from 10  $\mu$ sec to 100  $\mu$ sec in 10  $\mu$ sec steps, from 100  $\mu$ sec to 1 msec in 100  $\mu$ sec steps, from 1 msec to 10 msec in 1 msec steps, and from 10 msec to 90 msec in 10 msec steps. For the experiments, the input voltage ranges on the 12-bit channels were  $\pm 2.5$  volts and 0 to 5 volts while on the 15-bit channel the input voltage range was 0 to 4 volts. Consequently, voltage resolutions were 1.22 mV and 0.122 mV for the 12-bit and 15-bit channels, respectively. The maximum number of discrete samples which could be stored in memory was 2048 for each of the four A/D channels.

After a test, all discrete data was extracted from the static random access memory elements, passed through an audio cassette interface of in-house construction, and fed to an input jack of a cassette-type tape recorder within which was mounted on audio cassette tape of certified data quality. In the cassette interface, frequency shift keying (FSK) translates the high and low voltage logic levels into two different analog frequencies each of which is maintained for a certain number of cycles. If the audio cassette tape were to be played in a sound system, a listener would hear a continuously changing pattern of two different tones. To put the test data into a more accessible format, the audio cassette tape was replayed while the analog signal from an output jack of the tape recorder fed the cassette interface which in turn provided logical binary voltages to a computer. This computer was a model PDP-11/45 manufactured by Digital Equipment Corporation; it was used to construct a 9-track digital tape upon which was written the discrete voltages representing the four channels of experimental data. This 9-track tape was utilized by a computer program which ran on a CDC-6700 computer and put the data onto a demountable disk pack. Once on the disk, the data could be read via conventional FORTRAN read statements and used in further data reduction procedures.

As indicated by Figure 13, the four channels of experimental data were also recorded on a direct-writing analog recorder having a bandwidth of 125 Hz. This device was used as a precautionary backup for the A/D system, to record events past the maximum sampling duration of the A/D system, and to yield data with which calculations could be made of the initial pressures in the combustion fixture chambers. This data, which was the analog output of the two charge amplifiers, resulted from a sudden combustion fixture depressurization and the associated stress relaxation in the quartz crystals mounted in the pressure gages. The depressurization to atmospheric conditions was initiated immediately after a steady or dynamic test. Given the difference between the initial grounded or zero voltage and the negative voltage at pressure equilibrium with the atmosphere, the pressure on a gage at test start could be easily computed.

To initiate sampling by the A/D system and to trigger the capacitive discharges causing propellant ignition and activation of the valve inside the combustion fixture, a time delay sequencer was utilized. This instrument was fabricated in-house and its electrical schematic is shown in Figure 16. The time delay sequencer controlled the time of occurrence and sequence of three events. One of five selectable time resolutions, the minimum being 1  $\mu$ sec, could be independently established for each of two digitally selected delay periods. The two channel capacitive discharge circuit of in-house construction is shown in schematic form in Figure 17.

The combustion fixture shown in Figure 18 is comprised of two independently pressurizeable chambers separated by any one of three flow nozzles having throat diameters of 0.05, 0.10, and 0.15 in., respectively. A flow nozzle throat is sealed by a valve which is opened by the action of two m75-A pressure cartridges manufactured by Teledyne McCormick Selph Company. The test chamber contains the dual waveguide which holds the twin propellant strands. A given transient pressurization is caused by the flow of nitrogen gas from the large driver

chamber. The time of flow onset from the driver chamber as well as hot wire initiation for propellant ignition can be carefully controlled by use of the time delay sequencer. As a safety precaution against an overpressure situation, a rupture-disc assembly was positioned in the sidewall of the test chamber as shown in the offset section view in Figure 19. The large cylindrical combustion fixture housing and most internal components were constructed from AISI 4340 steel. Because of the anticipated problem with surface corrosion, all of these steel parts were coated with an electrolytic deposit of nickel.

A dual propellant waveguide was made of copper and the opening in each side was 4.000 in. long and had a rectangular cross section of  $0.298 \times 0.398$  in. Three such waveguides were fabricated. The cutoff frequency in an air filled waveguide of this dimension is 14.8 GHz. To determine the dielectric constant of the propellant chosen for use in the experiments, the shorted transmission line method was utilized.<sup>(33,34)</sup> Under conditions of room temperature and atmospheric pressure, the dielectric constant of M6 propellant was measured to be 3.238 at 10.0 GHz. When M6 fills the propellant waveguide the cutoff frequency is 8.24 GHz. By operating at 10.0 GHz only the dominant  $TE_{10}$  mode will propagate in the waveguide filled with M6 while no wave propagation will occur if the waveguide is empty. The composition, excluding residual volatiles, of the M6 propellant used in the experiments is presented in Table 2.

The dielectric transition window is a specialized coaxial-to-waveguide adapter incorporating two unique pressure sealing microwave feedthroughs. This window, without the feedthroughs in their respective ports, is shown in Figures 18 and 19 in two 90 degree opposed sectional views. The body of the dielectric transition window was fabricated from 17-4 PH stainless steel. A sectional view of a microwave feedthrough is shown in Figure 20. In the dielectric transition window the blind rectangular holes which mate with the dual propellant waveguide are filled with Stycast 2741 epoxide casting resin supplied by Emerson and Cuming, Inc. For

the most rigid formulation of this resin, the cured material has an experimentally determined dielectric constant of 3.10 at 10.0 GHz. The front face of the dielectric transition window along with two extra microwave feedthroughs is shown in Figure 21. A feedthrough connects a resin filled waveguide in the dielectric transition window to a 4.5 in. section of 0.0865 in.-dia. semi-rigid coaxial cable which in turn connects to standard X-band waveguide. This semi-rigid coaxial cable plus the attached connectors required to transition to an X-band waveguide flange are shown in Figure 22.

To determine the effectiveness of RF power transmission by the dielectric transition window, the voltage standing-wave ratio (VSWR) applicable to each side was measured as a function of frequency via a slotted section technique.<sup>(35)</sup> To utilize this method it was first necessary to construct a microwave load which would absorb all, or essentially all, of the RF energy which exited the front face of the dielectric transition window. This special twin load, which is shown in section view in Figure 23, was fabricated from one of the three dual propellant waveguides. The pyramidal tapers which accomplished the energy absorption were constructed from Eccosorb MF-124 magnetically loaded epoxy manufactured by Emerson and Cuming, Inc. The view in Figure 24 shows the load sitting upon the dielectric transition window. With the items in this configuration and by the use of a model 415E Hewlett-Packard SWR meter, measurements were made of the VSWR's relevant to the test and reference sides of the dielectric transition window. The results of these measurements are shown in Figure 25. At the operating frequency of 10.0 GHz, the test and reference side VSWR's were 1.65 and 1.83, respectively. These VSWR's translate, respectively, into percentages of power transmitted equal to about 94% and somewhat more than 91%. Clearly, the dielectric transition window was the major source of the microwave fixed reflections caused by impedance mismatches.

The dielectric transition window just discussed was the second and not the first version which was built. The first transition section was a waveguide-to-waveguide type.

This device was a single unit in which two side-by-side waveguides changed, over the course of 35 in., from standard X-band openings to special waveguide cross sections identical to those in the dual propellant waveguide. A view of this transition section with an attached X-band waveguide flange assembly is shown in Figure 26. Although considerable effort was expended to make this waveguide-to-waveguide transition section capable of containing the high pressure gas inside the combustion fixture, no success was achieved. Consequently, this first model of the dielectric transition section was never used in any of the experiments. The complete failure of the first model of the dielectric transition window forced the consideration of the coaxial-to-waveguide design implemented successfully in the second model.

Pressure sealing for a microwave feedthrough was accomplished by the use of inverted cones on the face and a copper washer on the external shoulder. Inverted cone-type seals were also utilized by the two electrical feedthroughs which passed the capacitive discharges causing propellant ignition and explosive valve actuation. At interfaces within the combustion fixture, the pressure was contained by the use of resilient metal c-type seals. For successful use, these resilient metal seals required that the squeezing surfaces have an RMS roughness of 16 micron, or less. The presence of an almost imperceptible nick across a seal line was enough to prevent pressure containment by the combustion fixture. To still be able to achieve some degree of pressurization if such a defect went undetected, elastomeric o-rings were put behind the metal seals on the major end caps of the driver chamber. However, for all the actual experiments, this precaution would have been unnecessary since the c-type metallic seals functioned perfectly. To verify the sealing capability of the entire combustion fixture, the driver and test chambers were independently pressured to 25 and 15 kpsi, respectively. As indicated by two Bourdon-type dial pressure gages, no significant loss of pressure from either chamber occurred during a 24 hour time period.

Shown in Figure 27 is a schematic of the pressurizing system used in the experiments. Located within the compression cylinder is a moveable aluminum piston sealed along its circumferential boundary so that compressed gas above the piston is prevented from leaking into the oil below the piston. To fully displace this piston from the bottom of the compression cylinder to the top required 42 minutes of operation by the oil pump. Each incremental pressurization stage was therefore equal to this time interval. The cumulative duration of booster pump operation depended upon the desired final gas pressure in a combustion fixture chamber. An overview of all equipment external to the large protective shelter is presented in Figure 28. At the left of this picture, near the nitrogen bottle, is the gas booster pump surrounded by a steel, box-like barricade. A closeup view of most of the waveguide circuitry is shown in Figure 29. The inside of the protective shelter is shown in Figure 30; in the center of this picture is the assembled combustion fixture connected to both the microwave circuitry and the remotely controlled valves.

In the steady-state burning tests, a single propellant strand burned within the combustion fixture in the large closed chamber which was formed by the removal of the explosively actuated valve, the flow nozzle and its retaining elements, and the test chamber volume-filler/flow-detector. The maximum volume of this closed chamber was 204 cubic in.; although on some steady burning tests, aluminum filler disks were used to reduce this volume and decrease the pumping time required to reach a high initial pressure. Since the propellant strand did burn in a closed chamber, there was some increase in pressure during a so-called steady-state test. However, the large volume of the combustion chamber kept this undesirable effect relatively small. When conducting a steady state burning rate test, the reference arm of the microwave circuitry was terminated by a fixed X-band waveguide short. This action insured that the reference signal voltage vector would be of constant magnitude and rotating at the microwave source angular frequency.

For every experiment whether it was steady or dynamic, the cancellation of fixed reflections was an important aspect of test procedure. In the steady tests, only the microwave fixed reflections in the arm relevant to the burning strand were cancelled. For the dynamic tests, however, the process utilized to cancel the fixed reflections was successively applied to both arms of the microwave system. In this process, use was made of the special twin load which had dimensions identical to a dual propellant waveguide. When the twin load was positioned in the combustion fixture, each of its elements could absorb essentially all the microwave radiation which would have entered the base end of a sample M6 propellant strand. Thus, all reflected power reaching the two entrance ports on the harmonic frequency converter would have been caused by the undesirable impedance mismatches in a given arm of the microwave system. Within each side of the system two types of waveguide hardware were available for use in reducing the fixed reflections. These items were the E-H tuner and the components in the cancellation loop; they could have been utilized either separately or both together. However, for all experiments the attenuators in the cancellation loops were set at maximum attenuation and only the E-H tuners were used to cancel fixed reflections.

When cancelling the fixed reflections within a specific side of the system, that arm was terminated by one element of the twin load. The residual reflected RF energy in this arm was fed into the so-called test side of the harmonic frequency converter while the main variable attenuator was set at minimum attenuation. In the other arm, a fixed X-band waveguide short was used as the termination. The main attenuator in this arm was adjusted until -23 dBm of power entered the so-called reference side of the harmonic frequency converter. By monitoring the meter deflection in the relative gain indicator, resetting the digital gain control on the network analyzer, and adjusting the two micrometers on the E-H tuner, the voltage level of the fixed reflections in the specific arm of the system being considered could be reduced to a value 45 dB less than the initial reference signal voltage. Implicit in this procedure is the assumption that the microwave fixed reflections will remain cancelled after the twin load is replaced by

a propellant filled dual waveguide and after the space about this waveguide is pressurized to some high initial pressure. Generally, as will be shown later, this is a poor assumption.

The ends of each M6 propellant strand were initially planar with the end surfaces of the dual waveguide. The body of each strand was machined such that its cross sectional dimensions were equal to  $0.288 \times 0.388$  in. with a tolerance of  $\pm 0.001$  in. Shown in Figure 31, next to a twin waveguide, are two strands of M6 propellant which have been operated upon by a two-lip end mill. The specific propellant sample confinement characteristics within a waveguide will be discussed in detail in the next section. When a strand was to be burned within a waveguide, a 0.007 in.-dia. nichrome wire was maintained against the uninhibited exposed face of the propellant sample. This wire was oriented parallel to the longest cross sectional dimension and along a centerline. A pyrotechnic paste (designated X-225 by the Naval Weapons Center at China Lake, California) was then painted on both the wire and the rectangular propellant surface until a layer about 0.01 in. thick was established. The finely powdered materials in this paste were potassium perchlorate ( $KClO_4$ ), titanium, and boron. The binder was a synthetic rubber (polyisobutylene or Vistanex) which had been dissolved in a hexane solvent. Table 3 gives the weight percentages of the paste components. To enhance the heat feedback to the propellant surface, a strip of transparent tape was placed over the coated M6 surface. When a 170  $\mu f$  capacitor at 175 volts discharges through the 0.8 ohm nichrome wire, the pyrotechnic paste is heated, ignites, and causes the sympathetic ignition of the M6 propellant surface. The Joule heating of the wire is completed in less than 1 msec.

## 6.0 RESULTS AND ANALYSIS

### 6.1 Phase Angle Resolution

Figures 32-36 characterize the analog phase noise associated with the phase angle measuring system depicted in Figure 13. In determining the results shown in these five figures, the microwave source was always stabilized at 10.0 GHz. By the use of the phasemeter scale factor of 1 deg/10 mV, the phase noise values were computed from the root-mean-square voltages measured by the true RMS voltmeter identified in list C of Appendix F. With respect to Figure 13, the observations of analog noise were made at the output of the filter-amplifier which conditioned phasemeter output. The dominant bandwidth limiting components in the measurement system were the network analyzer, phasemeter, and filter-amplifier. Respectively, the 3-dB bandwidths of these components are 10 kHz, 7.32 kHz, and 16 selectable frequencies. Consequently, the nominal system bandwidth was approximated by the following equation

$$f_{sys} = \left( \frac{1}{f_{na}^2} + \frac{1}{f_{pm}^2} + \frac{1}{f_{fa}^2} \right)^{-1/2} \quad (26)$$

where each frequency is relevant to the 3-dB amplitude point. As shown in Figure 32, the RMS phase noise is a cyclical function of measured phase angle. The control of phase angle was achieved by use of the variable phase shifter in the first part of the test arm. For the results in Figure 32, both the test and reference signals were reflections from fixed X-band waveguide shorts; the power of each

signal was -23 dBm at the input to the harmonic frequency converter. Bandwidth control of the system was accomplished by the use of the filter-amplifier. The maximum and minimum nominal system bandwidths identified in Figures 32-36 are associated with the extremes of the 16 lowpass settings on the filter-amplifier.

To determine whether or not the results in Figure 32 were dependent upon the spectral purity and stability of the microwave source, two other types of microwave source were used in place of the BWO. First to be considered was a reflex klystron oscillator which was in a Polarad signal generator, Model 1108A. The second type investigated needed no input from an external synchronizer; it was a microwave frequency synthesizer manufactured by Systron-Donner. This device was composed of a driver unit, Model 1600A option 02, and an output unit, Model 1611A option 3. Neither type of microwave source yielded results different from those in Figure 32. Both the cyclical noise behavior and the relatively large phase noise values were caused by the network analyzer.

If the power spectral density of noise is flat over the frequency range of interest, the RMS noise should be proportional to the square root of bandwidth.<sup>(36)</sup> The reasonably good agreement between the symbols and curves in Figures 33 and 34 show that the phase noise can be considered white. White noise implies only a flat spectrum and does not specify a distribution of amplitudes. However, it seems quite likely that the phase noise should have a Gaussian amplitude distribution. If this is the case, then a measured RMS noise value would equal  $\sigma$ , the standard deviation of a Gaussian amplitude distribution. Hence, the probability that the noise voltage will be less than  $\sigma$  volts is 0.683. Phase noise was also a function of test signal power and an indication of this dependence is given by the results in Figures 35 and 36. Indicated power levels are relevant to the input ports of the harmonic frequency converter. The conversion of phase noise to a spatial resolution associated with the translation of a propellant surface within a waveguide is

accomplished by multiplying a given RMS phase noise value by  $(2\beta_p)^{-1}$ , the reciprocal of twice the propellant phase constant.

As based upon the selected nominal system bandwidth and the growth of test signal power, all steady-state burning rate tests had an RMS phase noise of about 0.1 degree or less. On dynamic tests, the initial measured phase angle was established so that the phase noise was at a minimum (see Figure 32); also, the test and reference signal power levels were both set at -23 dBm. Depending upon the speed of pressurization on a given dynamic test and upon the sampling frequency chosen for the A/D system, the nominal system bandwidth was established at 3.012, 4.515, or 5.341 kHz.

As mentioned earlier, the major contributor to phase noise and, hence, the primary impediment to the realization of better phase angle resolution was the network analyzer. Recently, a modification to the basic microwave detected system used in this investigation has been reported.<sup>(37)</sup> In the new technique, the network analyzer was omitted; relative phase between test and reference microwave signals was preserved in a down-conversion process utilizing two double balanced RF mixers and two RF sources synchronized at frequencies separated by 500 kHz. Phase noise in the modified system was reported to be limited to that caused by the phasemeter.

## 6.2 Steady-State Burning Rate Tests

For the eleven steady tests conducted, Table 4 shows the relationships among side-wall inhibiting techniques, initial pressure, and the occurrence of non-planar burning within the waveguide. The strand configuration called type A was

consistent with that identified in the Design Rationale section as having the best chance for realizing the desired response similarity in the twin strand differential system. However, type A as well as strand configuration types B and C proved to be unsatisfactory for insuring that planar burning could be maintained over the entire 4 in. waveguide length when tests were conducted at pressures higher than about 1000 psig. Even less desirable was the fact that each type of inhibiting technique showed one instance where non-planar burning occurred immediately upon propellant ignition. The occurrence of significant non-planar burning was indicated by the highly erratic values of measured phase angle and relative amplitude and by the obvious increase in the normally small pressurization rate. Corroboration of this statement is contained in Figures 37 and 38 where raw data from the eleventh steady-state test is presented. In Figure 37 the measured phase angle begins its erratic behavior at about 0.97 second. At the same time in Figure 38 the pressure in the closed chamber begins a rapid rise because of a significant increase in burning area.

Burning rates were determined for eight of the eleven steady-state tests; the only tests not considered were the three in which non-planar burning began immediately upon propellant ignition. Perhaps the best way to show how all the data was analyzed is to consider the eighth test as an example case. Shown in Figure 39 is a plot of measured phaseangle based upon the linear connection of 2048 discrete data points which had been acquired by the A/D systems at the rate of one sample every 2 msec. The raw data in this figure represents the phase angle change as the propellant strand burned its full 4 in. The hot wire causing propellant ignition began its Joule heating at 0.020 sec. In Figure 40 the cyclical nature of the phasemeter output has been eliminated by a plot of unfolded measured phase angle. The relative amplitude change in decibels, as based upon output from the relative gain indicator, is shown in Figure 41. Note that this relative amplitude change is simply given by the instantaneous relative amplitude  $Y$  minus the initial relative amplitude  $Y_0$ ; i.e.,  $\Delta Y = Y - Y_0$ . The pressure history in the closed

chamber for the eighth steady-state test is shown in raw data form in Figure 42. Contrast the smoothness of this plot with the extreme pressure excursion depicted in Figure 38. The peak pressure in Figure 42 occurred at strand burnout. As would be expected for a planar burning sample, there is a well defined pressure peak which corresponds to a flat burning surface intersecting the plane of the dielectric transition window.

Although the information in Figure 41 was informative, there was a need to know the amplitude of the test channel in absolute and not just relative units. The following discussion explains how the test channel amplitude was determined in units of volts. At the input to the harmonic frequency converter, the power difference in  $\text{dB}_m$  between the test and reference sides can be expressed as

$$P_{T, \text{dB}_m} - P_{R, \text{dB}_m} = X_{\text{null}} - X + Y \quad (27)$$

The term  $X_{\text{null}}$  represents the test channel gain in dB which if internally imposed by the network analyzer would make the output from the relative gain indicator equal to zero volts. For the particular network analyzer used in the experiments,  $X_{\text{null}}$  equaled 24.8 dB. The term  $X$  indicates the dial setting of the digital test channel gain control on the network analyzer. Since the left-hand-side of equation (27) is in decibels, the following relation can be written

$$20 \log_{10} \left( \frac{V_T}{V_R} \right) = X_{\text{null}} - X + Y \quad (28)$$

Recall that  $V_R = (P_R Z)^{1/2}$  where  $Z$  is the input impedance in ohms of the harmonic frequency converter ( $Z = 50 \Omega$ ) and  $P_R$  is the reference side input power in watts. The operative equation can now be written as

$$V_T = (P_R Z)^{1/2} 10^{\left(\frac{X_{null} - X + Y}{20}\right)} \quad (29)$$

where  $P_R$  can be determined from the equation  $P_{R,dB_m} = 10 \log_{10}(P_R/1 \text{ mW})$ . The use of equation (29) allowed Figure 43 to be constructed. Clearly, equation (29) could be applied to the steady-state tests because  $P_R$  had a known fixed value during an experiment. Since the  $Y$  values in equation (29) are discrete, the resulting  $V_T$  values form set of discrete measured test signal magnitudes. These  $V_{T,i}$  are identical to the  $C_{m,i}$  written in equation (23).

To calculate the measured, apparent, or uncorrected burning rate, equation (17) was applied. A prerequisite to the use of this equation is knowledge of the phase wavelength  $\lambda_{pg}$ . An explicit expression for  $\lambda_{pg}$  is given by equation (9); however, computations cannot be directly undertaken with this relation because  $\Delta\psi_a$  is unknown. A solution to this problem is to realize that if  $\psi_m$  never backtracks on the Riemann surface, then  $\Delta\psi_m$  will nearly equal  $\Delta\psi_a$  and the phase wavelength can be approximated with low error by

$$\lambda_{pg} \cong \frac{720^\circ \ell_0}{\Delta\psi_m} \quad (30)$$

For the eighth steady-state test, the value of  $\lambda_{pg}$  from equation (30) was computed to be 1.240 in. Hence, the constant of proportionality,  $\lambda_{pg}/720^\circ$ , needed in equation (17) is  $1.722 \times 10^{-3}$  in./deg. To get the values of  $d\psi_m/dt$  needed in equation (17), central differences were applied to the raw data shown in Figure 40. Multiplying each  $d\psi_m/dt$  by the proportionality constant produced the plot shown in Figure 44. The gaps in the plot are relevant to sections of phase angle which

had been created by linearization; this artifice was necessitated by the cyclical phasemeter transitions from  $360^\circ$  to  $0^\circ$ . Because these phase angle sections were not "true" data they were not considered in the construction of Figure 44 or in any other analysis relating to phase angle derivatives.

Within the same computer program which constructed plots of raw data, the distributions over frequency of both amplitude and energy were computed for each sample set of discrete physical data acquired during a given test. The techniques utilized in determining this spectral information are given in detail in Appendix G. For the phase angle data in Figure 40, the amplitude and energy spectra out to the Nyquist frequency are shown, respectively, in Figures 46 and 47. Equation (G-7) was the basis for Figure 46 while Figure 47 was based upon equation (G-8). Analogous spectral information for the test signal amplitude data of Figure 43 is presented in Figures 48 and 49. The ordinate scales in Figures 46 and 48 are in units of decibels below the maximum spectral amplitude. Figures 46-49 show very little spectral content above 30 Hz. Hence, for both the phase angle data and the test signal amplitude data acquired on the eighth steady-state test, a pass band from 0 to 30 Hz should contain essentially all of the significant signal. This statement was found to also apply to the pressure history relevant to the eighth test. It must be noted that the establishment of this cutoff frequency was, fundamentally, a subjective decision. No technique of data processing can by itself allow one to determine what is the nature of the phenomenon which has been sampled. It can only show what is in the sampled data, assuming no frequency aliasing. Someone must decide what in the sampled data is pertinent to the phenomenon and what is not.

Having decided upon the appropriate cutoff frequency applicable to data from a given steady-state test, each sample set was operated upon by a lowpass nonrecursive digital filter. Both a smoothing and a differentiating digital filter were employed. Detailed descriptions of these two types of filters are presented in

Appendix G. For the eighth steady-state, the unfolded measured phase angle, combustion chamber pressure, and test signal amplitude are shown in filtered form in Figures 50-52, respectively. Compare these three figures with the corresponding original raw data presented in Figures 40, 42, and 43. Instead of using conventional central differences for  $d\psi_m/dt$ , the differentiating digital filter was utilized to give the time derivatives needed for the computation of the measured or apparent burning rate. For the eighth test, the product of these filter determined derivatives and the previously calculated proportionality constant is shown in Figure 53. In comparing this figure with Figure 44, note that the burning rates based upon central differences are indicated up to the essential burnout time of 3.398 seconds while those based upon the digital filter are not presented after 3.328 seconds.

Even though the plot in Figure 53 is less "noisy" than that in Figure 44, the apparent burning rate still has the significant undulations caused by the presence of fixed microwave reflections. The existence of these fixed reflections are perhaps better appreciated when the results in Figure 52 are interpreted within the context of the phasor diagram in Figure 11. As vector  $\vec{B}$  grows in magnitude during its rotation about the tip of vector  $\vec{A}$ , the resultant vector  $\vec{C}$  will be cyclically diminished and enhanced in magnitude. This behavior is evident in Figure 52 where the magnitude of vector  $\vec{C}$  is represented exactly by the experimental test signal amplitude.

In the determination of desired actual burning rates from experimental data which had been affected by microwave fixed reflections, the theory discussed in the Nonlinear Parameter Estimation section was applied to a given steady-state test. A separate computer program was written within which this theory was implemented. The key element in the approach was the reduction in the degree of disparity between measured and theoretically predicted test signal amplitudes. Both of these amplitudes were functions of measured phase angle. Hence, for the particular set of discrete measured phase angles being considered, the optimization process focused upon the minimization of  $\eta$ , the objective function given by equation (23). The

results of objective function minimization for the eighth test are presented in Figure 54. Filtered experimental data was always utilized in an optimization process and in Figure 54 this data is relative to the time interval from 0.040 to 3.328 seconds. With respect to equation (23), this time period corresponds to a summation index range of  $i = 21$  to 1665. Another way of demonstrating the degree of objective function minimization for a given test is exemplified by the results in Figure 55. This figure is a restructuring of the results in Figure 54 and it should be interpreted with the aid of Figure 11. Each curve in Figure 55 is a nondimensional phasor plot representing the path of the tip of vector  $\vec{C}$ ; one curve is theoretically based and the other is constructed from experimental data.

As part of the minimization of the objective function  $\eta$ , the constants  $\mu$ ,  $A$ ,  $B_0$ , and  $\alpha$  were necessarily determined. Hence, sufficient information was now available with which to evaluate equation (18) according to the directions given at the very end of section 4.0. Note that the computation of  $\dot{\psi}_a$  from equation (18) used the values of  $\dot{\psi}_m$  given by the differentiating digital filter. The deduced  $\dot{\psi}_a$  values plus the value of  $\lambda_{pg}$  given by equation (30) were then utilized in equation (7) to compute the actual burning rate  $r_a$ . This theoretically adjusted burning rate for the eighth test is shown in Figure 56. Compare this figure with the uncorrected or measured burning rate presented in Figure 53. In a slight departure from the focus on the eighth test, consider some results from the fifth steady-state test which are presented in Figures 57 and 58 and serve as another example of the significant differences between the uncorrected and theoretically adjusted burning rates. The development of the information in Figures 57 and 58 was analogous, respectively, to that for Figures 53 and 56.

In the computer program which calculated the actual burning rates, the corresponding actual phase angles were also computed. Given the four optimized constants and a specific  $\psi_m$  value, then each value of the actual phase angle  $\psi_a$  was a root of equation (19). Calculated actual phase angles for the eighth

experiment are shown in Figure 59. Compare this figure to Figure 50 and note the reduction in undulations exhibited by the plot of actual phase angle. In Figure 59 there are a few places where the value of a  $\psi_a$  root was held fixed for a small time interval. The necessity for creating these slight breaks in curve continuity has already been discussed in section 4.0. Note in this figure that the value of the actual phase angle at 3.328 seconds was just extended for the remaining time. During the time period from 0.040 to 3.328 seconds the actual phase changed by 2304.7 degrees while the measured phase angle decreased 2290.9 degrees during the same time span. Because these phase angle changes are almost the same and since both relate to the almost complete combustion of the original strand length, the assumption that  $\Delta\psi_m$  will nearly equal  $\Delta\psi_a$  is upheld and, consequently, the use of equation (30) is also sustained.

Having fully discussed the eighth test as an example case, the discussion of results will no longer be particularized to this one steady-state experiment. As based upon the measured dielectric constant for M6, the propellant waveguide dimensions, and the microwave operating frequency, the theoretical phase wavelength calculated by use of equation (10) was 1.158 in. Hence, the theoretically based value of the proportionality constant in equation (7) was  $1.608 \times 10^{-3}$  in./deg. Experimental results for these quantities are shown in Table 7. The mean values from this table, plus and minus one standard deviation, are  $1.176 \pm 0.051$  in. and  $(1.633 \pm 0.071) \times 10^{-3}$  in./deg for the phase wavelength and proportionality constant, respectively. Expressed as a percentage of the mean values, the standard deviations were about 4.3%. Note that the mean experimental phase wavelength is only about 1.5% higher than the theoretical value. Although the data is sparse, it appears that the experimental phase wavelength was not a function of pressure in the range from 1 atmosphere to about 10,000 psig. This experimental result in conjunction with the theoretical prediction from equation (10) seems to indicate that the dielectric constant of the relatively stiff M6 propellant was not significantly affected by strand compression when under a certain range of hydrostatic pressures.

Although significant non-planar burning did not occur on the sixth test, no results for this experiment are presented in Table 7. As shown by the plot in Figure 60, the measured phase angle did backtrack upon the Riemann surface and, thus,  $\Delta\psi_a$  could not be approximated by  $\Delta\psi_m$ . This lack of monotonic behavior in  $\psi_m$  was caused by the presence of large microwave fixed reflections. Another consequence of the large fixed reflections is shown in Figure 61 where raw data from the sixth test is plotted. Notice that for some values of the measured phase angle there are multiple values of test signal amplitude. Contrast Figure 61 with the more typical results in Figure 54. For regions where the values of  $\psi_m$  are not monotonic with respect to time, the objective function defined in equation (23) is inadequate for use in calculating an applicable set of optimized constants. The objective function definition presumed that for a given  $\psi_m$  there would be one  $C_m$  and one  $C_t$ . Hence, for the sixth test, equation (23) was applied only over that range of summation indices which excluded ambiguity in values of  $C_m$  and  $C_t$ .

Consider the attenuation of a  $TE_{10}$  wave in a rectangular waveguide filled with an imperfect dielectric. The attenuation constant  $\alpha_d$  in units of nepers/in. is given by<sup>(28)</sup>

$$\alpha_d = \frac{k \frac{\epsilon''}{\epsilon'}}{2 \left[ 1 - \left( \frac{f_c}{f} \right)^2 \right]^{1/2}} \quad (31)$$

where the wave number  $k$  can be written as  $k = 2\pi f(\mu\epsilon)^{1/2}$  and where the ratio of complex and real permittivities can be interpreted as the loss tangent; i.e.,  $\epsilon''/\epsilon' = \tan \delta$ . If it is assumed that  $\mu \cong \mu_0$  and if it is recognized that  $\epsilon = \epsilon_r \epsilon_0$  and  $c = (\mu_0 \epsilon_0)^{-1/2}$ , then equation (31) can be recast in the following form

$$\alpha_d = \frac{\pi f (\epsilon_r)^{1/2} \tan \delta}{c \left[ 1 - \left( \frac{f_c}{f} \right)^2 \right]^{1/2}} \quad (32)$$

For the specific situation of the microwave experiments with M6 propellant,  $\epsilon_r = 3.238$ ,  $f_c = 8.240$  GHz, and  $f = 10.000$  GHz. Thus, for this particular case equation (32) can be rearranged to yield

$$\tan \delta = \frac{\alpha_d}{8.453} \quad (33)$$

when  $\alpha_d$  is in the units of nepers/in.

Consider equation (15) wherein the value of  $\psi_a$  governs the magnitude of  $\vec{B}$ , the vector representing the moving surface microwave reflection. Suppose instead that this magnitude dependence is explicitly based upon the instantaneous length  $l_T$  of the test strand; i.e.,  $B = B_0 \exp(\mu' l_T)$  where  $\mu'$  is a new attenuation constant. If complete strand combustion is assumed, then  $\mu' l_0 = \mu \Delta \psi_a$  and  $\mu' = 4\pi\mu/\lambda_{pg}$ . While in the propellant waveguide, the  $TE_{10}$  wave is attenuated both on its way to and after its reflection from the moving propellant surface. Thus,  $\mu' = -2\alpha_d$  because  $\alpha_d$  in equation (31) relates only to a one-way loss. An expression for the original attenuation constant  $\mu$  can now be written as

$$\mu = - \frac{\alpha_d \lambda_{pg}}{2\pi} \quad (34)$$

For the case of complete strand combustion, assume that the total increase in measured test signal amplitude approximately equaled the total increase in the

magnitude of vector  $\vec{B}$ . This is a reasonable assumption and it allows values of  $\alpha_d$  to be computed directly from the total decibel increase in test signal amplitude; i.e.,  $2\alpha_d \cong (\Delta dB/\ell_0)(1 \text{ neper}/8.686 \text{ dB})$ . With  $\alpha_d$  known, equations (33) and (34) can be evaluated. Using this approach values of  $\tan \delta$  and  $\mu$  were computed for the steady-state tests; the results are shown in Table 8. Since individual experimental values of  $\lambda_{pg}$  could not be determined for tests 4, 5, 6, 7, 10, and 11, the calculation of  $\mu$  relevant to each of these tests was based upon the mean of those experimentally determined phase wavelengths given in Table 7. The mean of all values of  $\mu$  in Table 8 is  $-0.0516$  nepers/rad and the associated percent standard deviation is 14%. An indication of the invariant nature of the microwave attenuation in an M6 propellant strand is given by observing the variation in total test signal dB change for each steady-state test except number one. For these ten tests, the mean value of the total dB change was 19.27 dB and the standard deviation expressed as a percentage of the mean was 16%. The loss tangent corresponding to this mean dB change was 0.0328. Note that although the propellant samples were stored in an air conditioned room, no additional attempt was made to control the environmental humidity. Since the M6 propellant does exhibit some hygroscopicity, the propellant samples used in the tests may have had slightly differing amounts of retained water vapor and this might have influenced the microwave attenuation in the strands.

Consider now the results from the nonlinear parameter estimation theory as applied to the steady-state experiments. The optimized constants found by the use of the Hooke and Jeeves pattern search are shown in Table 9. Notice that the values of  $B_0$  in this table are, generally not much greater than the values of  $A$ . Since the initial value of  $\psi_a$  was positive, equation (15) shows that the magnitude of  $B$  at the start of strand burning will be even less than  $B_0$ . Only for test number eleven was the initial  $B$  value more than ten times larger than the value of  $A$ . Generally, the microwave fixed reflections which had been cancelled during the early stage of an experiment showed a significant magnitude growth by the time the propellant strand was ignited. The inability to keep the microwave fixed reflections

cancelled is attributed, primarily, to the behavior of the coaxial waveguide components which linked the standard X-band waveguide to the specially sized rectangular waveguide in the dielectric transition window. That is, these components have interfaces which are susceptible to impedance changes induced by the relative motion caused by increased stress, temperature variation, or slight vibration. Particularly sensitive interfaces are thought to have been the exit plane of a microwave feedthrough and the junction formed when the connector on the semi-rigid coaxial cable was attached to the subminiature jack on a feedthrough.

Results for test number one are not given in Table 9 because the A/D system did not function properly on this experiment and no discrete data was acquired. For tests 2, 3, 6, 8, and 9 no significant non-planar burning occurred, and the values of  $\mu$  based upon optimization agreed quite well with those previously calculated on the basis of the total dB change in test signal amplitude. The mean value of the optimized attenuation constants for these five tests is  $-0.052447$  nepers/rad and the standard deviation expressed as a percentage of the mean is 11%. Because planar burning ceased after a short time on tests 5 and 11, there was insufficient data available to allow the optimization technique to converge to  $\mu$  values which accurately defined the true nature of the exponential amplitude growth of the moving surface microwave reflection. Hence, in the optimization runs for each of these two tests the search interval for  $\mu$  was made extremely narrow and was centered about the value of  $\mu$  previously found from the total dB change in test signal amplitude. In these two cases, the objective function  $\eta$  was essentially only a function of  $B_0$ ,  $A$ , and  $\alpha$ .

In Table 10 a comparison is made of the mean steady-state burning rates and standard deviations for raw, filtered, and theoretically adjusted data. In calculating the instantaneous burning rates for tests 5, 6, and 11, use was made of the mean proportionality constant given by the results in Table 7. A summary of the primary results for the steady-state tests is presented in Table 11. The mean

burning rate for test number one as shown in Table 11 was actually unrelated to instantaneous measurements. Instead, this entry was based upon total measured phase angle change and total time interval of burning. Figure 62 graphically displays the most important information in Table 11. In this figure, the lines through the microwave results and through the data from Grollman and Nelson<sup>(45)</sup> were each based upon a least squares linear regression analysis. For the analysis performed on the eight microwave data points, the correlation coefficient was 0.9991. Curve A in Figure 62 represents typical closed bomb results for M6 propellant at 90°F.<sup>(46)</sup> Although not specifically stated by Grollman and Nelson, it is assumed that curve C is relevant to results for M6 propellant at "room temperature." The microwave results, curve B, are for M6 propellant at  $70 \pm 2^\circ\text{F}$ .

The interpretation of all the information shown in Figure 62 must be done within a framework of knowledge about the historical burning rate results from strand burners and closed bombs. It should be understood that substantial differences exist between data obtained by different investigators using either closed bomb or strand burner techniques. Quoting from a recent JANNAF Burn Rate Measurements Panel, "there is general lack of agreement between strand burner and closed bomb data as well as between laboratories using closed bombs or strand burners."<sup>(47)</sup> Some but not all of these differences may be associated with compositional variability in a given propellant. For example, a difference in residual solvent level of one percent has been noted to result in approximately a ten percent change in the burning rate.<sup>(48)</sup> Fortuitous or not, the microwave results in Figure 62 lie midway between curves A and C. For this figure the uncertainty in pressure for the microwave data is  $\pm 25$  psi or  $\pm 1\%$  of indicated pressure, whichever is larger. An indication of the uncertainty in microwave burning rates is given by the vertical bars through each data point except that for test number one. These bars encompass the mean steady-state burning rate plus and minus one standard deviation. The average of the percent standard deviations for seven microwave tests was 12%.

Some concern prompted by theoretical analyses has been expressed about the possible detrimental effects which microwave/plasma interactions might have upon the accuracy of burning rates determined from the microwave Doppler/phase shift technique.<sup>(3,4,49,50)</sup> Such effects would involve transient microwave reflections caused by variations in flame zone ion and electron concentrations. These effects would be manifested by a time dependence in the wave impedance at the burning propellant surface; it would no longer be possible to consider the term  $\psi_{ST}$  in equation (1) as time invariant. However, in a few papers based upon experimental investigations, good arguments have been made that microwave reflections from the flame zone can be discounted.<sup>(2,37,51)</sup> In references 2 and 37, the burnout of a propellant sample was not accompanied by any jumps or abrupt shifts in phase angle or test signal amplitude. In reference 51, the amplitude of the reflected microwave signal did not change when the burning process transitioned from a normal propellant strand to one of the same formulation but with 1/2% KCl added. Experimental results from the steady-state tests with M6 propellant were analogous to those just mentioned. Consider Figures 50 and 52 wherein typical data shows that neither the measured phase angle or the test signal amplitude exhibited sudden changes during strand ignition or burnout. If reflections from the flame zone had been important, then at burnout an abrupt change in test signal voltage should have been observed when the plasma rapidly decayed to a neutral gas. Hence, either essentially all the microwave energy was reflected by the solid/gas interface or, if the energy did not pass through, the concentration of ions and electrons was insufficient to reflect the microwave signal.

On each steady-state burning rate test a propellant ignition delay was observed. That is, there was a time interval between hot wire initiation and the onset of clearly defined M6 propellant combustion. These delays are indicated in Table 12.

## 6.3 Dynamic Experiments

### 6.31 Vibration Tests

The ability of the twin strand differential system to cancel propellant mechanical responses was evaluated in a series of vibration or non-burning dynamic tests. By the use of flow nozzles with throat diameters of 0.05 and 0.15 in., the pressurizations in these vibration tests were imposed at two distinctly different rates, one slow and one fast. Pressurizations were applied to twin propellant strands, a single strand, and the dielectric transition window alone. In vibration tests with twin propellant samples, the strand configurations which were investigated were types A and C as described in Table 4. Only the type C configuration was used in pressurizations of single strands. Presented in Table 13 is a summary of the more important physical circumstances associated with a given dynamic test. Note that dynamic tests refer to both the vibration tests and the transient burning tests. Common to all the dynamic experiments was the use in the test chamber of the volume-filler/flow deflector. The initial free volume of the driver chamber on each dynamic test was 88 in.<sup>3</sup> For the fourth, fifth, and twelfth vibration experiments, the initial free volume in the test chamber was 3.06 in.<sup>3</sup> On all other dynamic tests, the test chamber free volume was initially 2.11 in.<sup>3</sup> Other physical quantities which governed the pressurization rate on a given dynamic test are shown in Table 14.

Data for the ten vibration tests identified in Table 13 will be presented in a standard format consisting of a sequence of five figures. Hence, as a means of explaining this format consider the first vibration test as an example case. Figures 63-67 quantitatively define this test. The curves in these five figures as well as the plots for all other dynamic tests, are based upon discrete raw data which

was processed by digital signal analysis, primarily lowpass filtering. Appendix G in conjunction with Tables 6 and 15 fully specify the digital analysis technique applied to data from dynamic tests. Table 15 lists the digital lowpass cutoff frequencies for the physical quantities relevant to each dynamic test. As indicated in Table 13 the strand configuration on the first vibration test was type A; this configuration was initially believed to have the best chance for realizing the desired response similarity in the twin strand differential system. The pressure history of the test chamber during test number 1VT is shown in Figure 63. In this experiment as in all the other vibration tests, the capacitive discharge to the explosive valve was started at  $t = 1$  msec. For test number 1VT the time interval between pressure cartridge initiation and the onset of flow from the nozzle was 0.70 msec. Based upon all ten vibration tests, the mean value for this flow delay was 0.60 msec and the percent standard deviation was 11%. Shown in Figure 64 is the pressurization rate for the first vibration test.

For all dynamic experiments, power levels to the test and reference sides of the harmonic frequency converter were both initially established at -23 dBm. Hence, if the mechanical responses of the two propellant strands used in test 1VT had been equal, the plot of relative amplitude shown in Figure 65 would have remained very close to 0 dB for the entire pressurization. Clearly, the results in Figure 65 are contradictory to this ideal situation. An even better indication of the success or failure of mechanical response cancellation is given by the results of Figure 66 wherein three phase angles are plotted. Each of the three curves in this figure begin at flow onset. Curve A is the measured relative phase angle. Curve B represents a theoretical phase angle based upon the hypothetical combustion response of an M6 propellant strand; the burning process was assumed to be planar and in accordance with instantaneous test chamber pressure and the steady-state microwave burning rate results. Given these assumptions, this theoretical phase angle could be interpreted as the actual phase angle associated with the test signal; i.e.,  $\psi_{a,T}$  as depicted in Figure 10.

With the assumed M6 burning beginning at  $t = 0$ , each discrete value of the theoretical phase angle was calculated from the following equation

$$(\psi_{th})_n = \psi_{m,i} + \frac{720^\circ}{\lambda_{pg}} (\Delta\ell_T)_n \quad (35)$$

where,

$$(\Delta\ell_T)_n = (\ell_T - \ell_o)_n = - \sum_{j=1}^n B(p_2)_j^a T \quad (36)$$

In equation (35) the term  $\psi_{m,i}$  represents the measured phase angle at  $t = 0$  and  $\lambda_{pg}$  was the mean phase wavelength from the results in Table 7. The coefficient  $B$  and the exponent  $a$  had values of  $1.694 \times 10^{-3}$  and  $0.7441$ , respectively. Curve C in Figure 66 is a phase angle constructed from the measured phase angle plus the change in theoretical phase angle; that is,

$$(\psi_{sum})_n = (\psi_m)_n + [(\psi_{th})_n - \psi_{m,i}] \quad (37)$$

Successful nullification of the mechanical responses in the twin strands would yield curve A as a horizontal straight line and curves B and C as coincident traces. Negative slopes on the curves are associated with apparent recession within the waveguide while positive slopes indicate apparent motion in the opposite direction.

Shown in Figure 67 is the final set of results which help to define the capability of the twin strand differential system to nullify mechanical responses.

Each curve in this figure resulted from central differences applied to a phase angle. To compute velocities from these time derivatives of phase angle, the mean constant of proportionality from Table 7 was utilized. In Figure 67, trace B is a velocity relevant to the theoretical phase angle calculated from steady burning rate results. Curve C is a velocity based on the phase angle constructed from the sum of measured phase angle and the change of theoretical phase angle. Hence, curves B and C in Figure 67 follow directly from curves B and C in Figure 66. Had the desired mechanical response cancellation occurred, curves B and C in Figure 67 would have been coincident. Clearly, this was not the situation on the first vibration test.

To verify that the poor results on test 1VT were not an aberration, two additional vibration tests with the type A strand configuration were conducted. The pressurization rates on these twin strand differential experiments were analogous to that in test 1VT. Because ground loop effects in the microwave signal processing equipment caused significant loss of data, the results from these two tests are not presented in graphic form in this report. However, it was possible to deduce the overall behavior on these two additional tests. Results for the extra tests were very similar to those from test 1VT; that is, they were just as poor. It should be noted that no epoxy bond-line failures were observed on either the additional two tests or on the first vibration experiment. Different degrees of adhesion or bond strength between the propellant samples and the waveguide walls probably accounted for most of the mechanical response dissimilarity when the type A strand configuration was employed. Hence, in the remaining dynamic tests attention was focused upon the mechanical response behavior of propellant samples having the type C strand configuration as described in Table 4.

To determine the importance of the mechanical response associated with the dielectric transition windown alone, the tests identified as 4VT, 5VT, and 12VT were conducted. On experiments 4VT and 5VT the pressurizations were slow while

on test 12VT a fast pressurization was imposed. The results from these tests are presented in the following three sets of figures: 4VT in Figures 68-72, 5VT in Figures 73-77, and 12VT in Figures 78-82. Each set of figures is cast in exactly the same pattern as that just described for the first vibration test which served as the example case. Presented in each set are the time dependent values of pressure, pressurization rate, relative amplitude, phase angles, and velocities. Note that since no propellant was present in the dual waveguide, both the test and reference signals were microwave reflections from the free surfaces of the casting resin in the dielectric transition window. For the less severe pressurization rate applied in tests 4VT and 5VT, the mechanical response of the dielectric transition window was significant but not nearly as large as that displayed on test 12VT when the fast pressurization rate was imposed. To underscore this statement compare Figures 72 and 77 with Figure 82.

In tests 10VT and 11VT, respectively, slow and fast pressurizations were applied to single M6 propellant samples each of which had been positioned within a waveguide according to the type C strand configuration. The reference signal in these tests was the microwave reflection from an X-band waveguide short which was fixed in its location and underwent no relative motion during a pressurization. Figures 83-87 show the results from test 10VT and Figures 88-92 define test 11VT. Particularly interesting results from these two tests are contained in the phase angle plots shown in Figures 86 and 91. Relative to the initial conditions, both measured phase angles in these figures show an increase in magnitude by the time pressure equilibrium begins. These phase angle increases indicate an apparent growth or extension of the propellant strand within the waveguide. Although unexpected, this phenomenon easily could have been caused by some particular confinement geometry created when the propellant strand responded to a pressurization. That is, the physical situation about the strand could have allowed the formation along the sample perimeter area of time dependent, locally different tractions which acted to advance the microwave reflecting surface.

Notice in Figures 90 and 91, respectively, the sudden jumps in relative amplitude and measured phase angle which occurred upon the relaxation of the fast pressurization rate. As shown by the comparison of Figures 87 and 92, the more severe pressurization caused a larger mechanical response in the single M6 propellant strand. As was the case for all pressurizations involving the type C strand configuration, the propellant samples used in tests 10VT and 11VT did not lose their positional integrity with respect to a waveguide; that is, no epoxy bond-line failures were observed. Also no separation of the Formvar coating from a propellant sample was detected in any vibration test.

Two slow pressurizations were applied to the twin strand differential system in which the strand configuration was type C. Results for tests 6VT and 7VT are shown, respectively, in Figures 93-97 and Figures 98-102. Consider the phase angle plots in Figures 96 and 101; notice in each figure that only after the beginning of pressure equilibrium did the slope of curve C approach that of curve B. Note that the measured phase angle plots in these two figures were closer to being the desired horizontal straight lines than the measured phase angle plot in Figure 86. Thus, even though the results were very poor for the twin strand differential system when exposed to a slow pressurization, they were still slightly better than the results for a single strand responding to a slow pressurization.

The twin strand differential system with the type C strand configuration was also evaluated under the conditions of fast pressurization. Two such vibration tests were conducted; results from test 8VT are presented in Figures 103-107 while Figures 108-112 define test 9VT. The most obvious results from these two tests were associated with the relaxation of pressurization rate during the onset of pressure equilibrium. This phenomenon was associated with sudden jumps in both relative amplitude and measured phase angle; Figures 105-106 and Figures 110-111 clearly show the severe excursions in these measured quantities. Compare the velocity plots in Figures 107 and 112 with the analogous plots in Figure 92 which

are relevant to a single propellant sample experiencing a fast pressurization. In making this comparison note that the twin strand differential system showed mechanical response behavior as poor as that exhibited by the single M6 strand.

In summary, the twin strand differential system with either the type A or C strand configuration was not effective in cancelling mechanical responses in the test and reference propellant samples. For vibration tests which had the same physical circumstances and about the same pressurization rate (i.e., 4VT-5VT, 6VT-7VT, and 8VT-9VT) the results were, at best, qualitatively and not quantitatively reproducible. Finally, the dominant mechanical responses were in the propellant strands and not the dielectric transition window.

### 6.32 Transient Burning Tests

Although the results from the vibration experiments had been poor, two transient burning tests at different pressurization rates were conducted with the twin strand differential system and the type C strand configuration. Results for the fast and slow pressurization experiments are shown, respectively, in Figures 113-117 and Figures 118-122. In observing these figures, note that for each test the A/D system started at  $t = 0$ , the hot wire which controlled test strand ignition began its response at  $t = 1$  msec, the pressure cartridges in the valve were initiated at  $t = 21$  msec, and gas from the driver chamber began to flow through the nozzle at about 21.6 msec. In the preparation of each reference strand used in tests 1TBT and 2TBT, the Formvar coating was established over the entire surface of the propellant sample. This thin thermal barrier was intended to prevent reference strand ignition until, at least, the end of the significant pressure transient caused by flow from the driver chamber. After study of the strip chart records for relative amplitude and phase angle, it was deduced that reference strand ignition occurred at about  $t = 180$  msec on test 1TBT and about  $t = 292$  msec on test 2TBT.

The histories of pressure and pressurization rate for test 1TBT are shown, respectively, in Figures 113 and 114. On this experiment the test chamber pressure rose 115 psi during the time interval  $t = 1$  to  $t = 21$  msec. Consistent with the results from vibration tests with fast pressurization, both the relative amplitude and the relative phase angle showed abrupt changes during the relaxation in pressurization rate. In Figures 115 and 116 at about  $t = 26$  msec these jumps are evident. The results in these figures also suggest the presence of non-planar burning, i.e., burning along the longitudinal perimeter area of the propellant strand. The test strand did, in fact, experience this type of burning. The test propellant sample was fully consumed at about  $t = 180$  msec, the same time at which the reference strand began to burn. The total relative amplitude increase observed during test strand burning on experiment 1TBT was 18.2 dB. All of this relative amplitude increase occurred after the events depicted in Figure 115.

The final collection of results for the first transient burning test are the velocities shown in Figure 117. Curve B in this figure represents a theoretical burning rate computed by the use of the instantaneous test chamber pressure in conjunction with the microwave steady-state burning rate correlation given in Figure 62. This hypothetical combustion response was assumed to start at  $t = 1$  msec, the instant of hot wire initiation on the test side. Curve A in Figure 117 was calculated by the direct application of equation (17) with  $\lambda_{pg}$  given by the mean of the experimental values in Table 7. Time derivatives of measured phase angle were based upon central differences. Because of the approach to coincidence exhibited by the traces in Figure 117, it can be argued that the propellant had just ignited or was close to being ignited by  $t = 21$  msec. Such a 20 msec ignition delay would not have been substantially dissimilar from the results in Table 12. The certainty of unequal strand mechanical responses in addition to test side non-planar burning serve to completely invalidate the apparent experimental burning rate shown in Figure 117.

The results for the transient burning test conducted under the conditions of slow pressurization are presented in Figures 118-122. The information in these five figures exactly parallels that just presented in Figures 113-117. On test 2TBT between  $t = 1$  and  $t = 21$  msec the test chamber pressure increased by 82 psi. At  $t = 89$  msec, which is near the end of the pressure transient caused by the influx of gas from the driver chamber, the test chamber pressure from Figure 118 was 7142 psi. The last data point on this figure is at  $t = 184.9$  msec and the pressure was 9070 psi at this time. As indicated by predictions from the gas dynamic model described in Appendix C, this dramatic pressure increase could not possibly have been caused by planar burning of the test propellant strand. Hence, burning along the longitudinal perimeter area of the test sample was definitely present on experiment 2TBT. In fact, by analysis of the strip chart records for relative amplitude and phase angle, it was deduced that the test strand was fully consumed by about  $t = 292$  msec. At this time the test signal amplitude had increased by 19.2 dB, a value fully consistent with those presented in Table 8. Most of this increase in relative amplitude occurred after the events depicted in Figure 120.

Just as in test 1TBT, the reference propellant strand in test 2TBT ignited, purely by chance, at about the same time that the test sample burned out. The reference strand on test 1TBT exhibited intermittent instances of significant non-planar burning over the course of combustion. However, the reference strand on test 2TBT burned planarly during almost all of its period of combustion. The basis for this statement is the regularity of change exhibited by the measured phase angle trace on the strip chart record. With the exception of opposite slope, the appearance of this trace was analogous to that of the data in Figure 39. Over a two second time interval near the end of reference strand burning, the strip chart record showed that the measured relative phase angle increased by 1630 degrees. Multiplying (1630 deg/2 sec) by  $1.633 \times 10^{-3}$  in./deg, the mean proportionality constant from Table 7, yielded 1.331 in./sec. This operation was, essentially, the application of equation (17) without the minus sign. During this same 2 second

time period, the test chamber pressure was nearly steady, decreasing only from 8350 psig to 8126 psig. Hence, the linear average pressure relevant to this time span was 8238 psig. The coordinate pair consisting of 1.331 in./sec and 8238 psig form a point which lies very near the linear regression line through the microwave data in Figure 62. This result helps to corroborate the burning rate correlation found from the steady-state microwave experiments.

The velocities in Figure 122 were calculated via the same techniques used in the construction of the information in Figure 117. The meaning of the apparent burning rate shown in Figure 122 was totally destroyed by the presence of unequal mechanical responses in the propellant strands and by the essentially immediate occurrence of non-planar test side burning.

## 7.0 CONCLUSIONS

The microwave Doppler/phase shift technique was used successfully to measure the steady burning rates of solid M6 gun propellant at pressures from 500 to nearly 10,000 psig. This M6 data was intermediate to that derived from conventional closed bomb and strand burner tests. The mean experimentally determined phase wavelength of the microwave signal in the propellant filled waveguide was within about 1.5% of the corresponding theoretically predicted phase wavelength. The standard deviation of the experimental phase wavelength was just over 4% when expressed as a percentage of the mean value. As based upon five data points over the observed pressure range, this phase wavelength showed no discernible dependence upon pressure. This information is significant since it is the phase wavelength which establishes the proportionality constant linking burning rate with the time derivative of relative phase angle. Based upon the demonstrated pressure sealing performance of the combustion fixture, particularly that of the specially designed dielectric transition window, it should be possible to use the microwave technique for determining the steady burning rates of other propellants at higher pressures ( $\sim 25,000$  psi). However, the proven inability to reliably maintain small magnitudes for the microwave fixed reflections would require that a relatively complicated theoretical adjustment be applied to the raw data in order to reduce the uncertainty in measured burning rates.

For the steady-state burning rate tests, propellant recession was spatially described via a one-dimensional theoretical model. With the use of four optimized constants this model yielded predictions which compared favorably with experimental observations. This agreement indicates that an aggregate type of planar burning can exist within the propellant waveguide. Supporting this statement are the relatively small standard deviations associated with the steady-state burning rate results. It was, of course, recognized that the physically burning M6 propellant surface was really

not perfectly planar in a mathematical sense. At any instant of time, an actual propellant burning surface might have irregularities. That is, it might possess a characteristic surface roughness, have local pits or craters, or be at some angle other than 90 degrees from the longitudinal waveguide axis. However, when using the microwave technique, the only allowable interpretation of the state of the microwave reflecting surface is that it is perfectly planar. Hence, application of the microwave technique presumes time invariance in the spatial relationship between the actual burning propellant surface and the effective surface which reflects the microwaves. With respect to the combustion of M6 propellant, the experimental evidence suggests that microwave/plasma interactions should not seriously compromise the basic microwave Doppler/phase shift technique. For the steady-state tests, the effects of any instantaneous irregularities in the surface of the burning M6 propellant were collectively diminished by averaging a great many instantaneous burning rates together in order to yield one representative value.

On a transient burning test the propellant burns only a very small distance during the time interval of pressurization and individual instantaneous burning rates become extremely important. Thus, in dynamic burning tests propellant burning surface irregularities may, potentially, have significant impact on the values of some instantaneous burning rates. Even if an "ideal" twin strand differential system could satisfactorily isolate the combustion response during a dynamic pressure transient, to what degree would burning surface irregularities compromise the meaning of the velocity of the effective microwave reflecting plane? This question becomes very difficult to answer when it is realized that the required distance resolution of the measuring technique, say  $3.93 \times 10^{-4}$  in., might be much smaller than the local imperfections in the burning propellant surface. Also, the growth and occurrence of these imperfections might be significantly time dependent over the pressurization time interval. Finally, different strands of the same propellant might exhibit different burning surface geometry. Only after many test replications with an "ideal" system and after considerable statistical analysis could the question be answered. The

preceding question relates to a problem which is inherent when a nearly microscopic measurement technique is applied for the purpose of quantifying what is really a macroscopic phenomenon.

The microwave twin strand differential system built and evaluated in this research effort was unsatisfactory for use in the determination of burning rates of solid propellant when under significant pressure transient. Two major problems in the system were immediately evident. They are as follows:

1. At even slow pressurization rates (say,  $40 \times 10^3$  psi/sec), the mechanical responses of the twin propellant strands and, to a lesser extent, of the dual components in the dielectric transition window did not exhibit sufficiently similar synchronized amplitude characteristics.
2. During propellant combustion within the test-side waveguide, gross departures from planar burning were unpredictable in their occurrence.

Governing the existence of these two intimately related problems were the confinement geometry of a strand within a waveguide and the method of burning inhibition used on the longitudinal perimeter area of a propellant sample. No progress in using a microwave Doppler/phase shift technique for dynamic burning rate determination will occur until these two major problems are overcome.

Four other deficiencies in the presently configured microwave system have been identified. These less severe or second order problems in dynamic burning rate determination are as follows:

1. Phase noise by the network analyzer limits the spatial resolution to a value at least 20 times larger than that associated with the phasemeter alone.

2. In a dynamic pressure environment there is no certainty that the so-called fixed microwave reflections actually are fixed; and if they were fixed, their probable large magnitude would necessitate a theoretical adjustment to measured or apparent instantaneous burning rate.
3. Although reasonably good indirect evidence of its occurrence did exist, the ignition time of the reference strand is not directly indicated.
4. With respect to the time periods of both slow and fast pressurizations, the ignition delay time for the test strand is significantly variable.

Work toward the solution of these four second order problems would be warranted only after the resolution of the two previously identified first order problems.

APPENDIX A

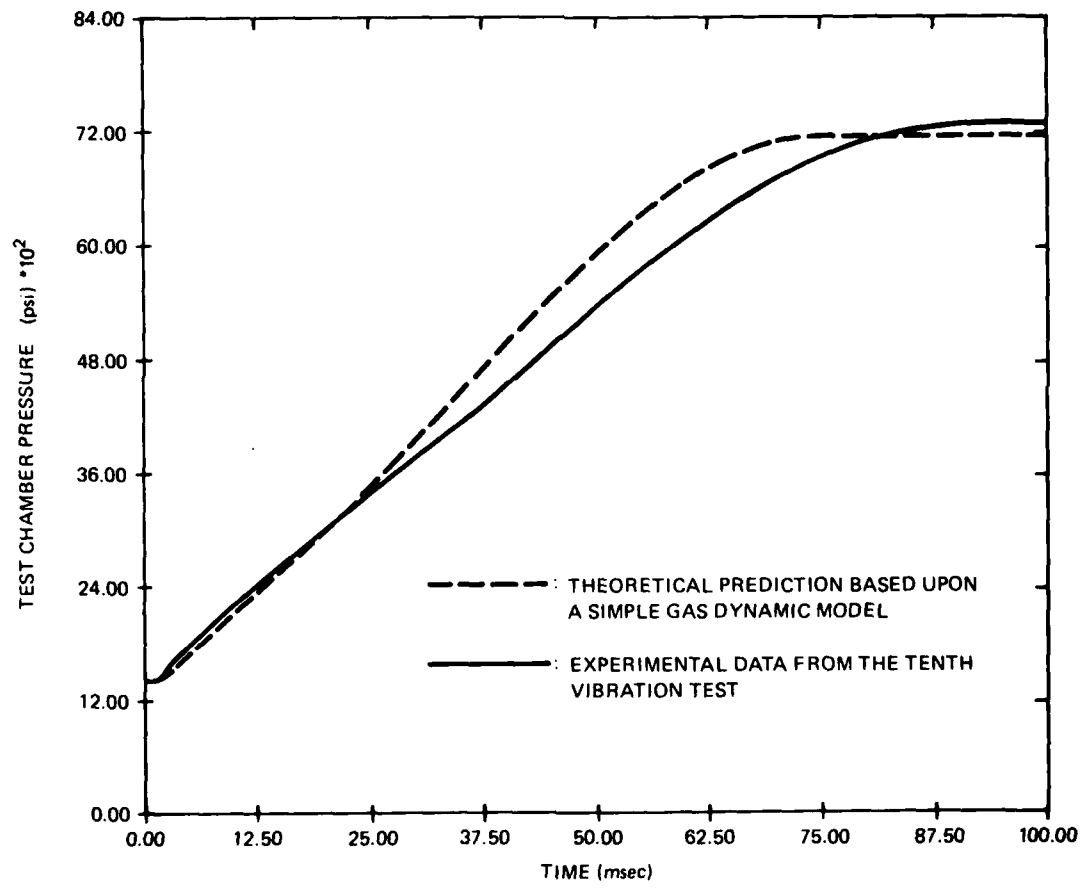


Figure 1. Comparison of the Prediction of the Gas Dynamic Model with Experimental Data from a Typical Slow Pressurization

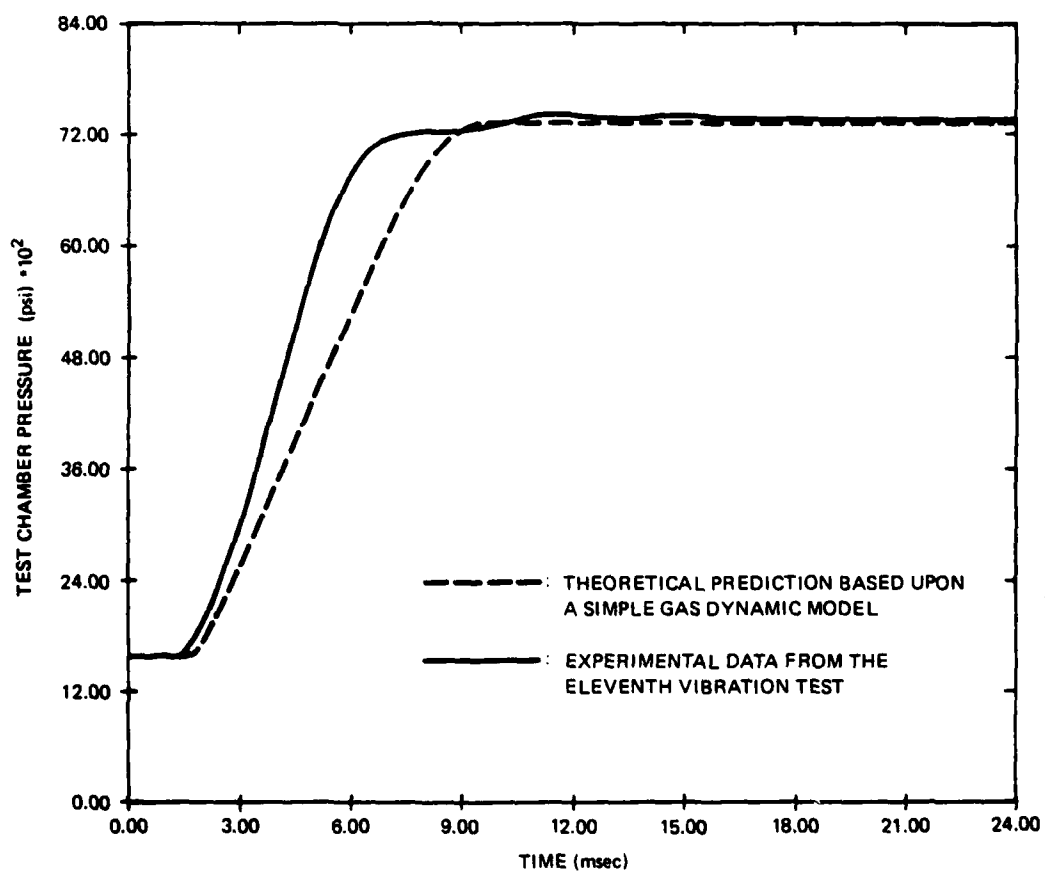


Figure 2. Comparison of the Prediction of the Gas Dynamic Model with Experimental Data from a Typical Fast Pressurization

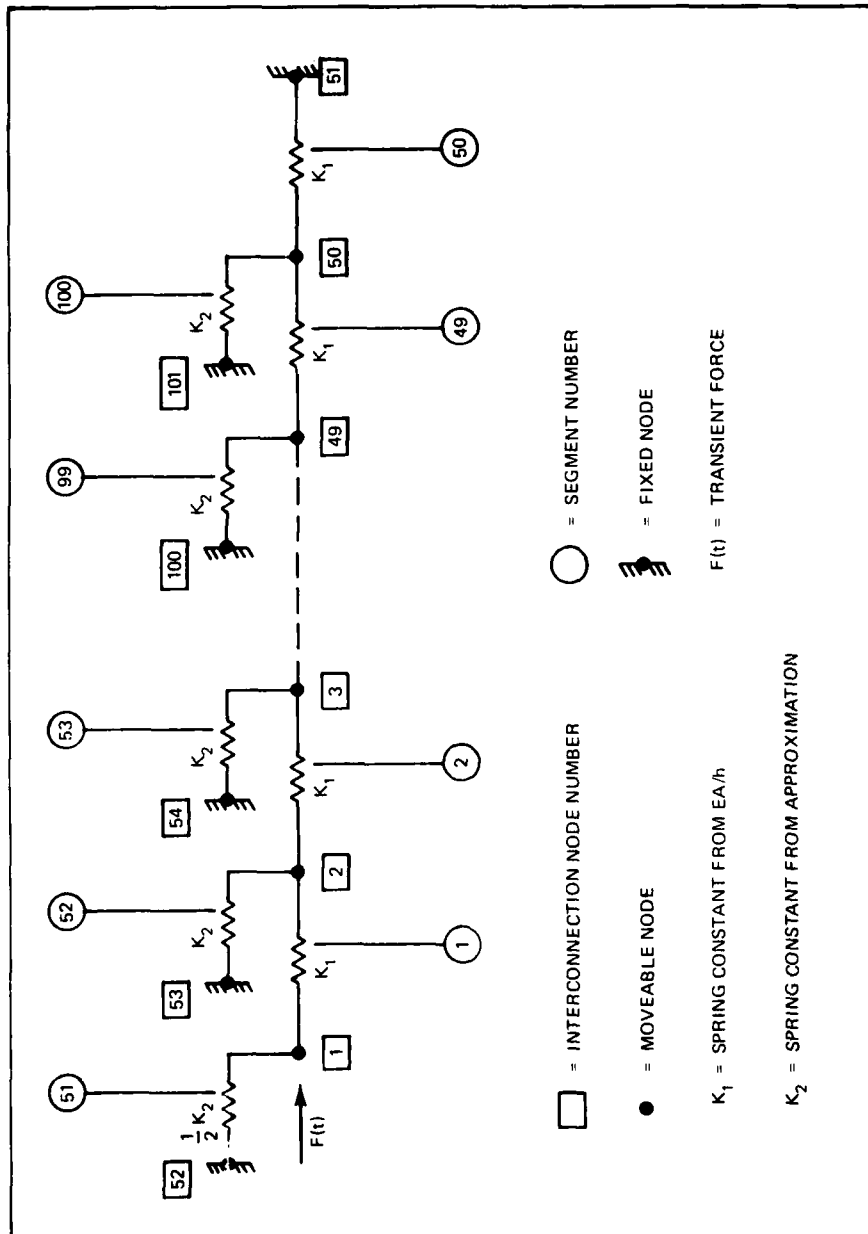
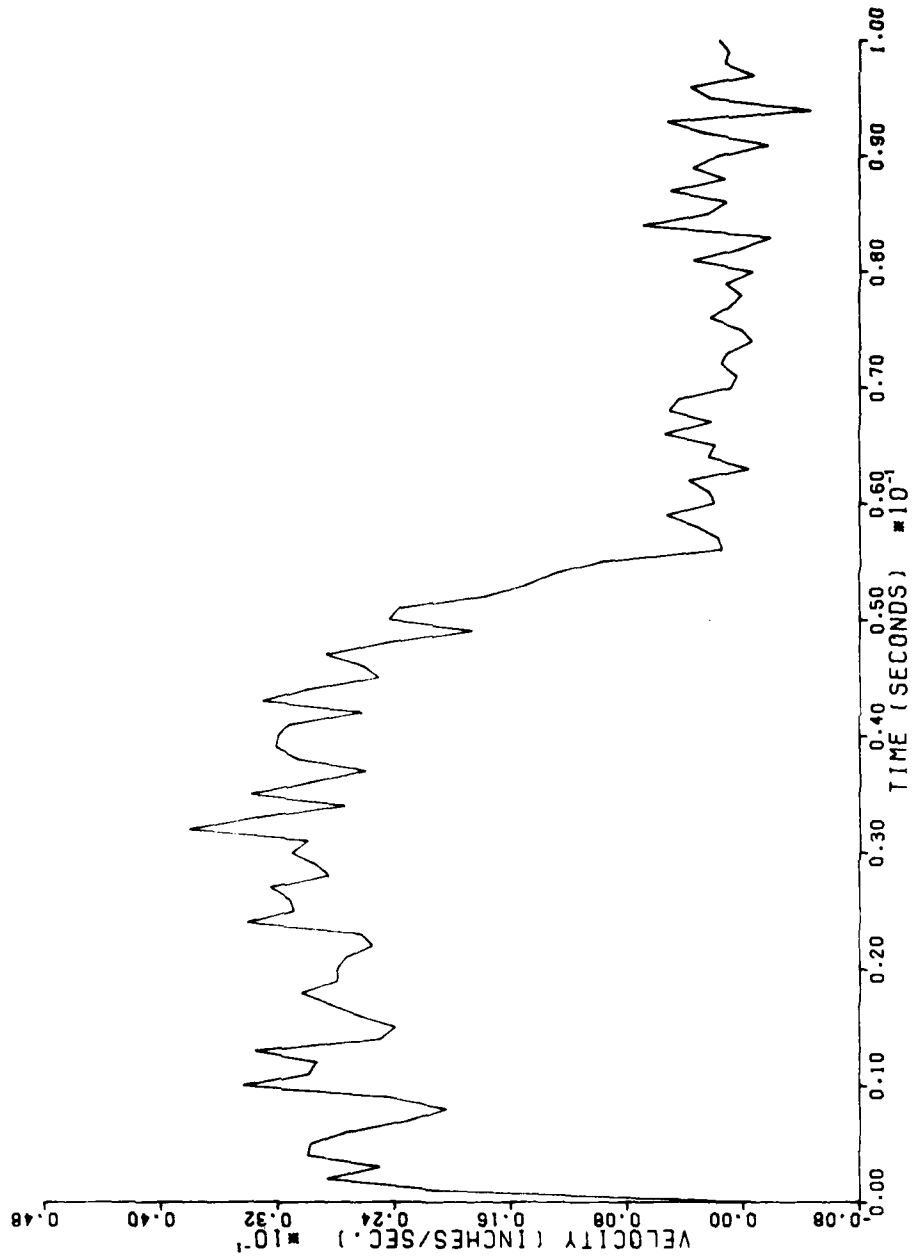


Figure 3. Structural Idealization of Dielectric Material Epoxy-Bonded Within a Waveguide



**Figure 4. Mechanical Response Velocity Caused by a Theoretical Pressurization and Relevant to Node Number One in the Structural Idealization**

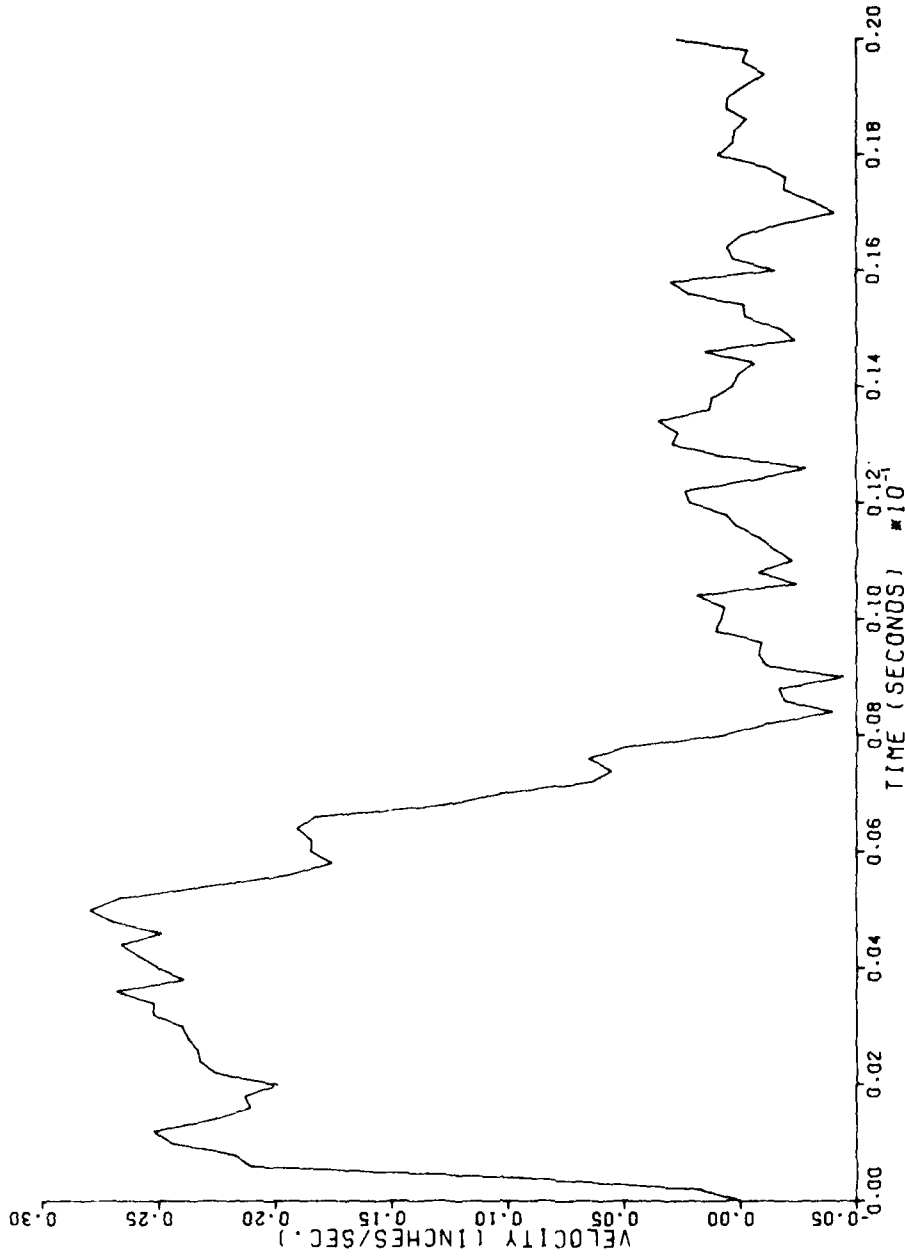


Figure 5. Mechanical Response Velocity Caused by a Theoretical Pressurization and Relevant to Node Number One in the Structural Idealization

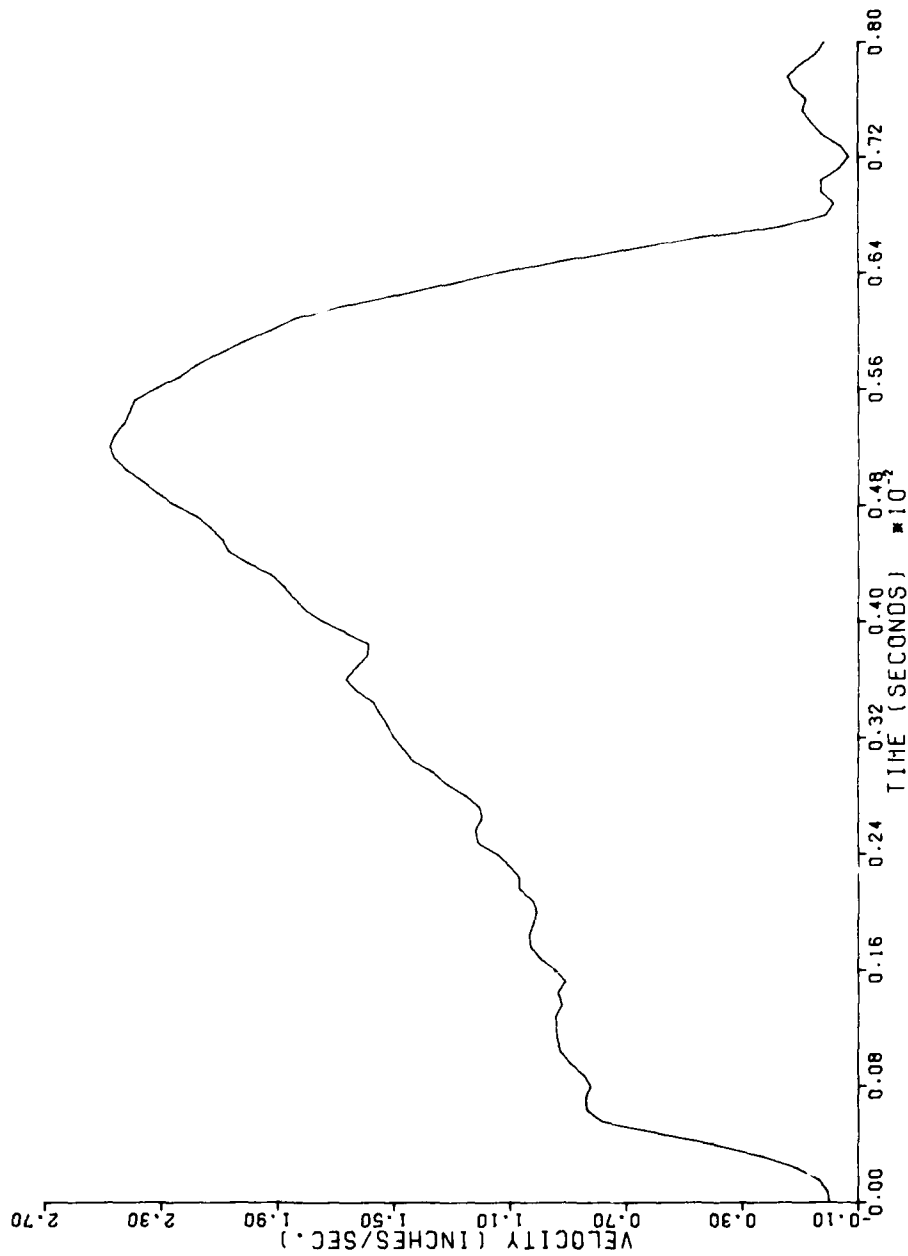


Figure 6. Mechanical Response Velocity Caused by a Theoretical Pressurization and Relevant to Node Number One in the Structural Idealization

AD-A079 791

NAVAL SURFACE WEAPONS CENTER DAHLGREN LAB VA  
BURNING VELOCITIES OF A SOLID PROPELLANT, VIA A MICROWAVE TECHN--ETC(U)  
OCT 79 L H RUSSELL

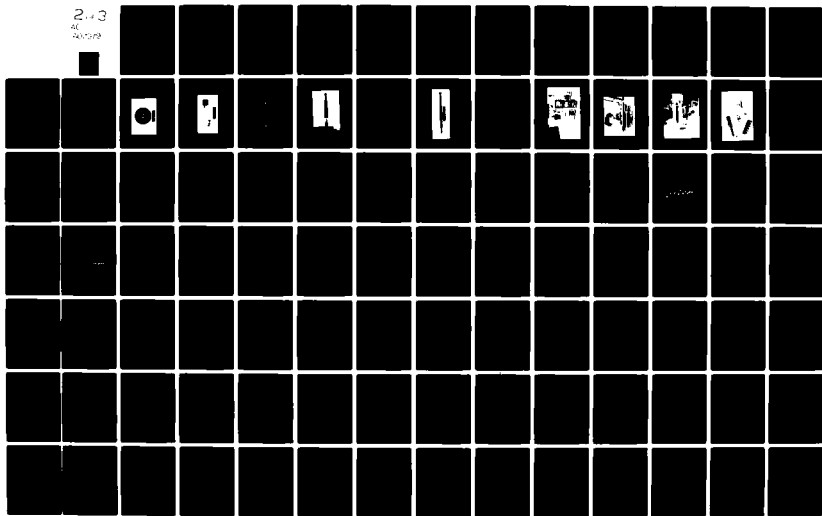
F/6 21/9.2

UNCLASSIFIED

NSWC/TR-79-378

NL

2 of 3  
AL  
RUSSEL



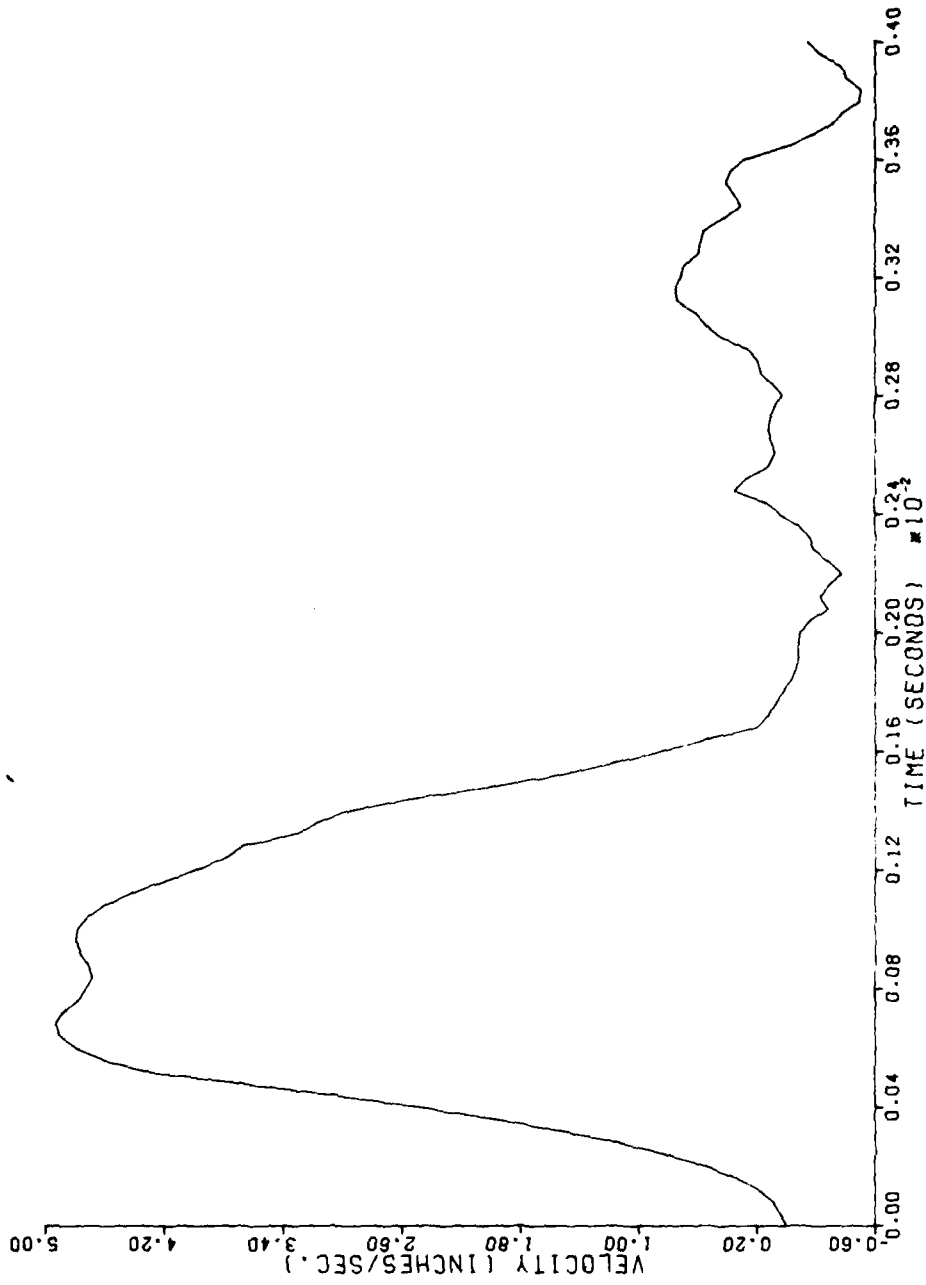
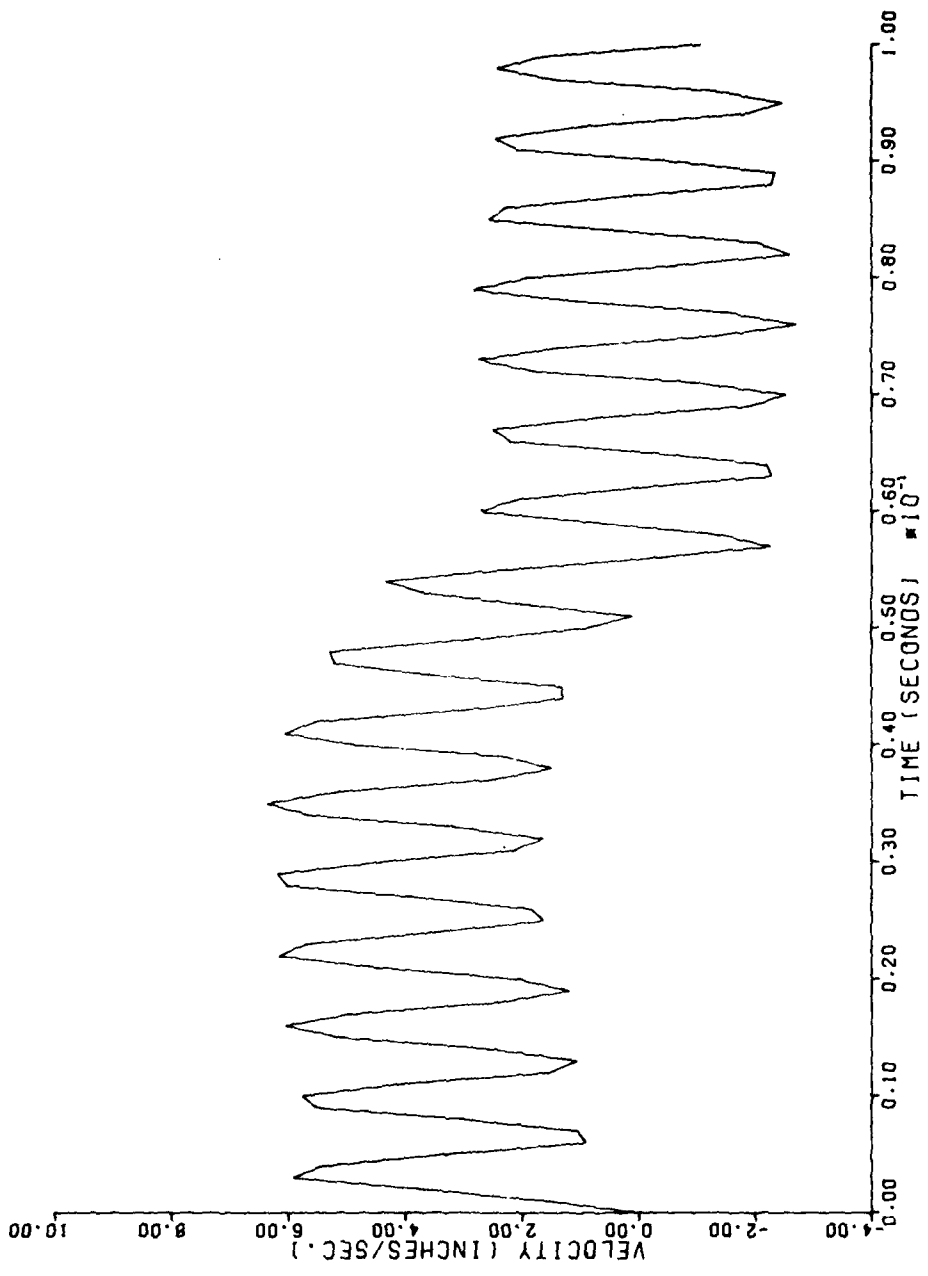


Figure 7. Mechanical Response Velocity Caused by a Theoretical Pressurization and Relevant to Node Number One in the Structural Idealization



**Figure 8. Mechanical Response Velocity Caused by a Theoretical Pressurization and Relevant to Node Number One in a Less Rigid Form of the Structural Idealization**

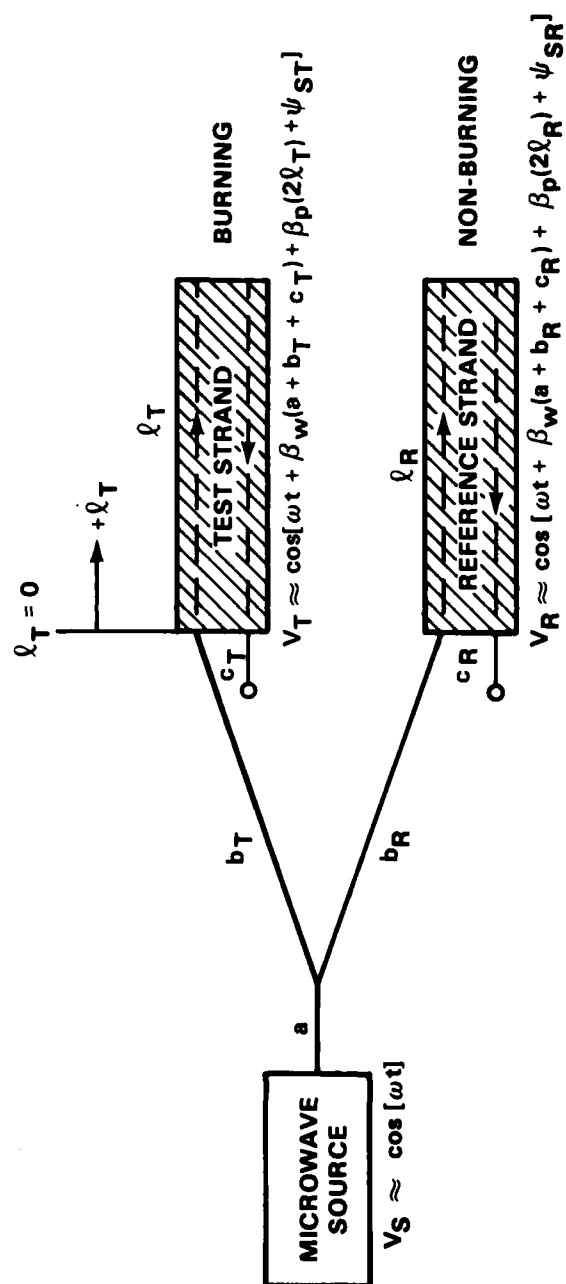


Figure 9. Schematic of the Twin Strand Differential System

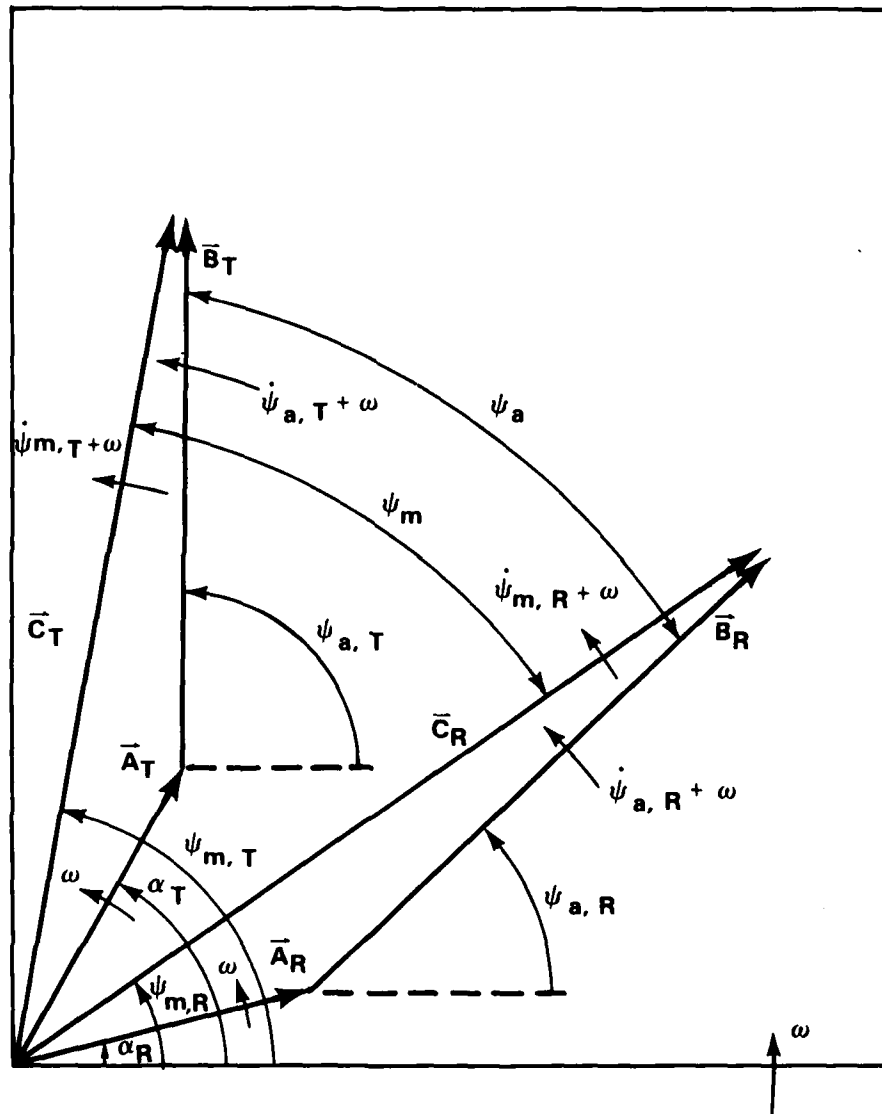


Figure 10. Phasor Diagram Applicable to the Twin Strand Differential System

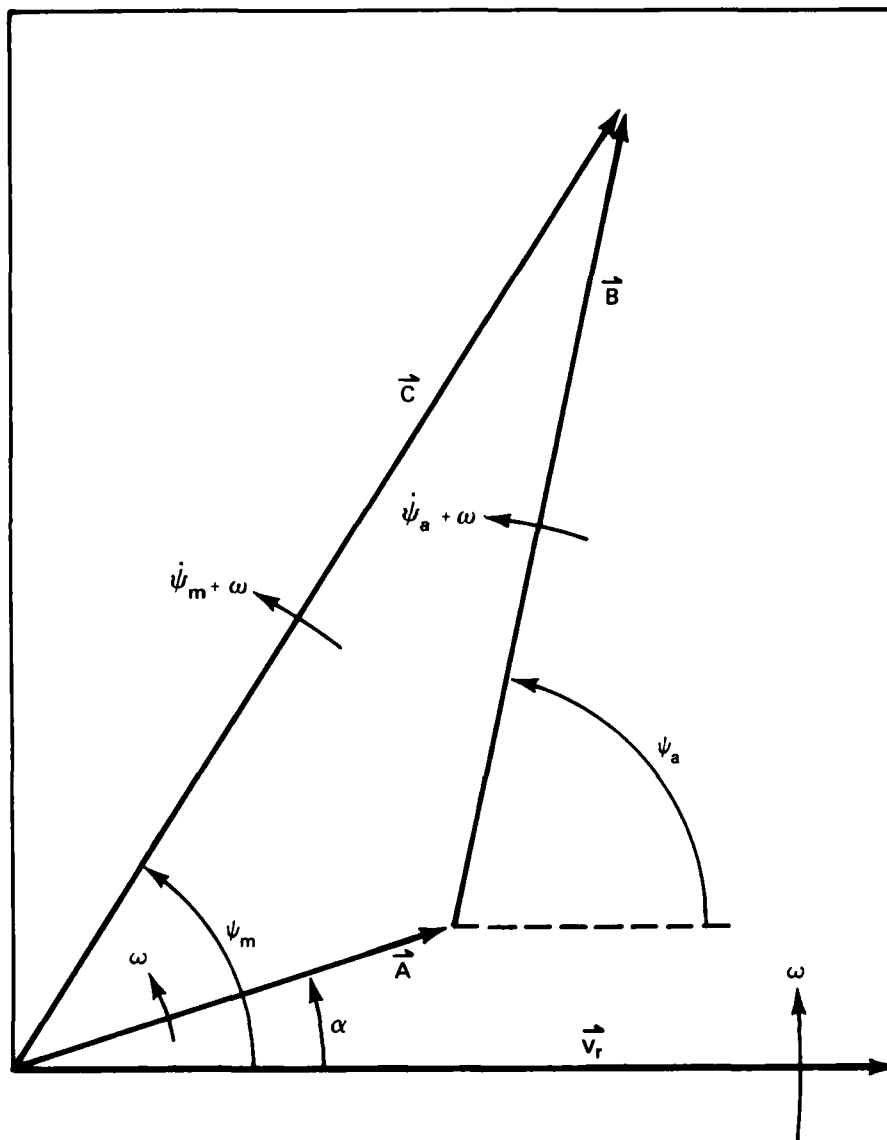


Figure 11. Phasor Diagram Applicable to a Single Propellant Strand and a Spatially Fixed Reference Plane

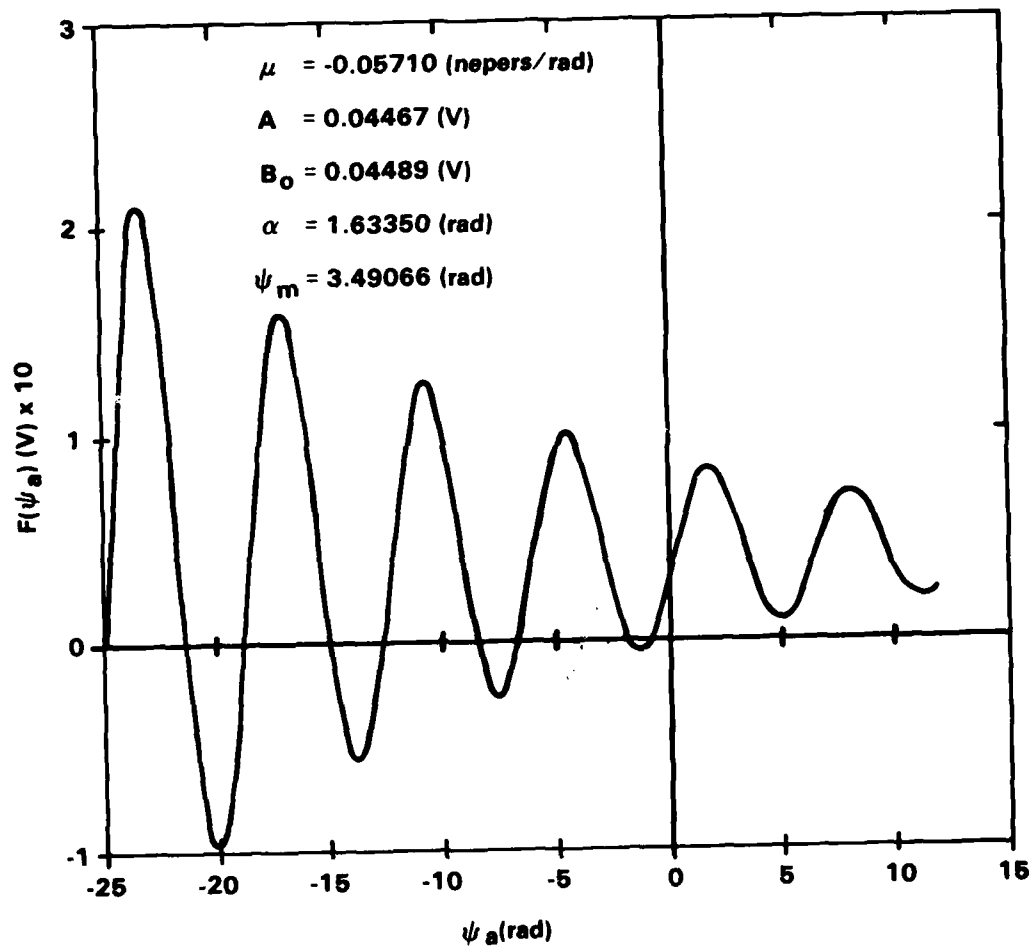


Figure 12. Governing Equation as a Function of Actual Phase Angle

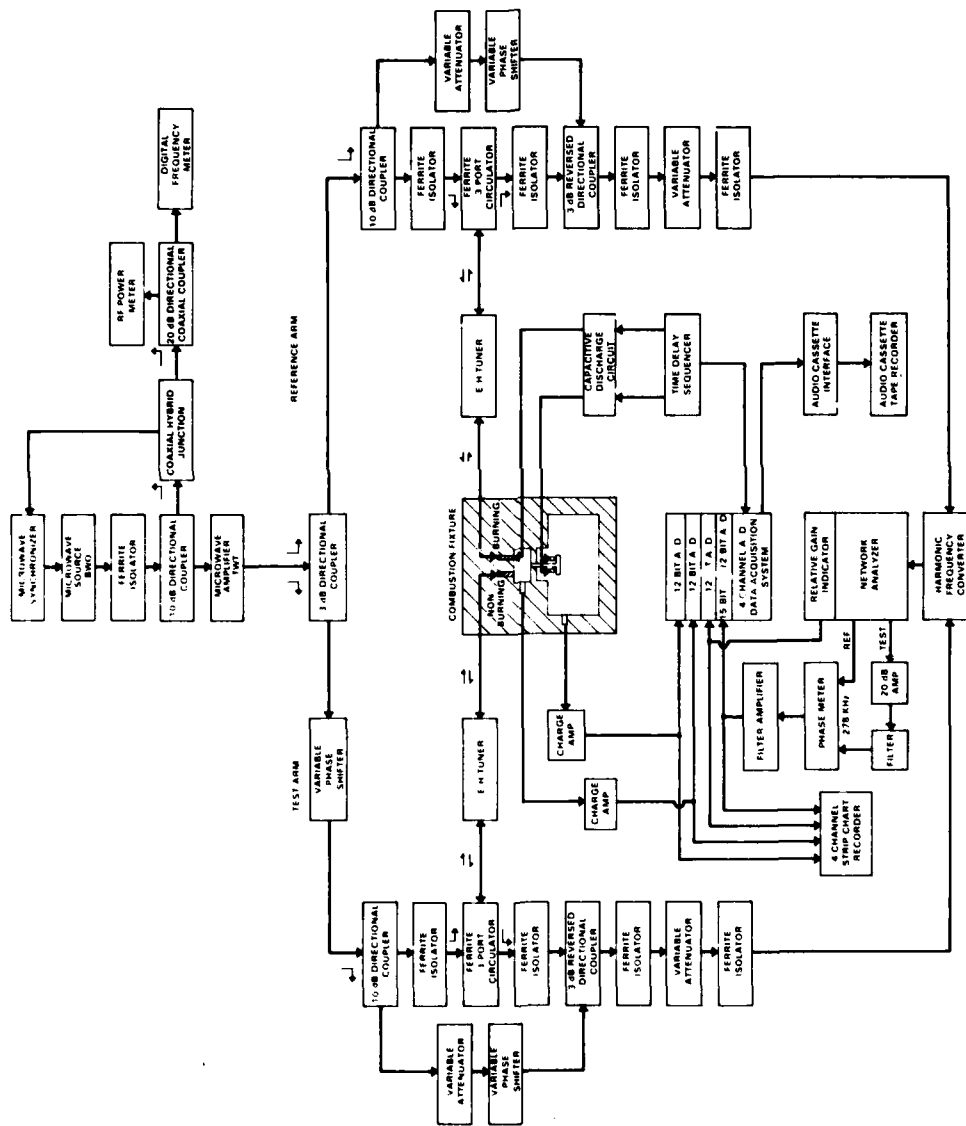
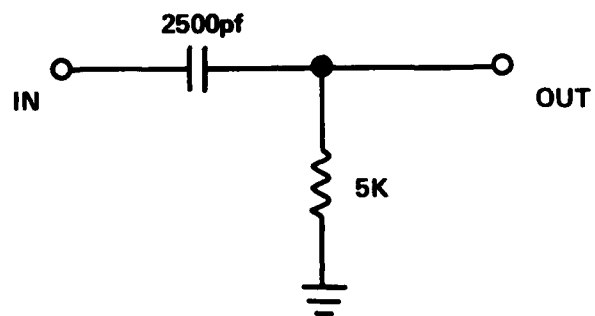


Figure 13. Schematic of the Overall Experimental System



NOTE: ALL RESISTANCE IN OHMS

Figure 14. Electrical Schematic of Simple Highpass Filter

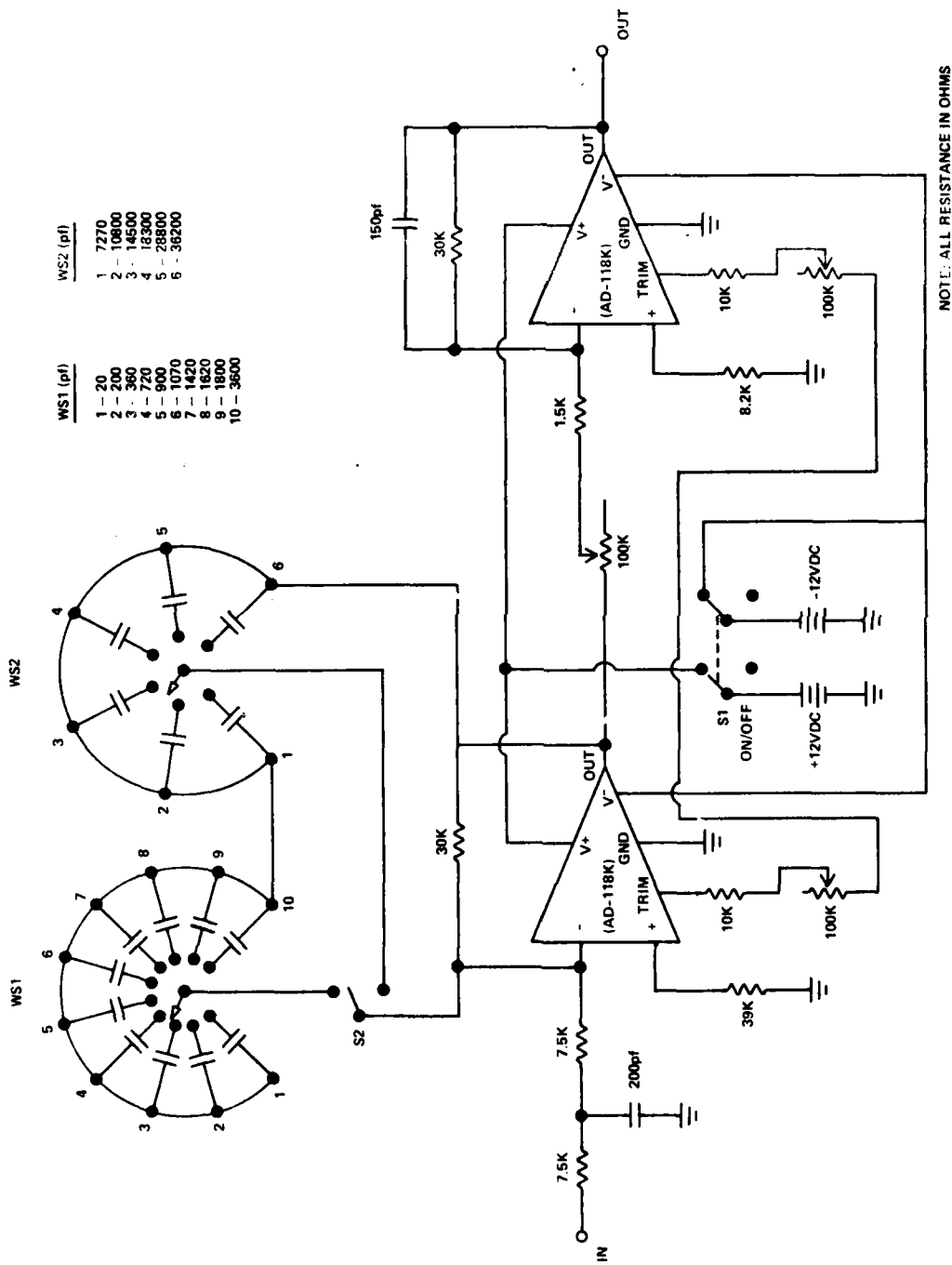


Figure 15. Electrical Schematic of Filter-Amplifier





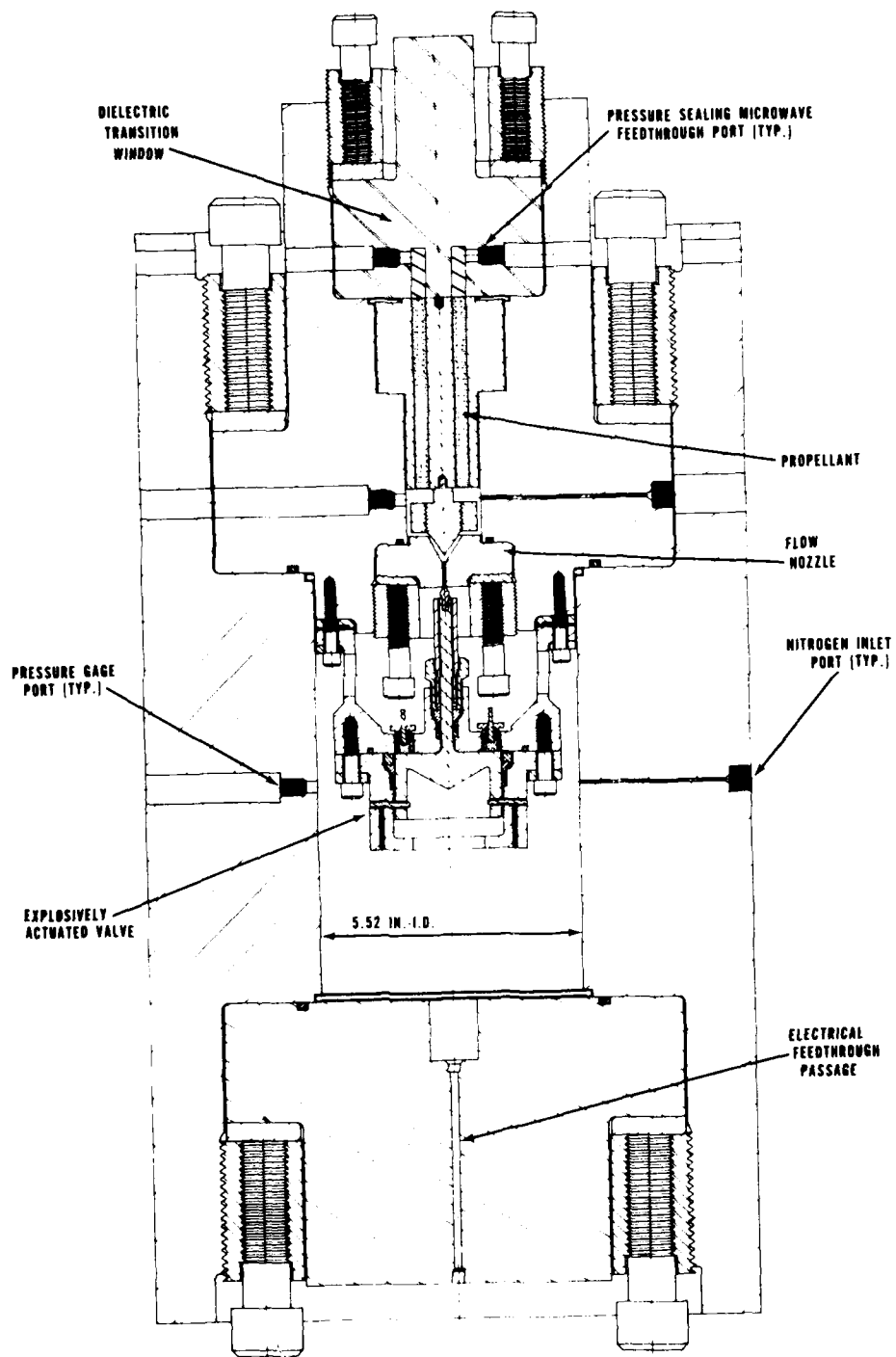


Figure 18. Combustion Fixture Section View

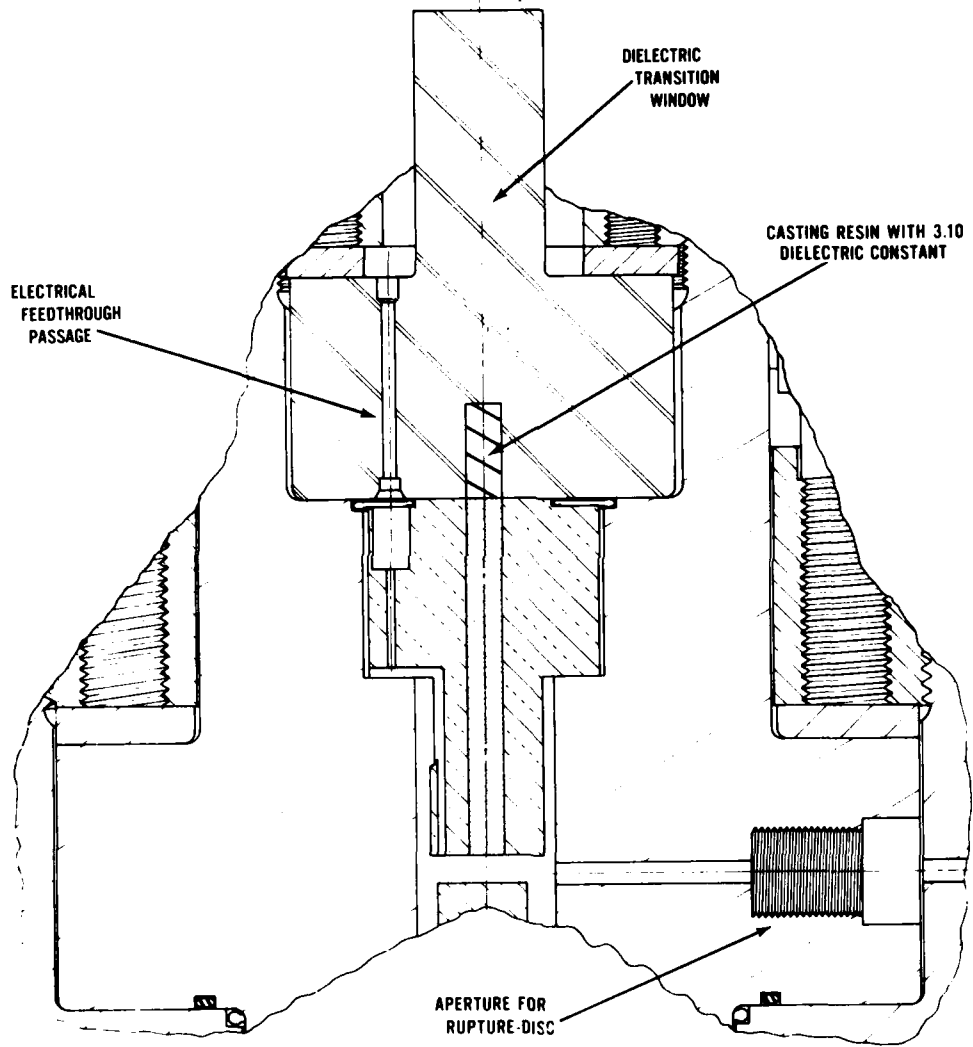


Figure 19. Combustion Fixture Offset Partial Section View

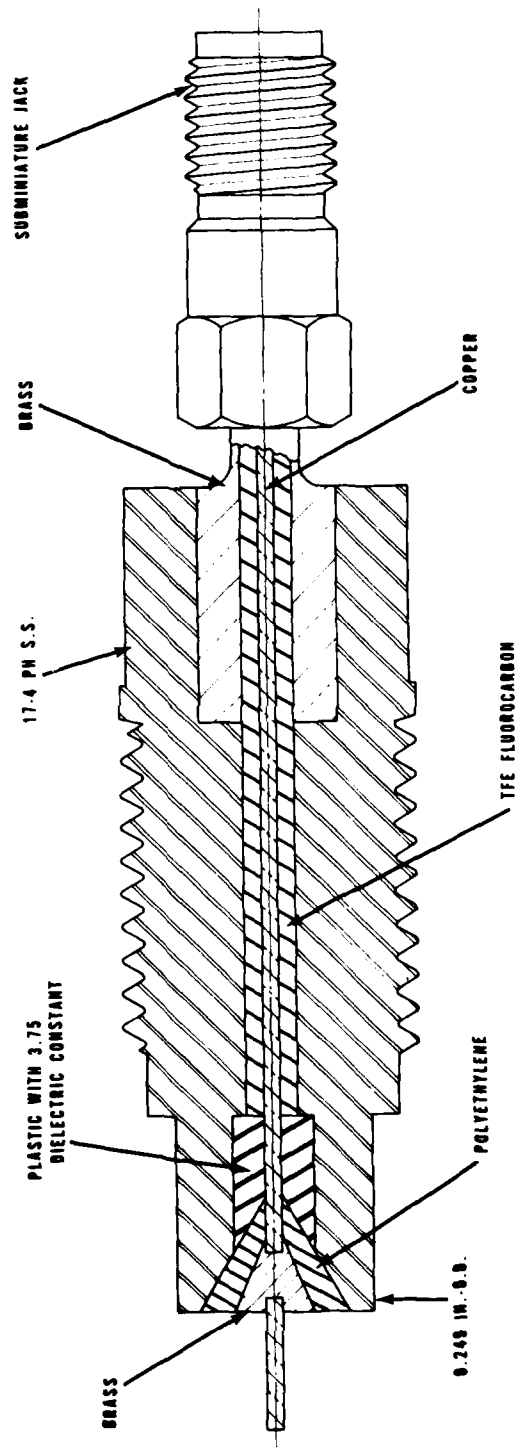


Figure 20. Section View of Pressure Sealing Microwave Feedthrough



Figure 21. Front Face of Dielectric Transition Window with Two Adjacent Microwave Feedthroughs

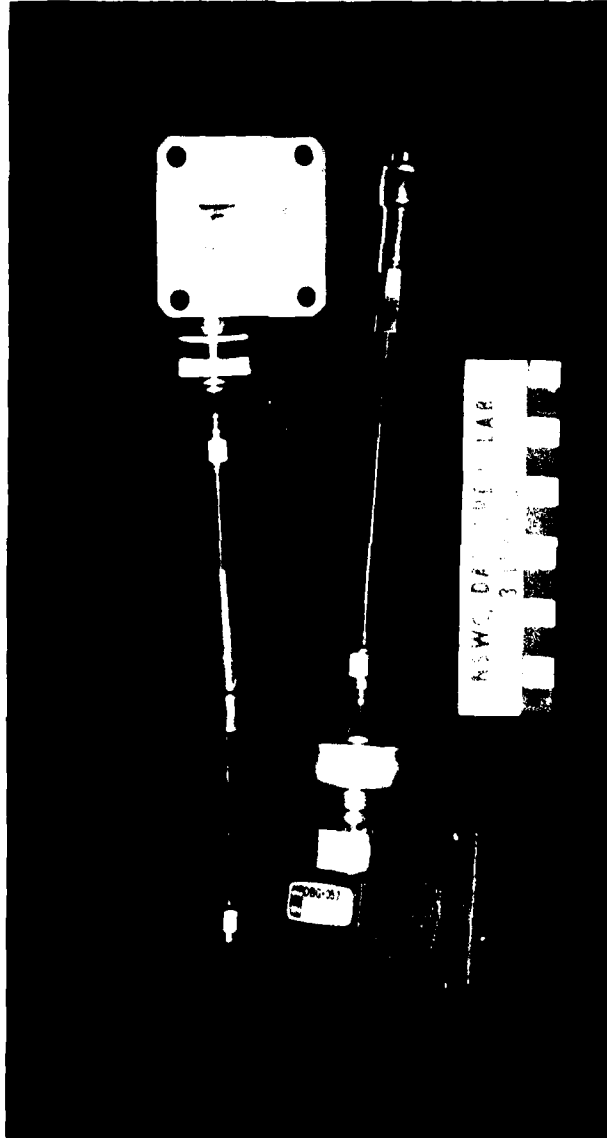


Figure 22. Sections of Semi-Rigid Coaxial Cable Which Connect the Dielectric Transition Window to the X-Band Waveguide

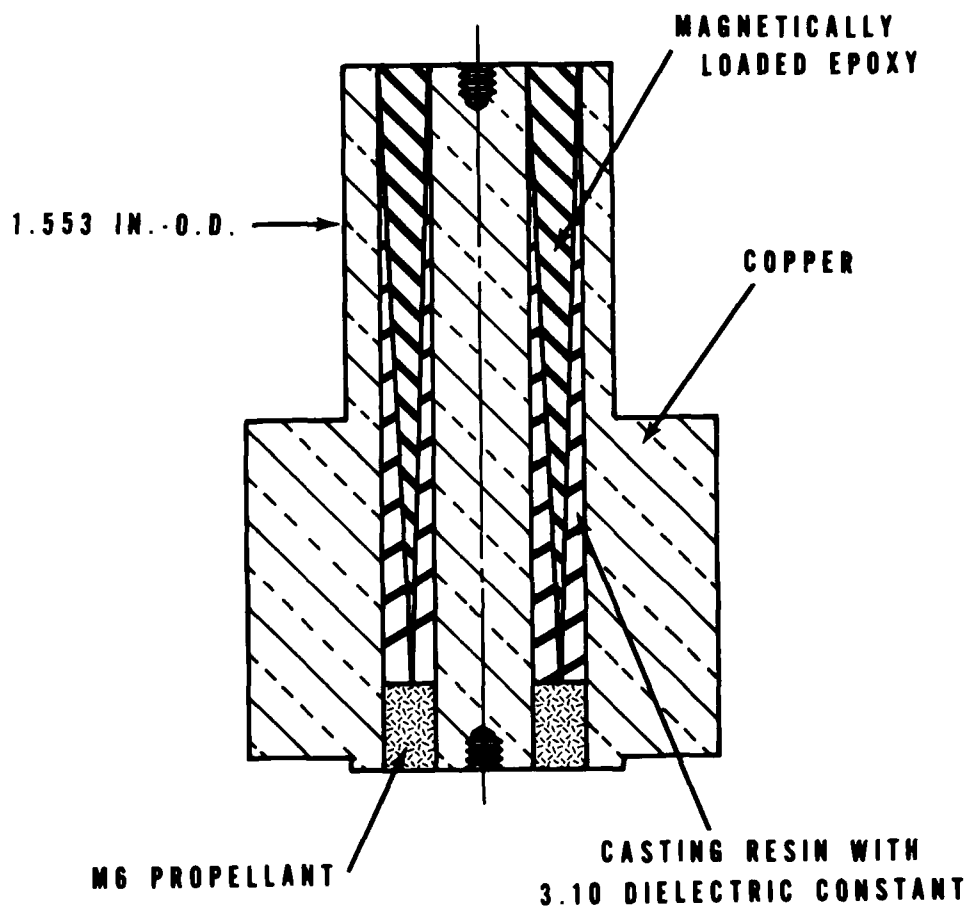


Figure 23. Section View of Twin Load

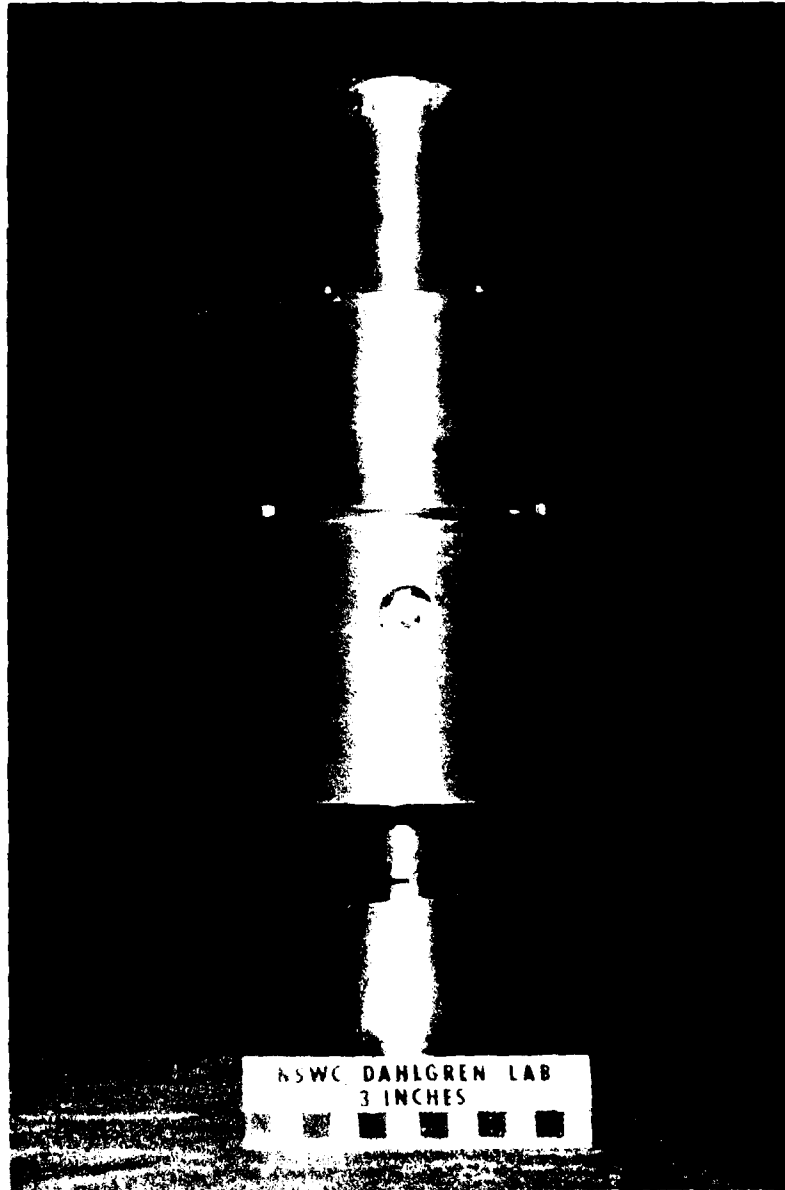


Figure 24. Twin Load Sitting Upon the Dielectric Transition Window

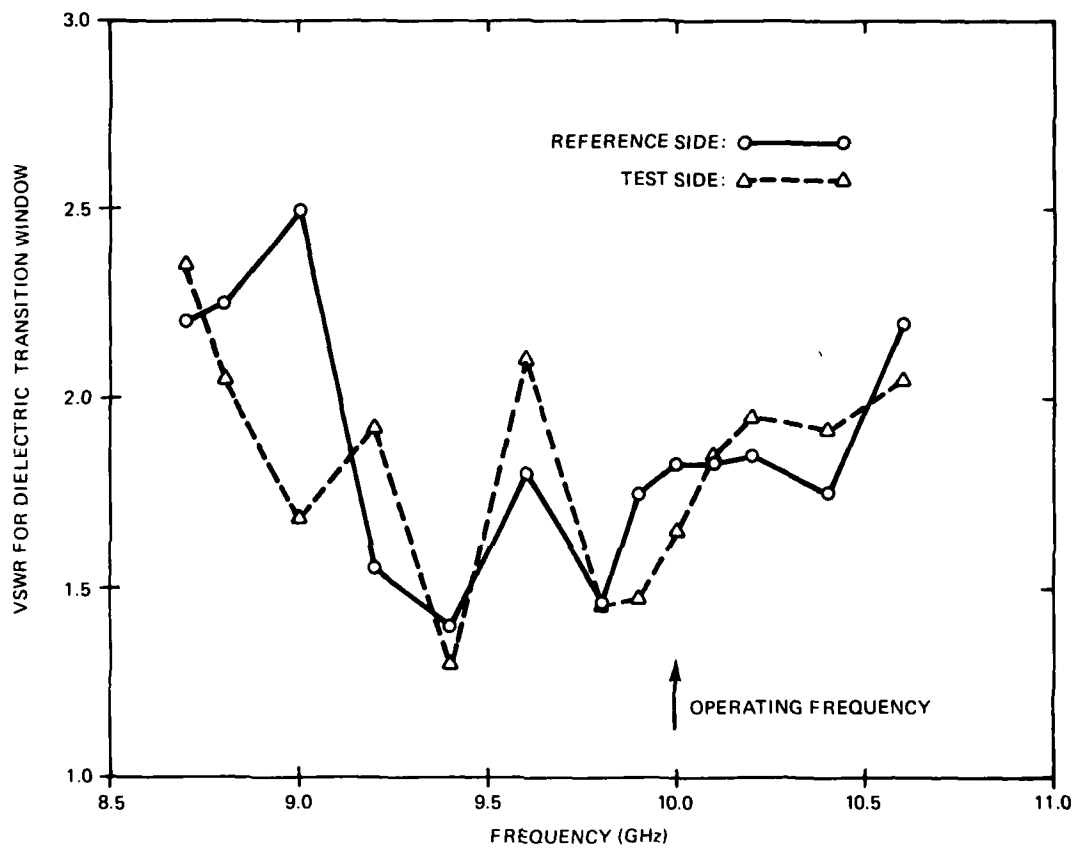


Figure 25. Voltage Standing Wave Ratio (VSWR) for the Dielectric Transition Window

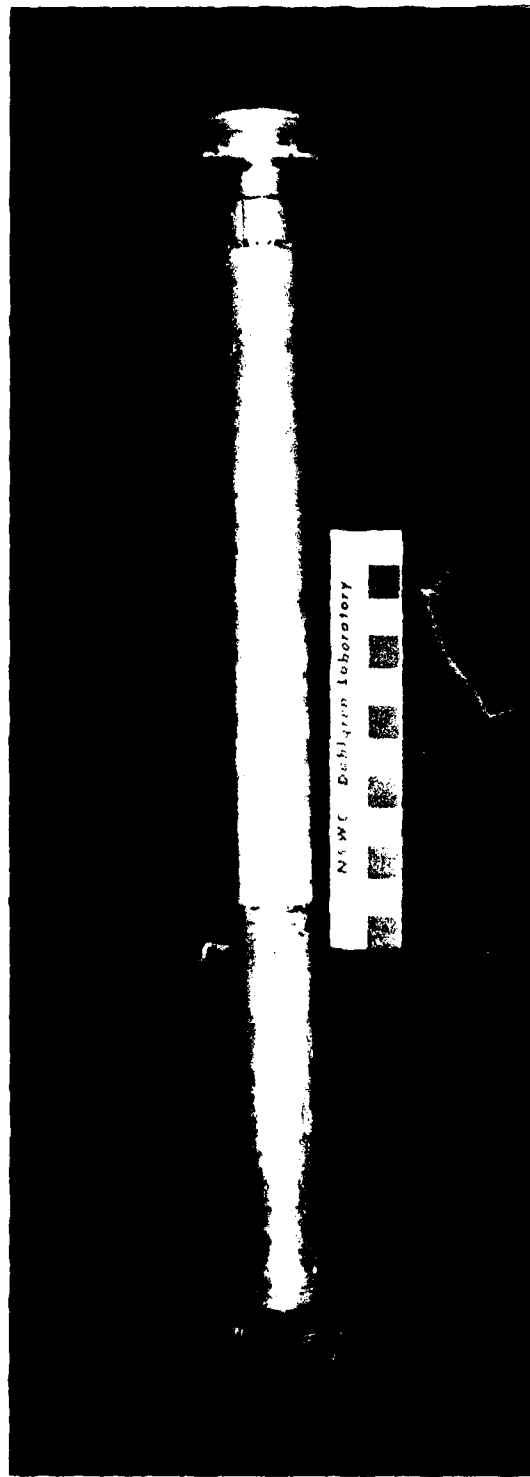
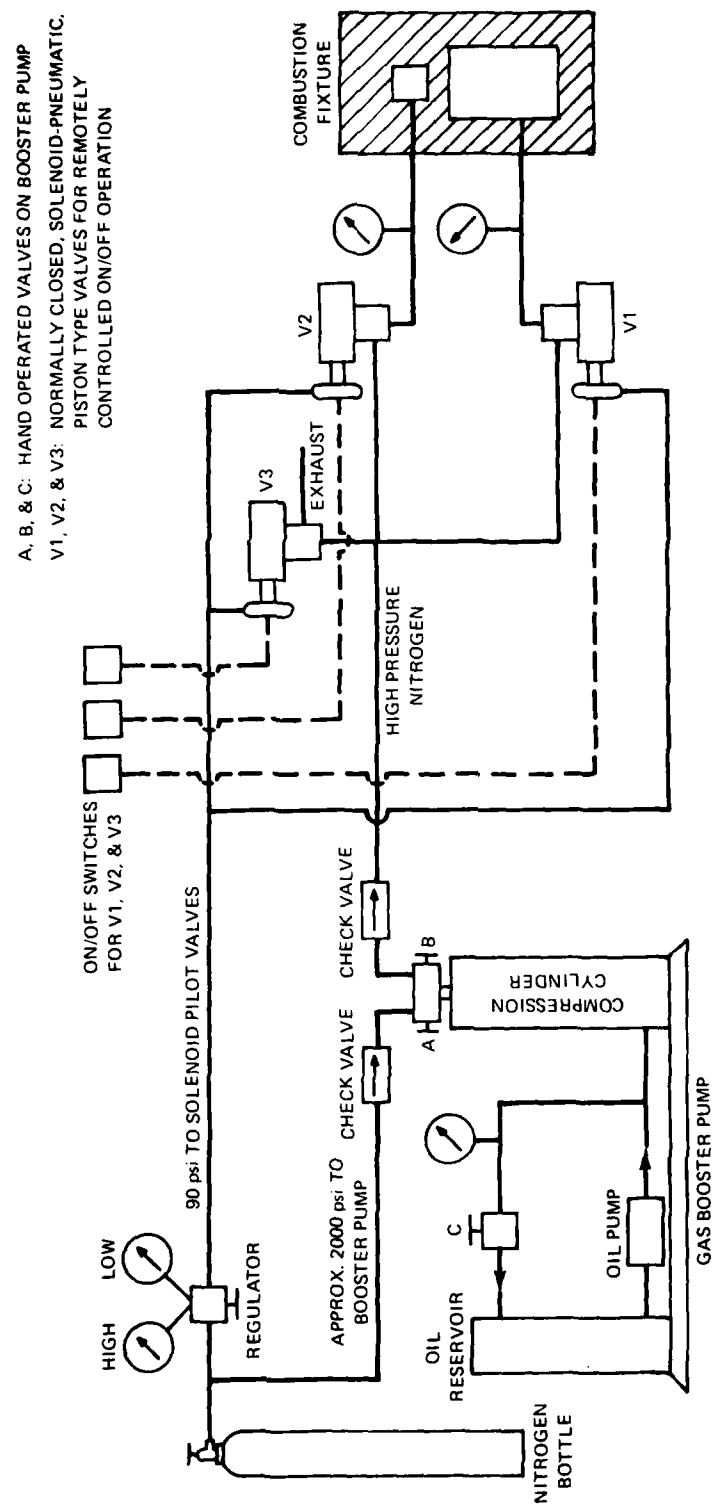


Figure 26. Waveguide-to-Waveguide Version of the Dielectric Transition Window



A, B, & C: HAND OPERATED VALVES ON BOOSTER PUMP  
V1, V2, & V3: NORMALLY CLOSED, SOLENOID-PNEUMATIC,  
PISTON TYPE VALVES FOR REMOTELY  
CONTROLLED ON/OFF OPERATION

Figure 27. Schematic of Pressurizing System



Figure 28. Overview of Experimental Facility



Figure 29. Closeup View of Waveguide Circuitry

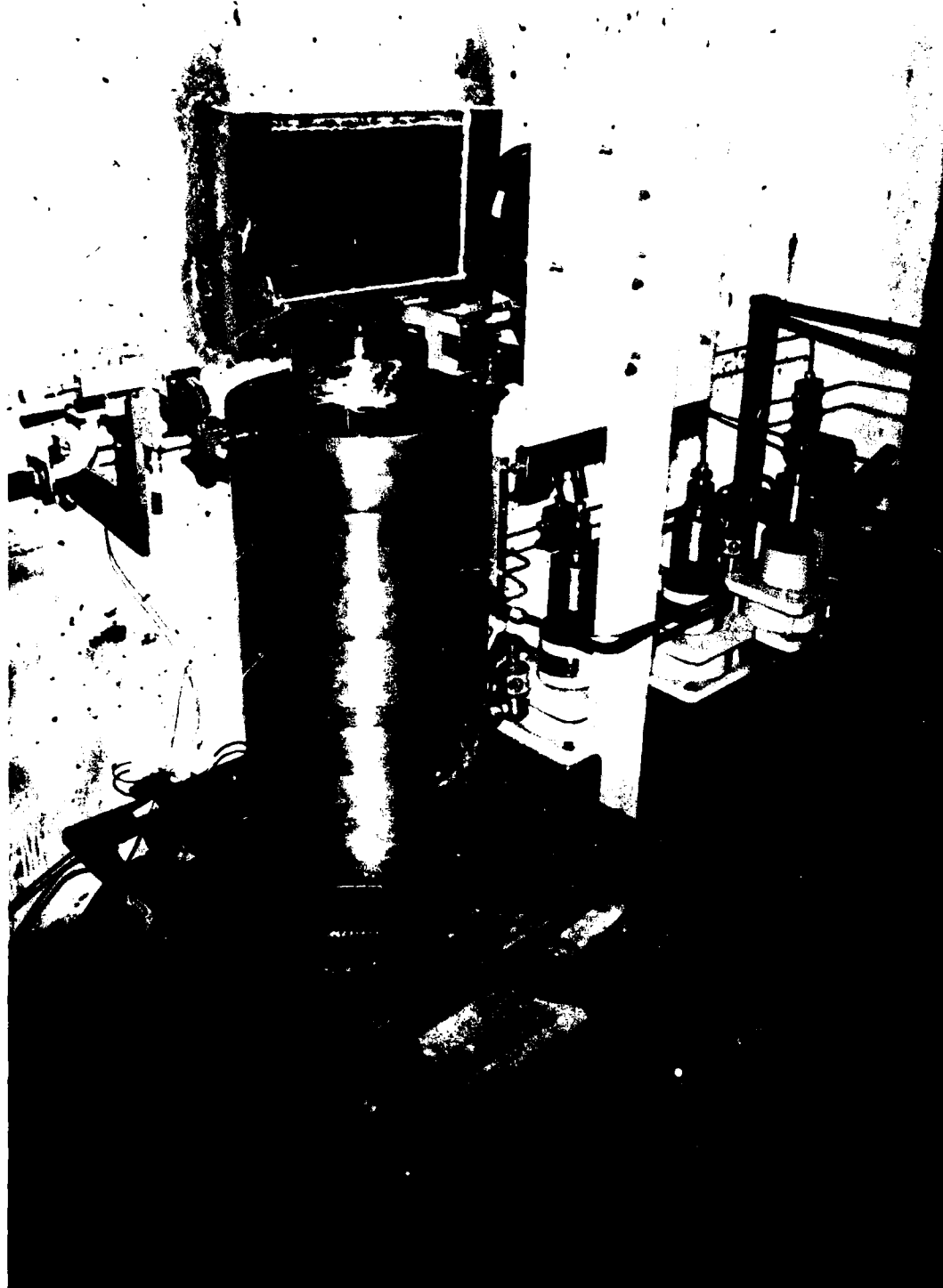


Figure 30. View Inside of the Protective Shelter

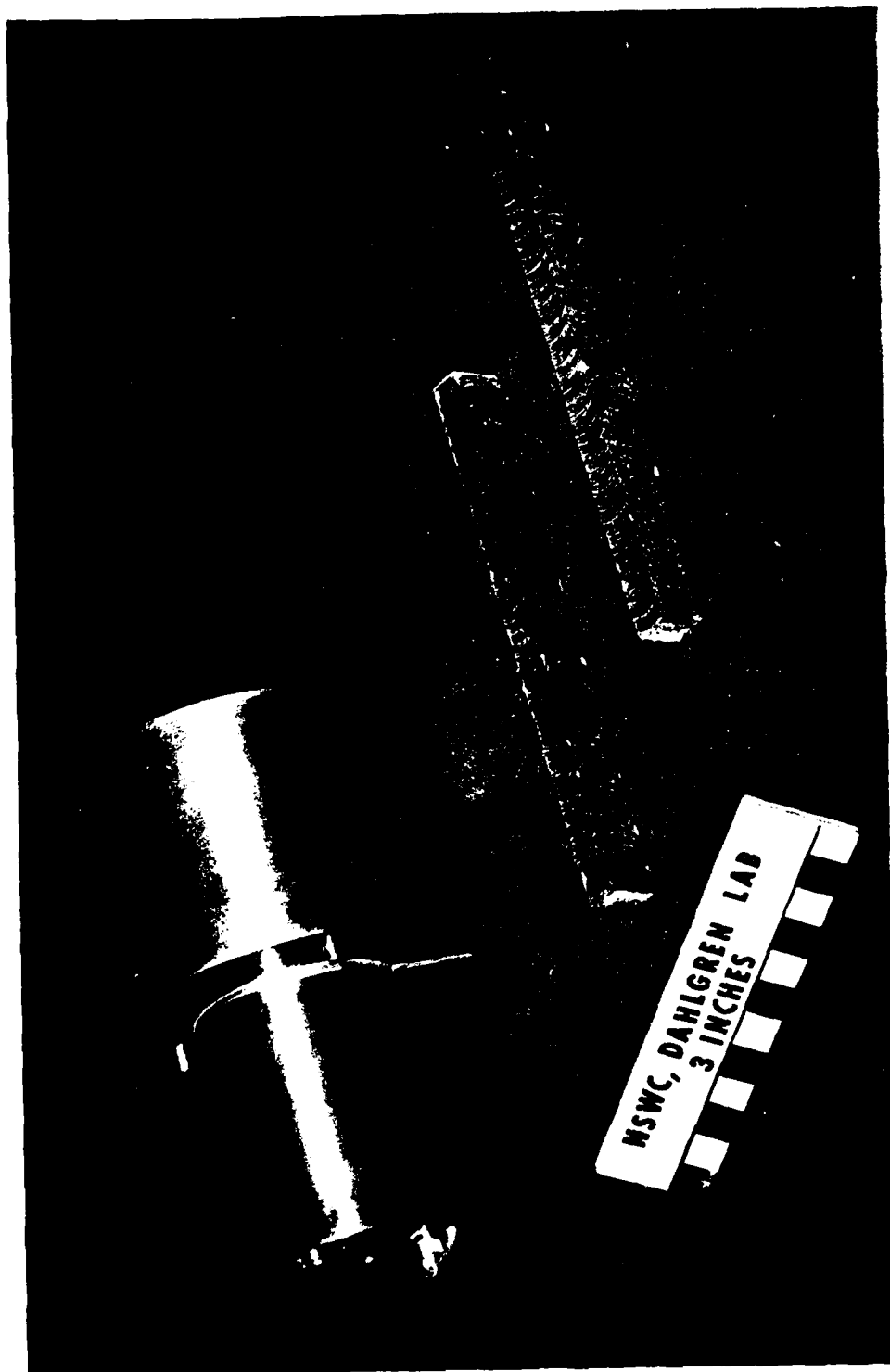


Figure 31. Dual Propellant Waveguide and Two M6 Propellant Strands

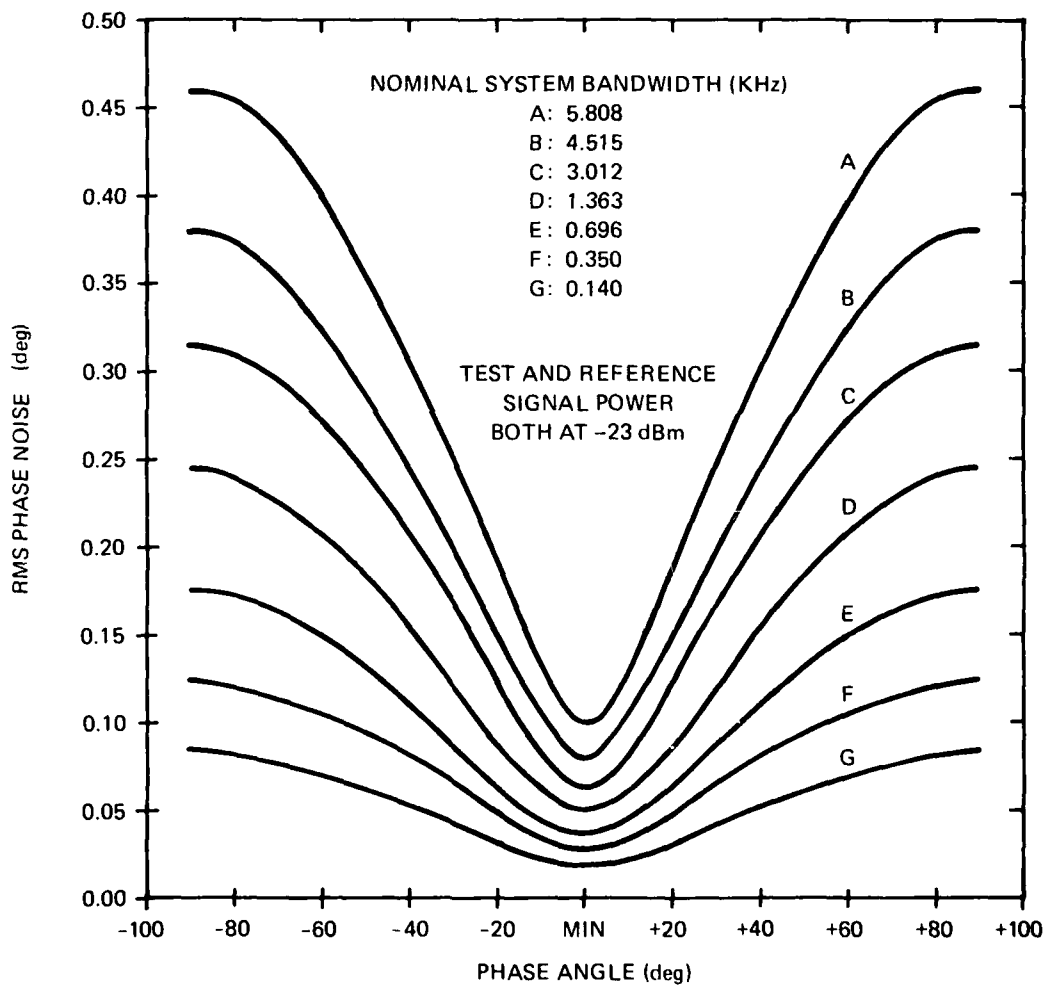


Figure 32. Phase Noise versus Phase Angle

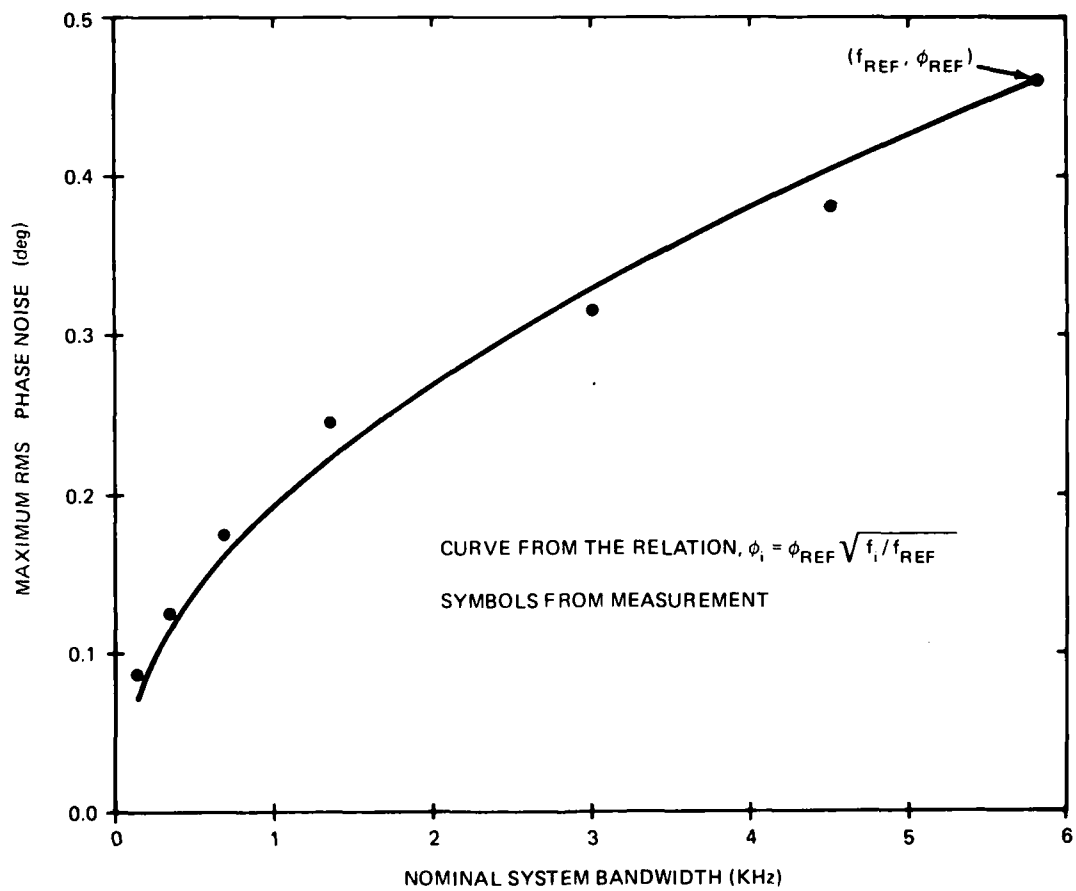


Figure 33. Maximum RMS Phase Noise versus Nominal System Bandwidth

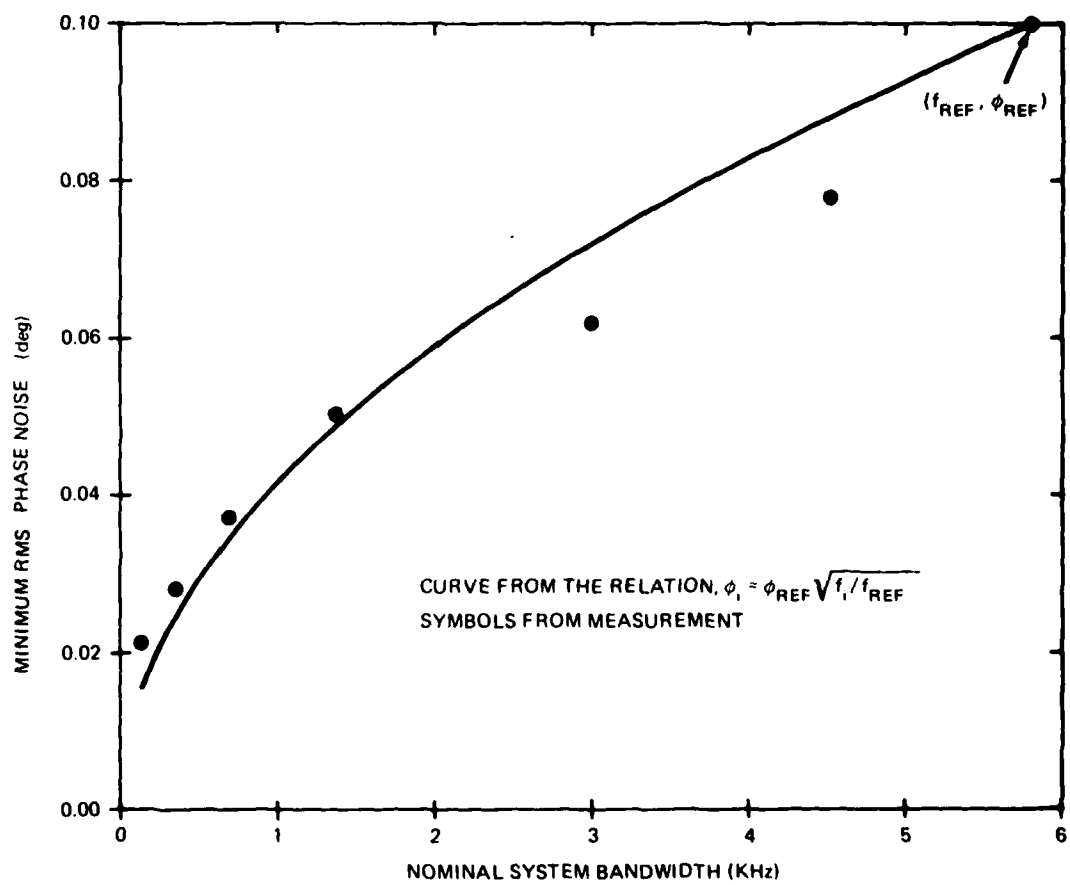


Figure 34. Minimum RMS Phase Noise versus Nominal System Bandwidth

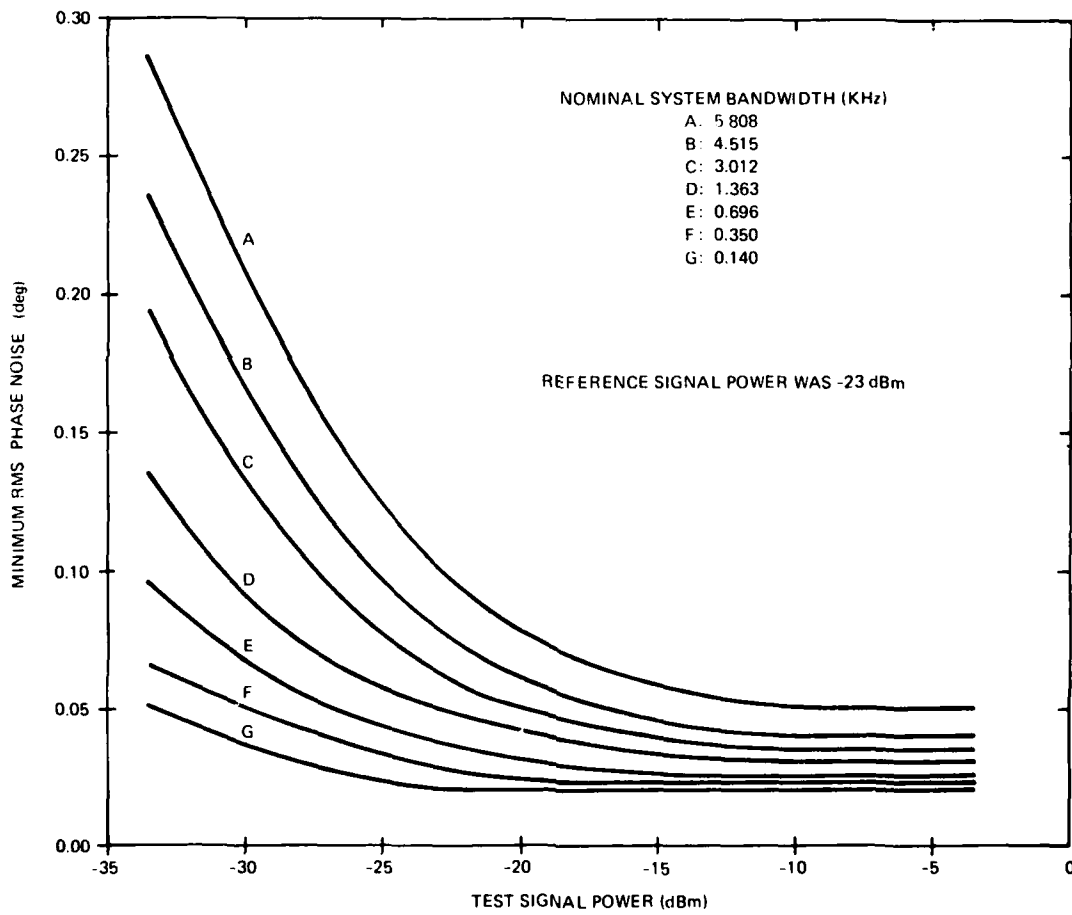


Figure 35. Minimum RMS Phase Noise versus Test Signal Power

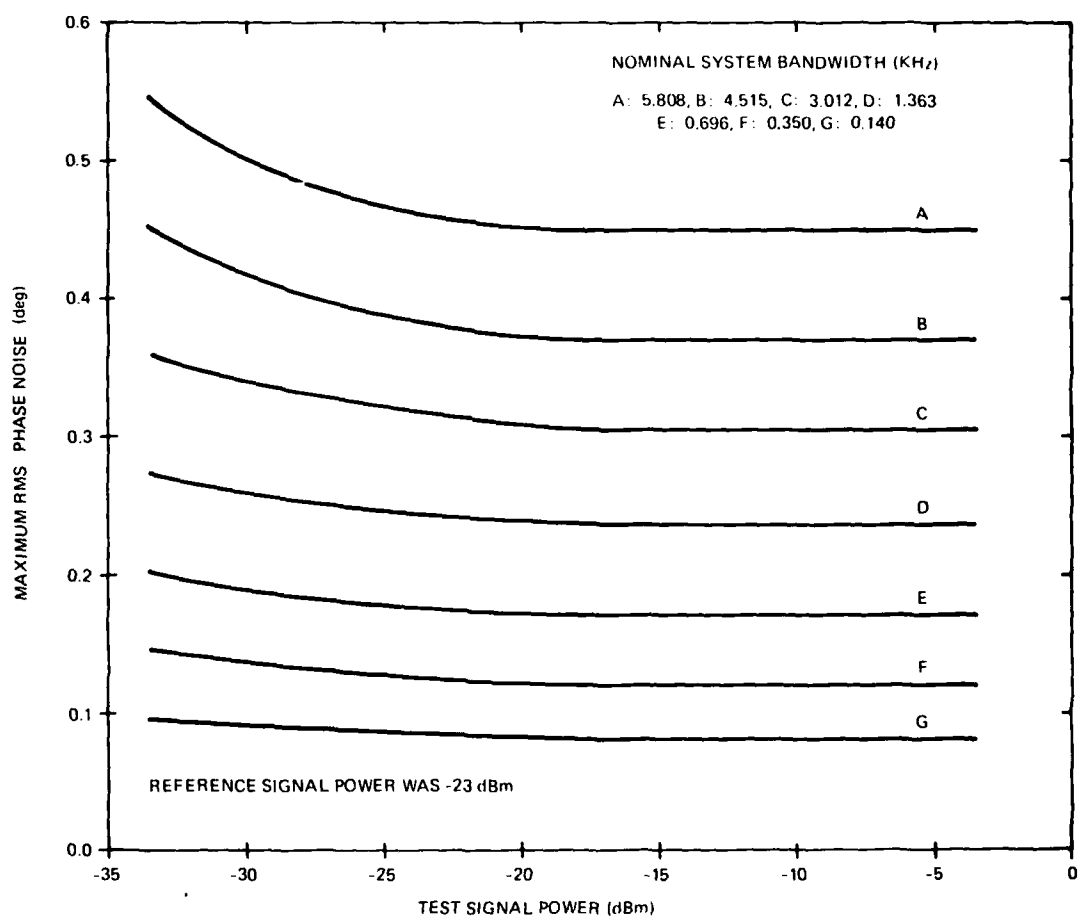


Figure 36. Maximum RMS Phase Noise versus Test Signal Power

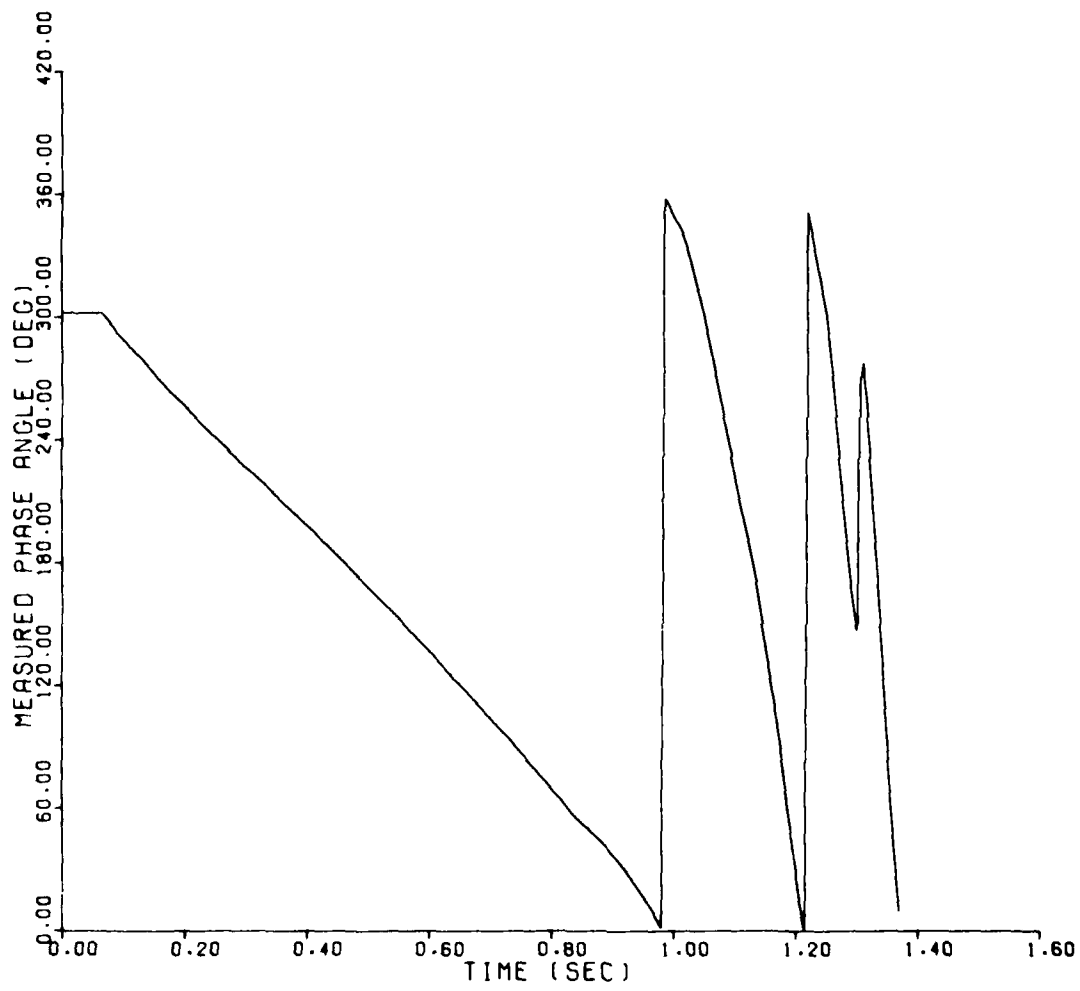


Figure 37. Measured Phase Angle on the 11<sup>th</sup> Steady-State Test

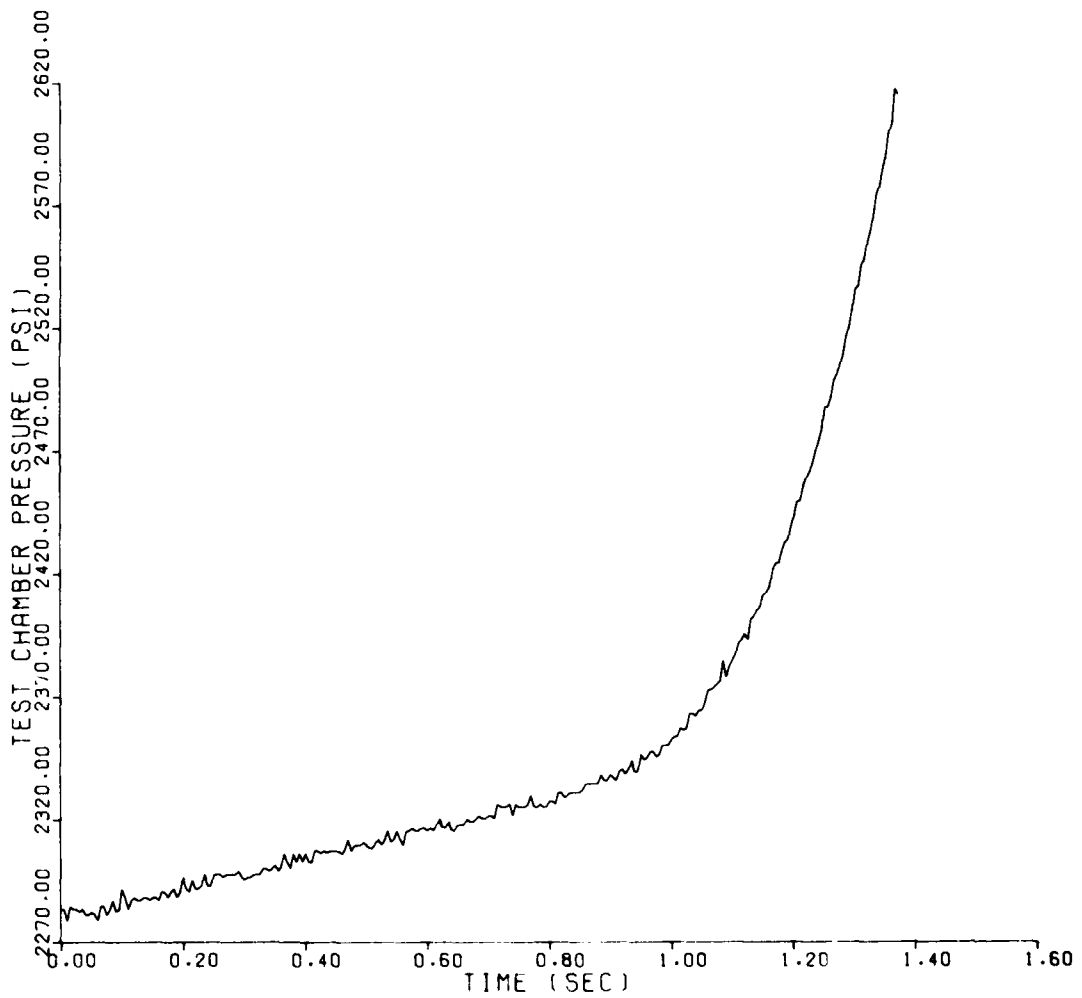


Figure 38. Test Chamber Pressure on the 11<sup>th</sup> Steady-State Test

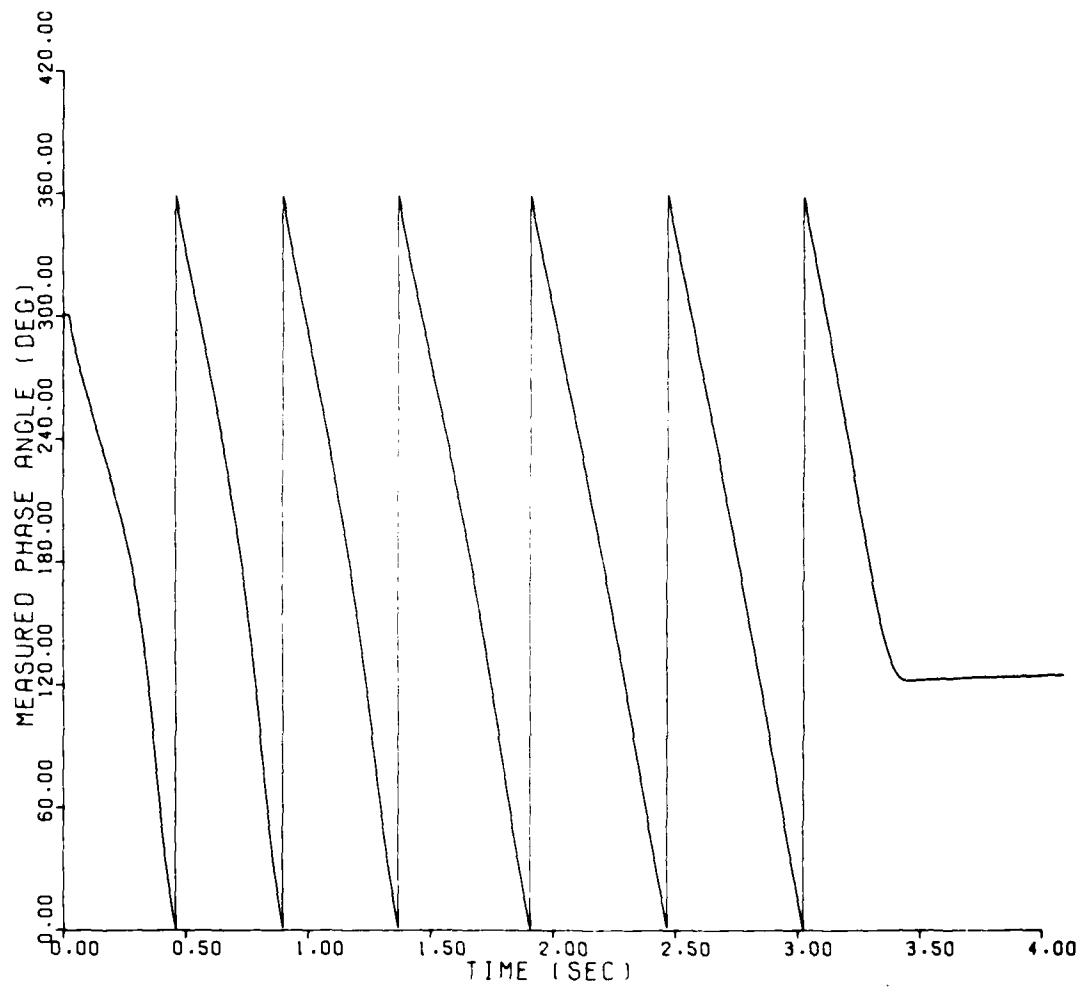


Figure 39. Measured Phase Angle on the 8<sup>th</sup> Steady-State Test

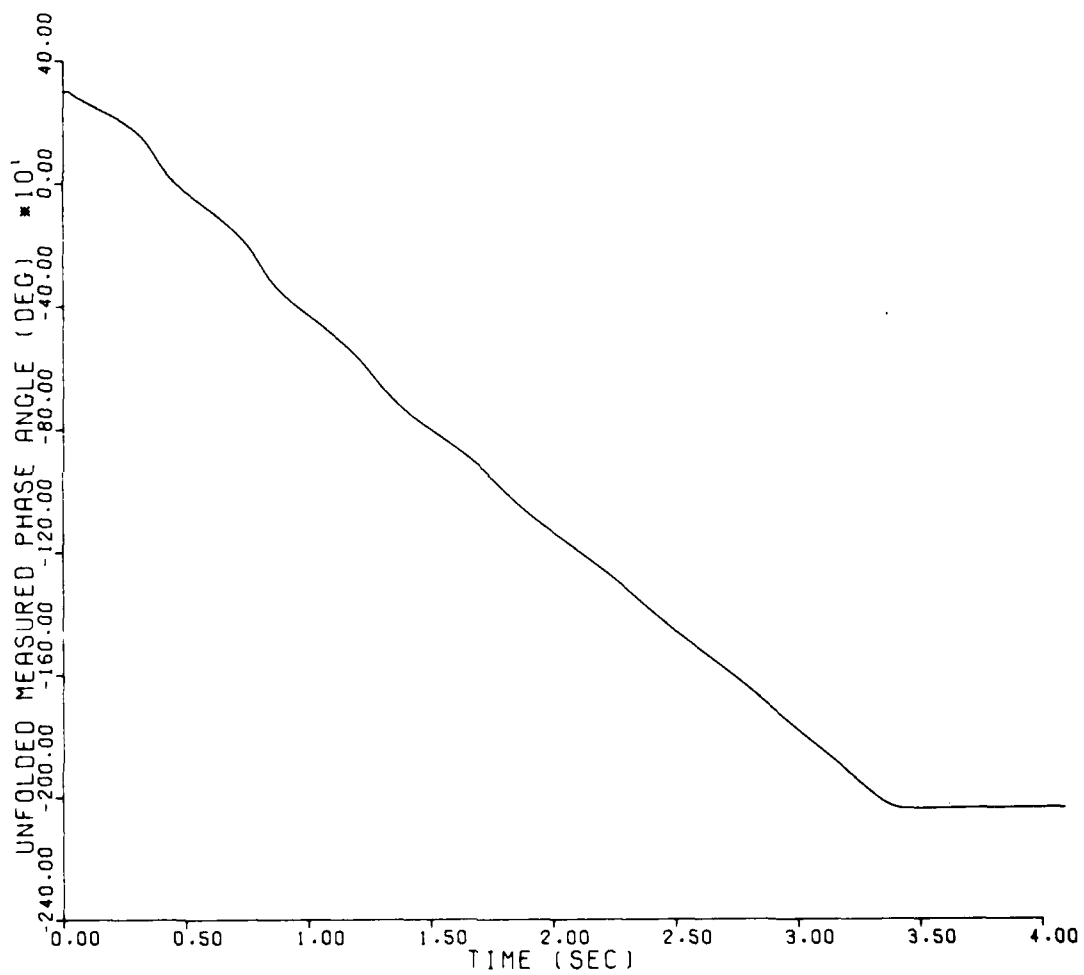
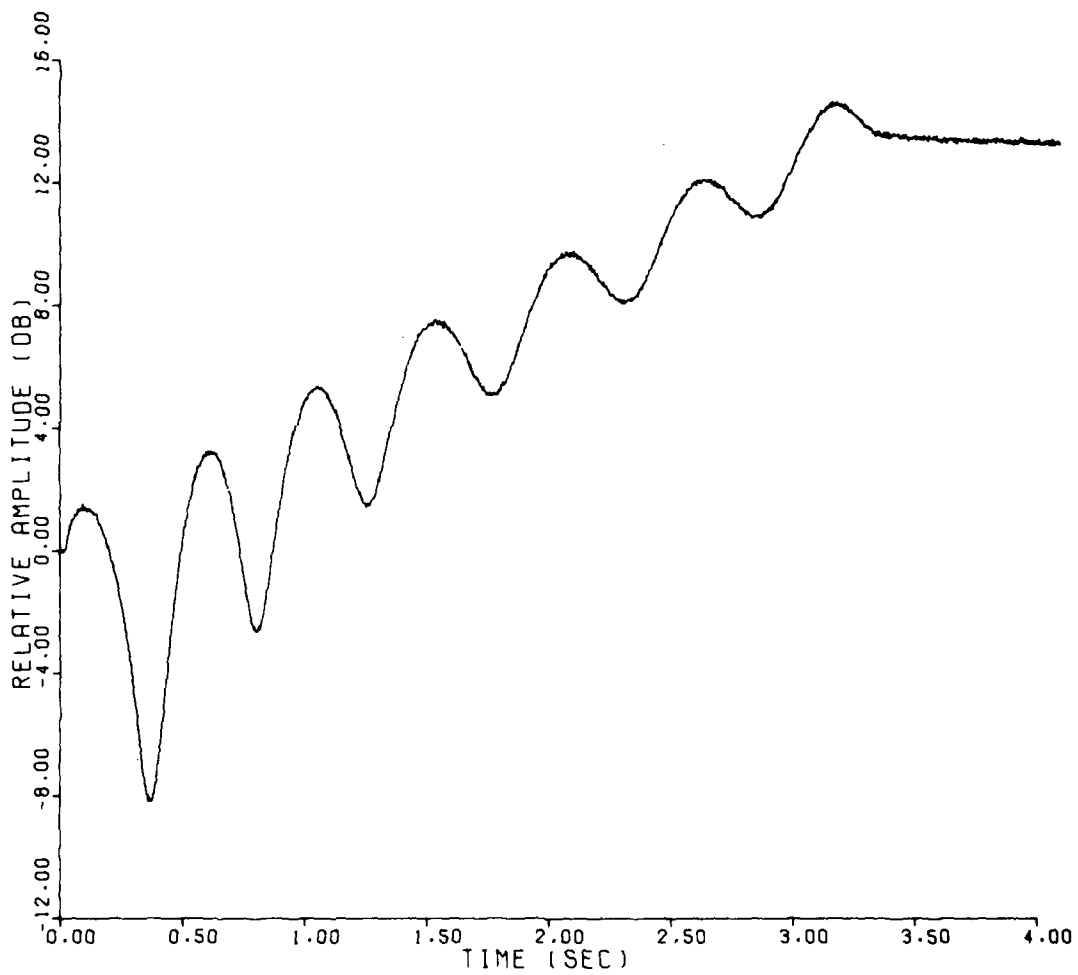


Figure 40. Unfolded Measured Phase Angle on the 8<sup>th</sup> Steady-State Test



**Figure 41. Change in Relative Amplitude of the Test Signal on the 8<sup>th</sup> Steady-State Test**

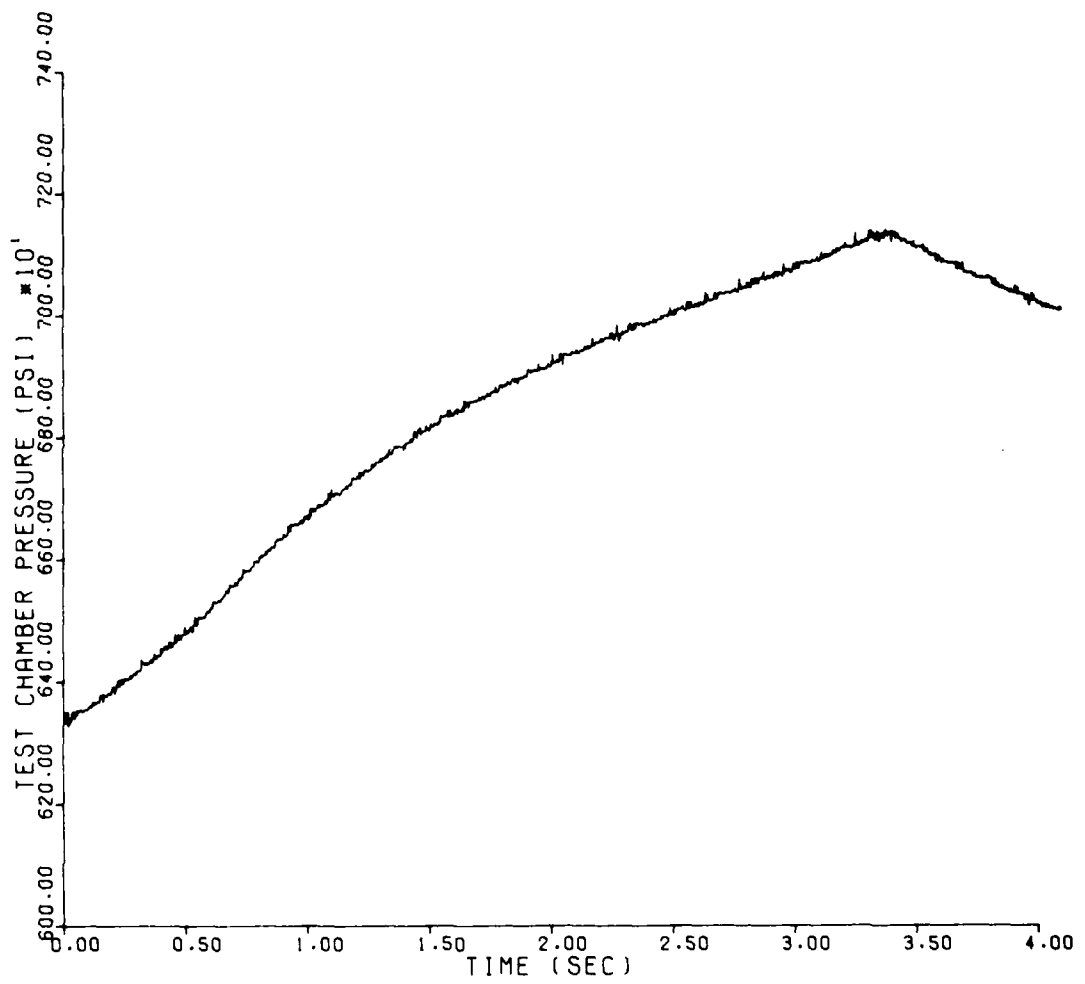


Figure 42. Test Chamber Pressure on the 8<sup>th</sup> Steady-State Test

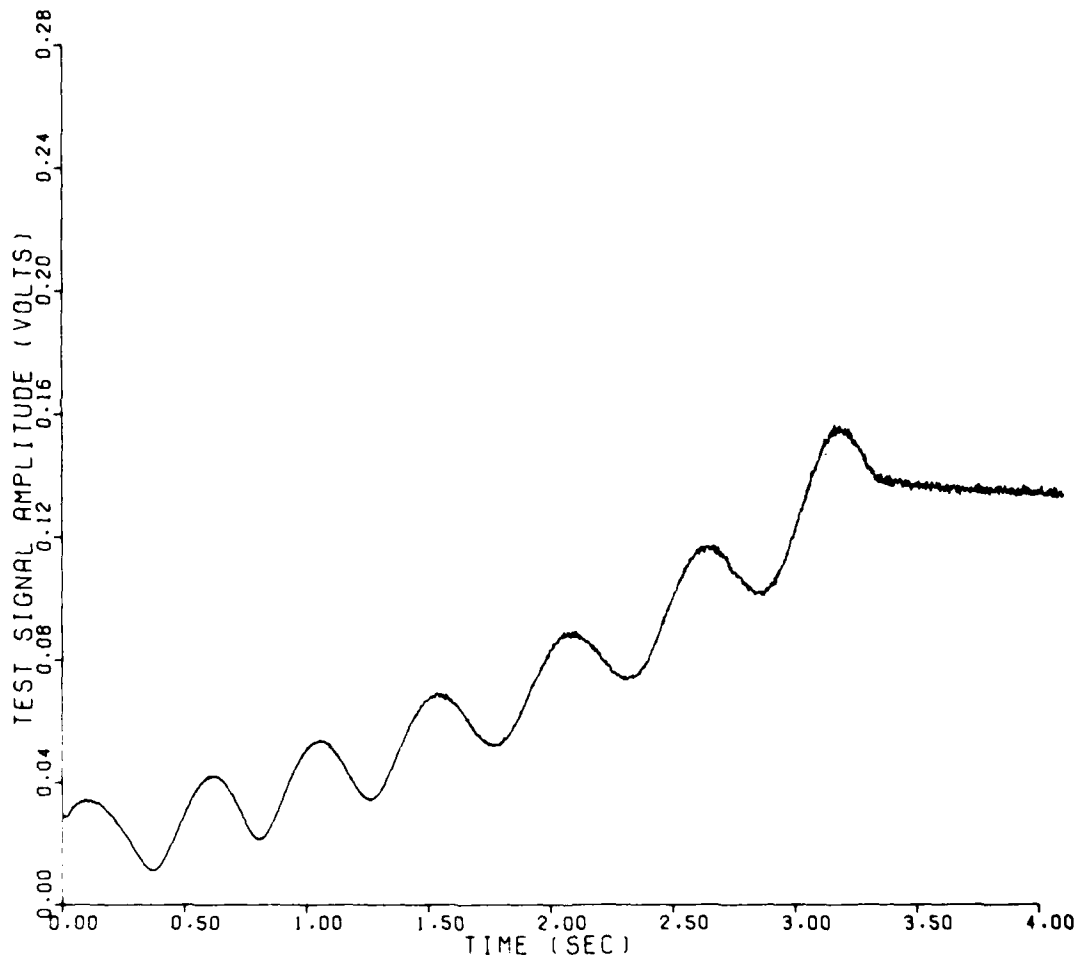


Figure 43. Test Signal Amplitude on the 8<sup>th</sup> Steady-State Test

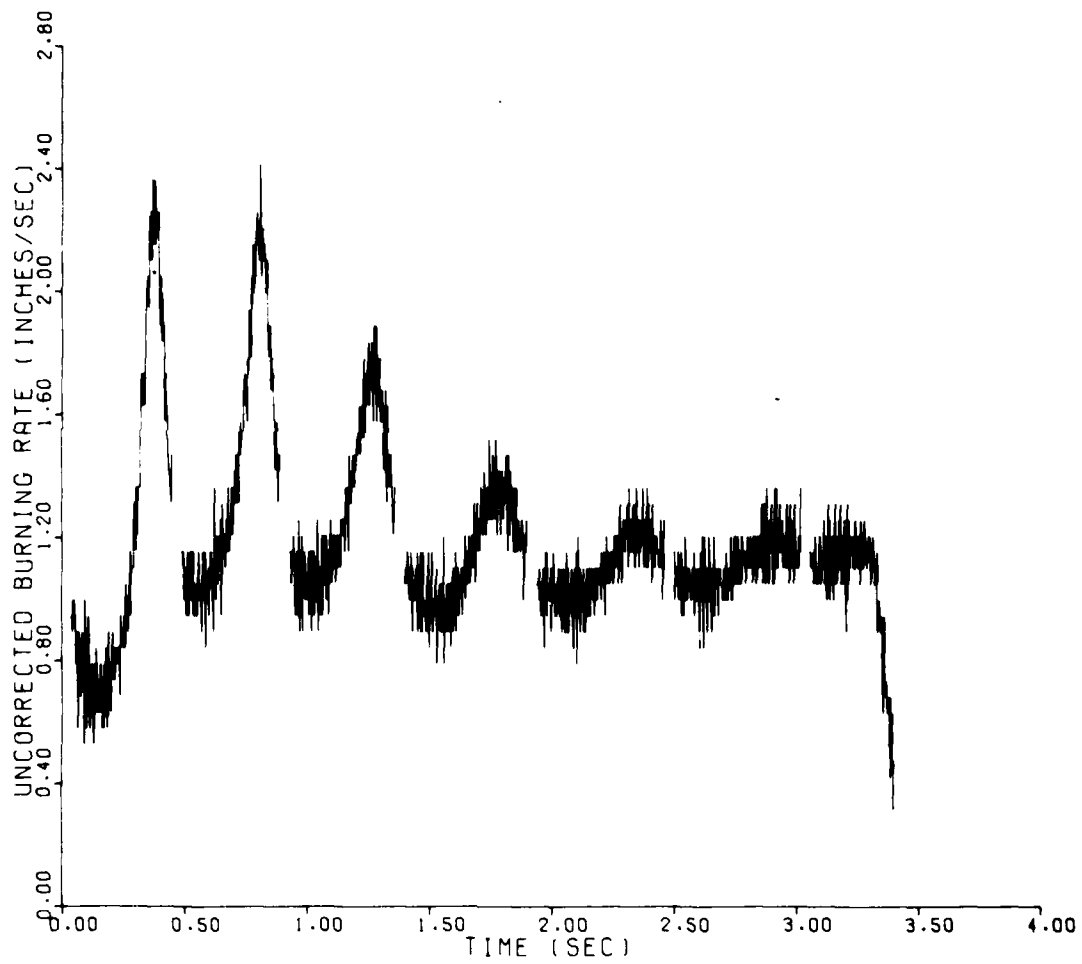


Figure 44. Apparent or Uncorrected Burning Rate on the 8<sup>th</sup> Steady-State Test; Determined by the Use of Central Differences Applied to Raw Data

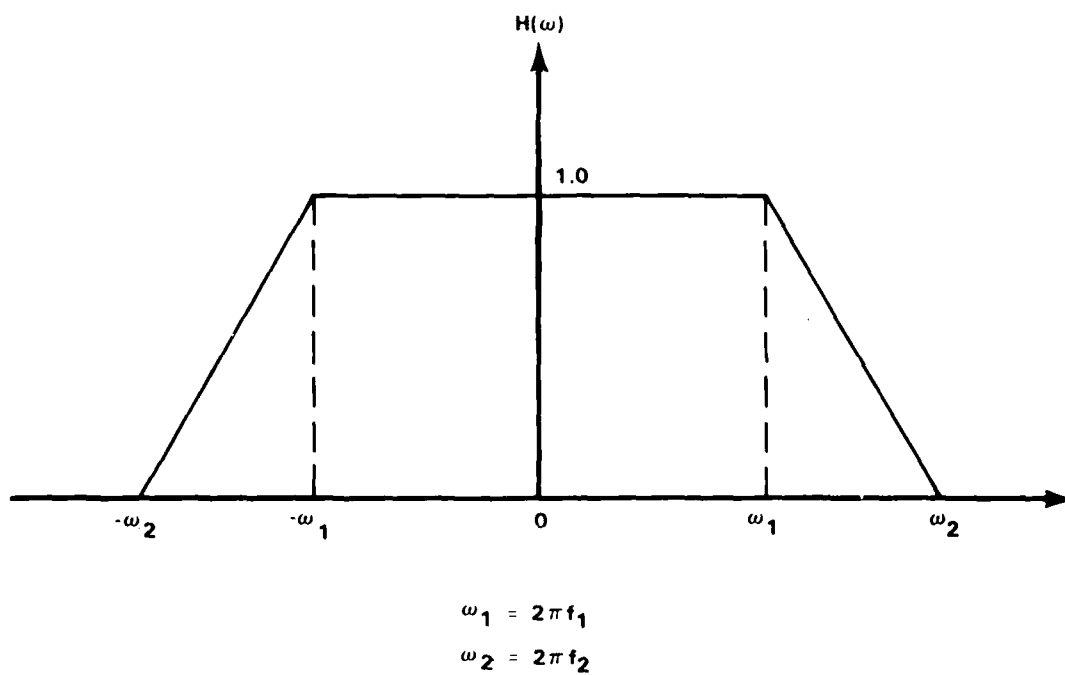


Figure 45. Real Symmetric Transfer Function Used in Lowpass Digital Filtering

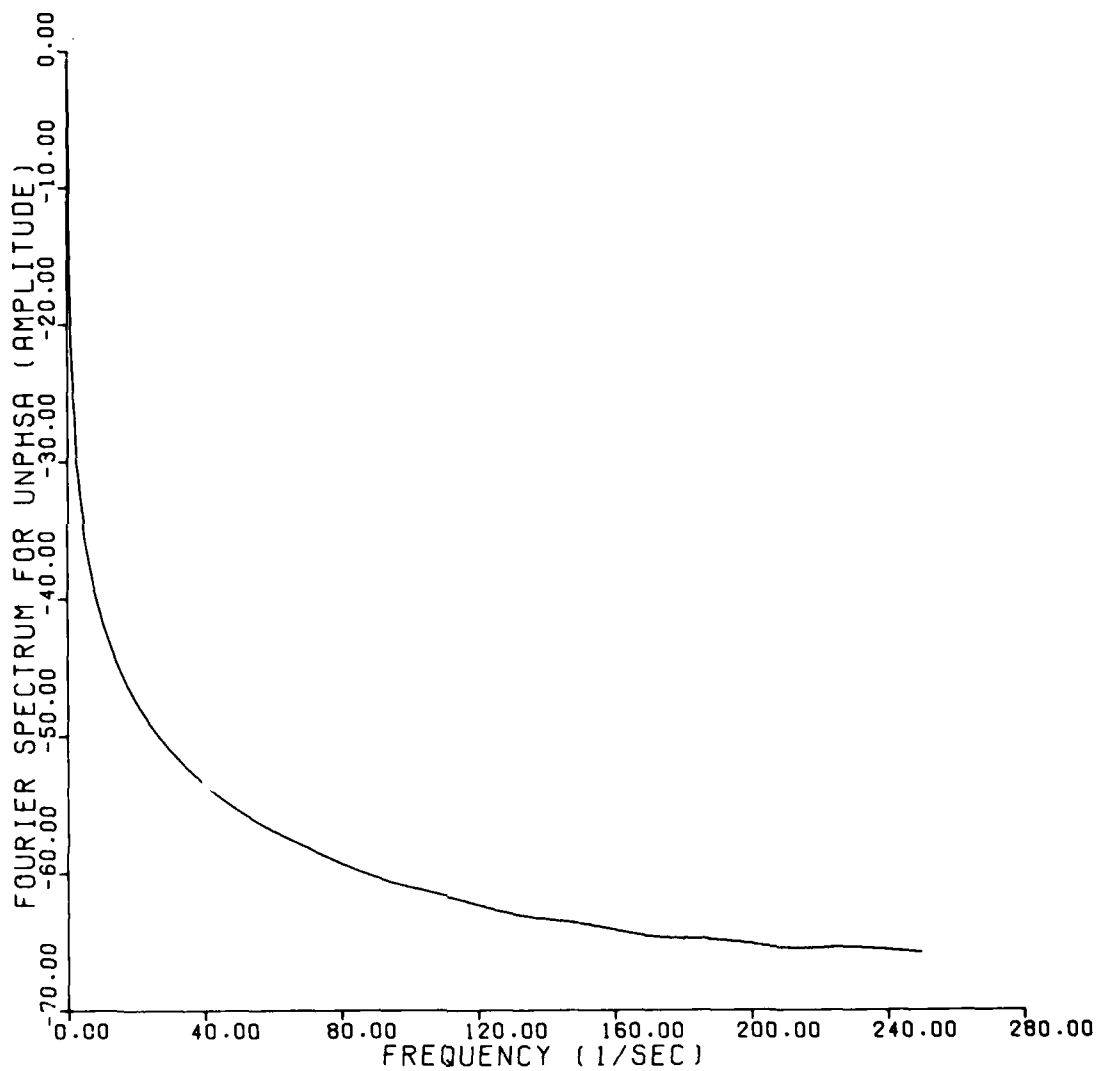


Figure 46. Hybrid Amplitude Spectrum in dB for the Unfolded Measured Phase Angle on the 8<sup>th</sup> Steady-State Test

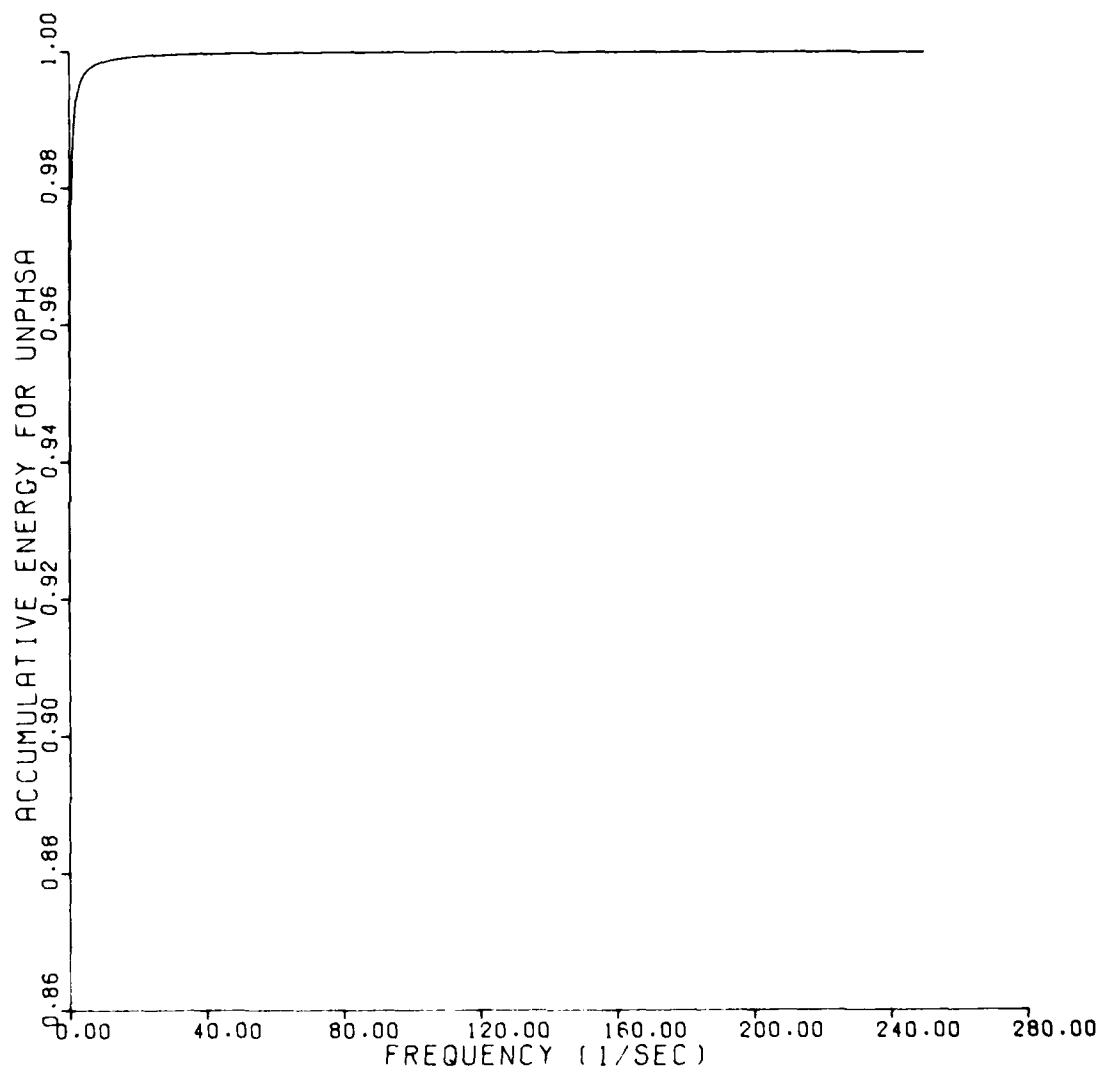


Figure 47. Accumulative Energy Spectrum for the Unfolded Measured Phase Angle on the 8<sup>th</sup> Steady-State Test

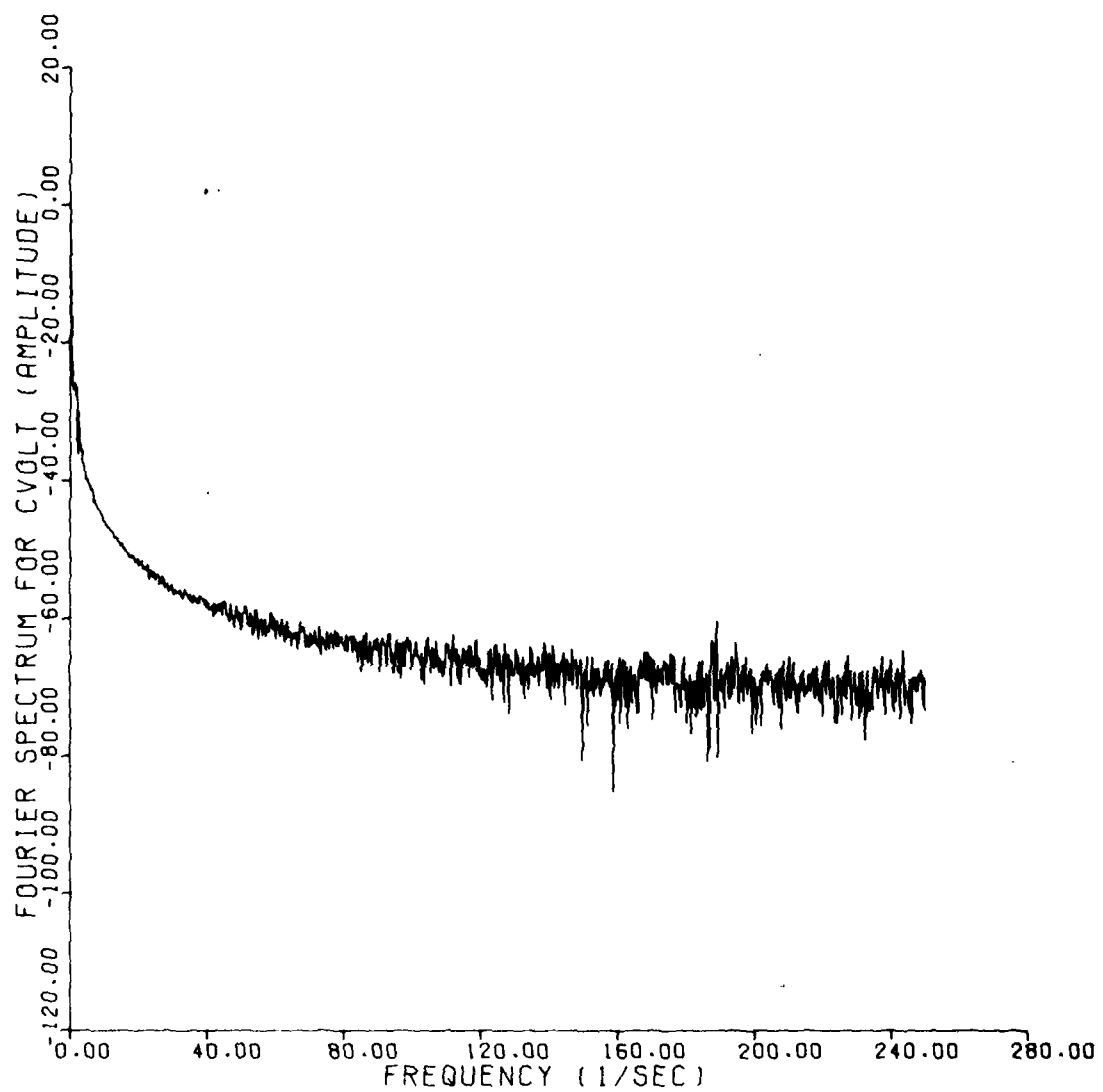


Figure 48. Hybrid Amplitude Spectrum in dB for the Test Signal Amplitude on the 8<sup>th</sup> Steady-State Test

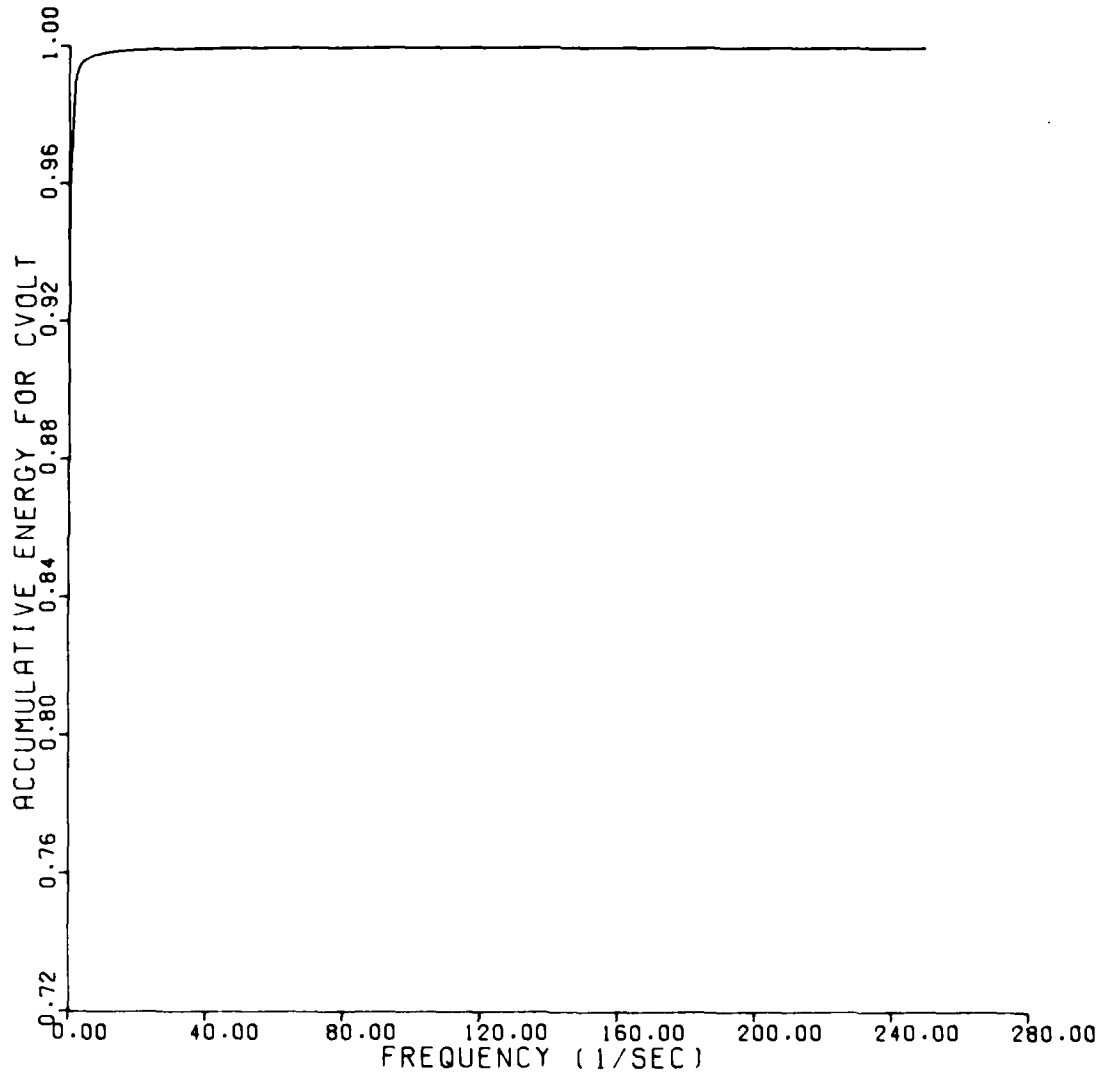


Figure 49. Accumulative Energy Spectrum for the Test Signal Amplitude on the 8<sup>th</sup> Steady-State Test

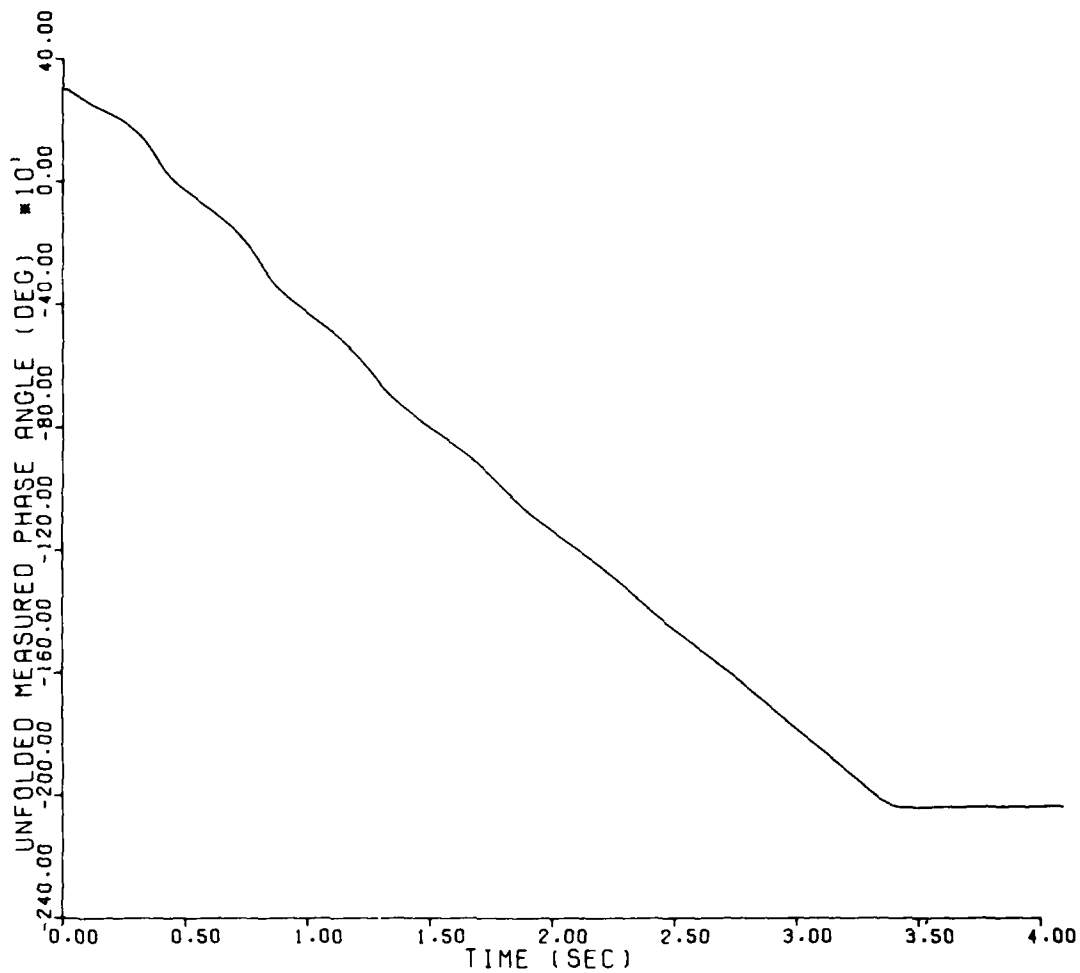


Figure 50. Filtered Unfolded Measured Phase Angle on the 8<sup>th</sup> Steady-State Test

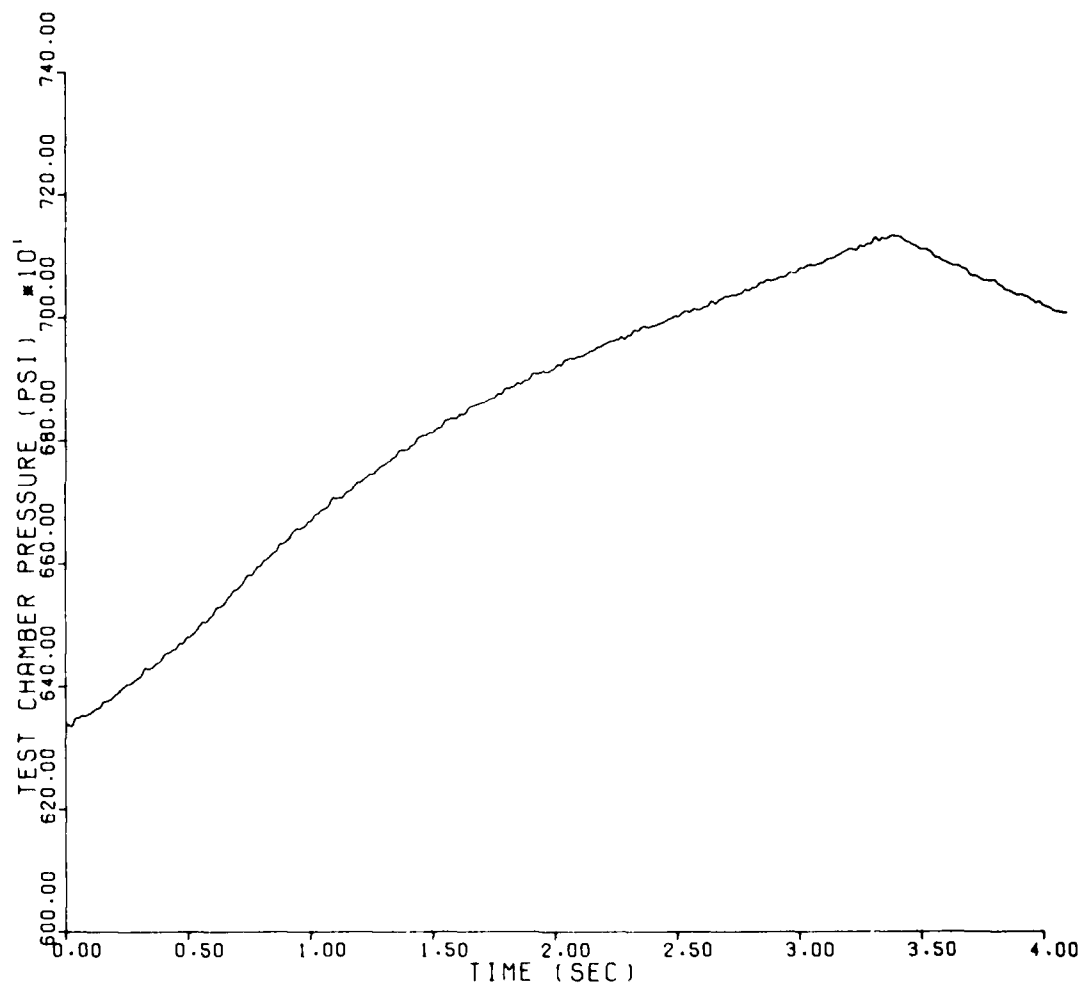


Figure 51. Filtered Test Chamber Pressure on the 8<sup>th</sup> Steady-State Test

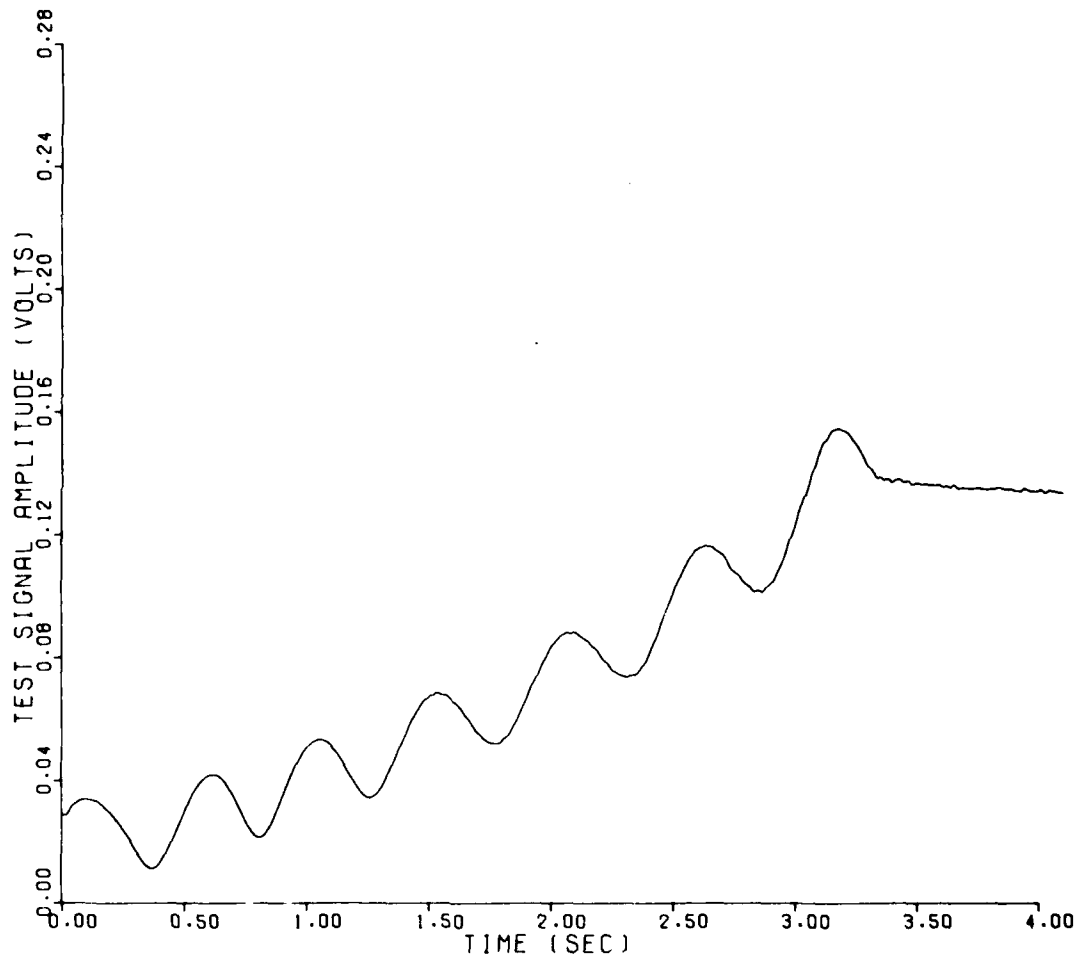


Figure 52. Filtered Test Signal Amplitude on the 8<sup>th</sup> Steady-State Test

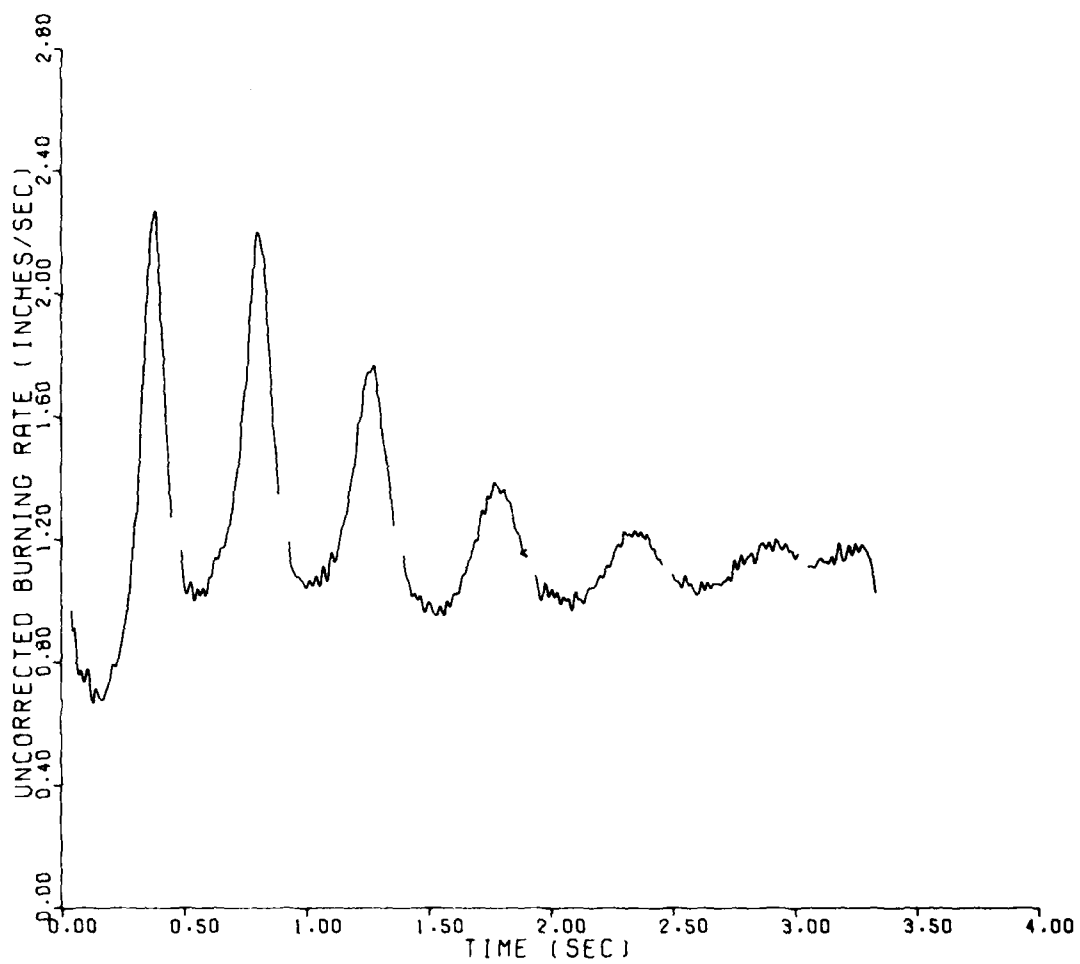


Figure 53. Apparent or Uncorrected Burning Rate on the 8<sup>th</sup> Steady-State Test; Determined by the Use of the Differentiating Digital Filter

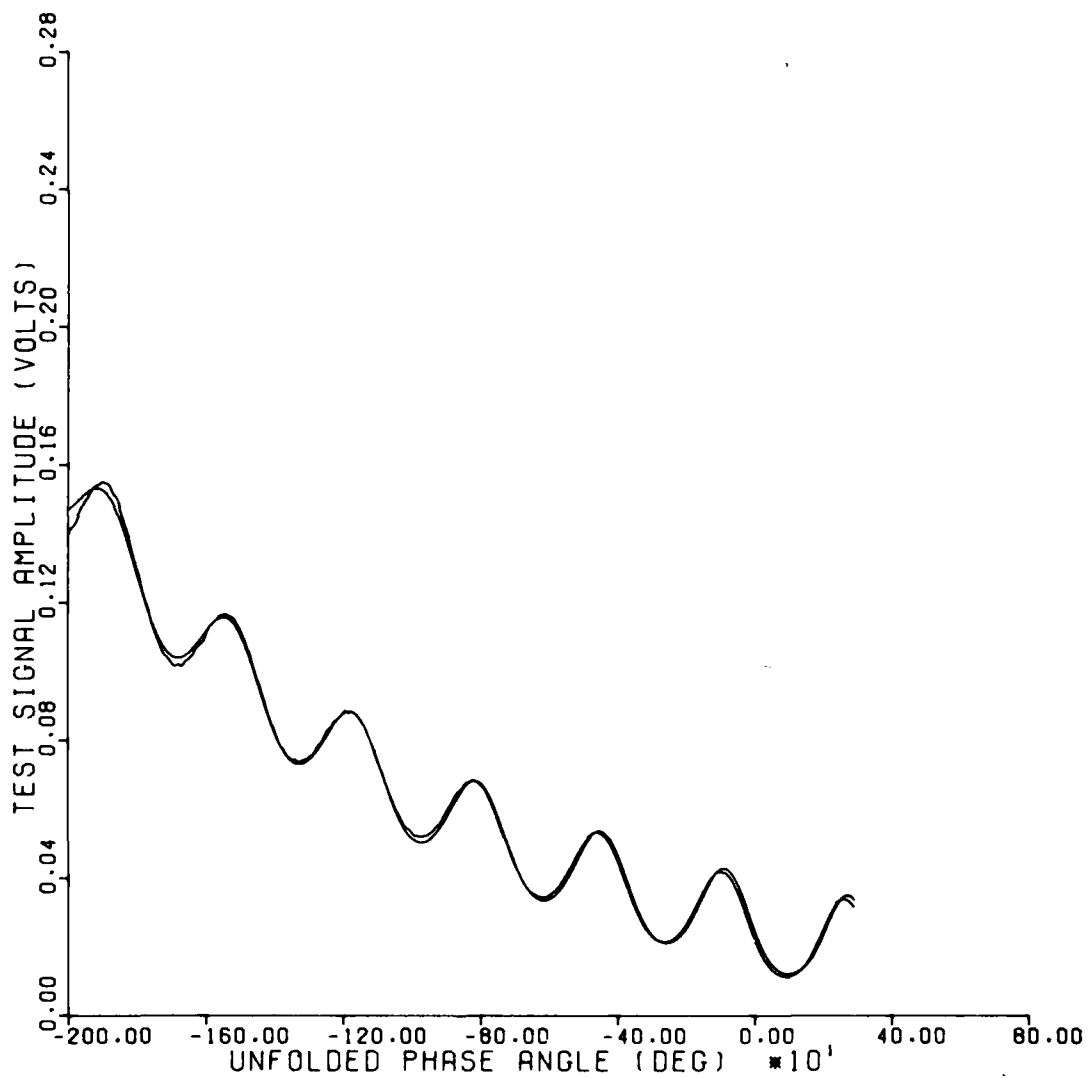
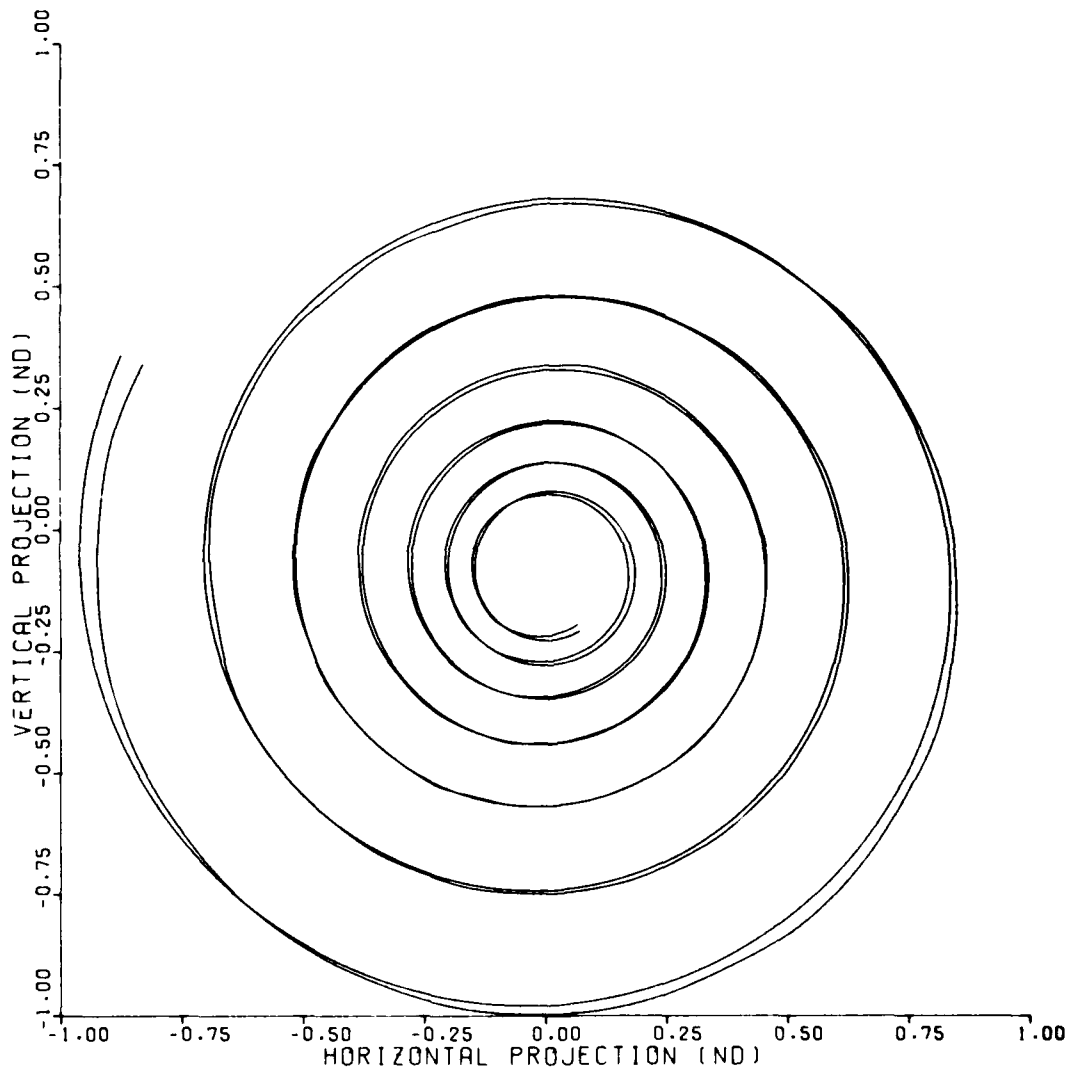


Figure 54. Test Signal Amplitude versus Unfolded Measured Phase Angle for the 8<sup>th</sup> Steady-State Test: Optimized Theory Compared to Filtered Experimental Data



**Figure 55. Nondimensional Phasor Plot of the Tip of Vector  $\vec{C}$  for the 8<sup>th</sup> Steady-State Test: Optimized Theory Compared to Filtered Experimental Data**

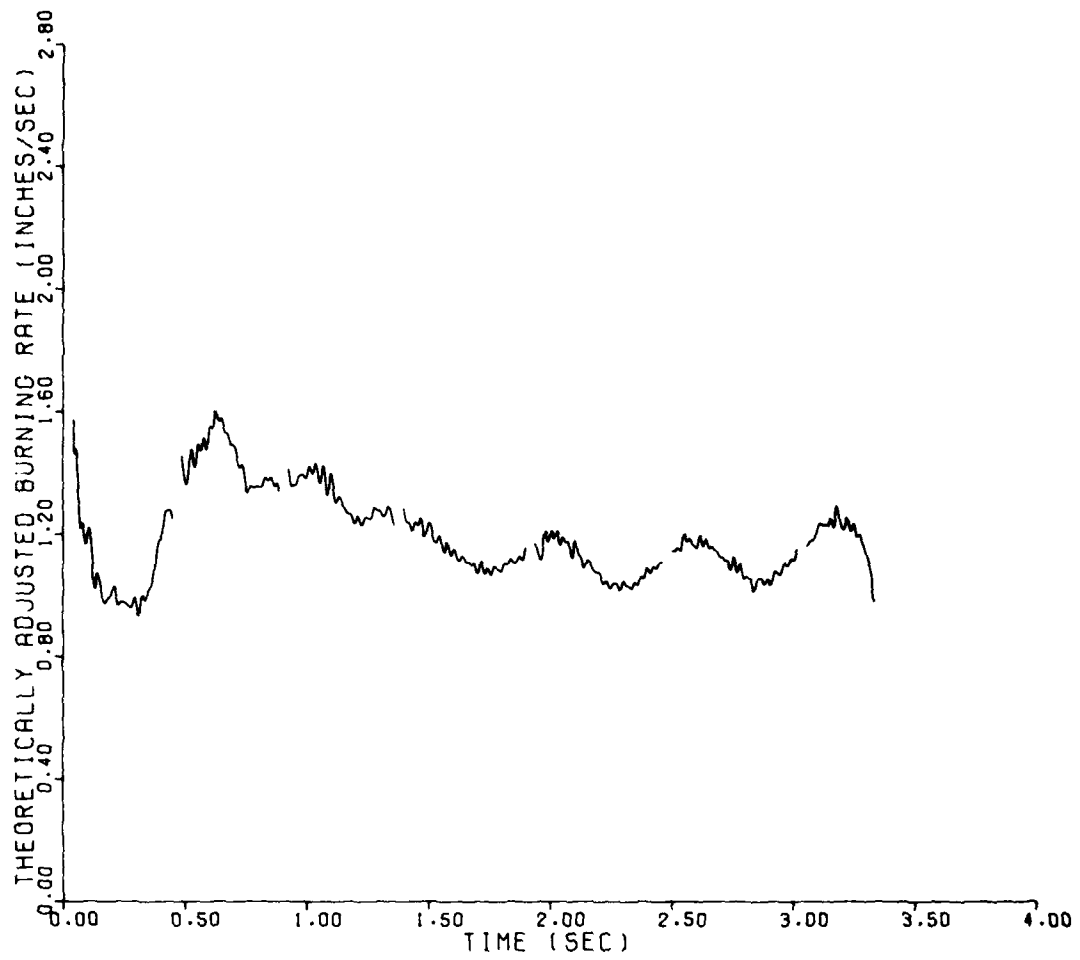


Figure 56. Theoretically Adjusted Burning Rate for the 8<sup>th</sup> Steady-State Test

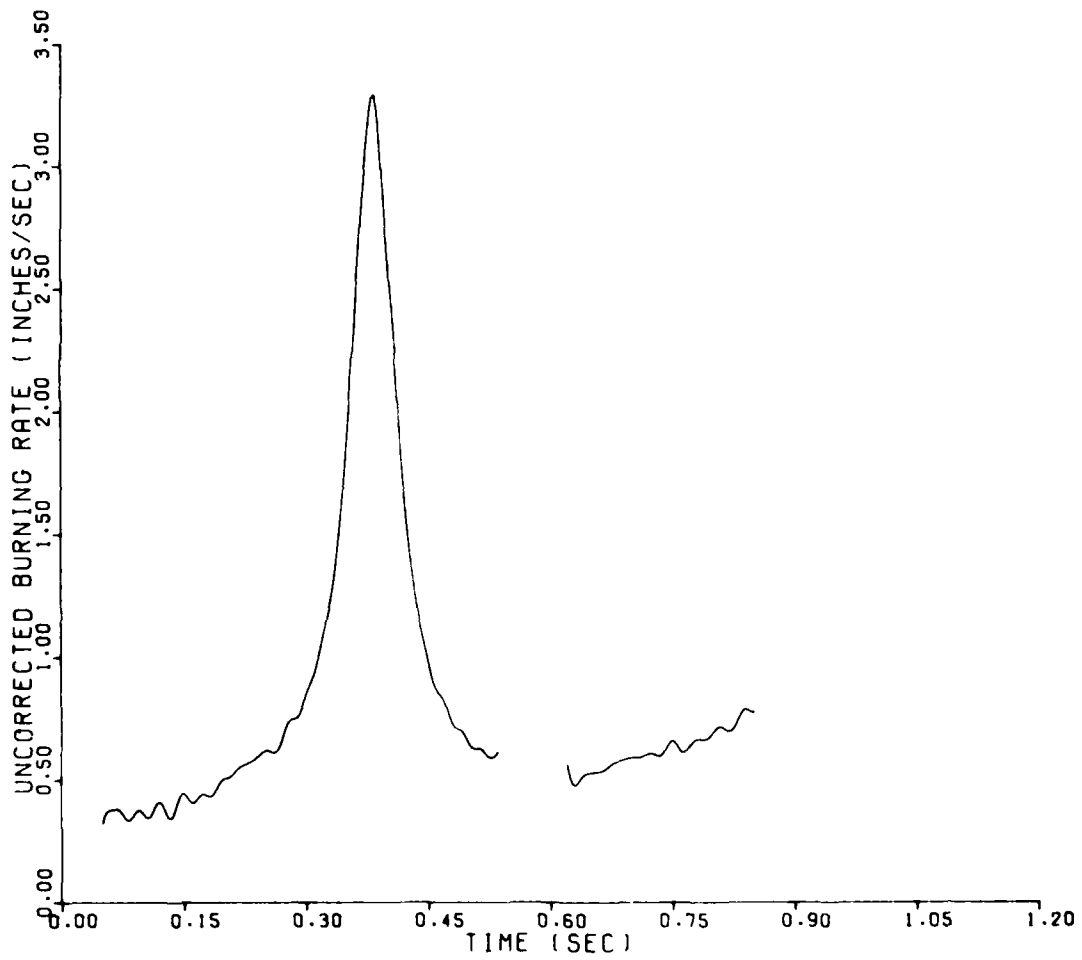


Figure 57. Apparent or Uncorrected Burning Rate on the 5<sup>th</sup> Steady-State Test; Determined by the Use of the Differentiating Digital Filter

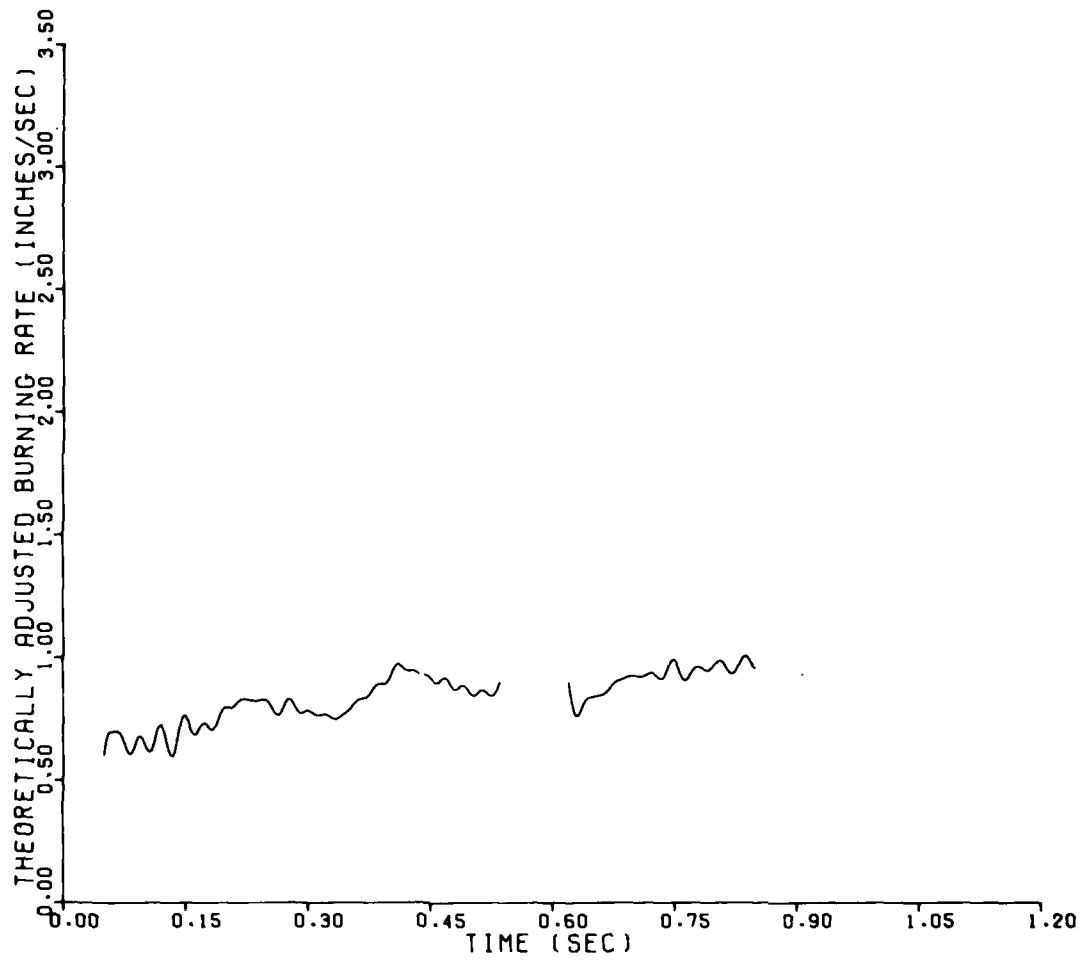


Figure 58. Theoretically Adjusted Burning Rate for the 5<sup>th</sup> Steady-State Test

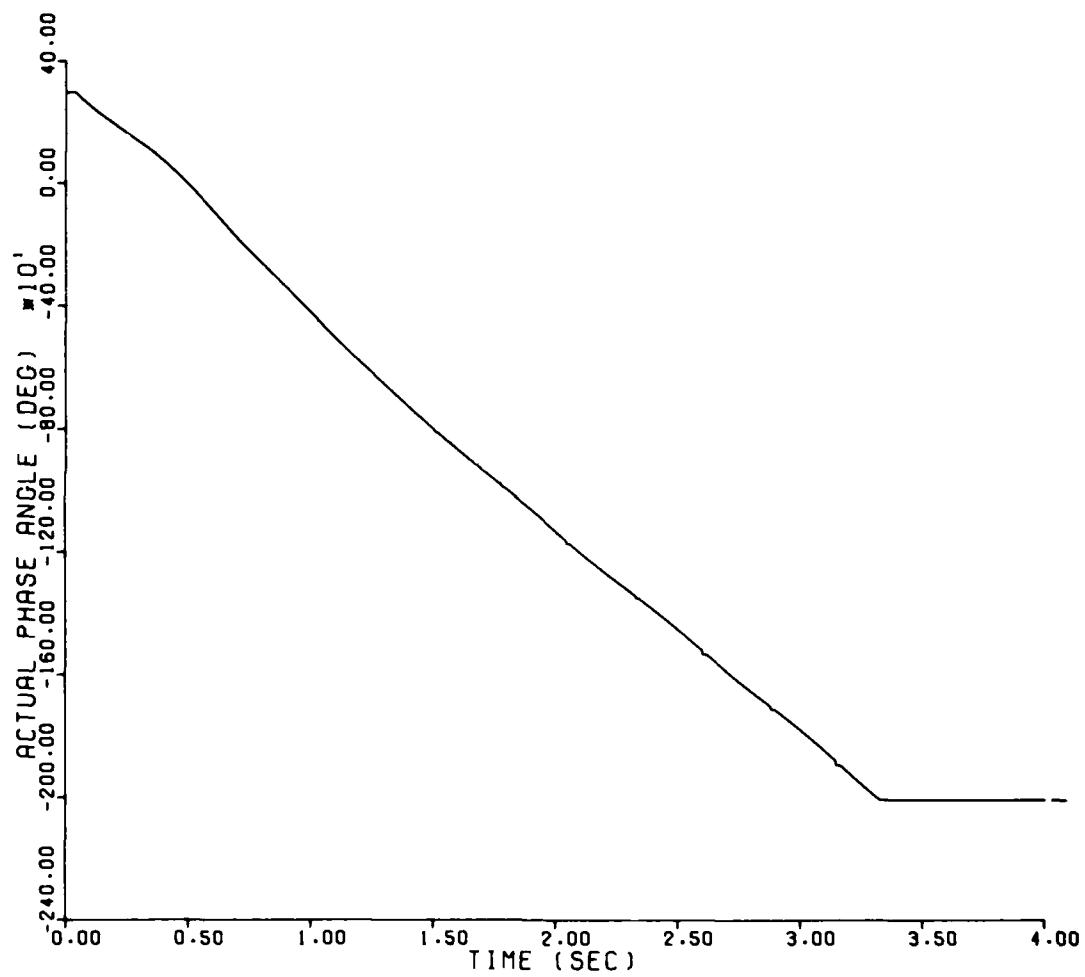


Figure 59. Actual Phase Angle for the 8<sup>th</sup> Steady-State Test

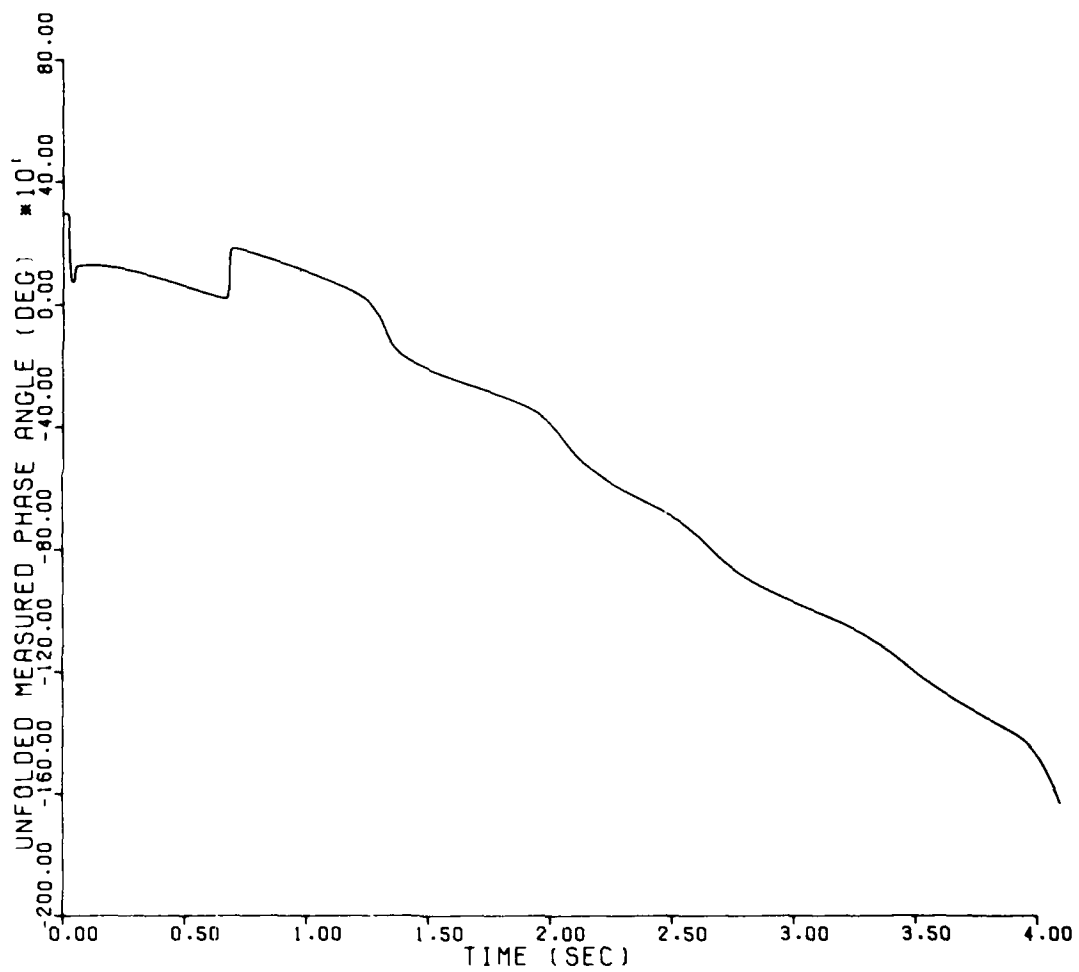


Figure 60. Unfolded Measured Phase Angle on the 6<sup>th</sup> Steady-State Test

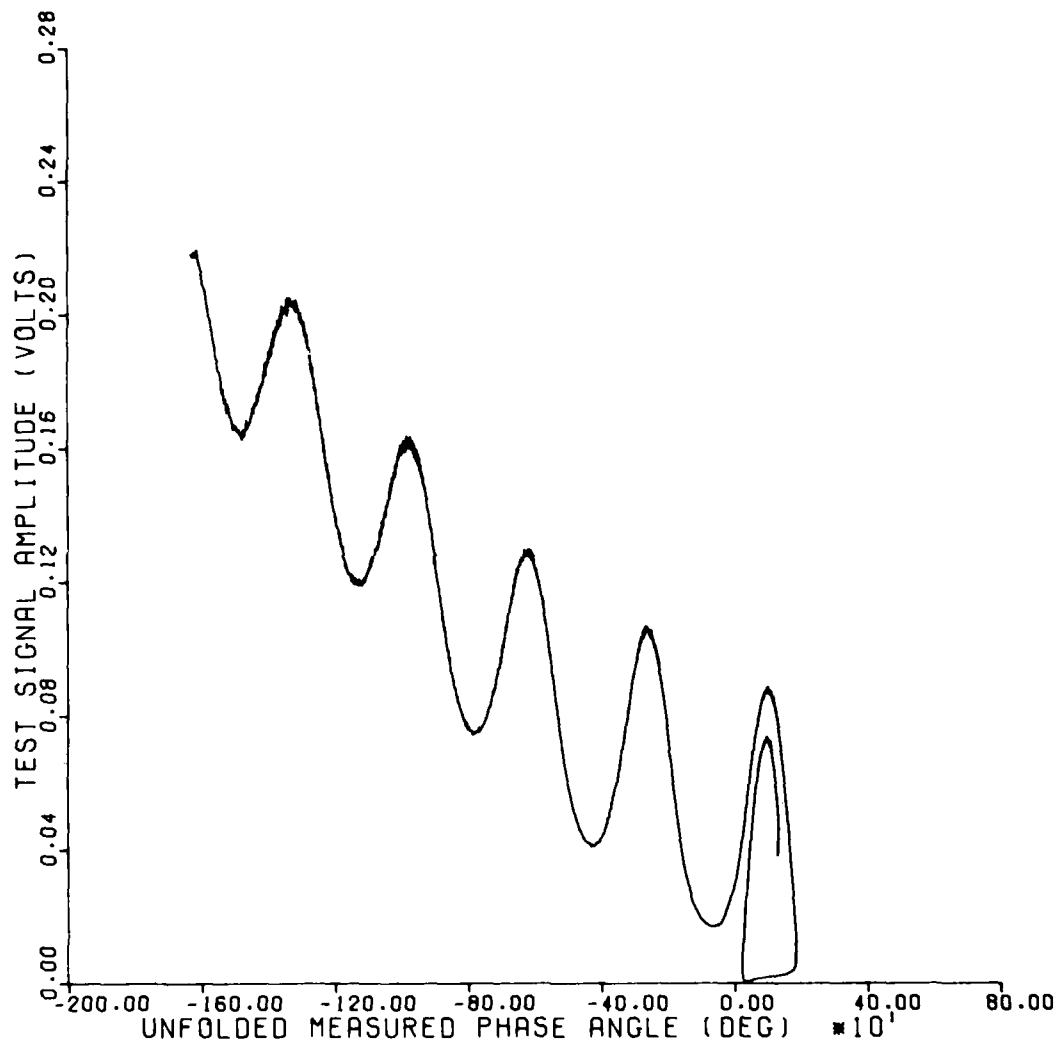


Figure 61. Test Signal Amplitude versus Unfolded Measured Phase Angle for the 6<sup>th</sup> Steady-State Test (Raw Data)

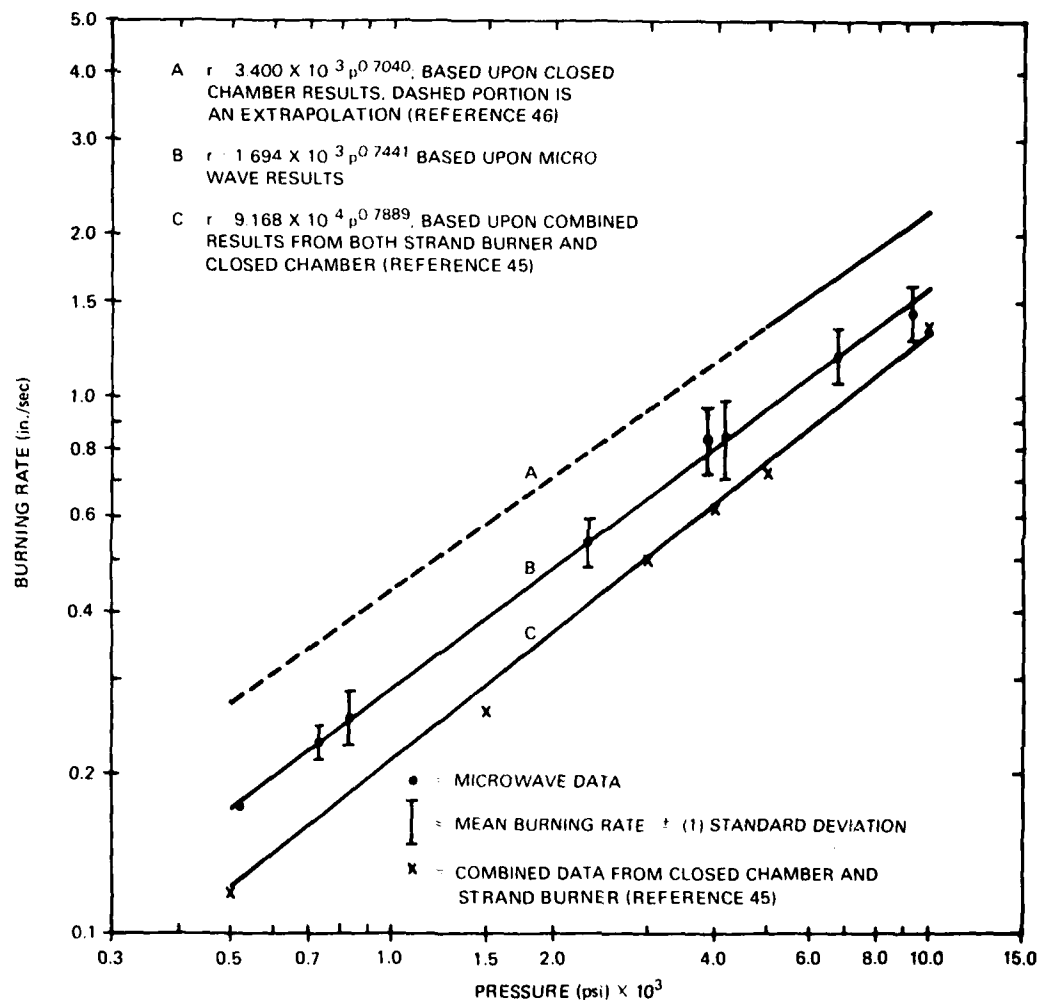


Figure 62. Burning Rate versus Pressure for M6 Propellant

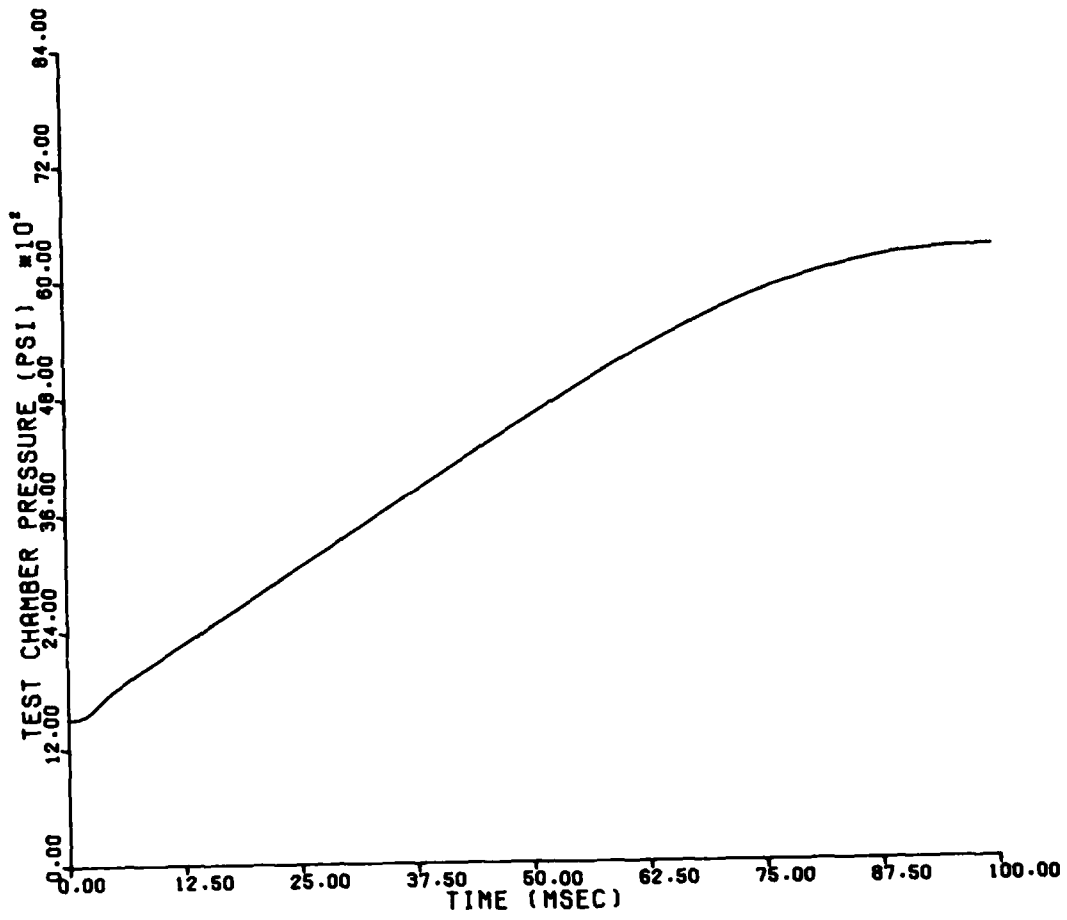


Figure 63. Test Chamber Pressure on Vibration Test 1VT

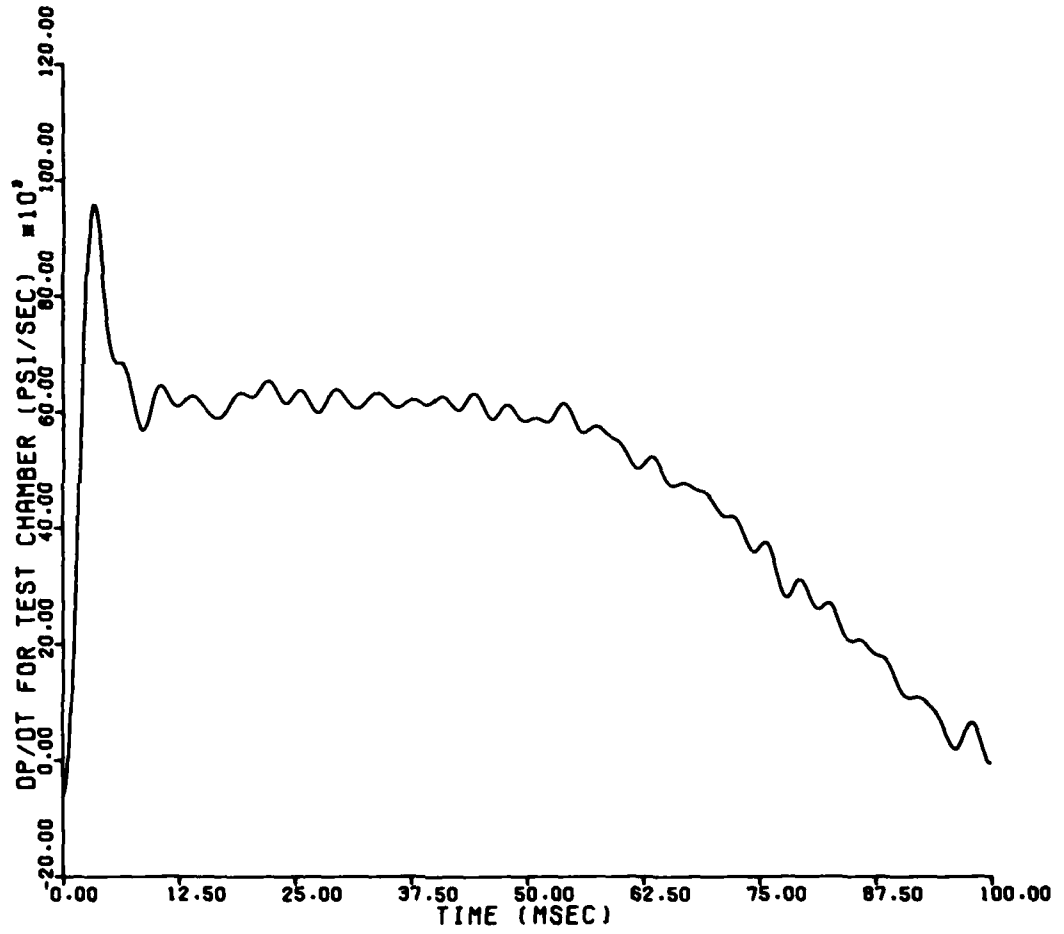


Figure 64. Test Chamber Pressurization Rate on Vibration Test 1VT

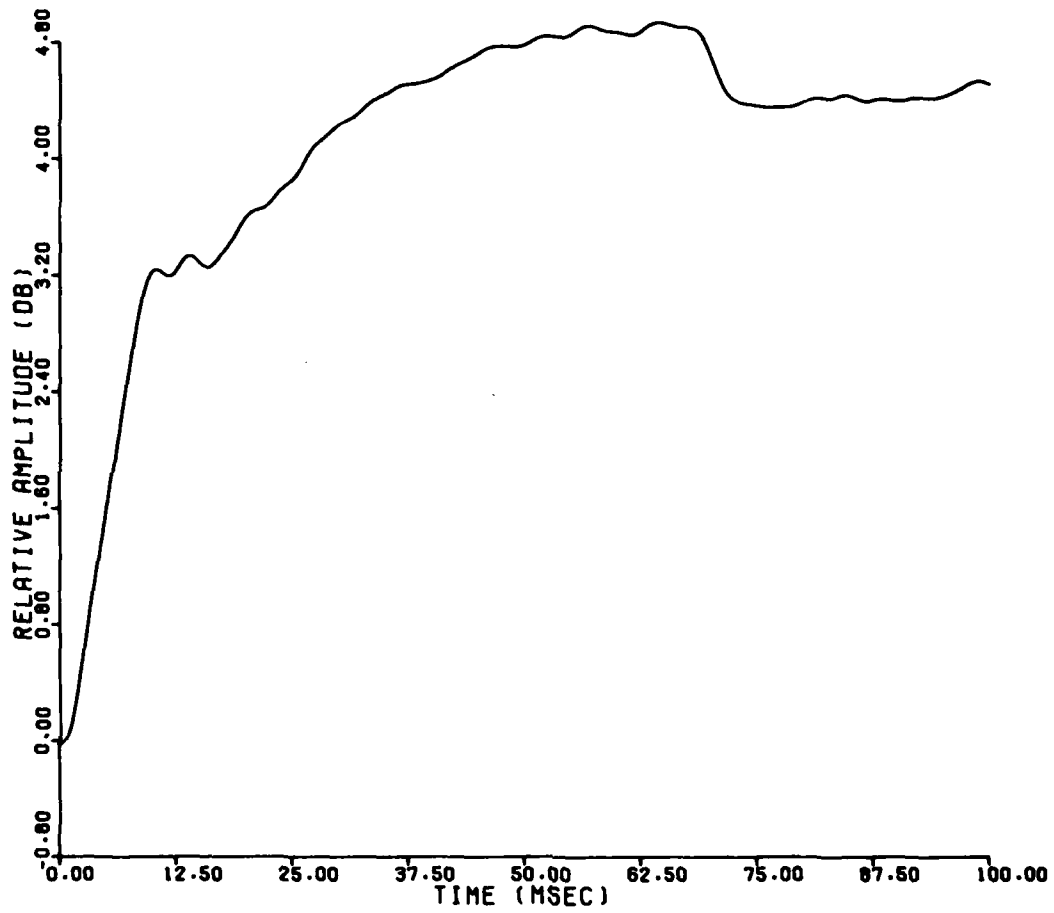


Figure 65. Change in Relative Amplitude Between the Test and Reference Signals on Vibration Test 1VT

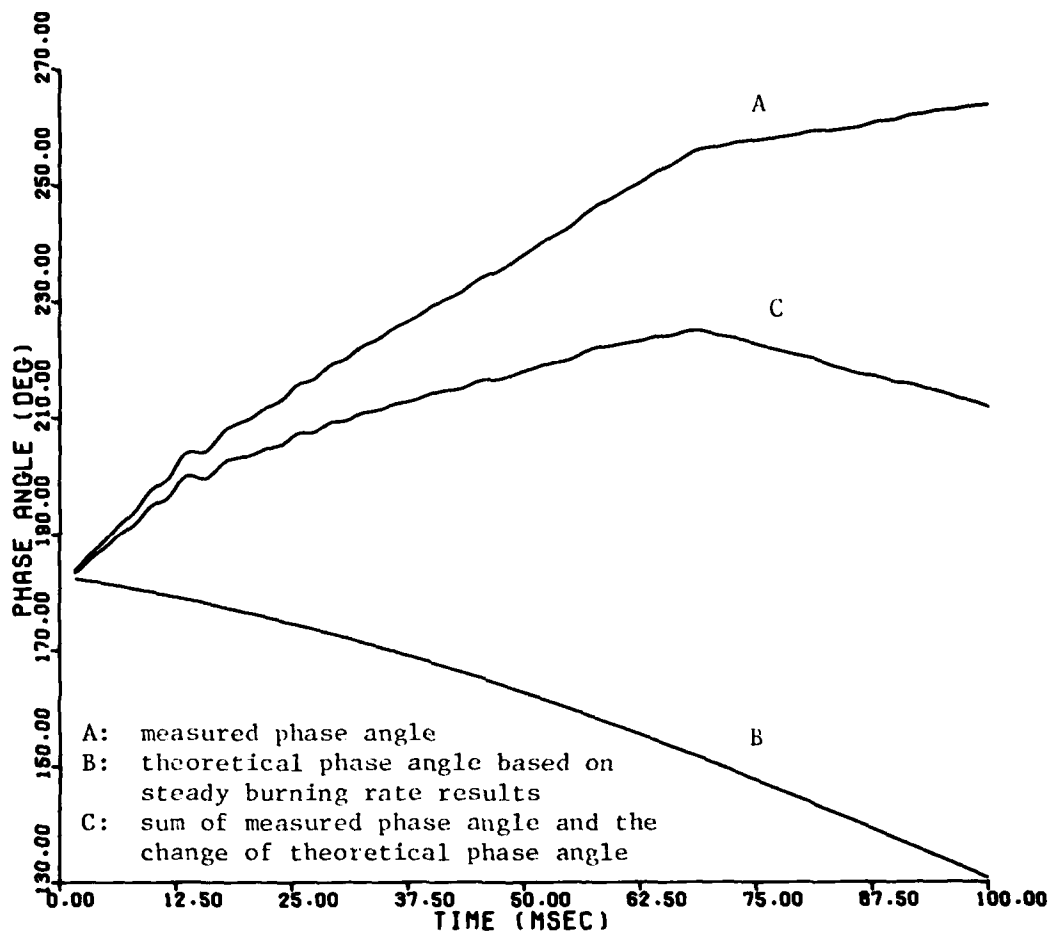


Figure 66. Measured, Theoretical, and Combined Phase Angles for Vibration Test 1VT

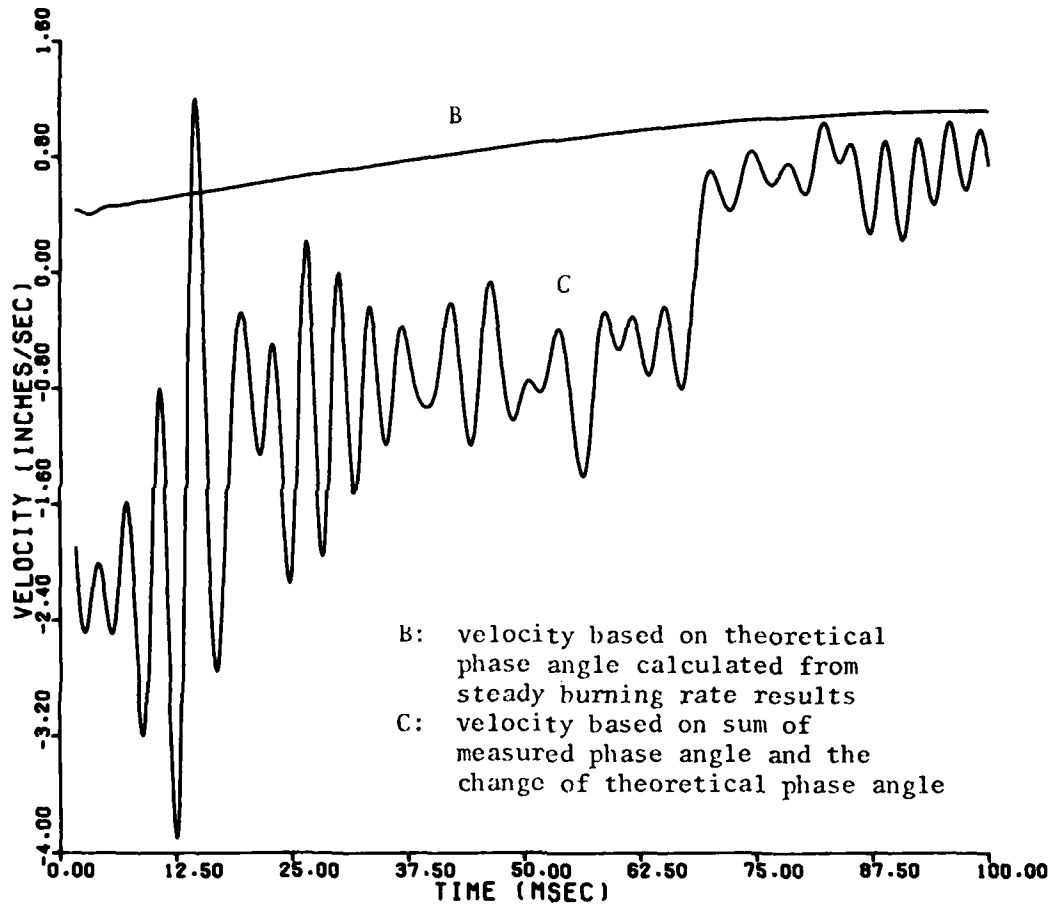


Figure 67. Theoretical and Pseudo-Experimental Velocities for Vibration Test 1VT

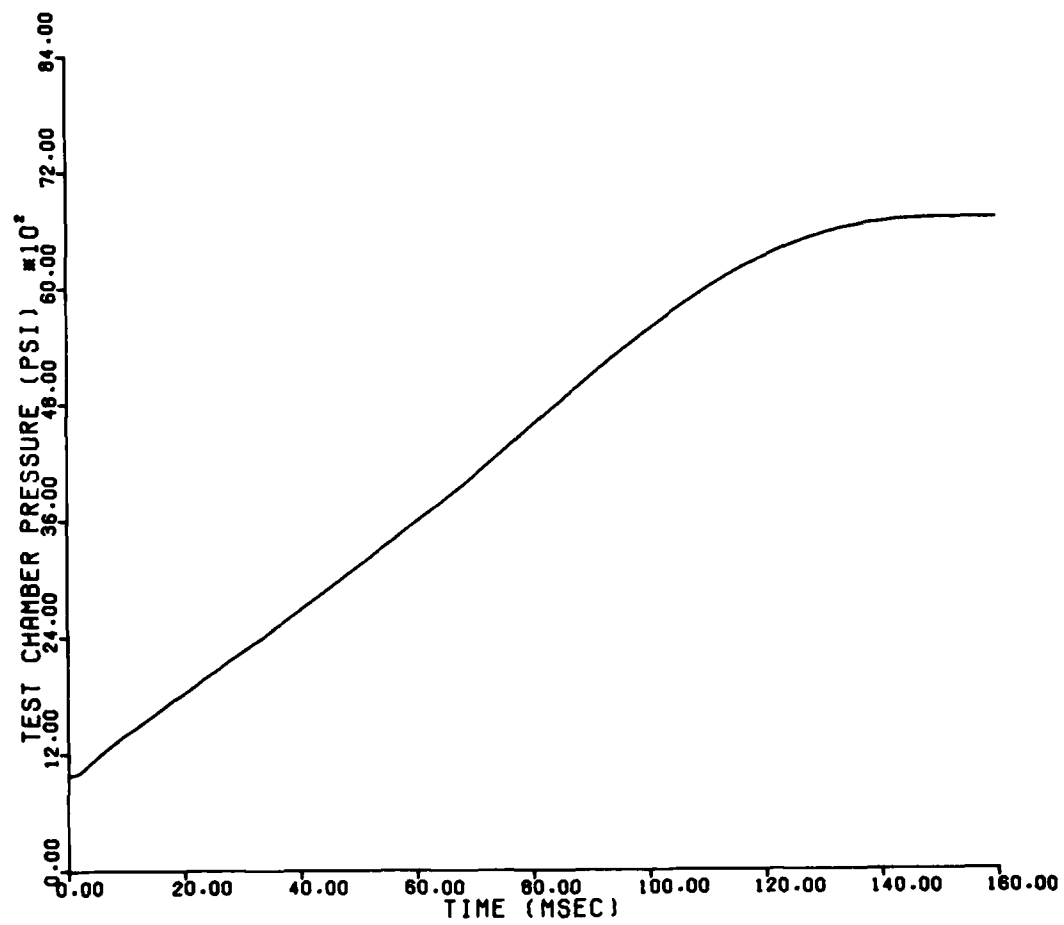


Figure 68. Test Chamber Pressure on Vibration Test 4VT

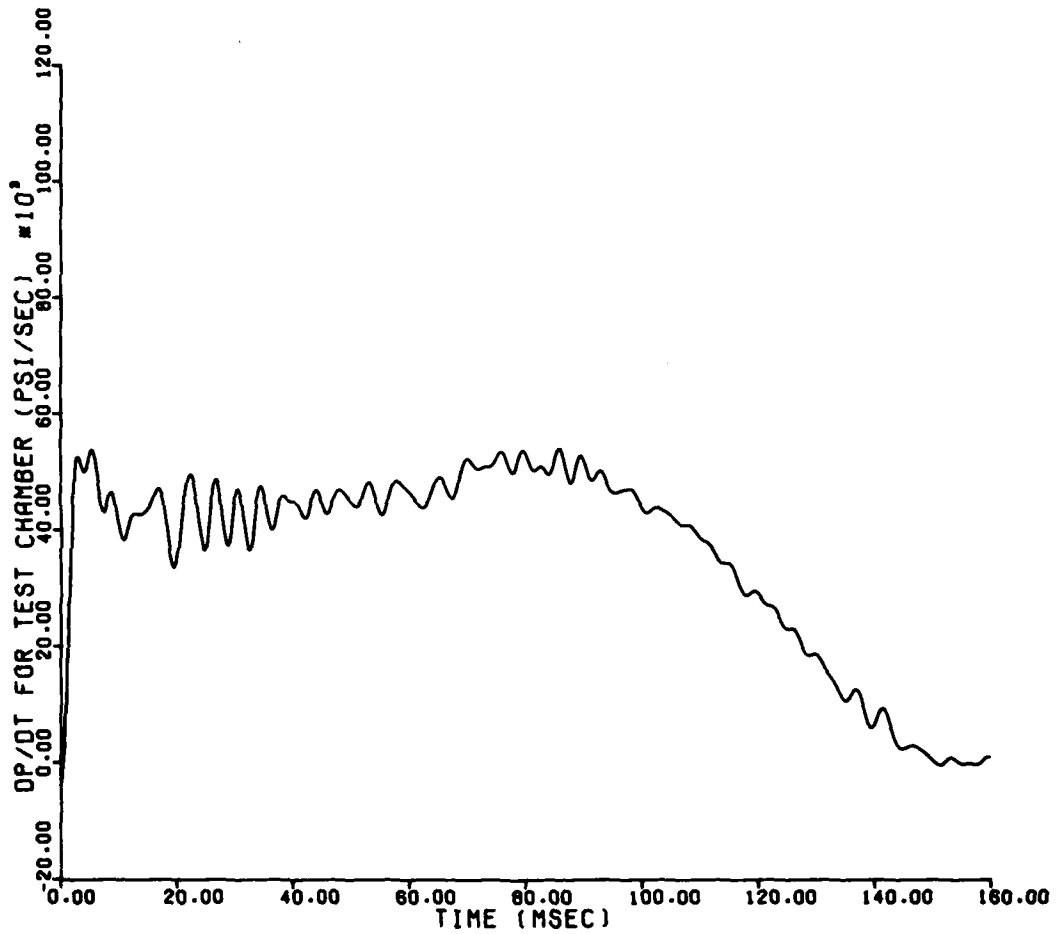


Figure 69. Test Chamber Pressurization Rate on Vibration Test 4VT

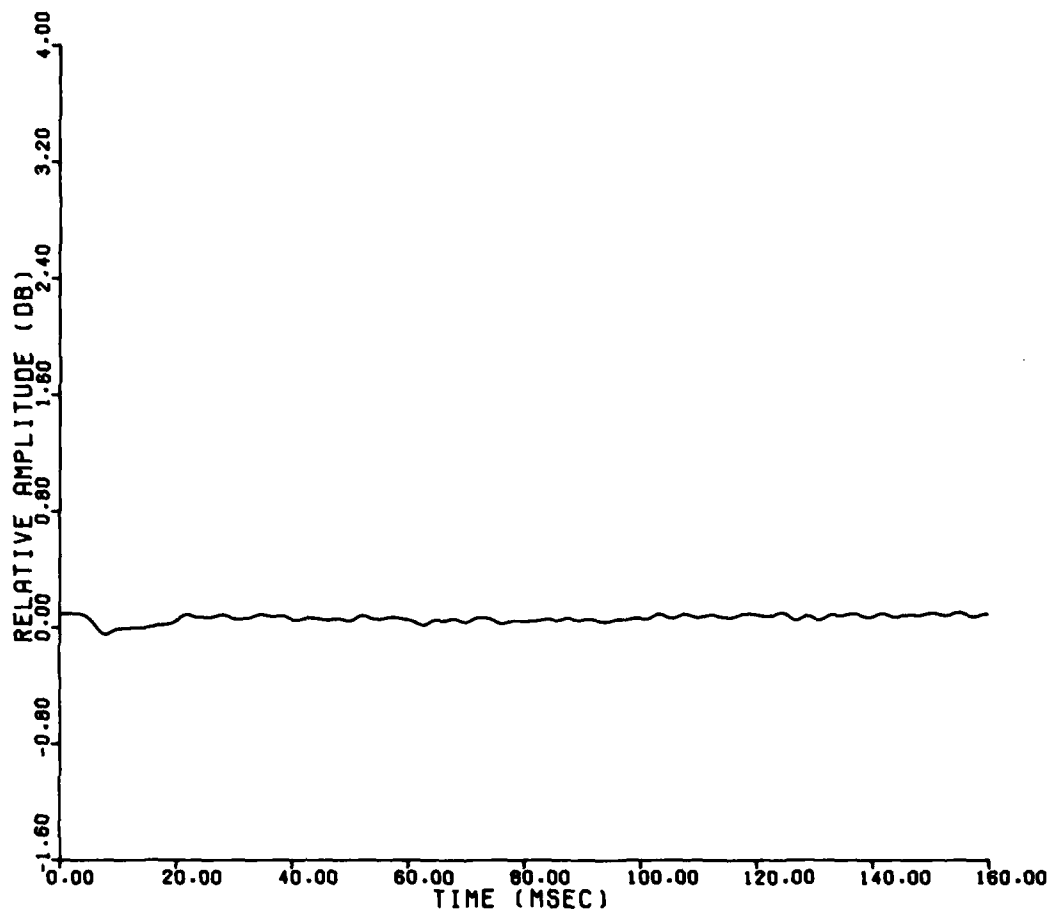


Figure 70. Change in Relative Amplitude Between the Test and Reference Signals on Vibration Test 4VT

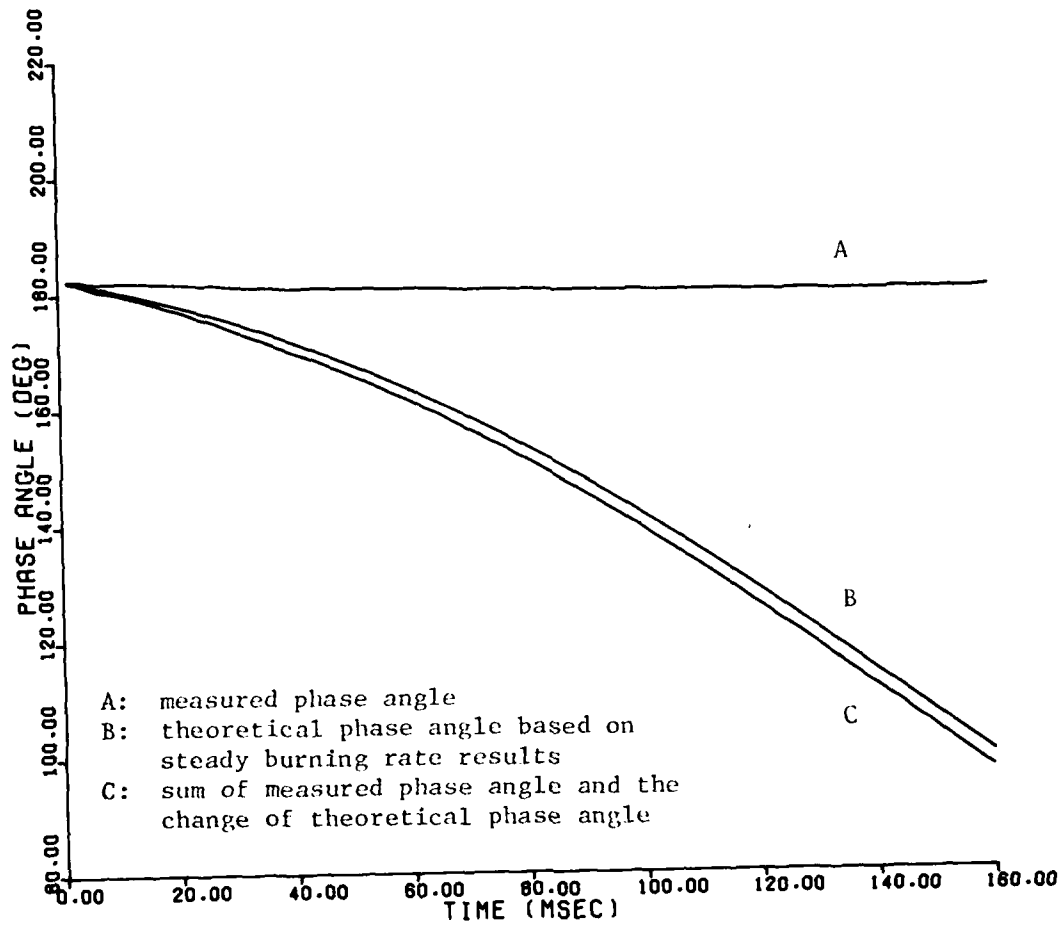


Figure 71. Measured, Theoretical, and Combined Phase Angles for Vibration Test 4VT

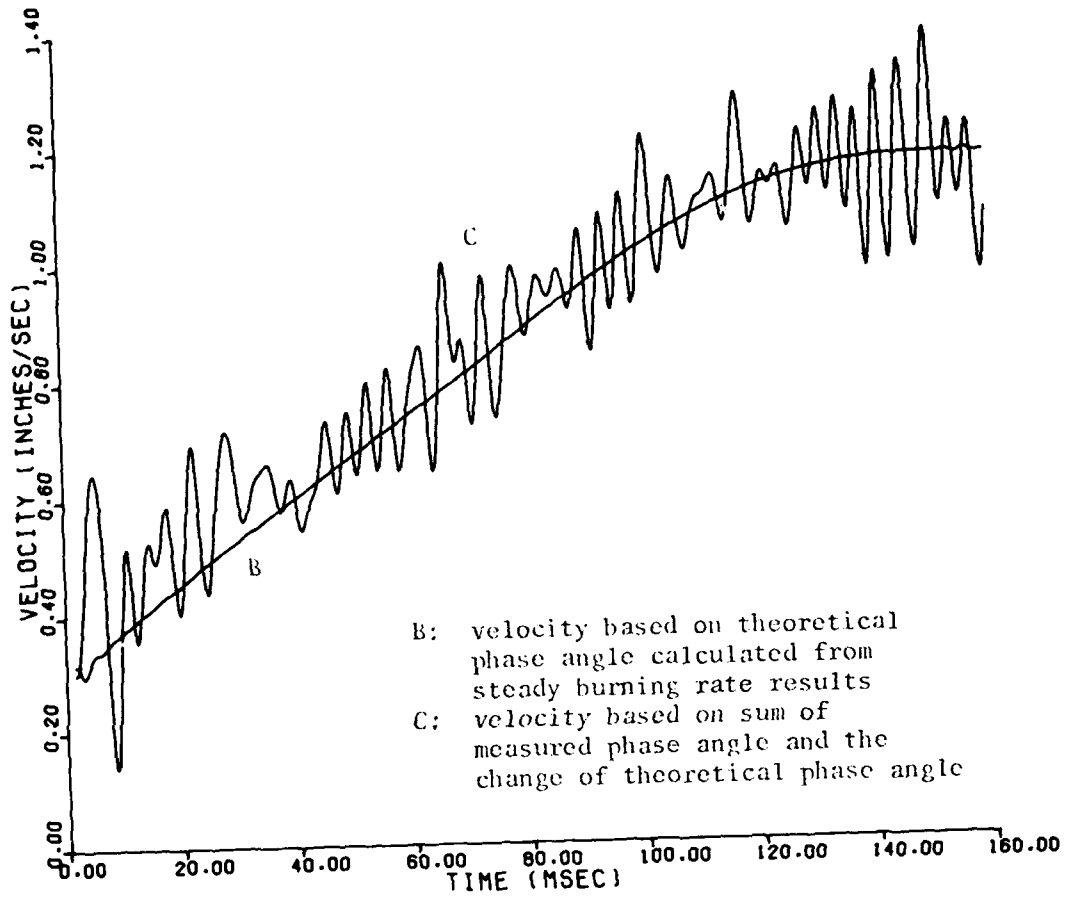


Figure 72. Theoretical and Pseudo-Experimental Velocities for Vibration Test 4VT

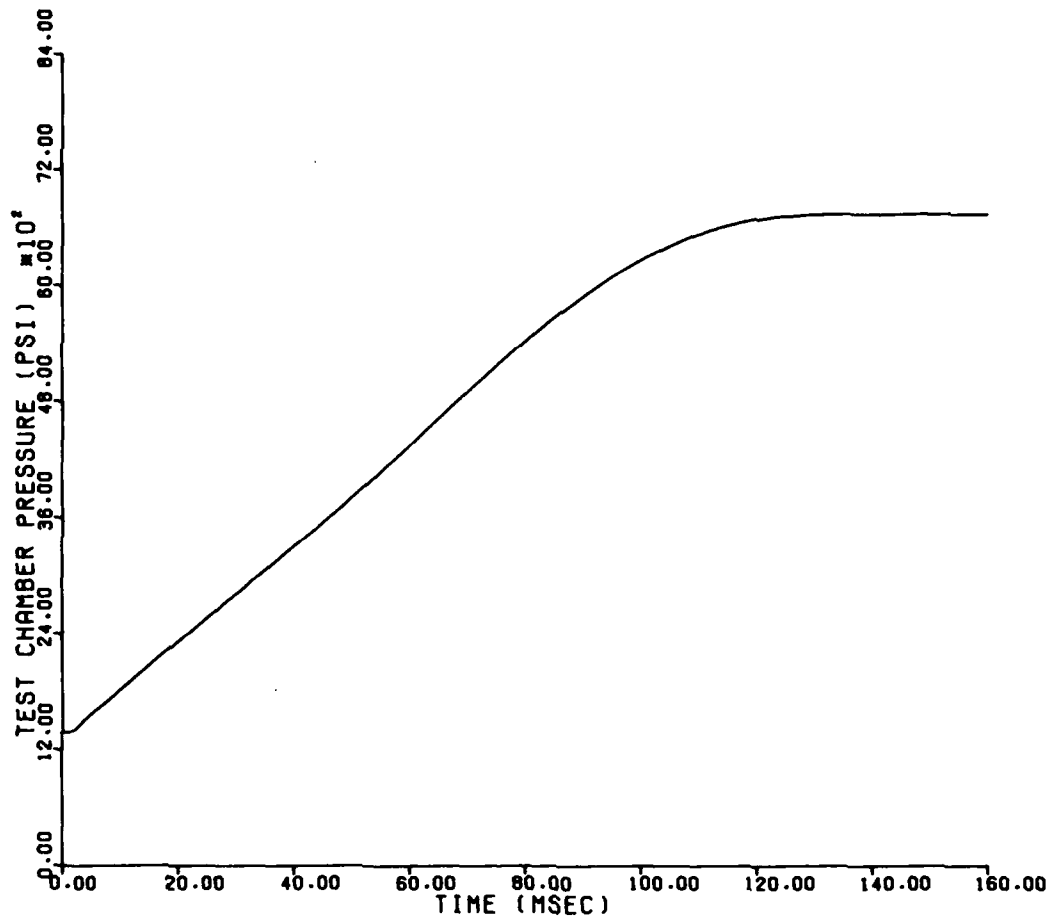


Figure 73. Test Chamber Pressure on Vibration Test 5VT

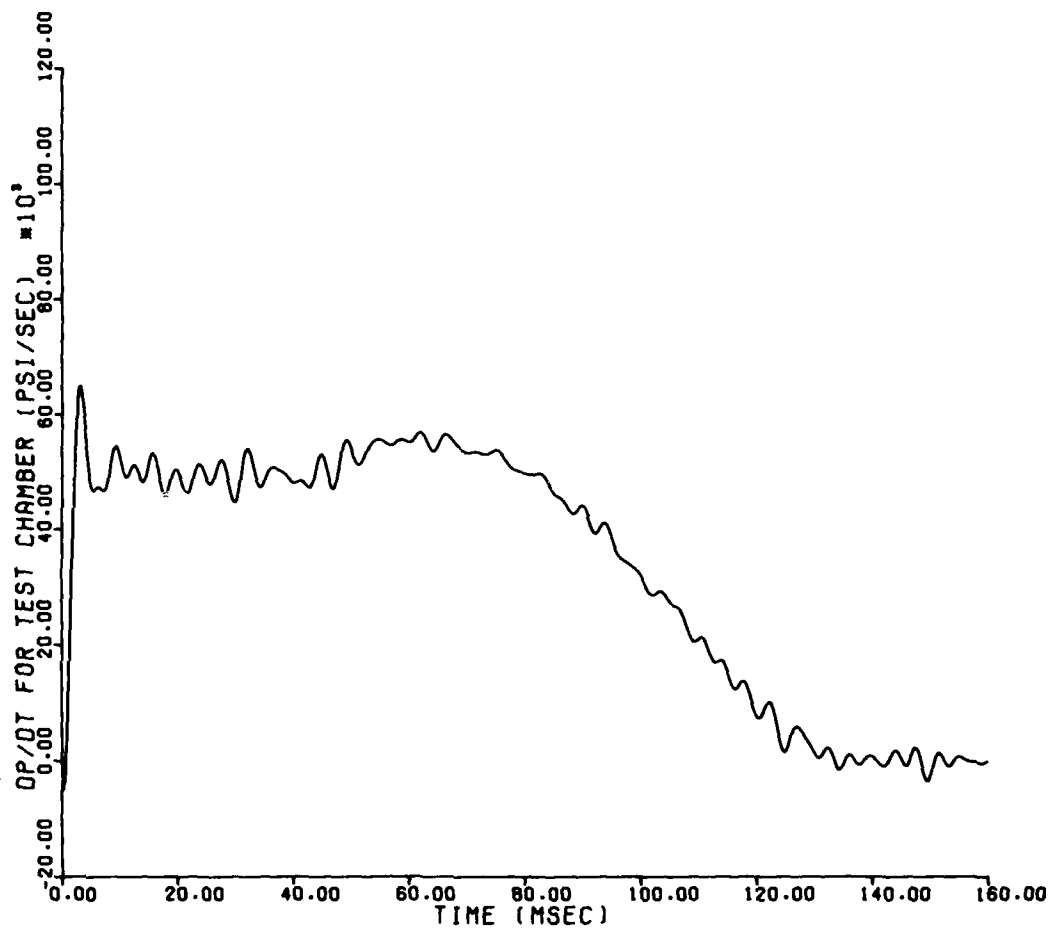


Figure 74. Test Chamber Pressurization Rate on Vibration Test 5VT

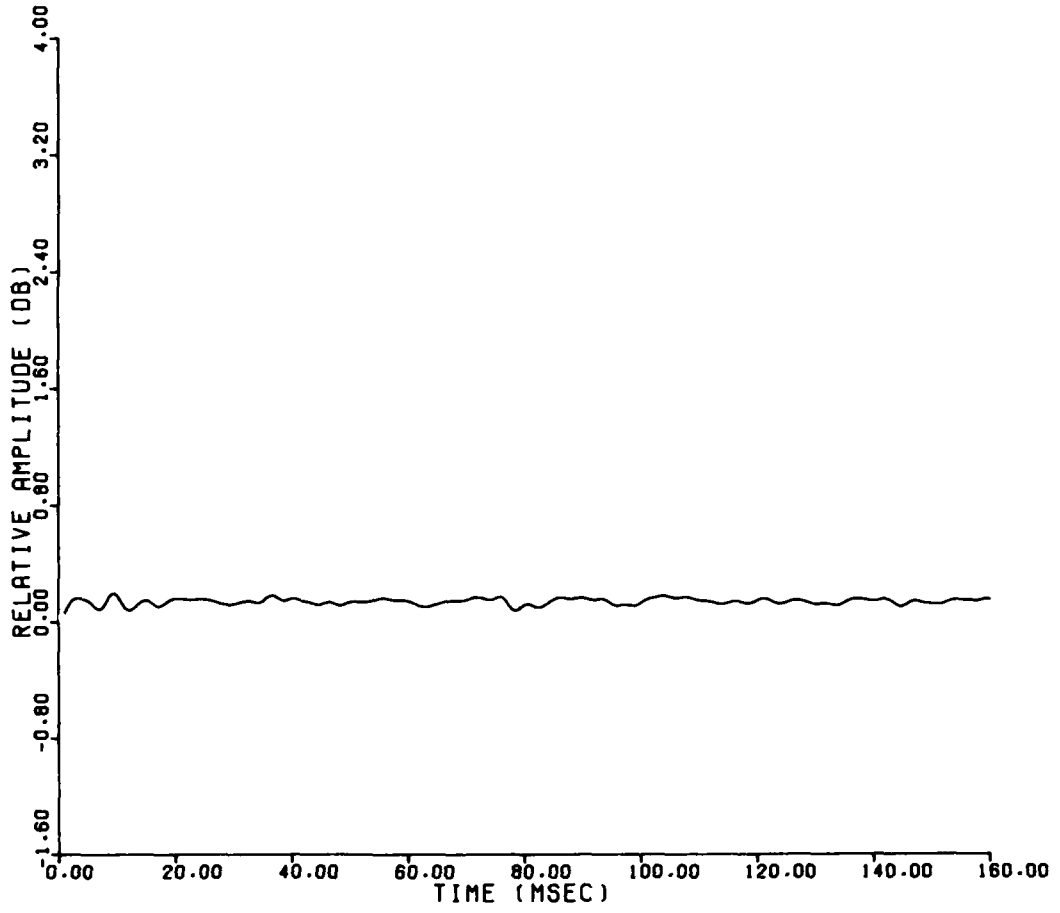


Figure 75. Change in Relative Amplitude Between the Test and Reference Signals on Vibration Test 5VT

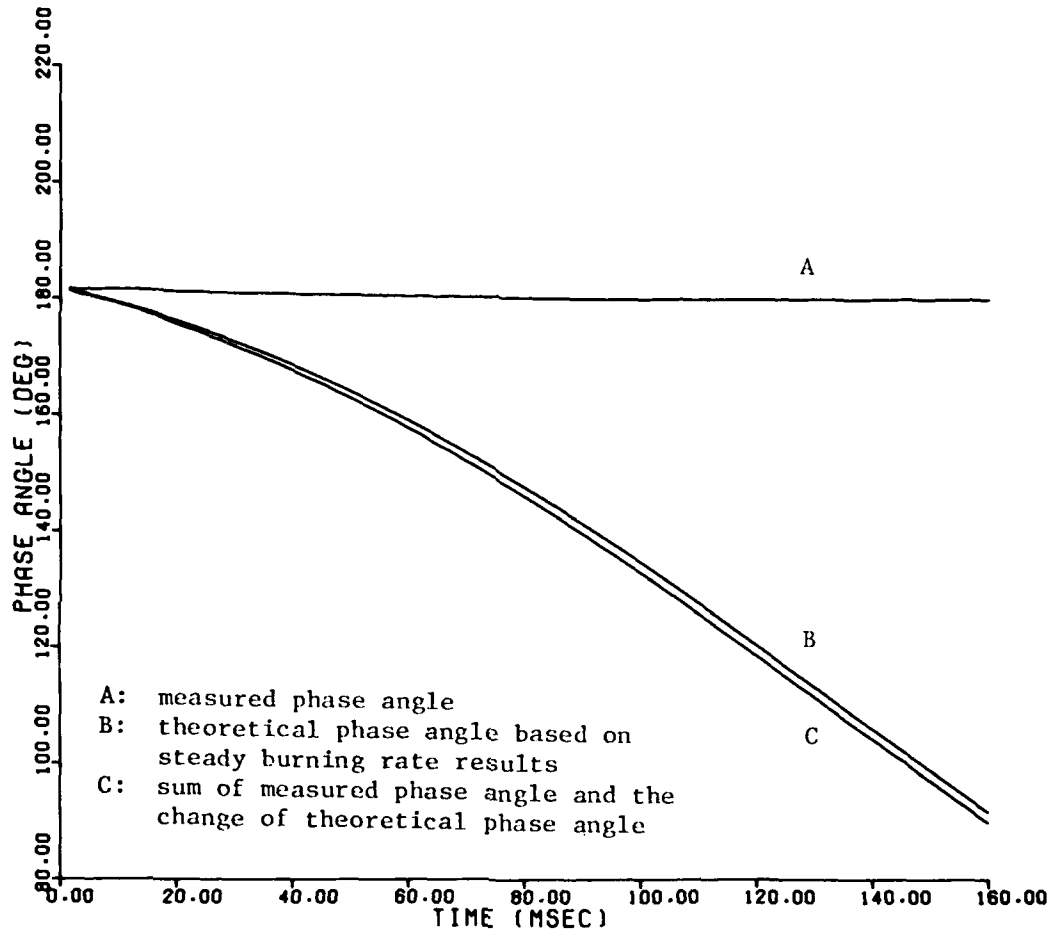


Figure 76. Measured, Theoretical, and Combined Phase Angles for Vibration Test 5VT

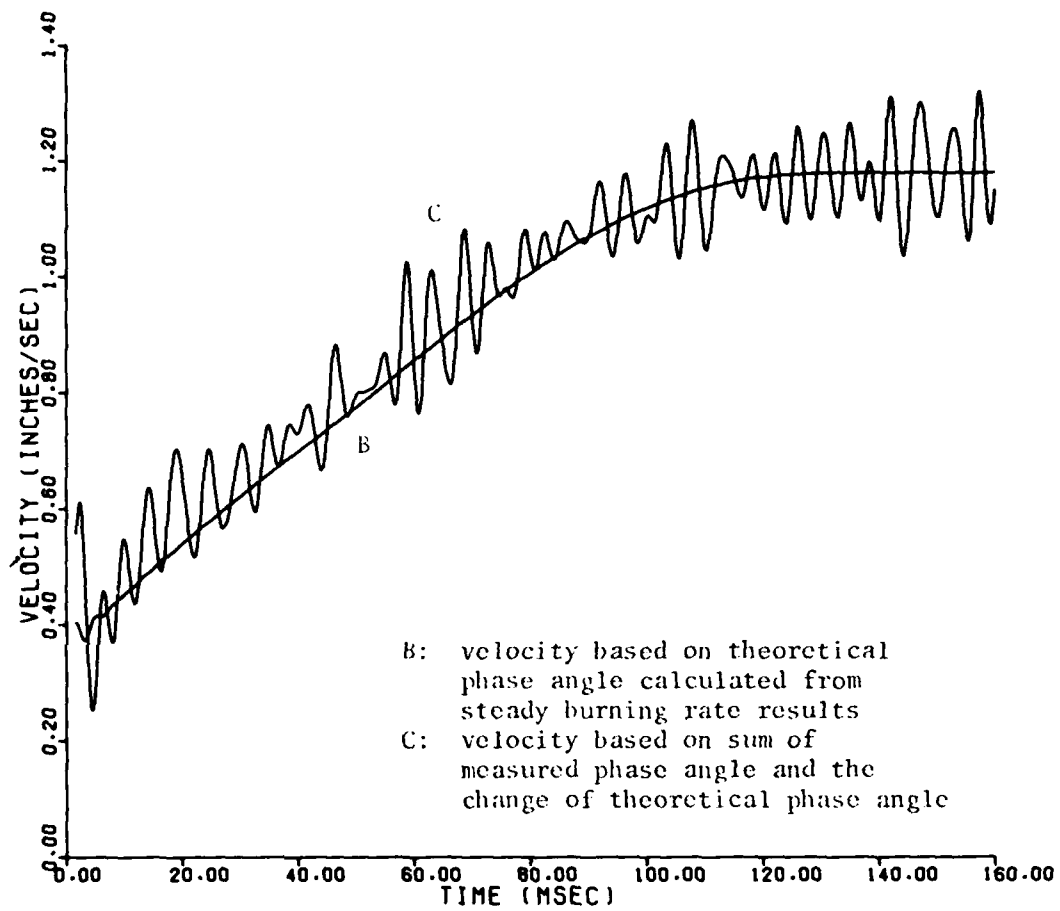


Figure 77. Theoretical and Pseudo-Experimental Velocities for Vibration Test 5VT

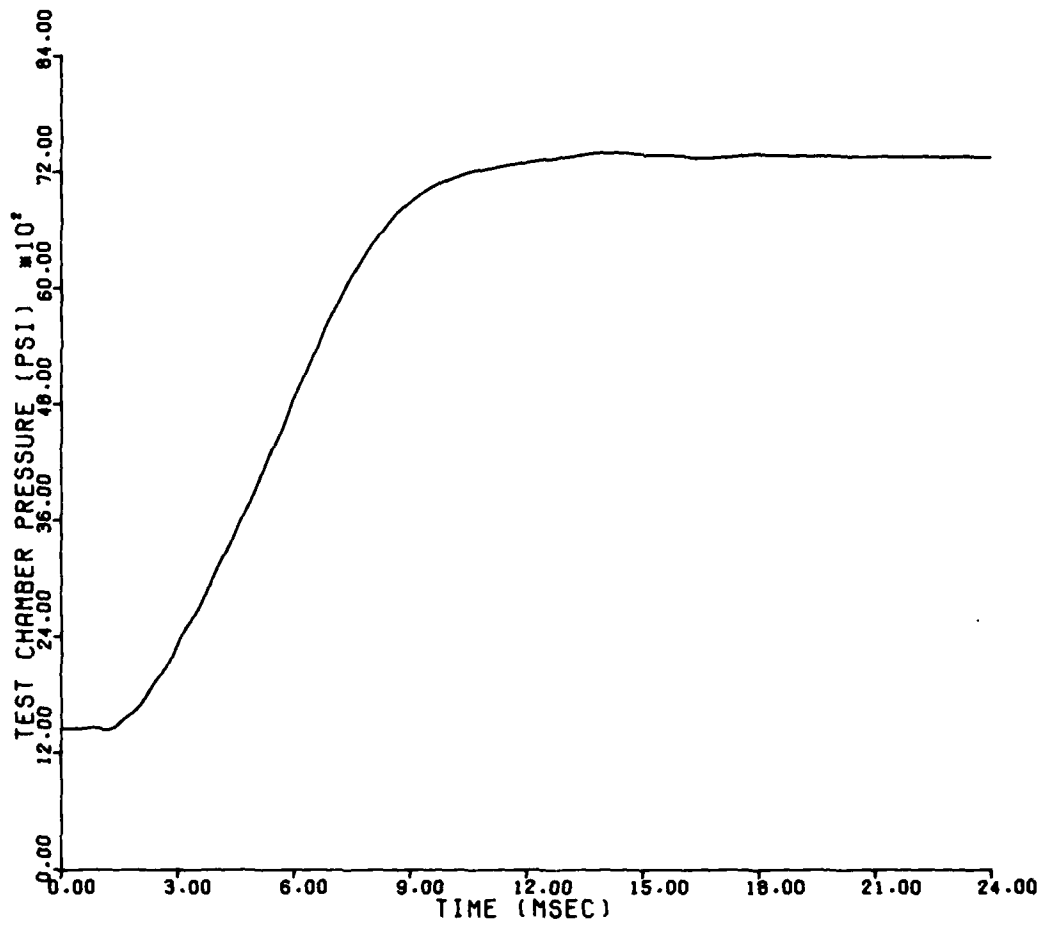


Figure 78. Test Chamber Pressure on Vibration Test 12VT

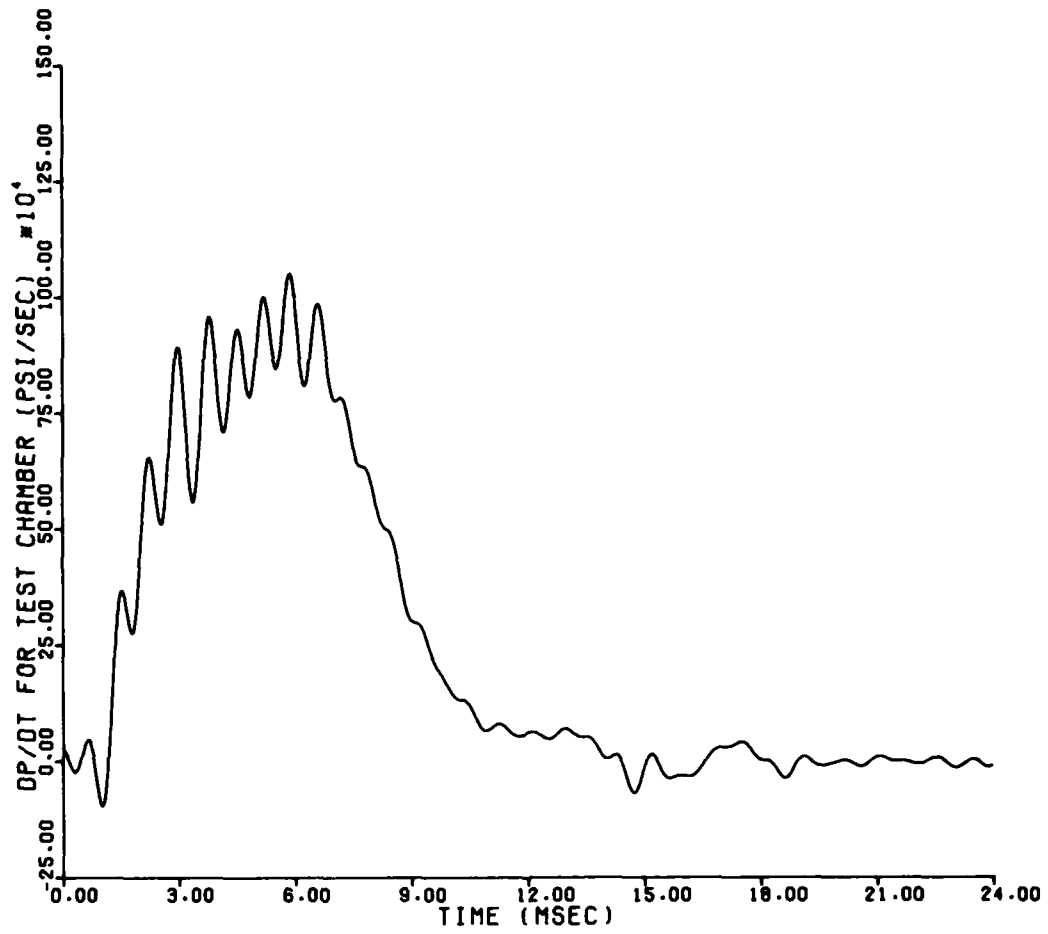


Figure 79. Test Chamber Pressurization Rate on Vibration Test 12VT

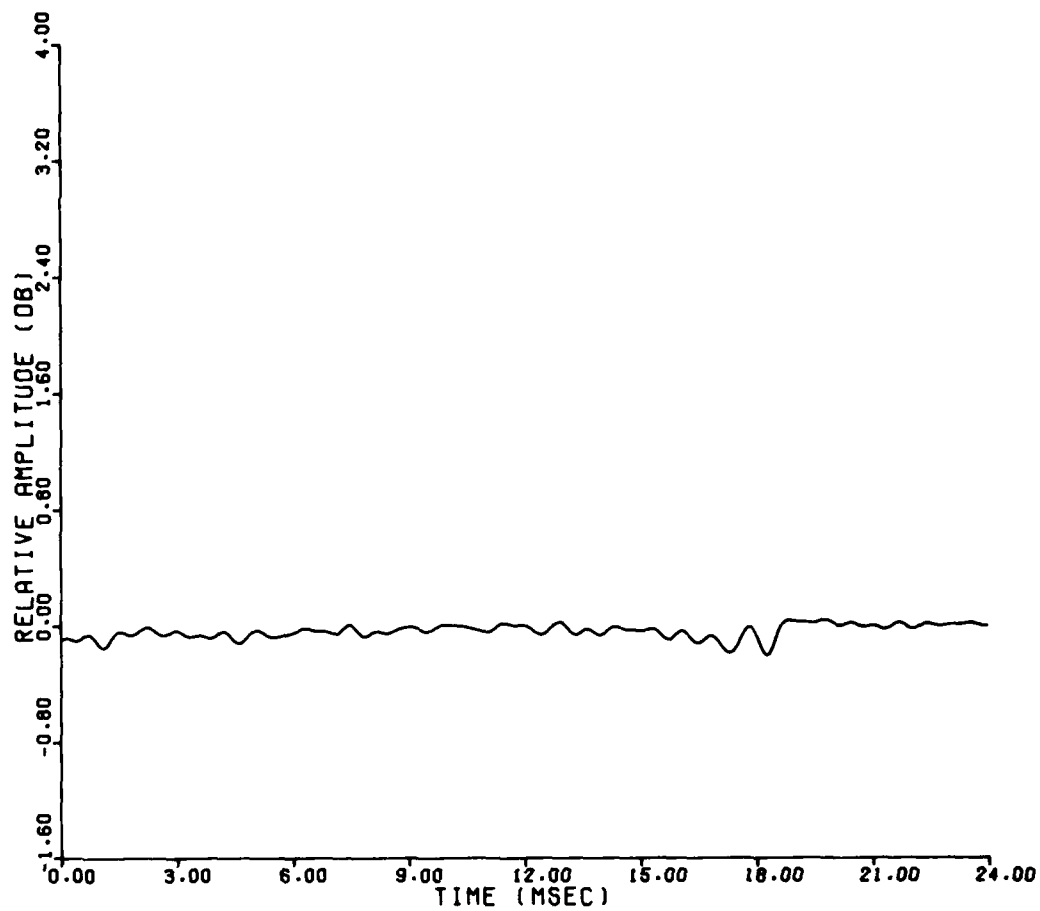


Figure 80. Change in Relative Amplitude Between the Test and Reference Signals on Vibration Test 12VT

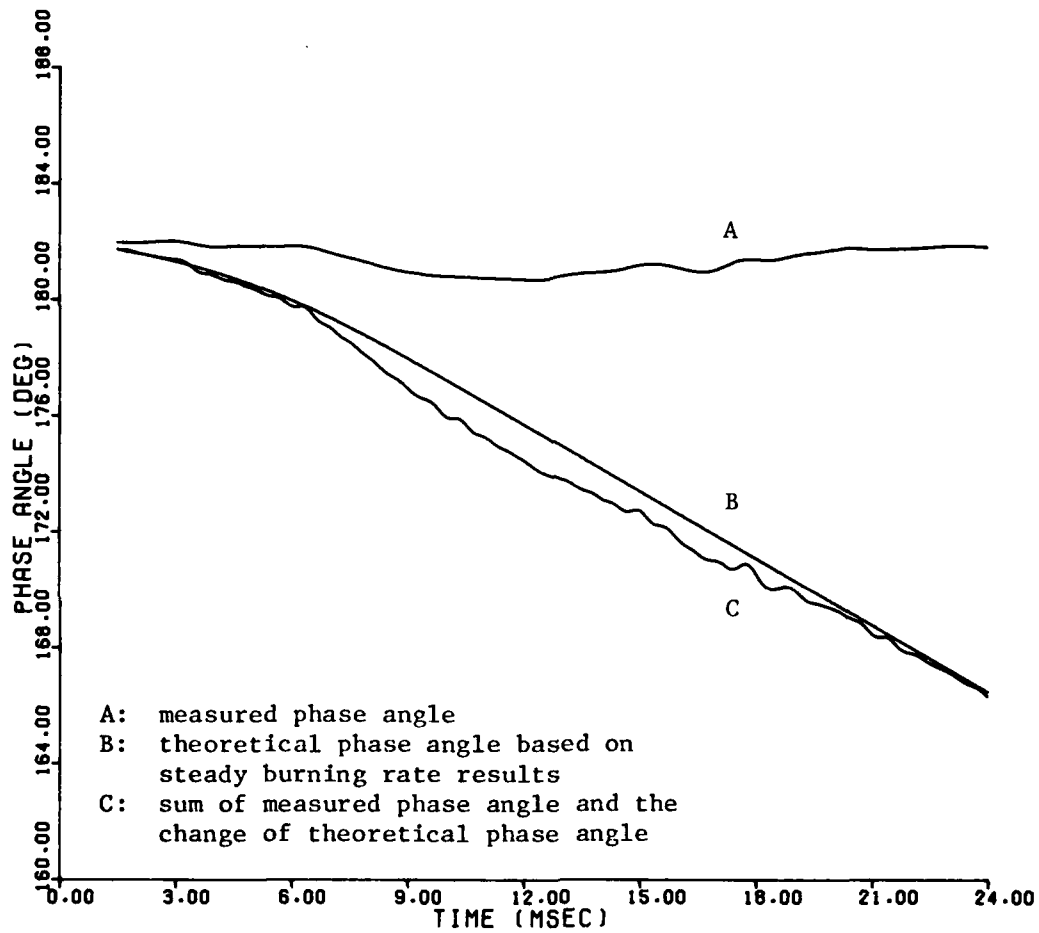


Figure 81. Measured, Theoretical, and Combined Phase Angles for Vibration Test 12VT

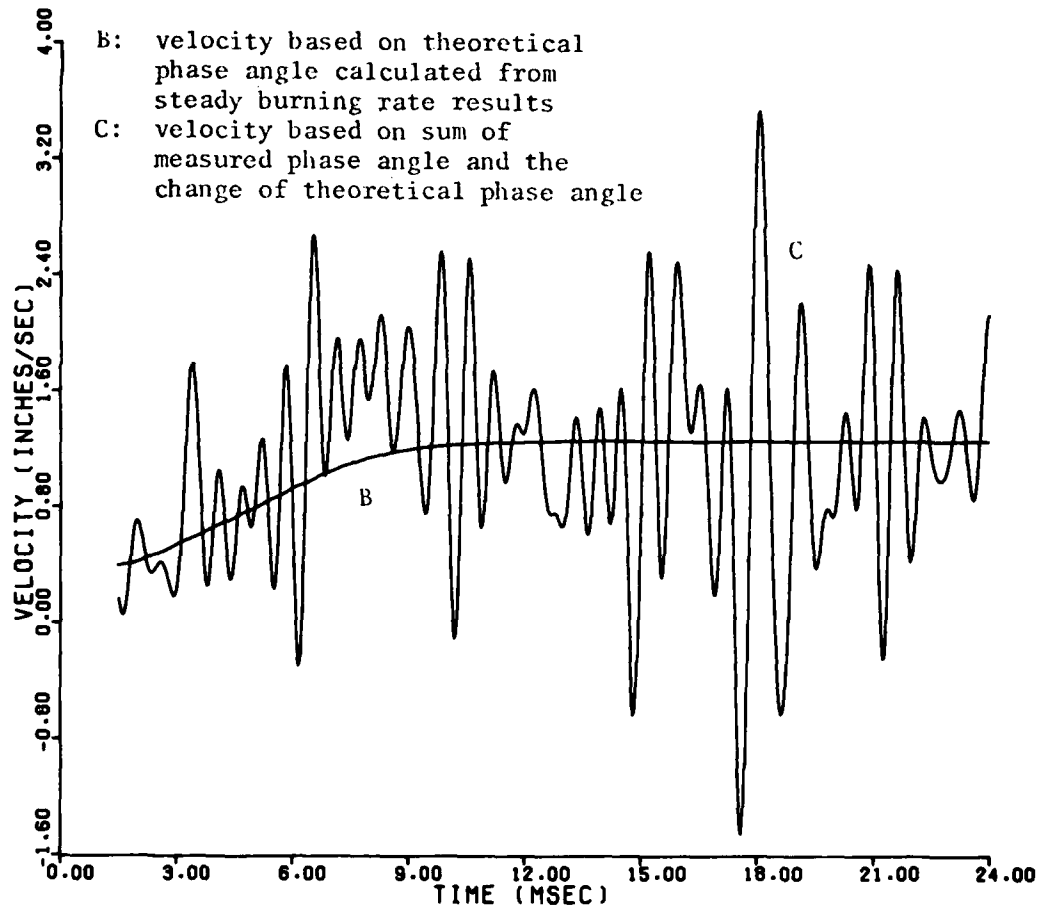


Figure 82. Theoretical and Pseudo-Experimental Velocities for  
Vibration Test 12VT

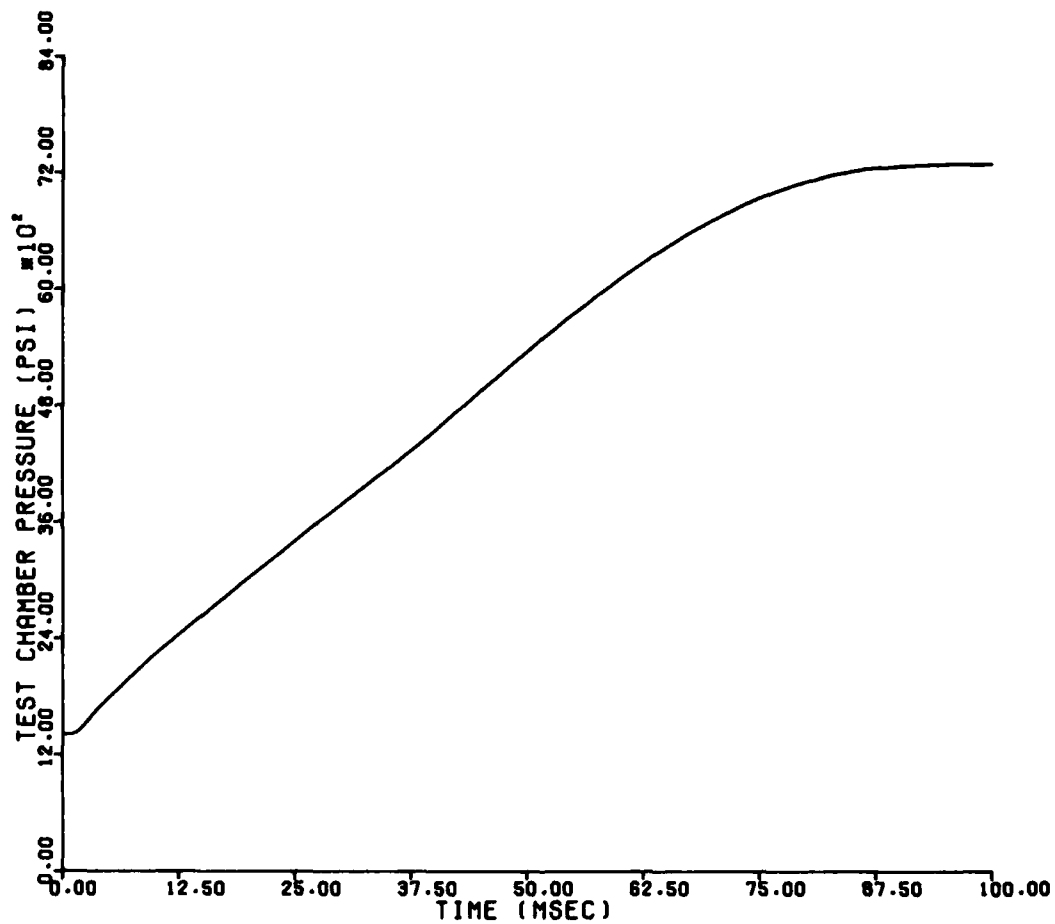


Figure 83. Test Chamber Pressure on Vibration Test 10VT

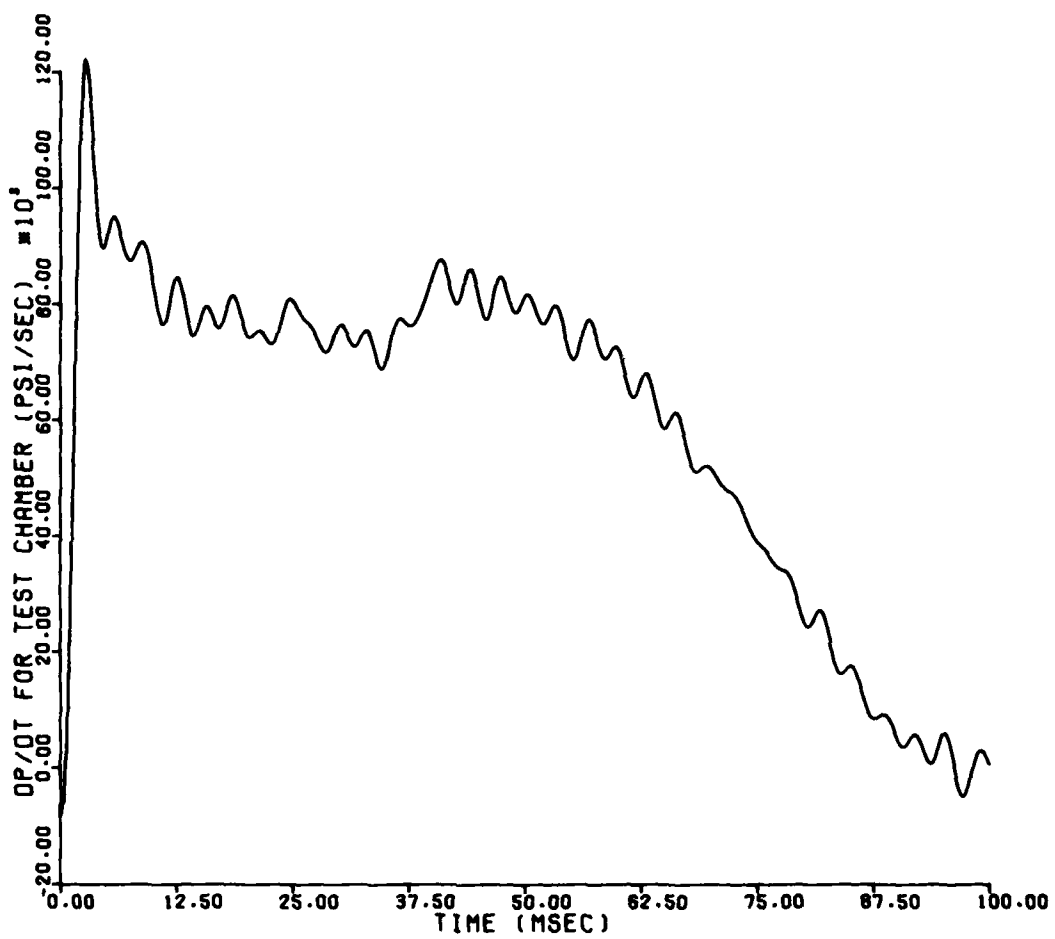


Figure 84. Test Chamber Pressurization Rate on Vibration Test 10VT

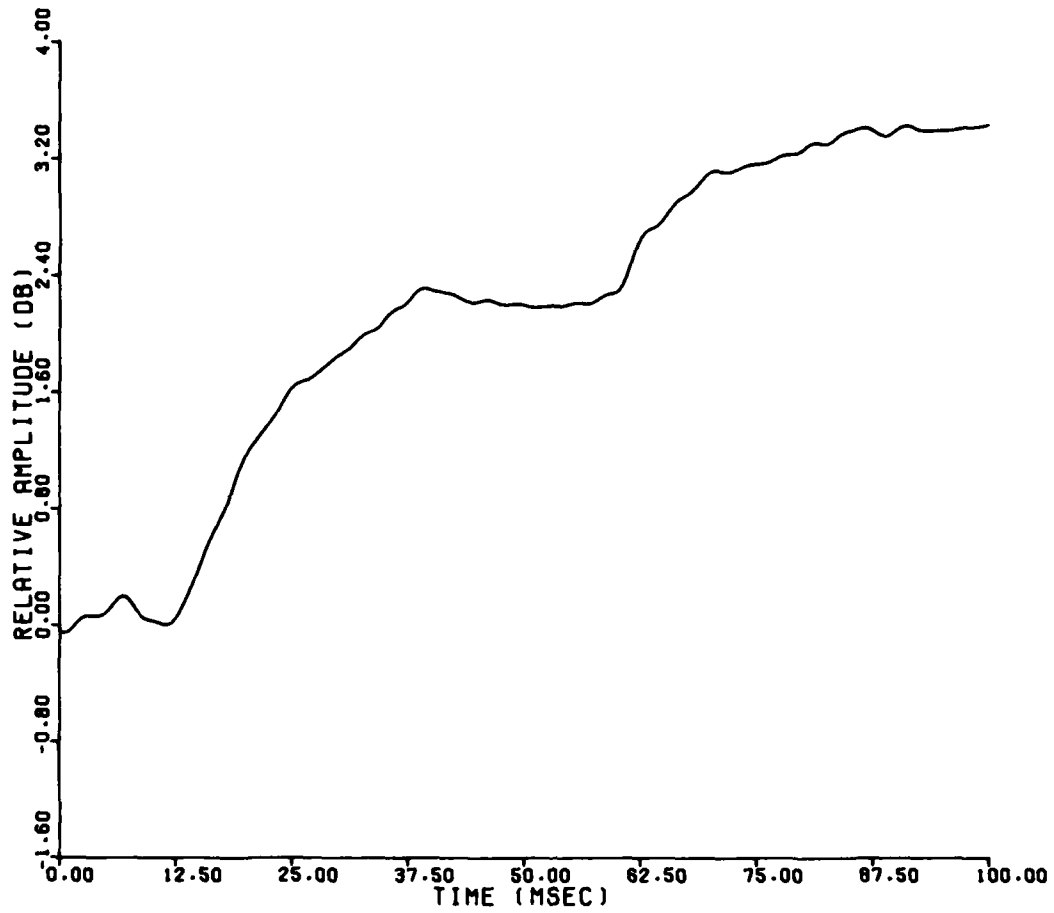


Figure 85. Change in Relative Amplitude Between the Test and Reference Signals on Vibration Test 10VT

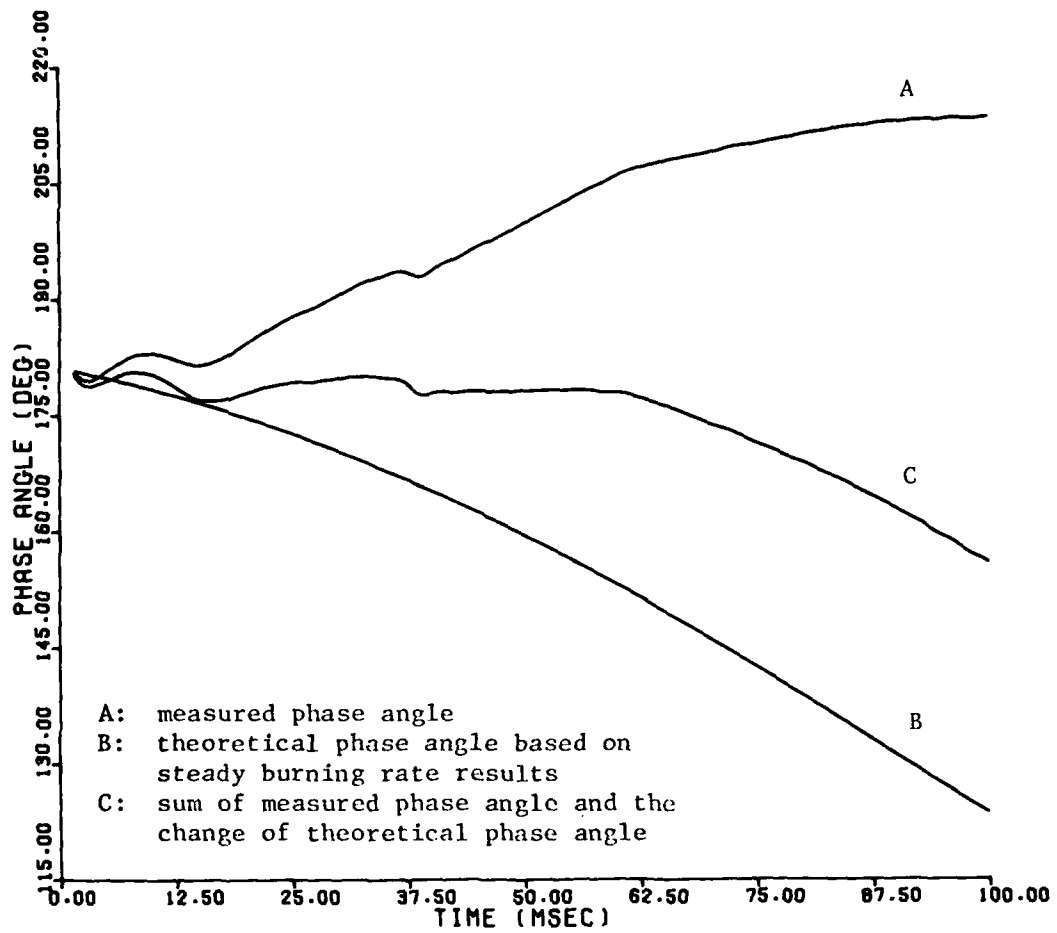


Figure 86. Measured, Theoretical, and Combined Phase Angles for Vibration Test 10VT

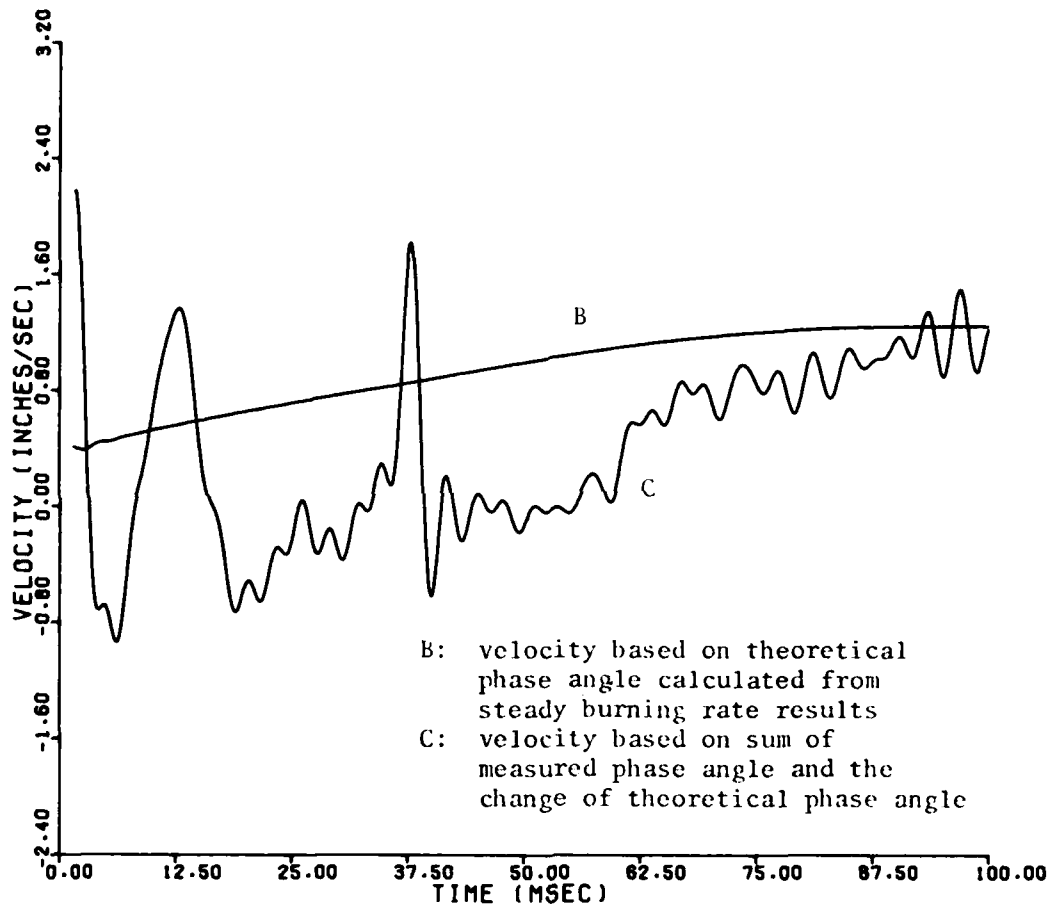


Figure 87. Theoretical and Pseudo-Experimental Velocities for Vibration Test 10VT

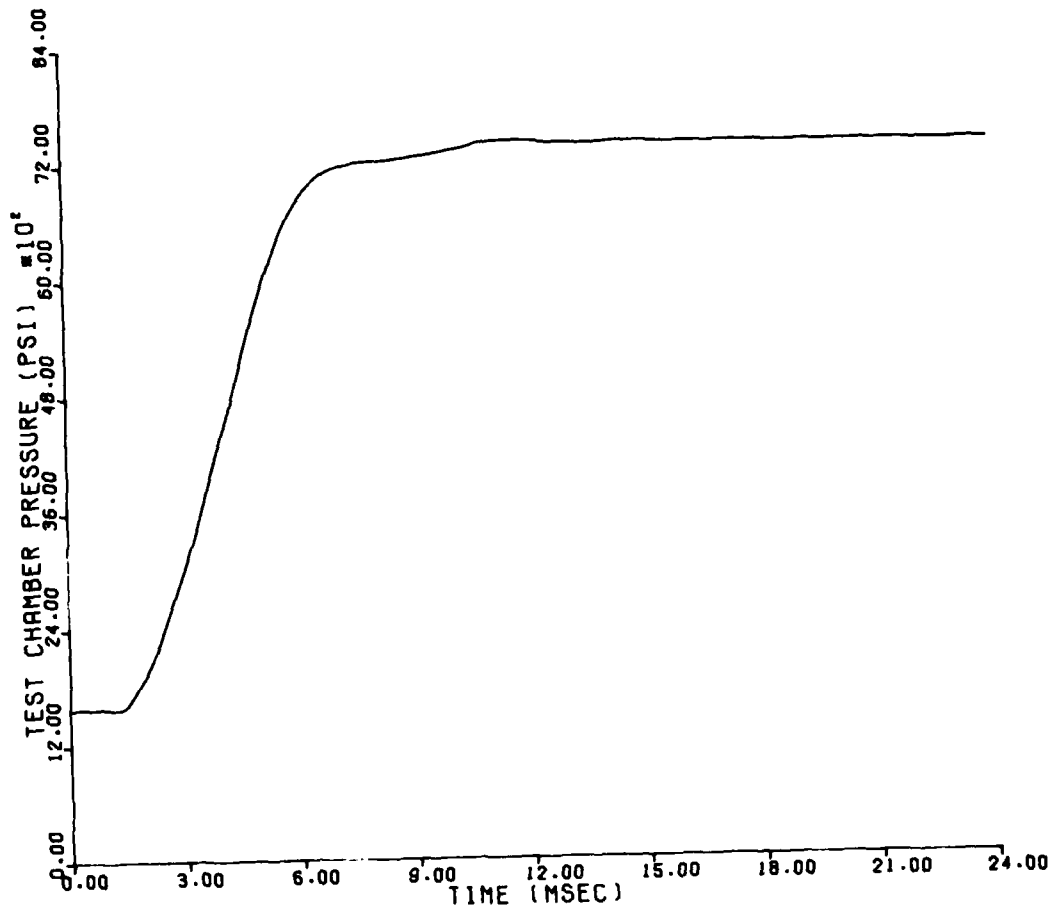


Figure 88. Test Chamber Pressure on Vibration Test 11VT

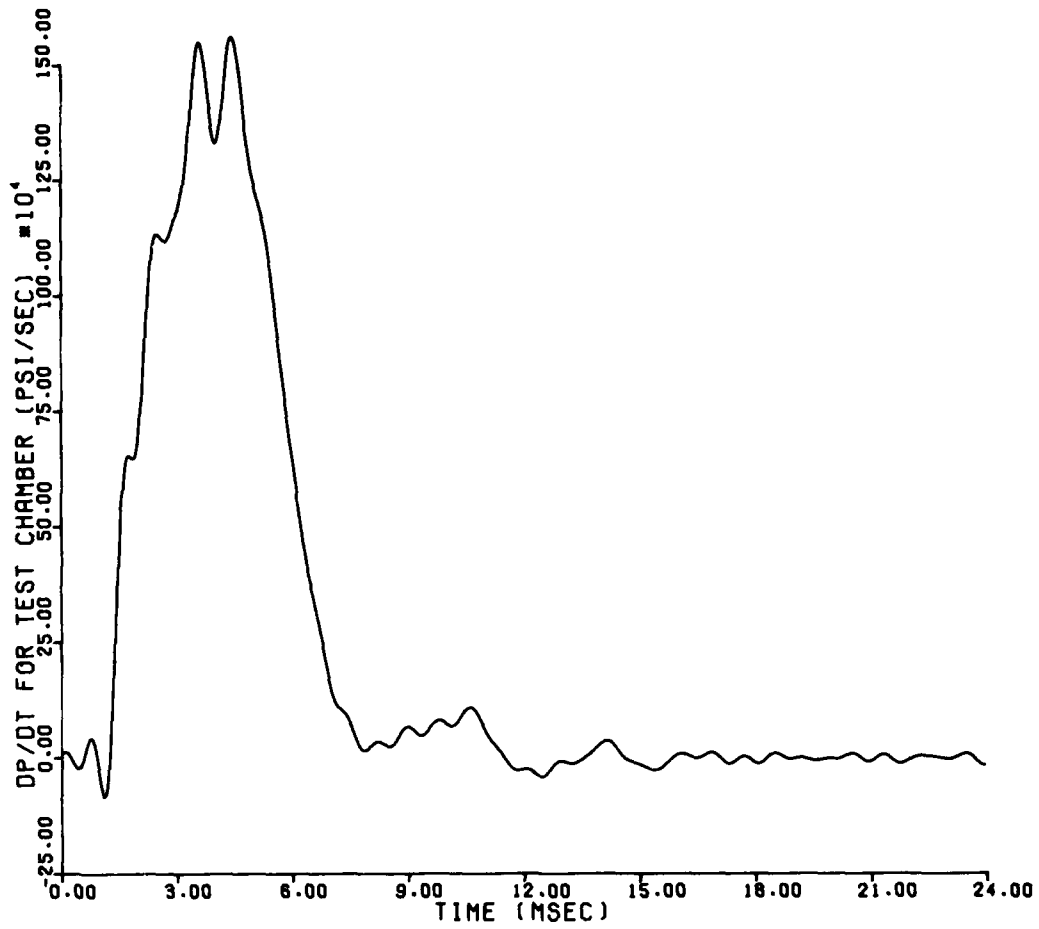


Figure 89. Test Chamber Pressurization Rate on Vibration Test 11VT

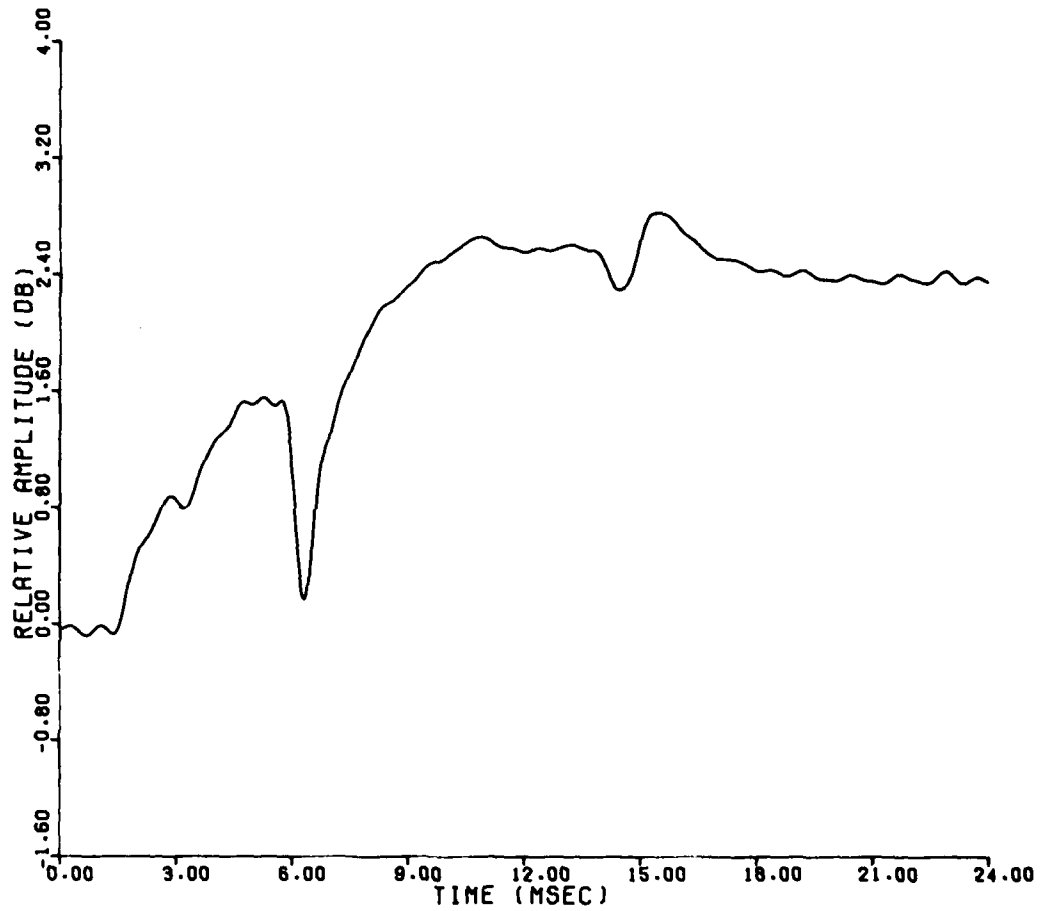


Figure 90. Change in Relative Amplitude Between the Test and Reference Signals on Vibration Test 11VT

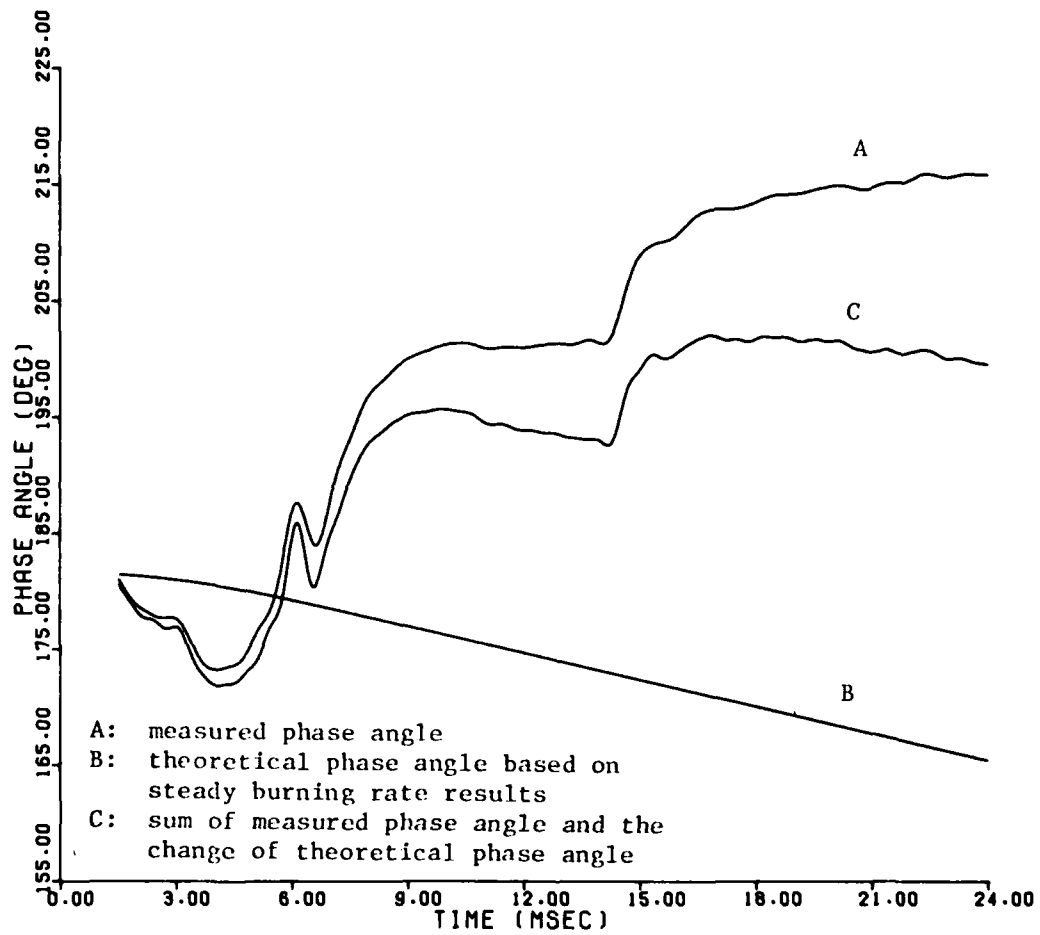


Figure 91. Measured, Theoretical, and Combined Phase Angles for Vibration Test 11VT

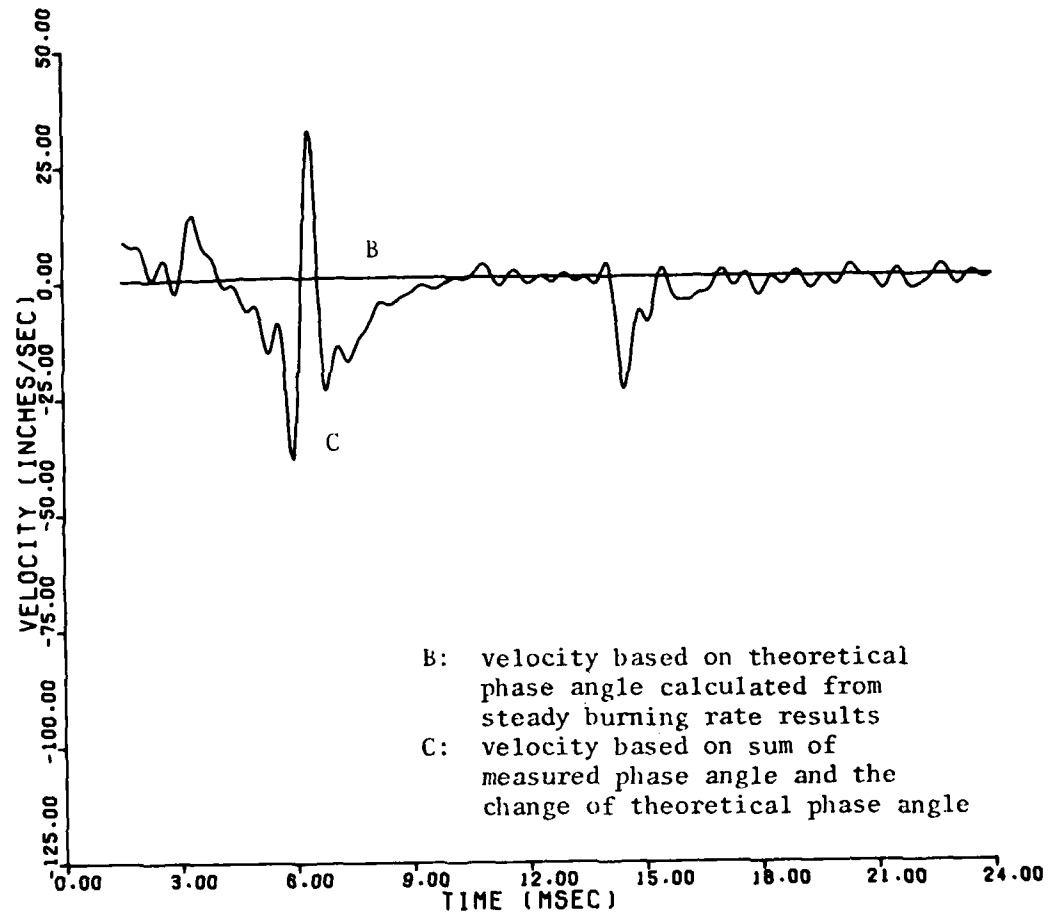


Figure 92. Theoretical and Pseudo-Experimental Velocities for Vibration Test 11VT

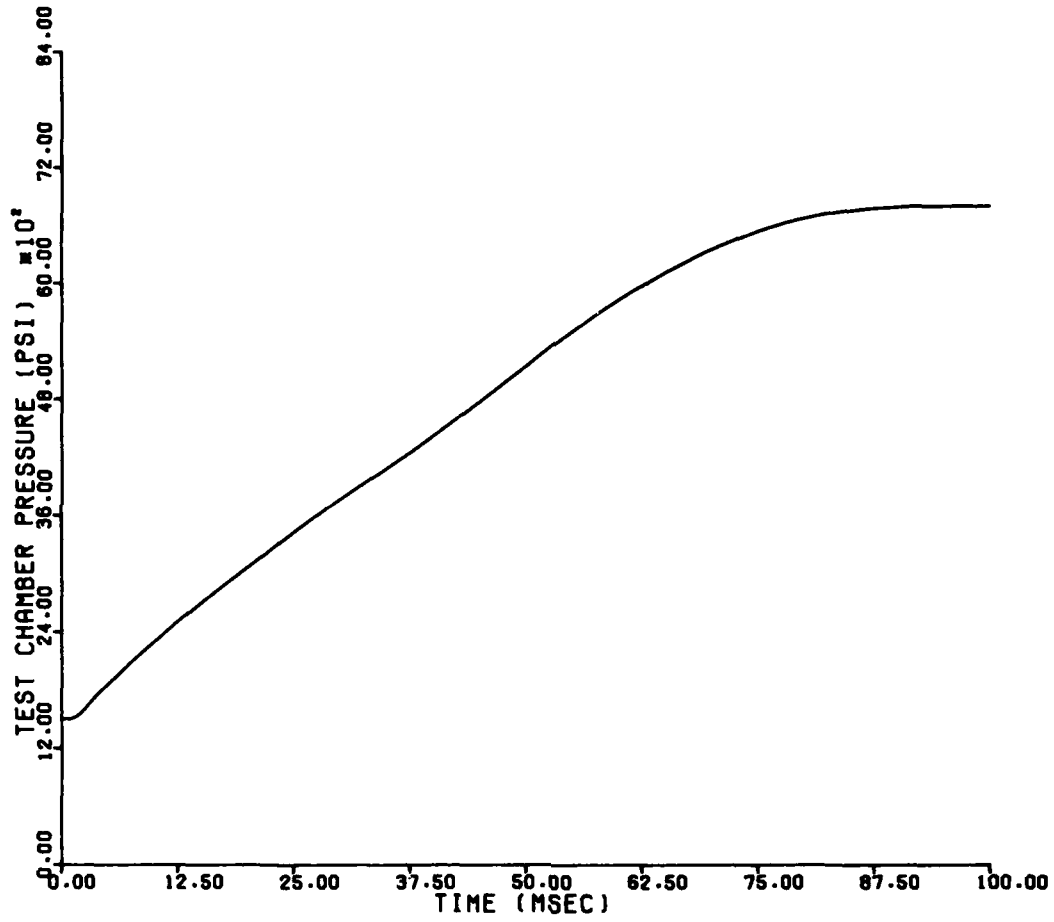


Figure 93. Test Chamber Pressure on Vibration Test 6VT

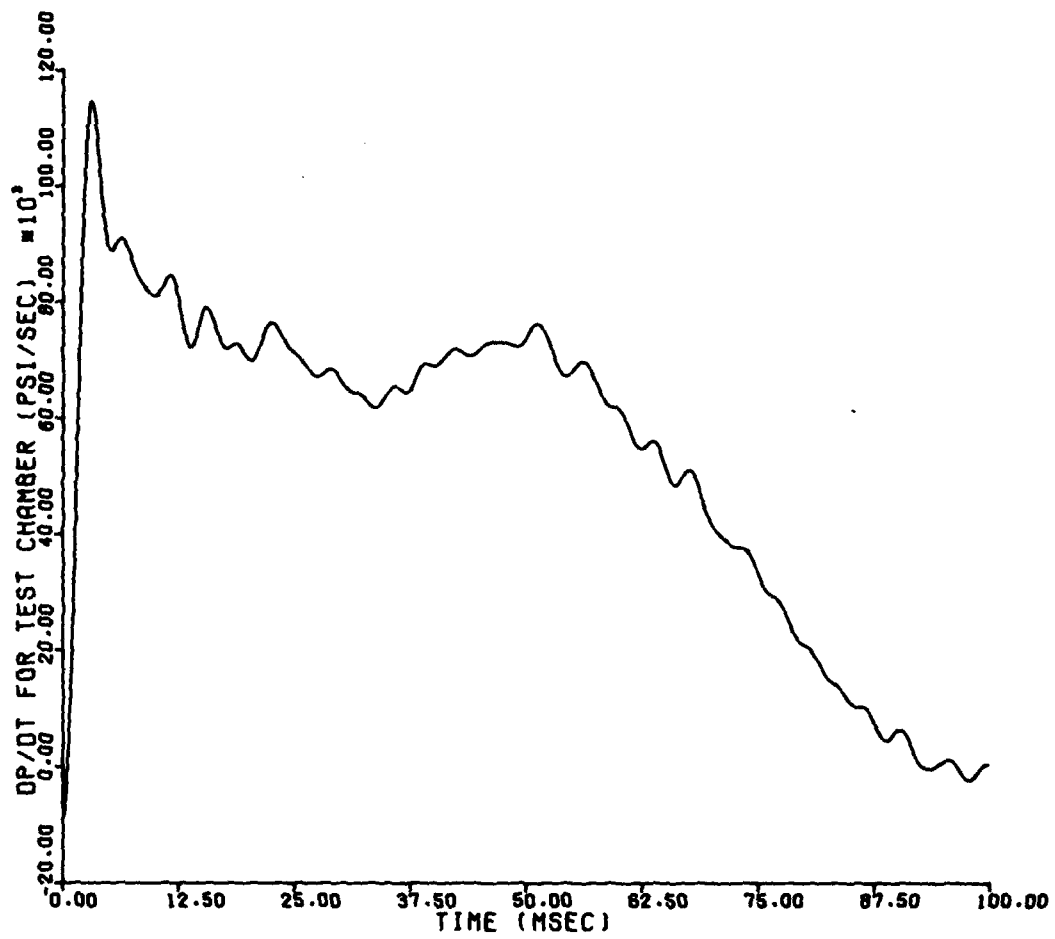


Figure 94. Test Chamber Pressurization Rate on Vibration Test 6VT

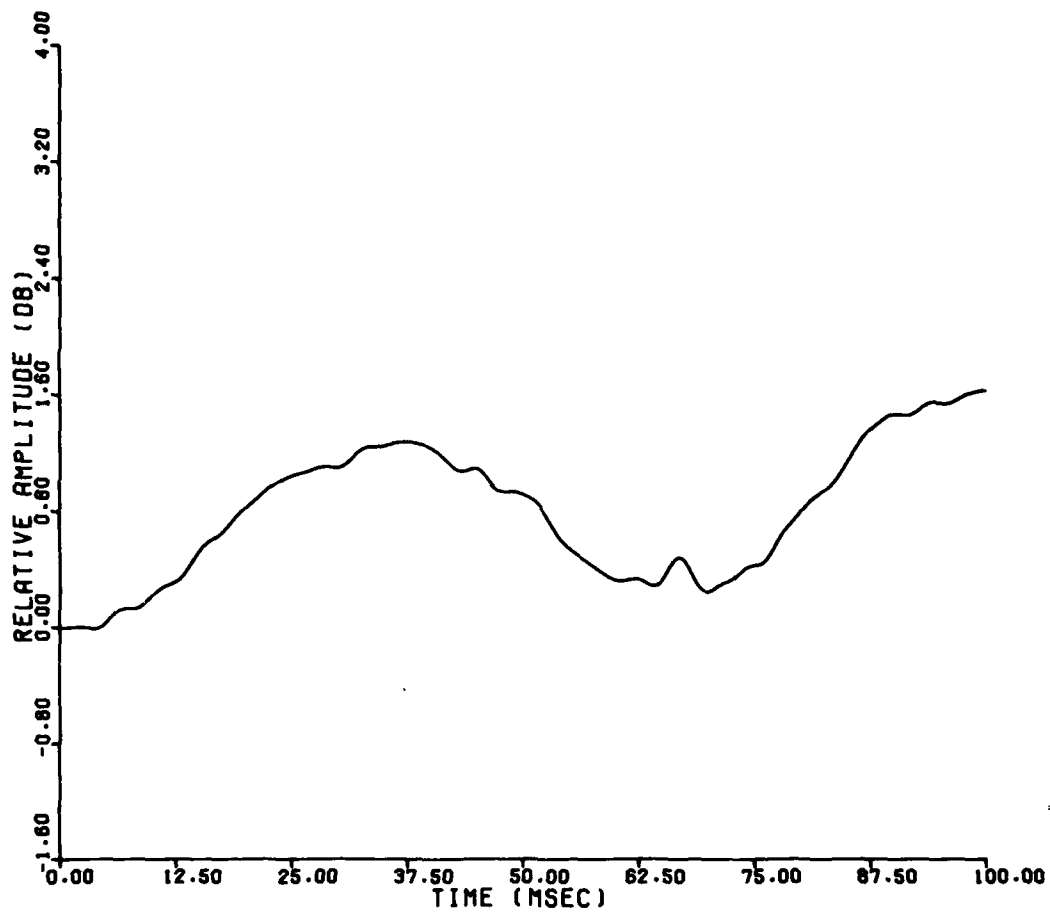


Figure 95. Change in Relative Amplitude Between the Test and Reference Signals on Vibration Test 6VT

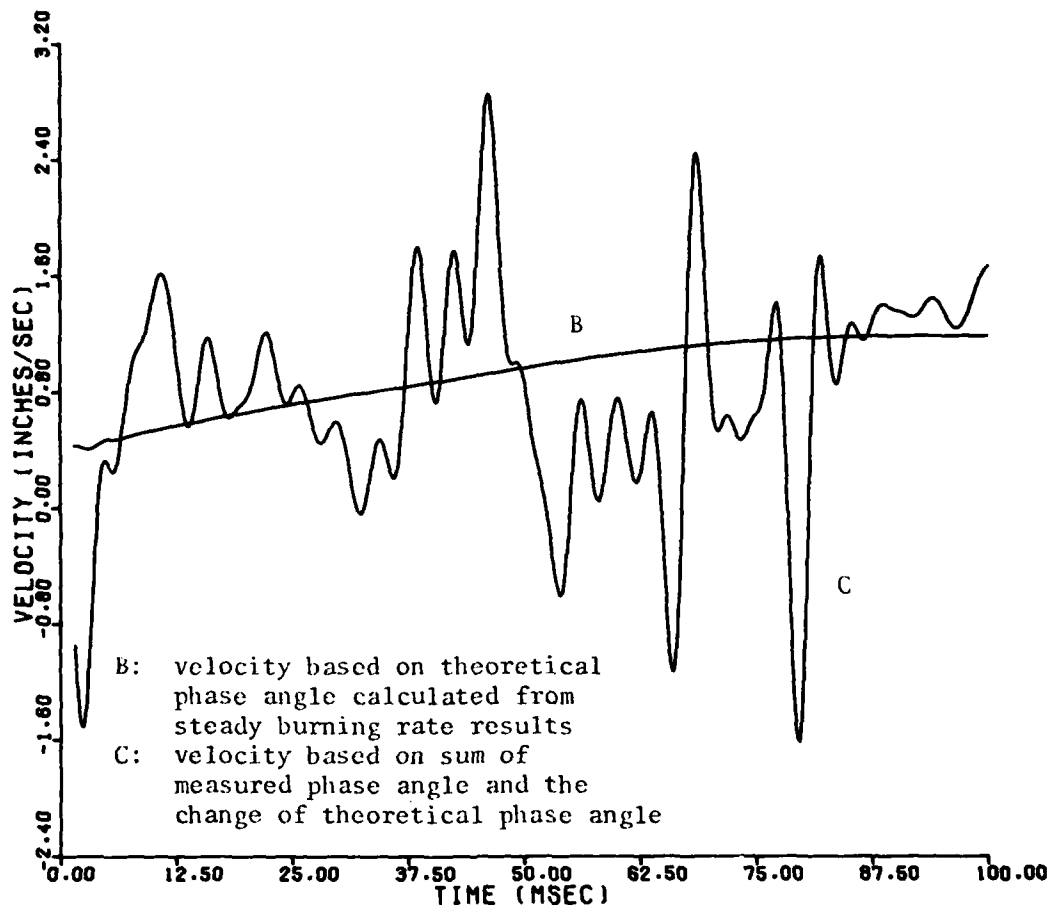


Figure 96. Measured, Theoretical, and Combined Phase Angles for Vibration Test 6VT

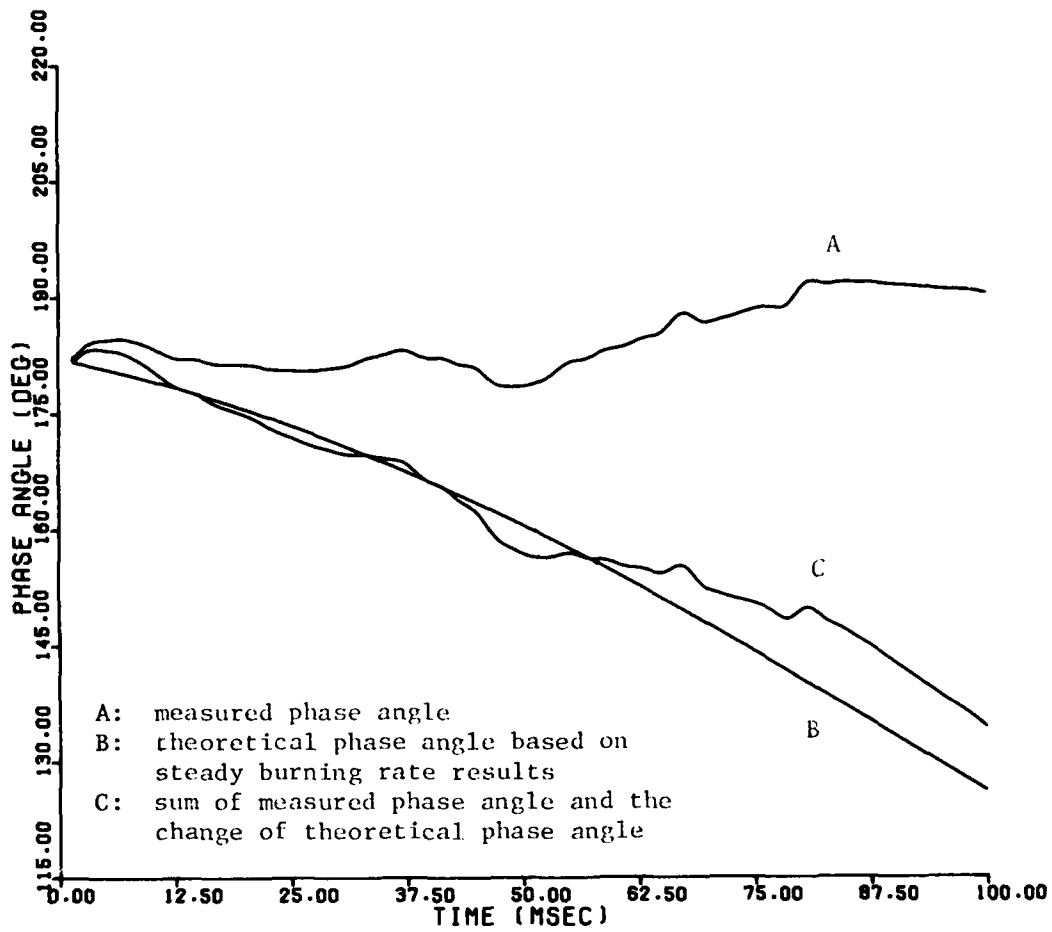


Figure 97. Theoretical and Pseudo-Experimental Velocities for Vibration Test 6VT

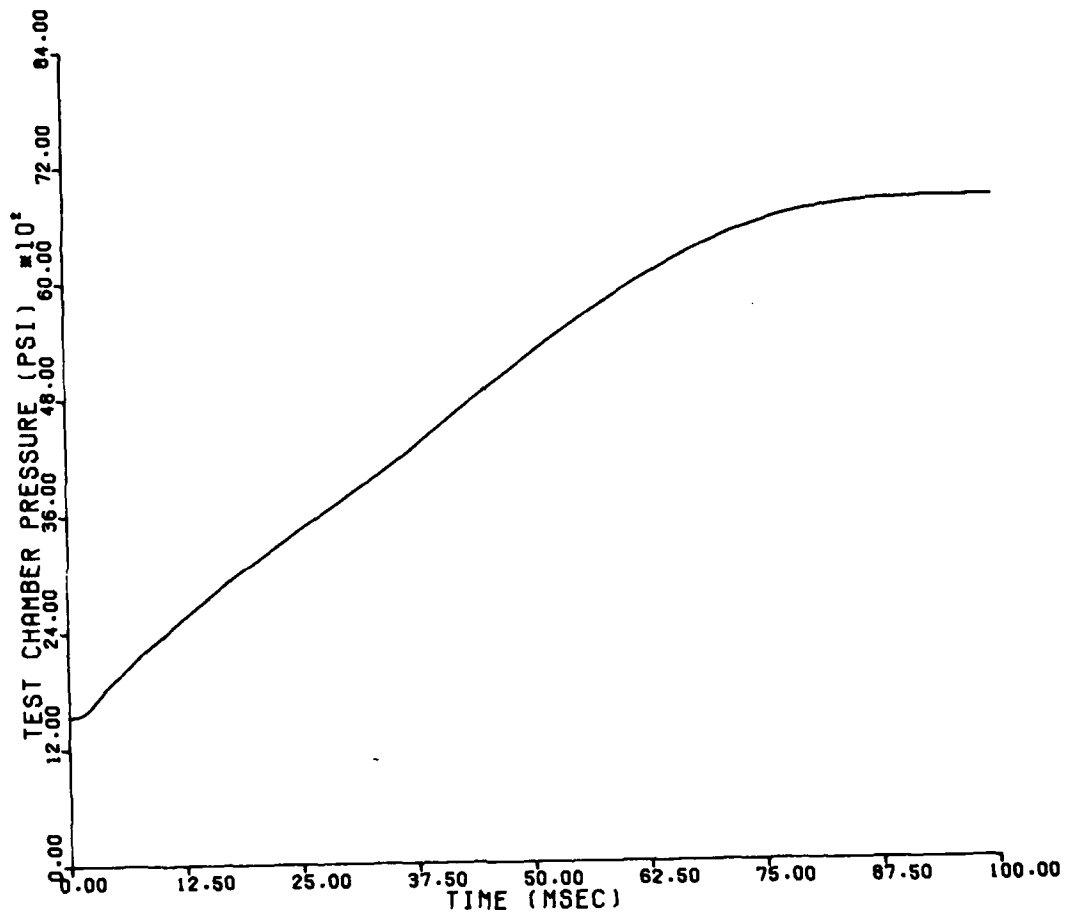


Figure 98. Test Chamber Pressure on Vibration Test 7VT

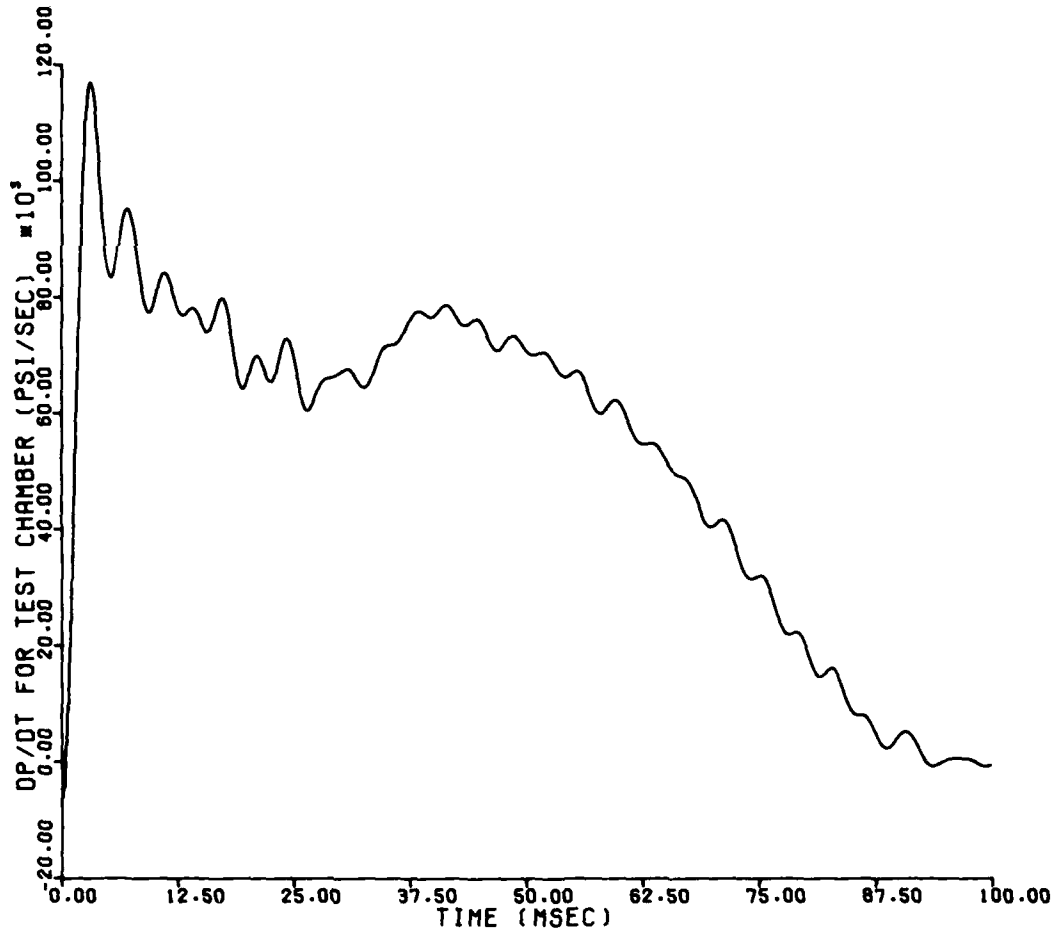


Figure 99. Test Chamber Pressurization Rate on Vibration Test 7VT

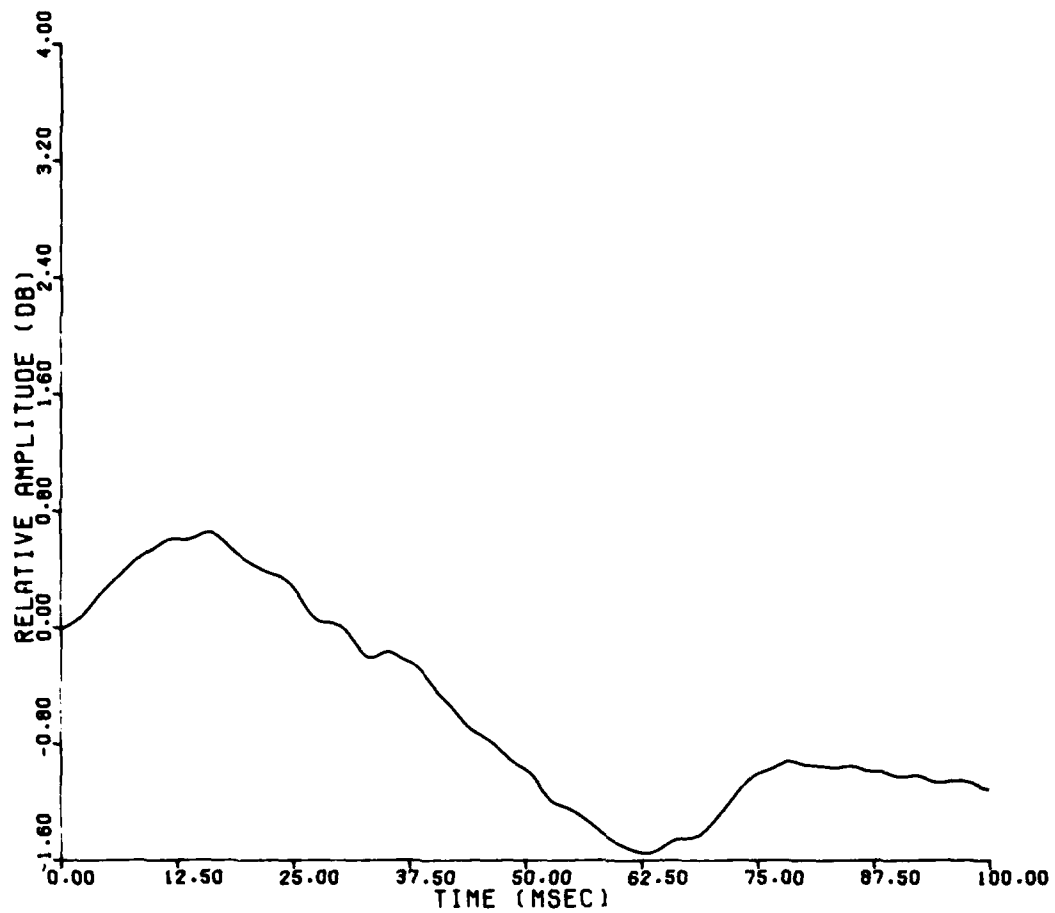


Figure 100. Change in Relative Amplitude Between the Test and Reference Signals on Vibration Test 7VT

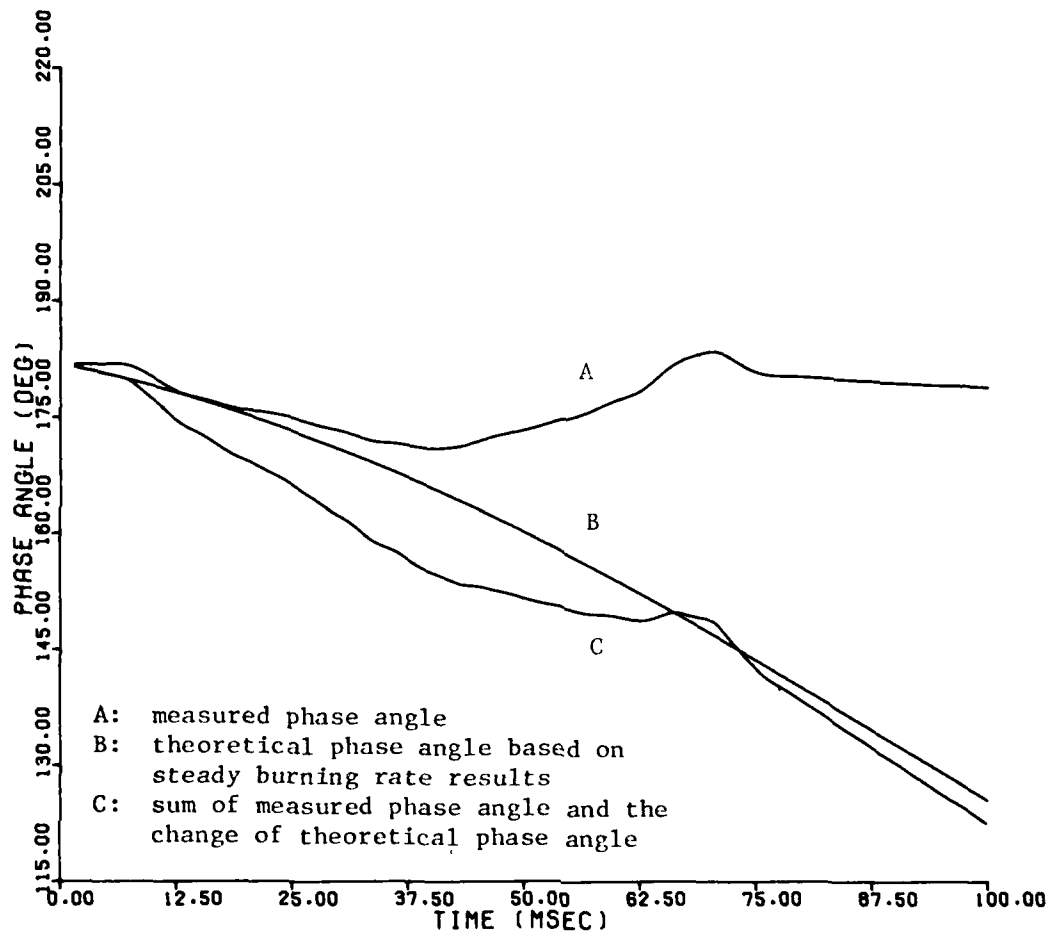


Figure 101. Measured, Theoretical, and Combined Phase Angles for Vibration Test 7VT

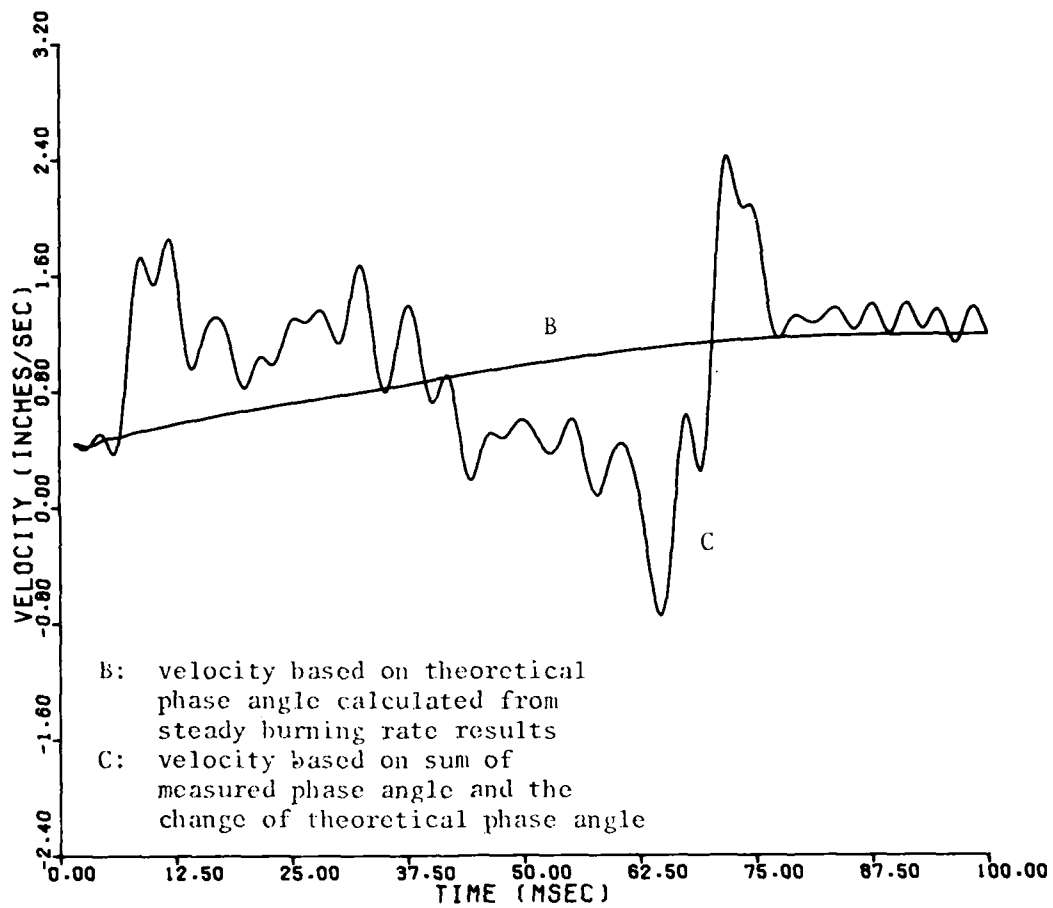


Figure 102. Theoretical and Pseudo-Experimental Velocities for Vibration Test 7VT



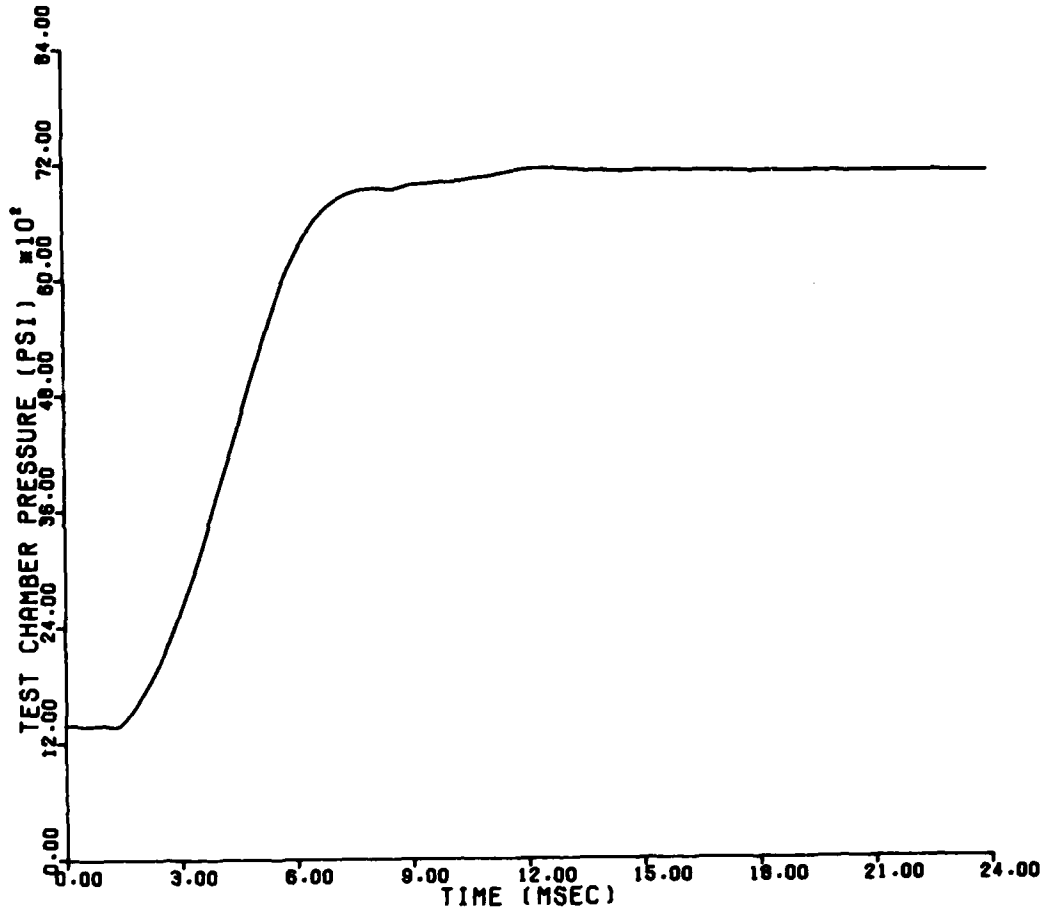


Figure 103. Test Chamber Pressure on Vibration Test 8VT

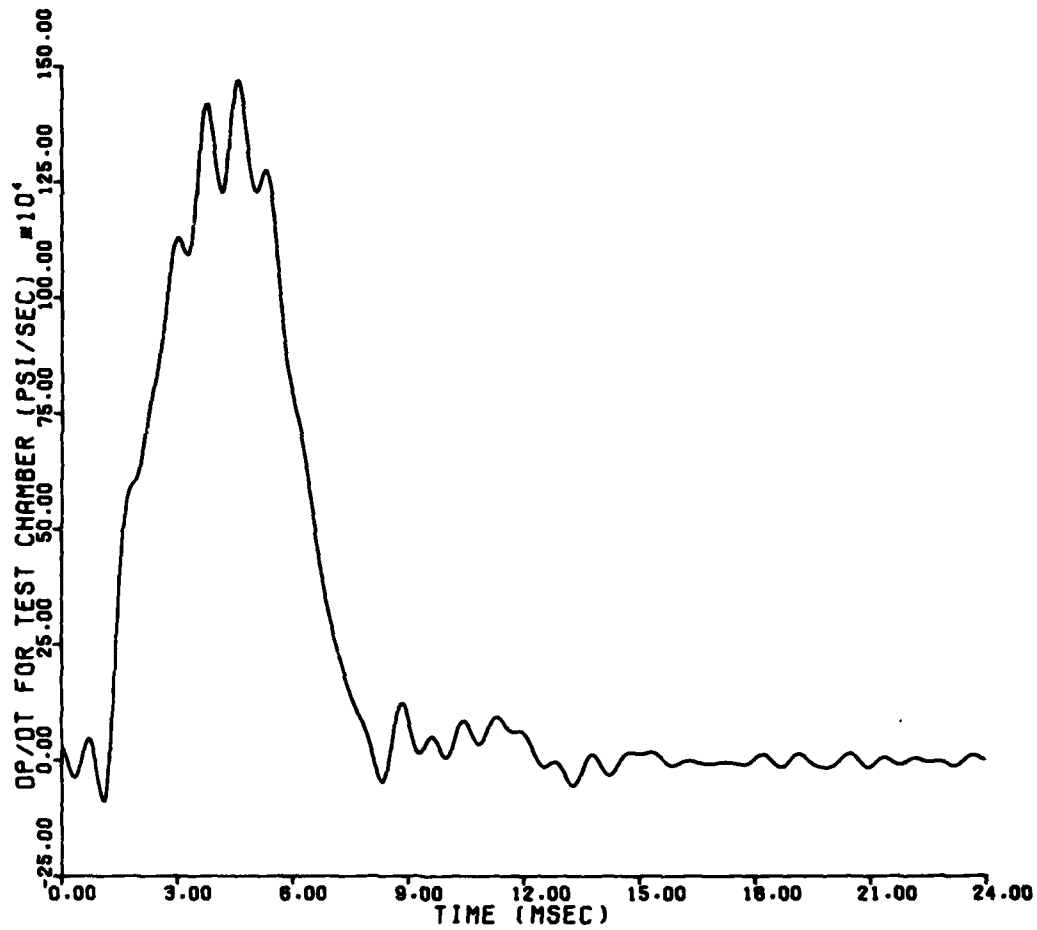


Figure 104. Test Chamber Pressurization Rate on Vibration Test 8VT

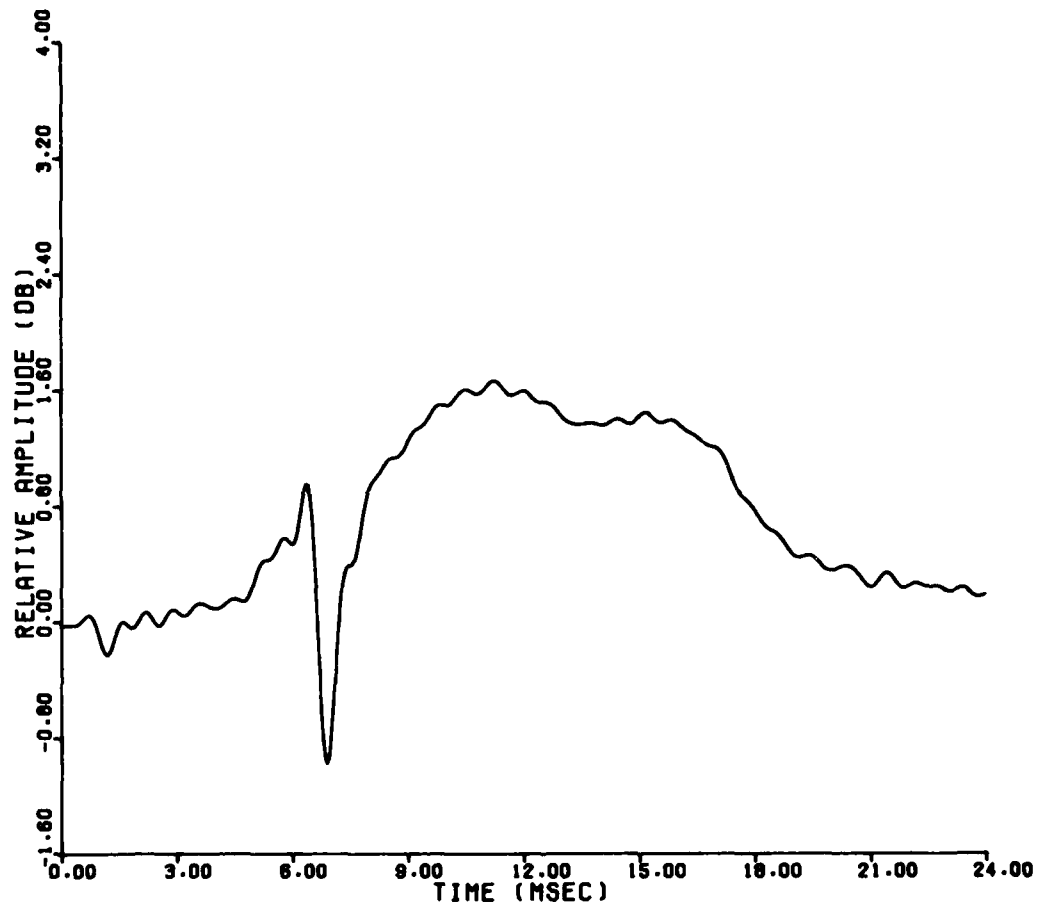


Figure 105. Change in Relative Amplitude Between the Test and Reference Signals on Vibration Test 8VT

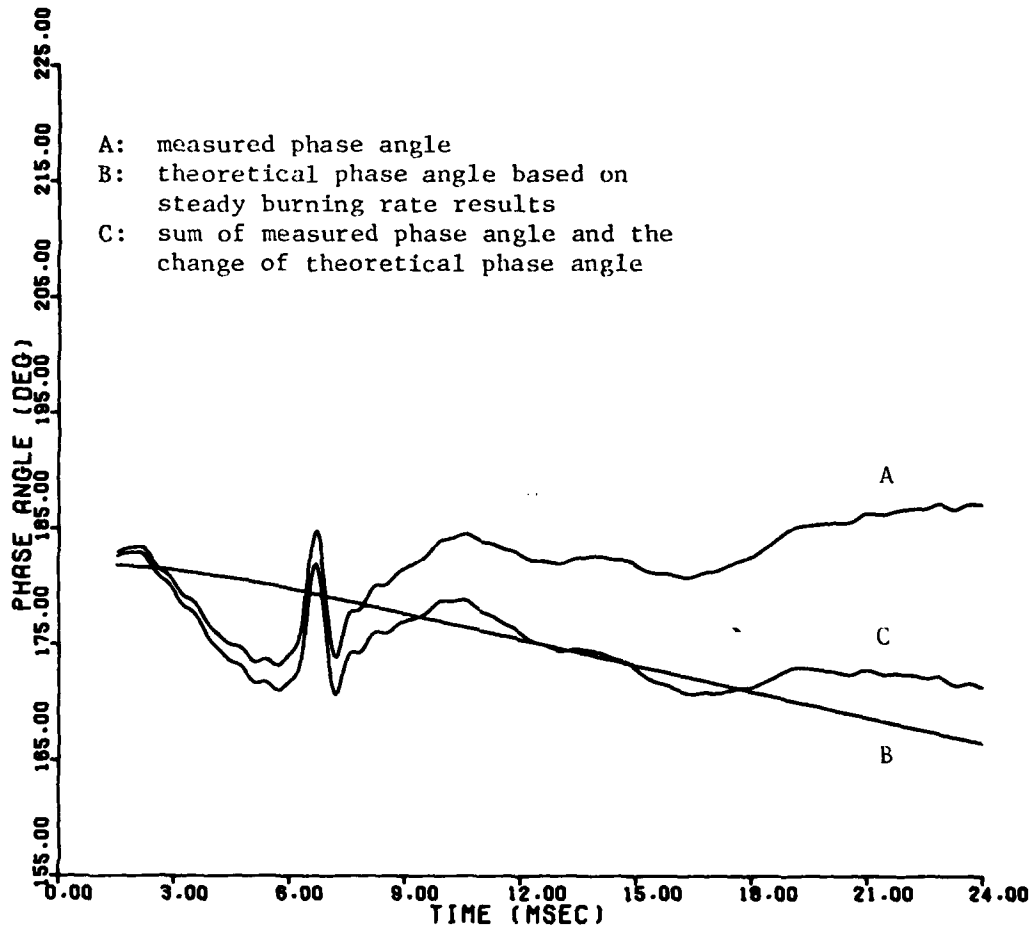


Figure 106. Measured, Theoretical, and Combined Phase Angles for Vibration Test 8VT

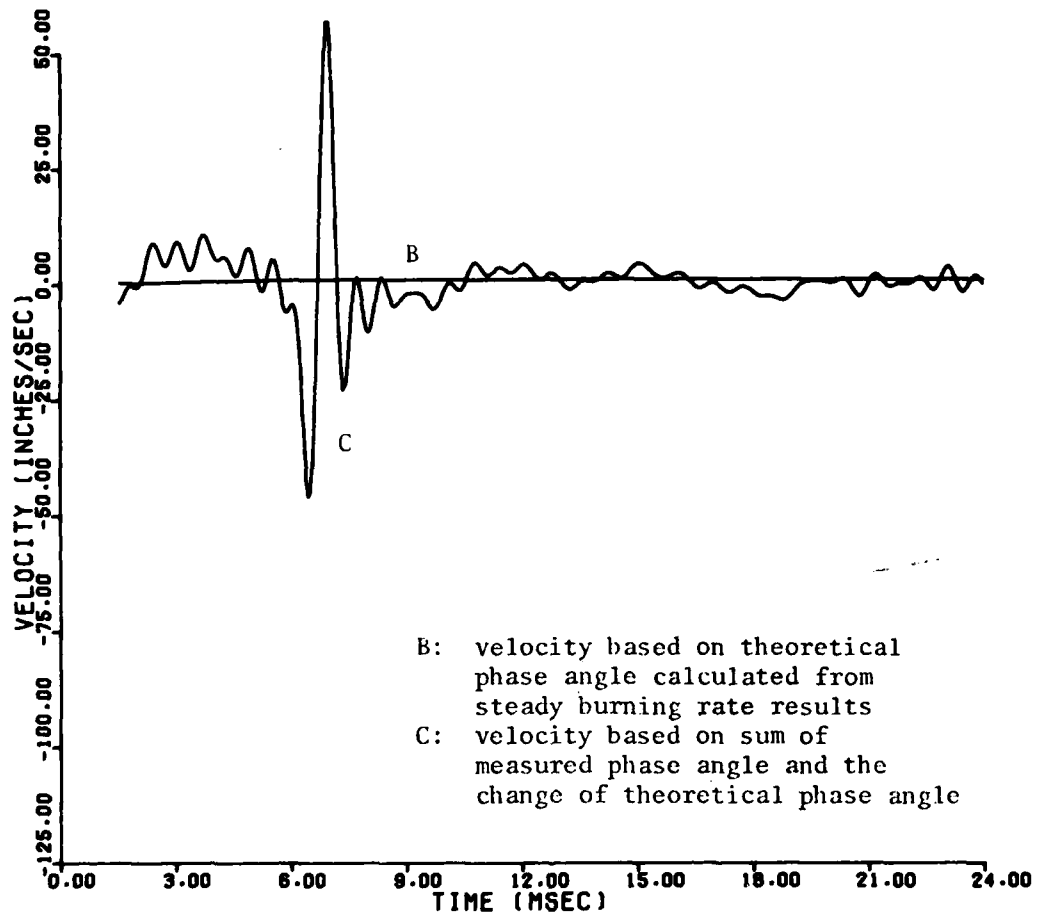


Figure 107. Theoretical and Pseudo-Experimental Velocities for Vibration Test 8VT

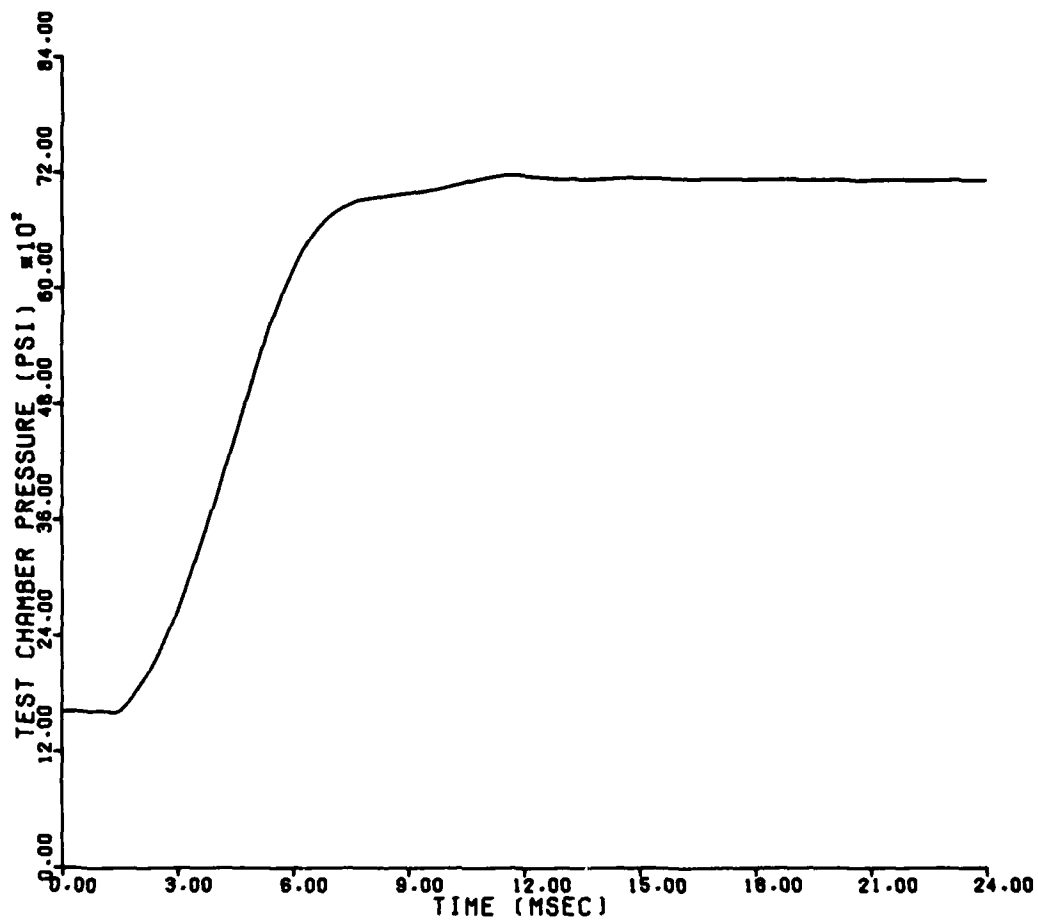


Figure 108. Test Chamber Pressure on Vibration Test 9VT

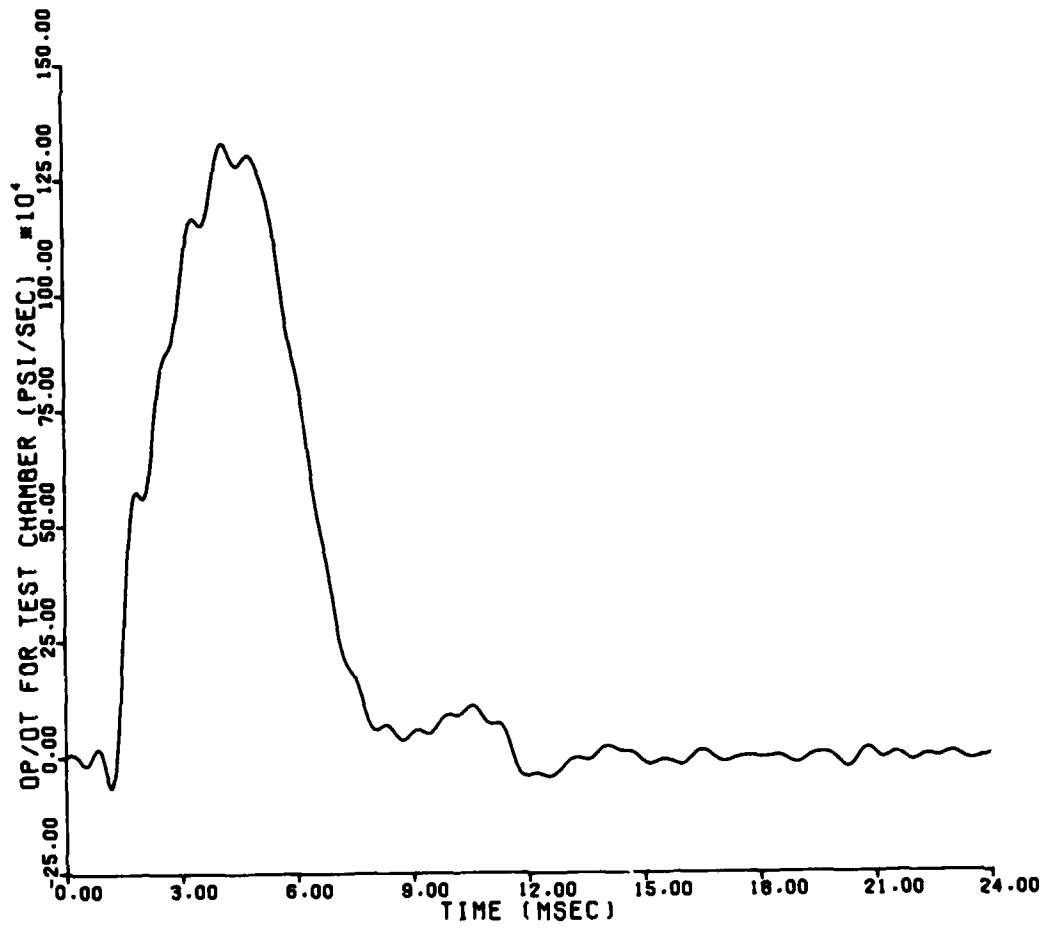


Figure 109. Test Chamber Pressurization Rate on Vibration Test 9VT

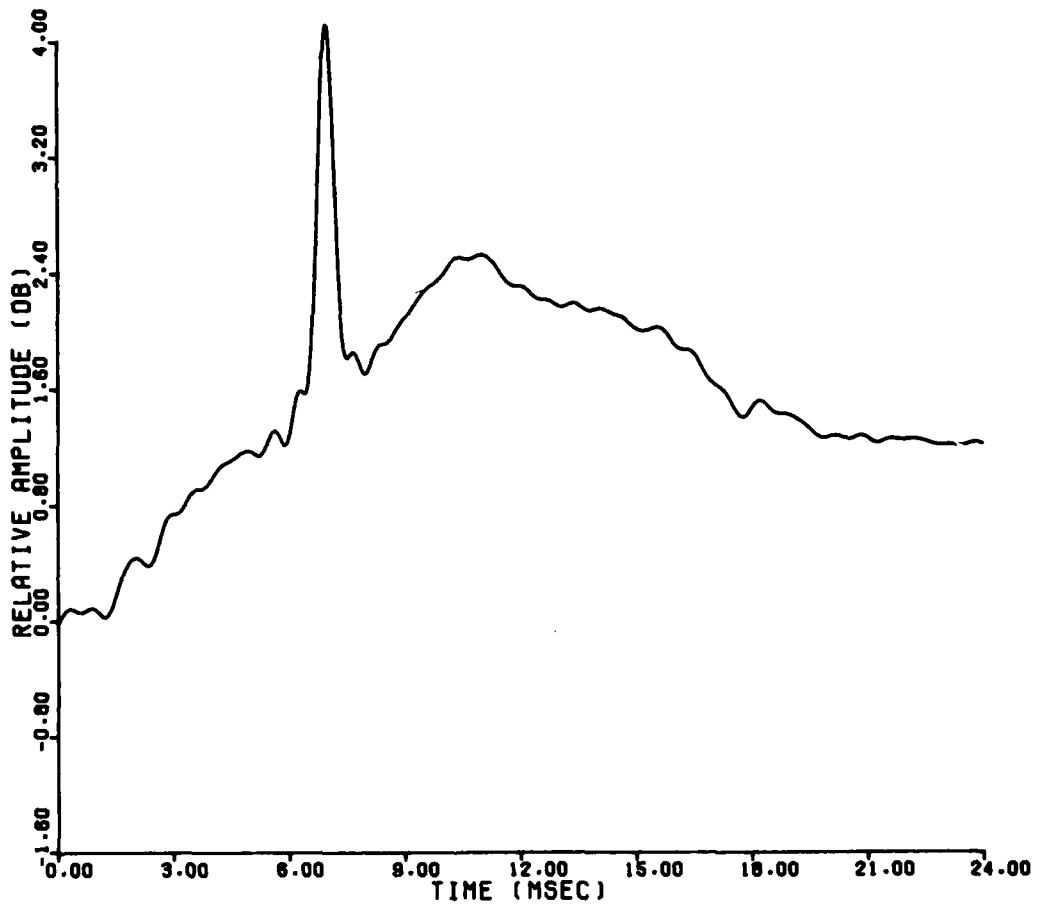


Figure 110. Change in Relative Amplitude Between the Test and Reference Signals on Vibration Test 9VT

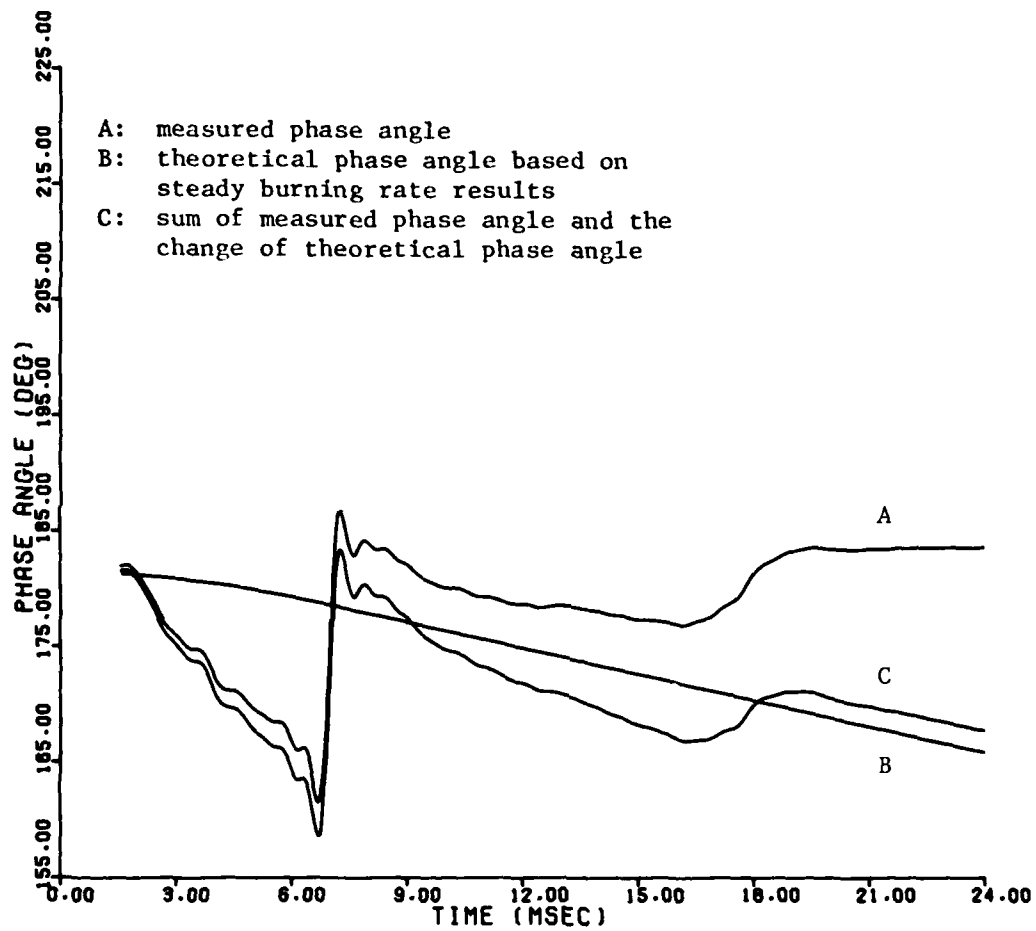


Figure 111. Measured, Theoretical, and Combined Phase Angles for Vibration Test 9VT

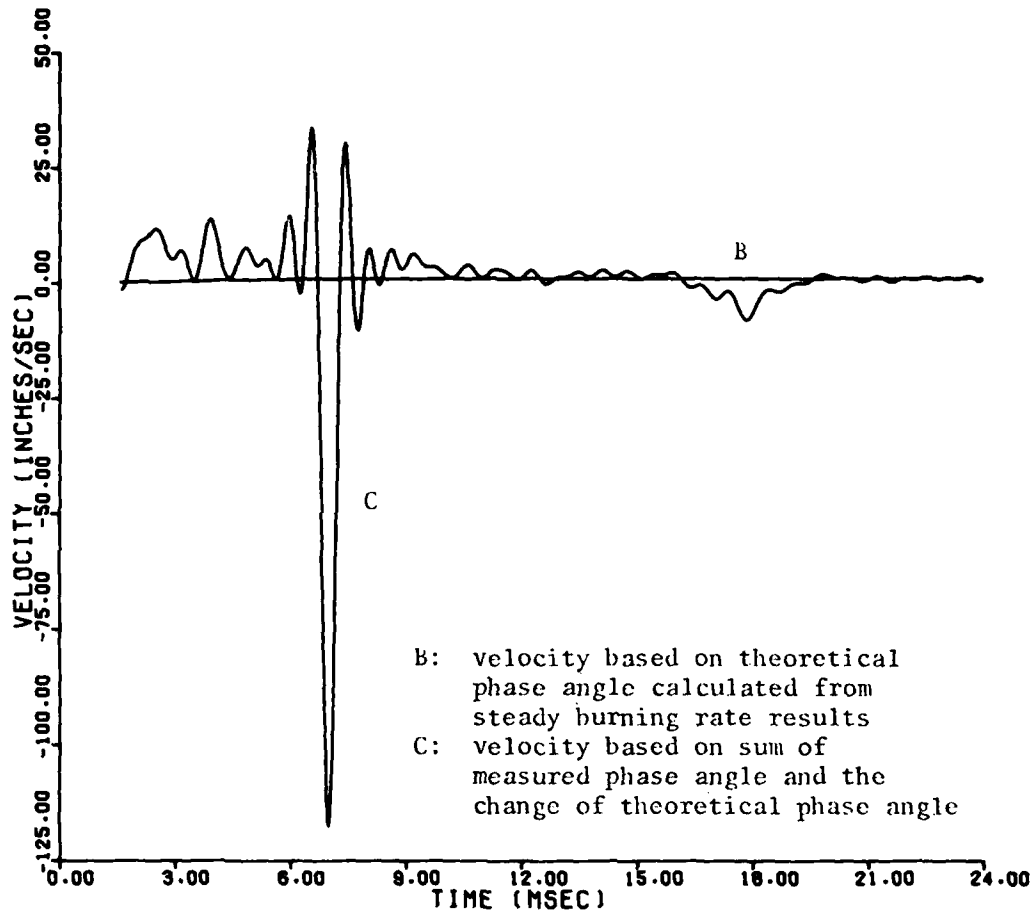


Figure 112. Theoretical and Pseudo-Experimental Velocities for Vibration Test 9VT

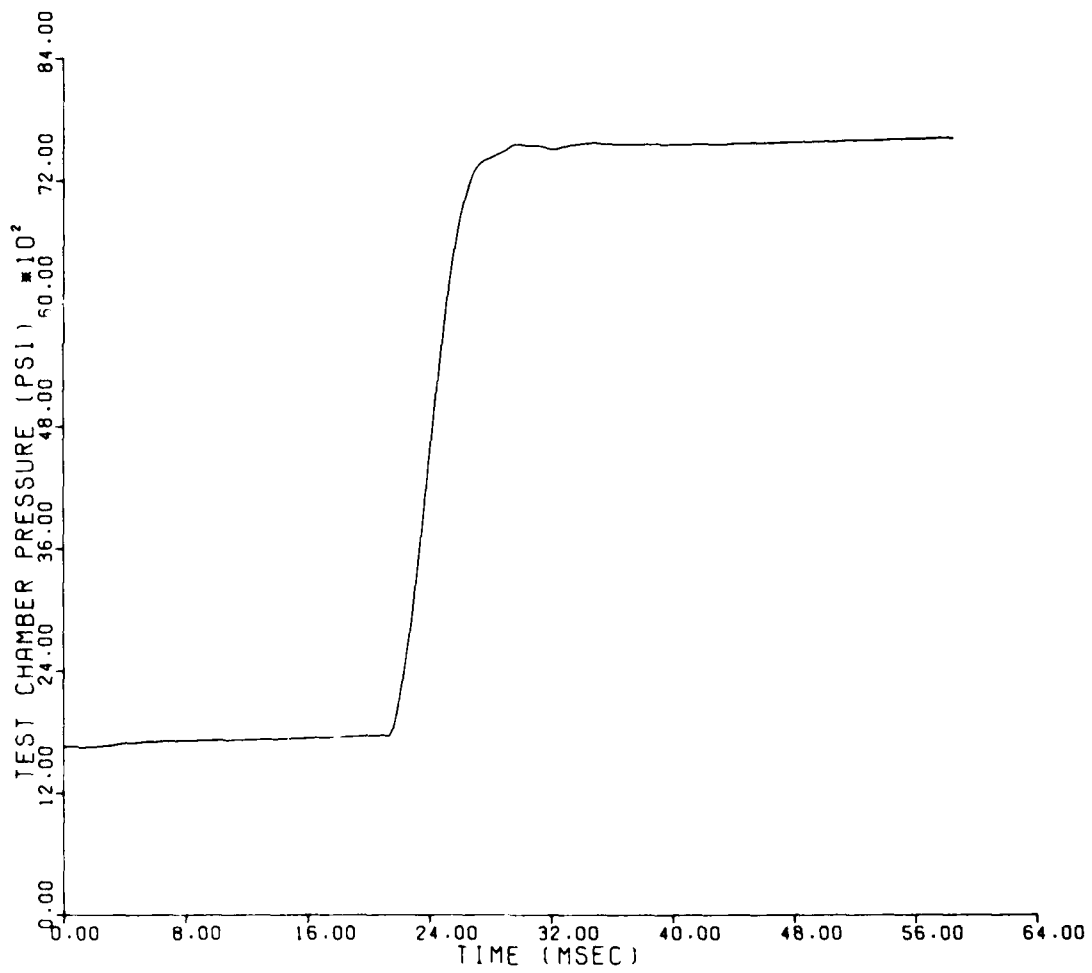


Figure 113. Test Chamber Pressure on Transient Burning Test 1TBT

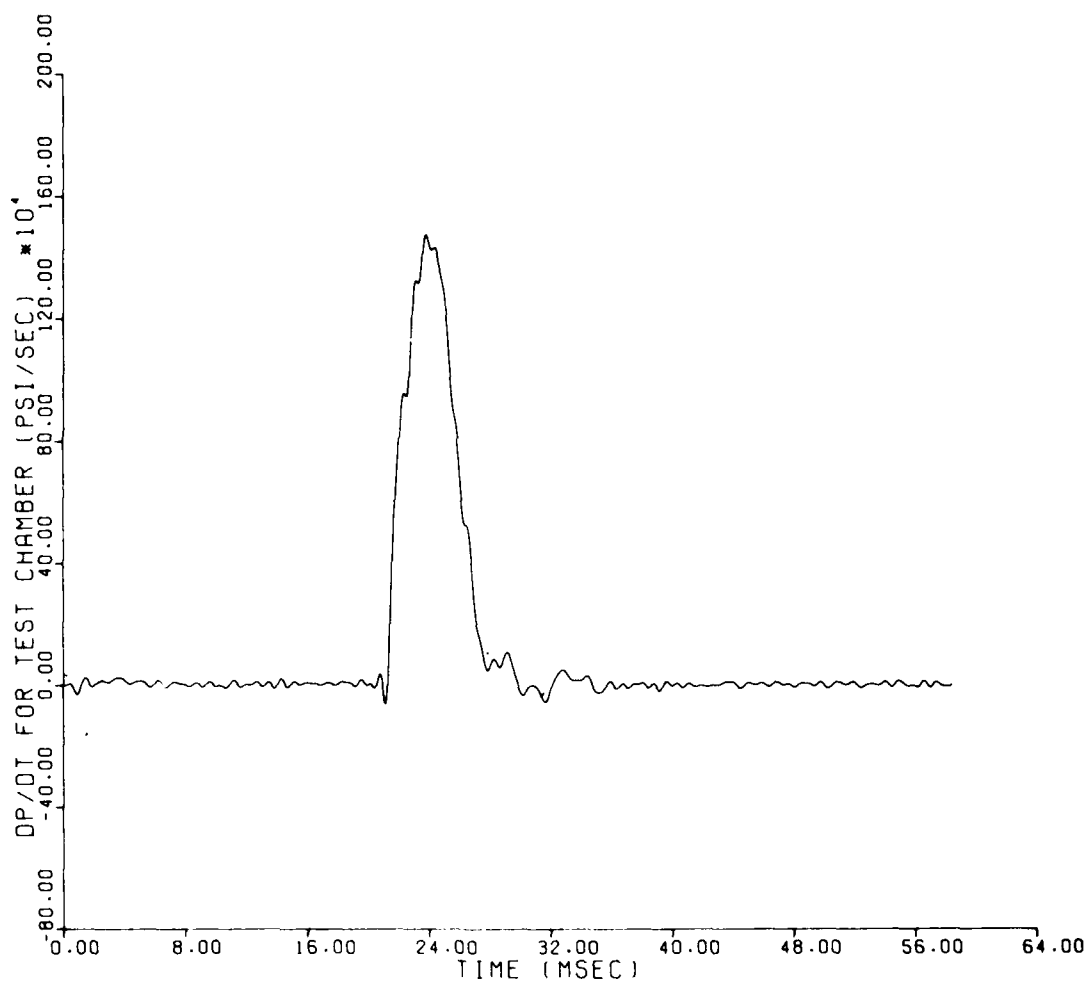
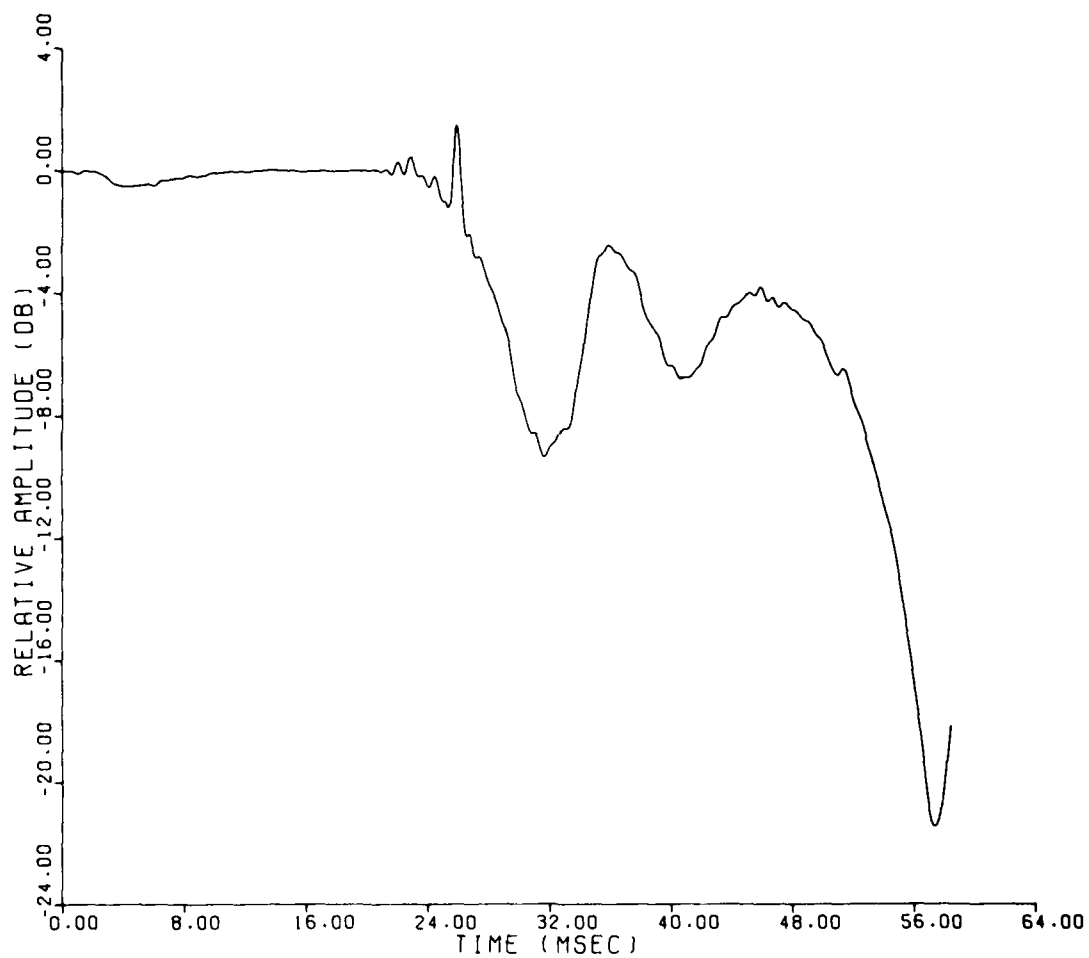


Figure 114. Test Chamber Pressurization Rate on Transient Burning Test 1TBT



**Figure 115. Change in Relative Amplitude Between the Test and Reference Signals on Transient Burning Test 1TBT**

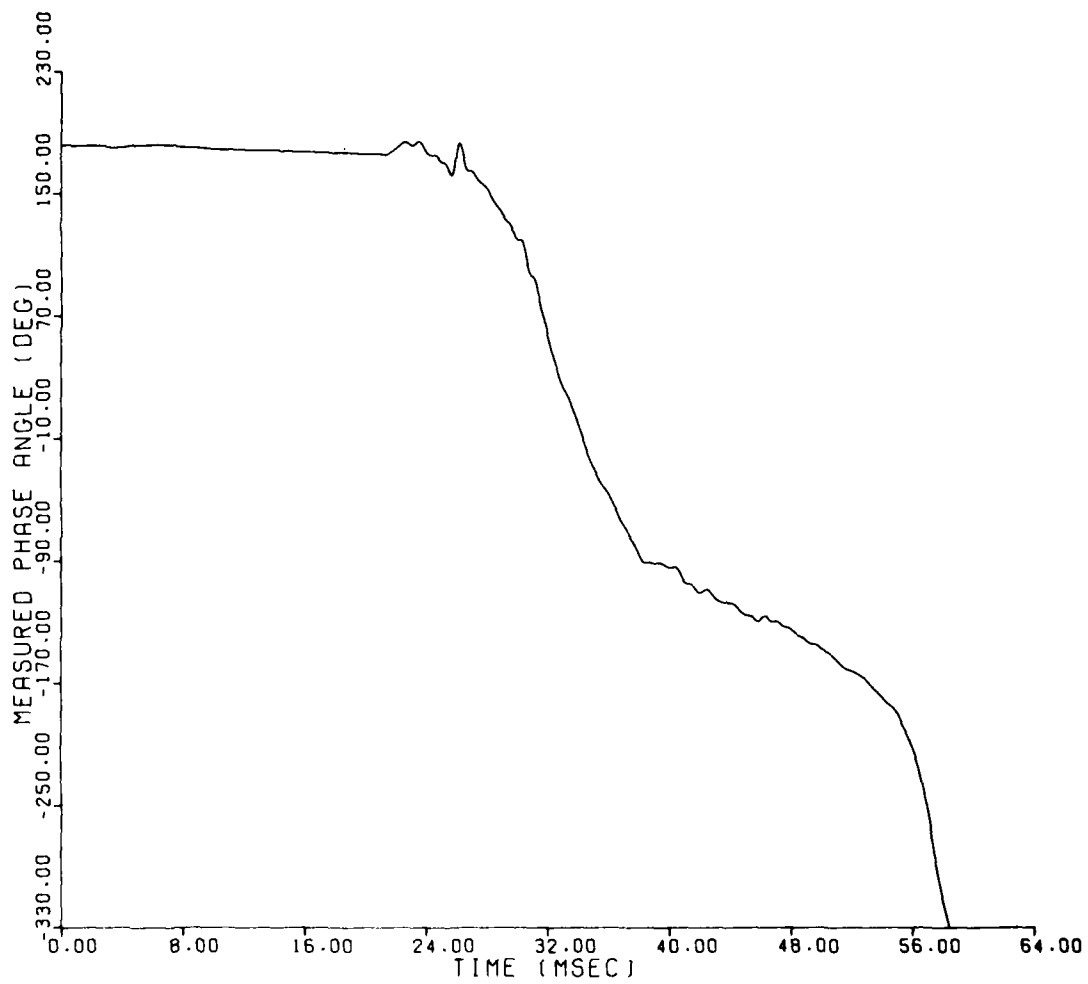


Figure 116. Measured Phase Angle on Transient Burning Test 1TBT

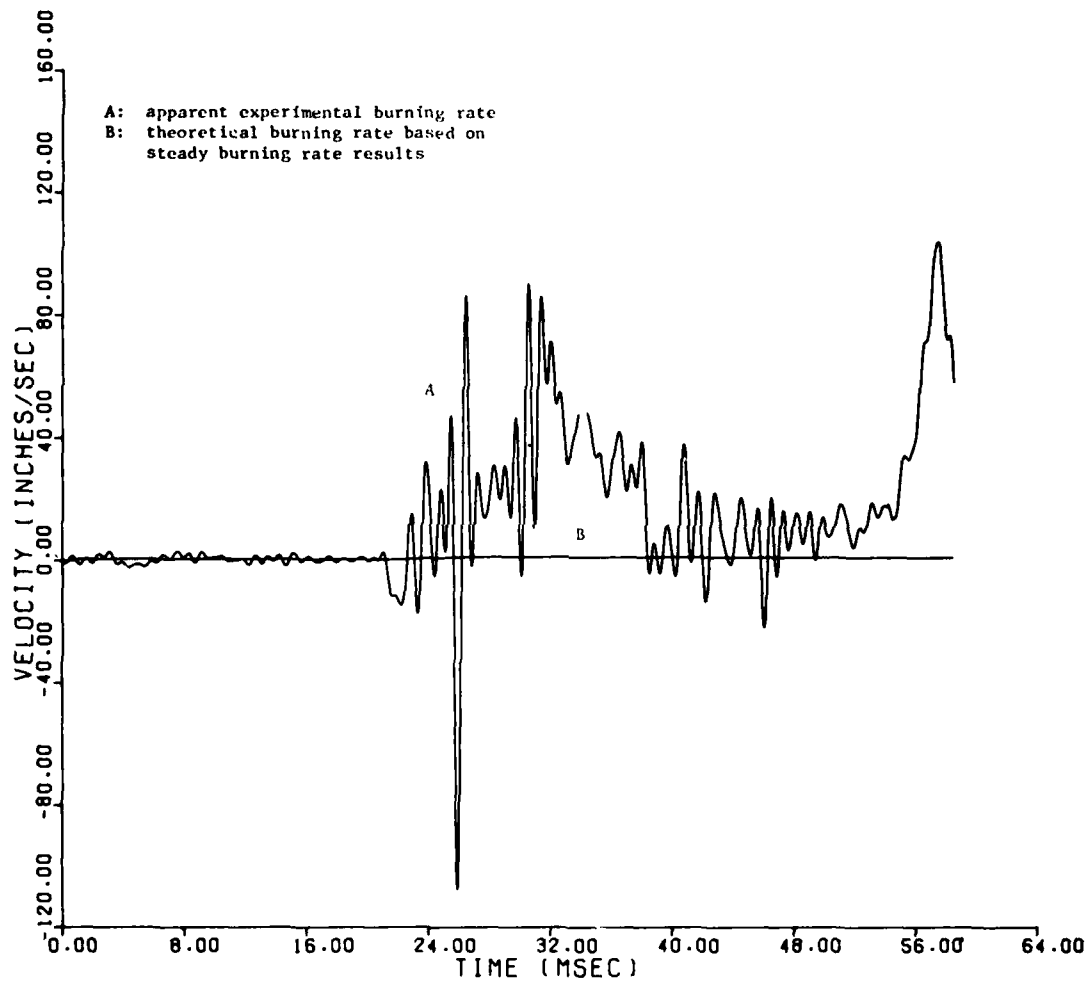


Figure 117. Theoretical and Apparent Experimental Burning Rates for Transient Burning Test 1TBT

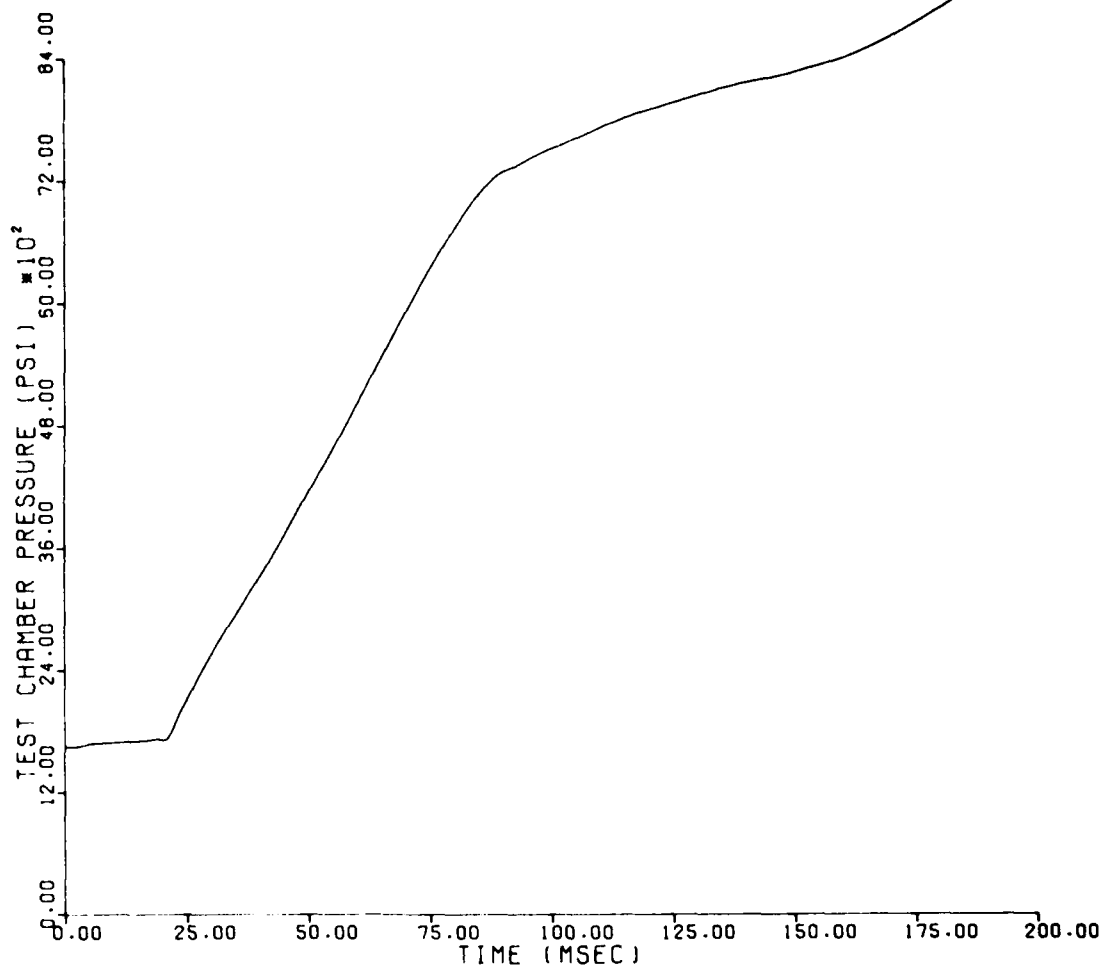


Figure 118. Test Chamber Pressure on Transient Burning Test 2TBT

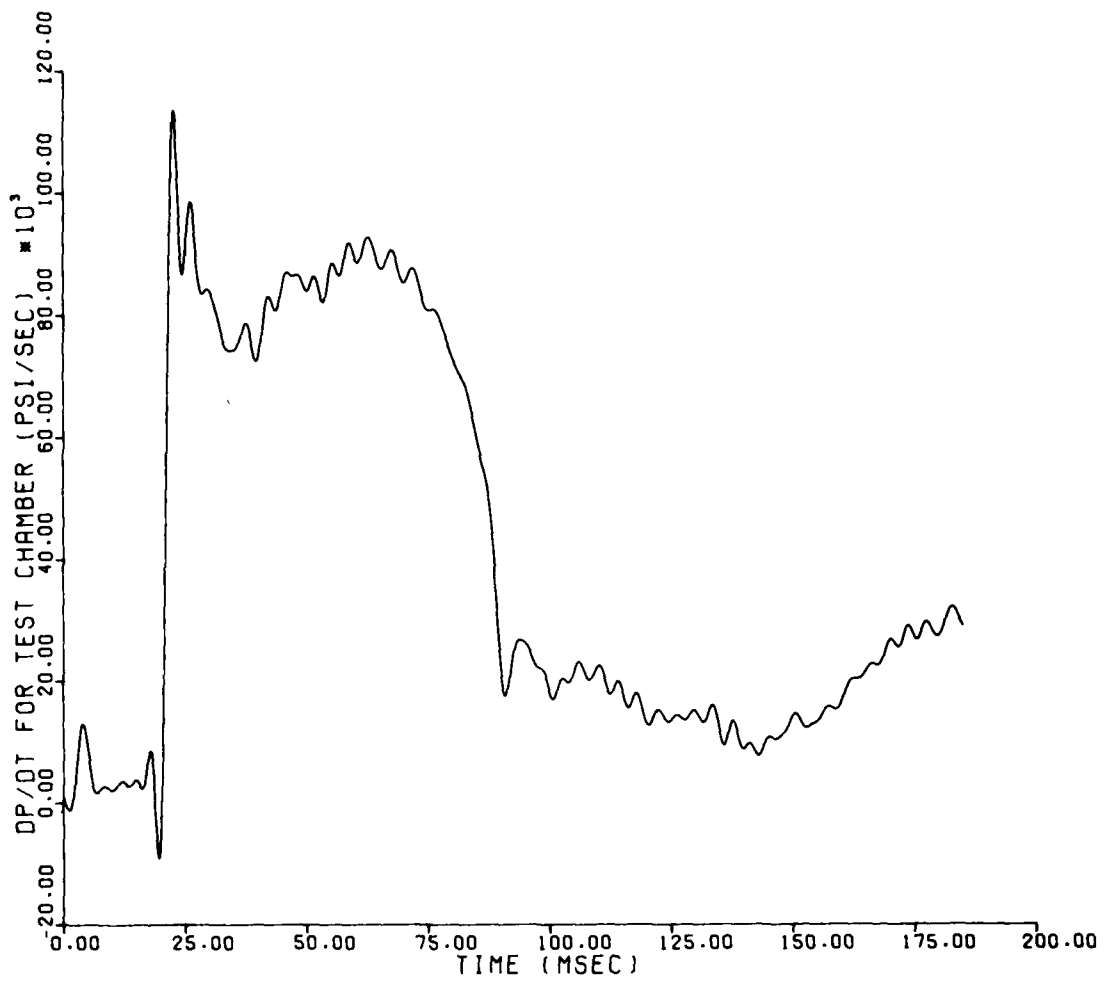
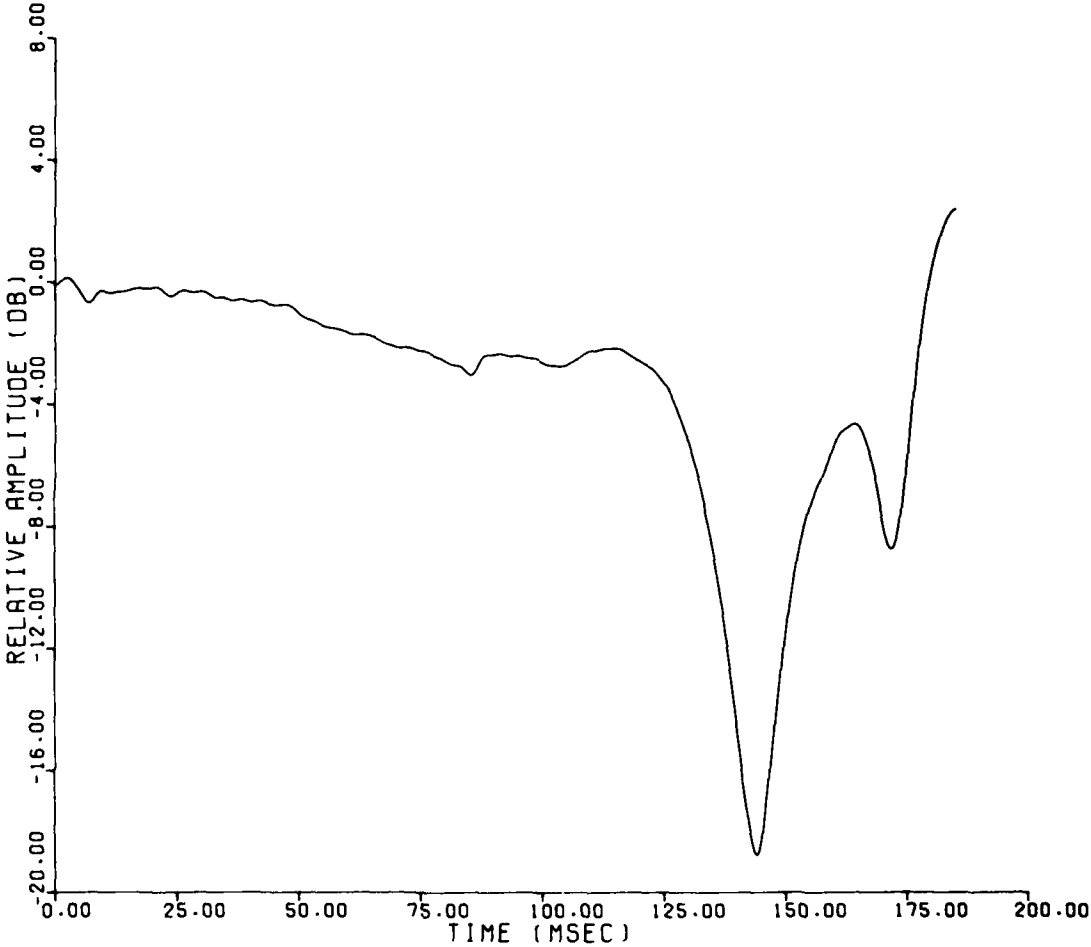


Figure 119. Test Chamber Pressurization Rate on Transient Burning Test 2TBT



**Figure 120. Change in Relative Amplitude Between the Test and Reference Signals on Transient Burning Test 2TBT**

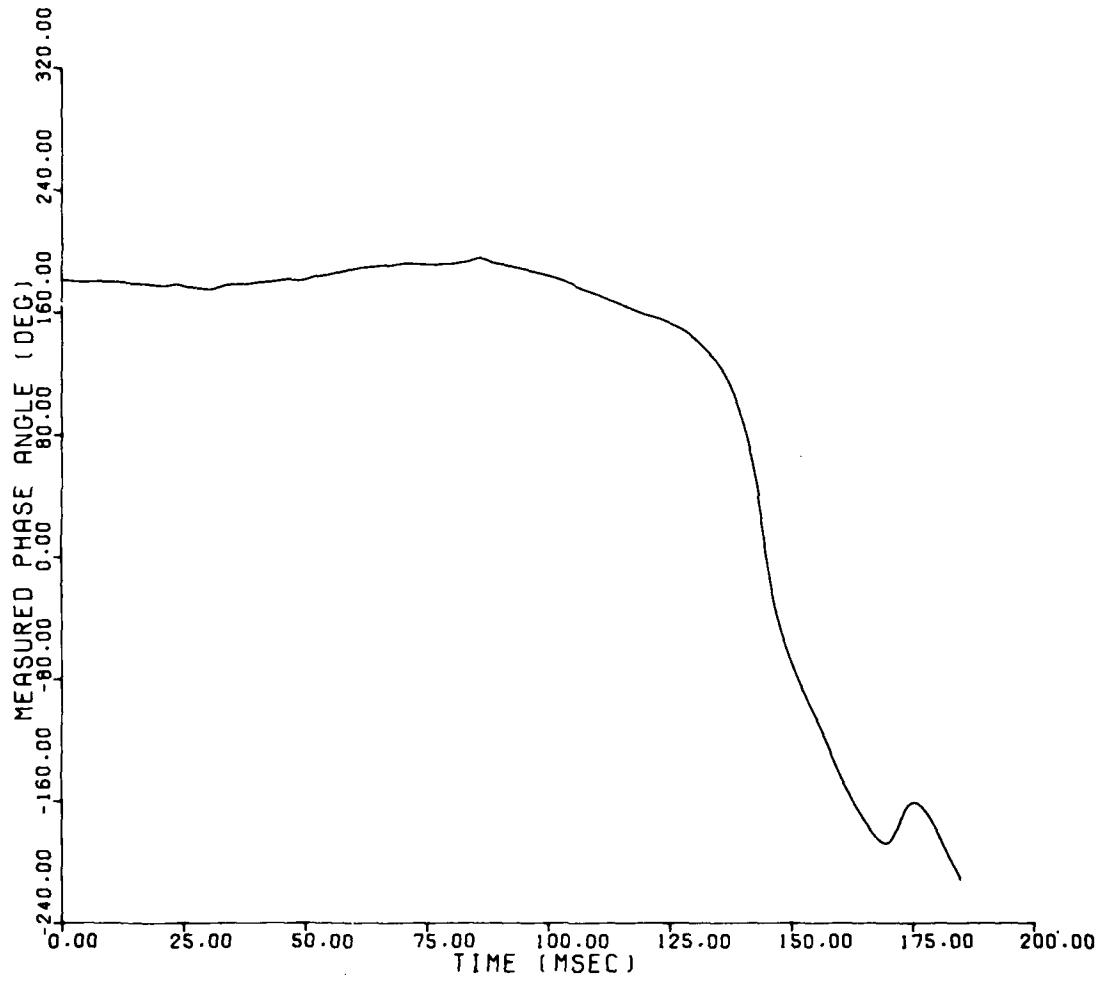


Figure 121. Measured Phase Angle on Transient Burning Test 2TBT

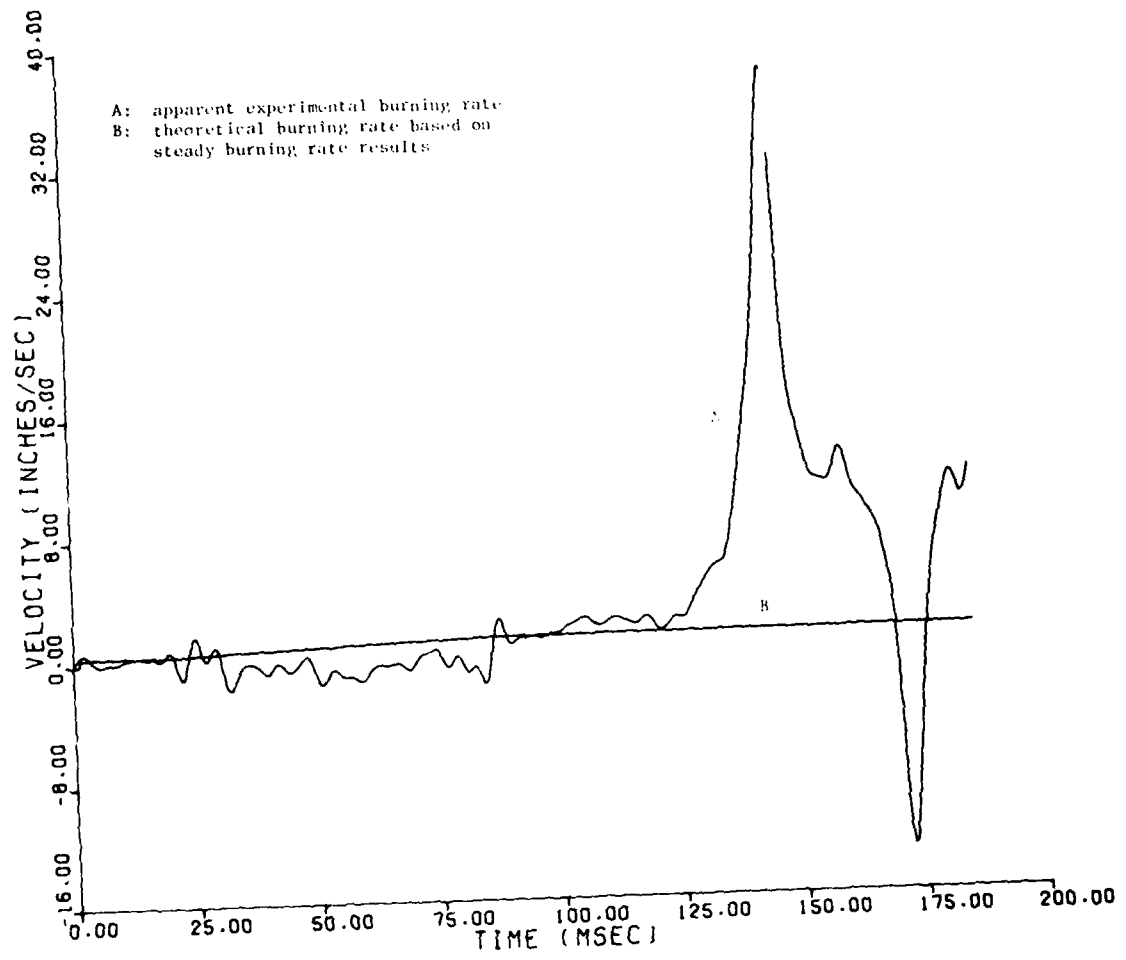


Figure 122. Theoretical and Apparent Experimental Burning Rates for Transient Burning Test 2TBT

APPENDIX B

**Table 1. Characteristics of Theoretical Pressurizations  
Used in Finite Element Analysis**

Relevant Figure Number	Init. Dr. Ch. Press. (psig)	Init. Test Ch. Press. (psig)	Flow Nzl. Throat Dia. (in.)	Max dp/dt (psi/sec)	Time of Max dp/dt (msec)
4,8	7500	1500	0.05	$1.22 \times 10^5$	32.0
5	7500	1500	0.15	$9.50 \times 10^5$	4.0
6	40000	1	0.15	$9.00 \times 10^6$	5.3
7	40000	20000	0.15	$18.30 \times 10^6$	0.8

**Table 2. Composition of M6 Propellant Used in Microwave Tests**

Constituent	Weight Percentage
nitrocellulose at 13.15% nitration	84.04
dinitrotoluene	11.10
dibutylphthalate	3.79
diphenylamine	1.07

**Table 3. Composition of Pyrotechnic Paste Used in Microwave Tests**

Constituent	Weight Percentage
Potassium perchlorate	72.3
Titanium	14.8
Boron	6.9
Polyisobutylene or Vistanex	6.0
Hexane	Sufficient amount to give the desired mixture viscosity

**Table 4. Relationships Among Inhibiting Techniques, Pressure, and Non-Planar Burning**

Steady-State Test Number	Initial Pressure (psig)	Occurrence of Significant Non-Planar Burning	Inhibiting Coating	Strand Config.
1	479	no	Hysol: EA-9309	A
2	680	no	Hysol: EA-9309	A
3	793	no	Hysol: EA-9309	A
4	3561	immediately upon propellant ignition	Hysol: EA-9309	A
5	3797	after about 0.7 in. of planar burning	Hysol: EA-9309	A
6	3999	no	Shell: Epon 815 & V40 curing agent	B
7	6460	immediately upon propellant ignition	Shell: Epon 815 & V40 curing agent	B
8	6349	no	Formvar solution	C
9	8772	no	Formvar solution	C
10	2295	immediately upon propellant ignition	Formvar solution	C
11	2283	after about 0.5 in. of planar burning	Formvar solution	C

A: The complete perimeter area of the strand was coated with epoxy as was the entire inside wall area of the waveguide. The strand was then pushed into the waveguide and the epoxy was allowed to cure to a nominal bond-line thickness of 0.005 in.

B: The epoxy was painted on the entire perimeter area of the propellant and permitted to cure. The cured coating was lightly sanded until its thickness just allowed the strand to fit within the waveguide.

The strand was then pushed into the waveguide to within 3/8 in. of the waveguide end after all but the last 3/8 in. of strand had been coated with a film of Dow Corning DC-4 silicone dielectric lubricant. A film of Hysol Epoxi-Patch was applied to the inside waveguide walls over the 3/8 in. length which would be closest to the dielectric transition window. The strand was then pushed the remaining distance into the waveguide and the small area of epoxy was permitted to cure, thus insuring the positional integrity of the strand during subsequent handling.

C: The propellant was dipped in the Formvar solution and allowed to dry; then the process was sequentially repeated until the coating thickness just allowed the strand to fit within the waveguide. (See second paragraph under item B for remaining procedures.)

The Formvar solution was comprised of 220 ml of toluene, 147 ml of ethanol, and 25 gm of polyvinylformal.

**Table 5. Digital Filter Parameters Applicable to All Discrete Data Acquired on a Given Steady-State Burning Test**

Steady-State Test Number	$f_1$ (Hz)	$f_2$ (Hz)	$f_s$ (Hz)	$\lambda_R$ (N.D.)	N (N.D.)
2	2	4	50	0.04	200
3	8	16	200	0.04	200
11	40	48	200	0.04	200
5	35	55	500	0.04	200
6	25	45	500	0.04	200
8	30	50	500	0.04	200
9	40	60	500	0.04	200

**Table 6. Digital Filter Parameters Applicable to All Discrete Data Acquired on a Given Dynamic Test**

Dynamic Test Number	$f_s$ (kHz)	$\lambda_R$ (N.D.)	N (N.D.)
1VT	10.0	0.010	200
4VT	10.0	0.010	200
5VT	10.0	0.010	200
6VT	10.0	0.010	200
7VT	10.0	0.010	200
8VT	20.0	0.010	200
9VT	33.0	0.012	200
10VT	10.0	0.010	200
11VT	33.3	0.012	200
12VT	33.3	0.012	200
1TBT	33.3	0.012	200
2TBT	10.0	0.010	200

VT = Vibration Test  
TBT = Transient Burning Test

Table 7. Experimentally Determined Microwave Parameters

Steady-State Test Number	Phase Wavelength for M6 - Filled Waveguide (in.)	Proportionality Constant, ( $\lambda_{pg}/720^\circ$ ) (in./deg)
1	1.202	$1.669 \times 10^{-3}$
2	1.103	$1.533 \times 10^{-3}$
3	1.157	$1.606 \times 10^{-3}$
8	1.240	$1.722 \times 10^{-3}$
9	1.178	$1.636 \times 10^{-3}$

Table 8. Attenuation Constants and Loss Tangents Based Upon Theory and the Total Change in Test Signal Amplitude

Steady-State Test Number	Test Signal Amp. Incr. (dB)	$\alpha_d$ (nepers/in.)	$\lambda_{pg}$ (in.)	$\mu$ (nepers/rad)	$\tan \delta$ (N.D.)
1	N.A.	N.A.	1.202	N.A.	N.A.
2	24.32	0.3500	1.103	-0.0614	0.0414
3	18.95	0.2727	1.157	-0.0502	0.0323
4	17.29	0.2489	(1.176)	-0.0466	0.0294
5	17.87	0.2572	(1.176)	-0.0481	0.0304
6	19.80	0.2849	(1.176)	-0.0533	0.0337
7	22.50	0.3238	(1.176)	-0.0606	0.0383
8	13.50	0.1943	1.240	-0.0383	0.0230
9	17.09	0.2459	1.178	-0.0461	0.0291
10	20.00	0.2878	(1.176)	-0.0539	0.0340
11	21.40	0.3080	(1.176)	-0.0576	0.0364

(1.176) = mean wavelength based on tests 1, 2, 3, 8, and 9.

Table 9. Constants from Optimization Solutions

Steady-State Test Number	$\mu$ (nepers/rad)	$B_o$ (mV)	A (mV)	$\alpha$ (rad)
2	-0.061875	34.373	15.941	0.289941
3	-0.053109	13.399	1.497	0.957626
11	-0.057884	39.750	2.000	3.621250
5	-0.048880	18.517	12.488	5.399102
6	-0.051250	53.500	34.500	1.866250
8	-0.049000	27.500	13.250	4.773185
9	-0.047000	34.375	14.750	0.340625

Table 10. Comparison of Mean Steady-State Burning Rates and Standard Deviations for Raw, Filtered, and Theoretically Adjusted Data

Steady-State Test Number	No. of Inst. Burning Rates	raw data		filtered data		theor. adj. data	
		r (in./sec)	$\sigma$ (in./sec)	r (in./sec)	$\sigma$ (in./sec)	r (in./sec)	$\sigma$ (in./sec)
1	N.A.	0.172	N.A.	N.A.	N.A.	N.A.	N.A.
2	687	0.235	0.073	0.235	0.067	0.229	0.017
3	1884	0.257	0.048	0.256	0.041	0.255	0.030
11	180	0.529	0.067	0.530	0.068	0.535	0.057
5	360	0.848	0.654	0.848	0.652	0.844	0.121
6	1476	0.790	0.399	0.790	0.397	0.843	0.139
8	1531	1.194	0.299	1.193	0.290	1.196	0.143
9	1118	1.470	0.507	1.470	0.504	1.437	0.168

Table 11. Summary of Results for Steady-State Burning Tests

Steady-State Test Number	No. of Inst. Burning Rates	Sampling Frequency (Hz)	Digital Lowpass Cutoff Frequency (Hz)	Initial Pressure (psig)	Final Pressure (psig)	Average Pressure (psig)	Mean of Inst. Burning Rates (in./sec)	S. Dev. of Inst. Burning Rates (in./sec)
1	N.A.	N.A.	N.A.	479	559	519	0.172	N.A.
2	687	50	2	680	772	730	0.229	0.017
3	1884	200	8	793	869	831	0.255	0.030
11	180	200	40	2283	2347	2315	0.535	0.057
5	360	500	35	3797	3919	3858	0.844	0.121
6	1476	500	25	3999	4299	4149	0.843	0.139
3	1531	500	30	6349	7127	6738	1.196	0.143
9	1118	500	40	8772	9730	9251	1.437	0.168

Table 12. Propellant Ignition Delays

Steady-State Test Number	Delay Between Hot Wire Initiation and Onset of Clearly Defined M6 Combustion (msec)
2	40
3	50
11	20
5	30
6	30
8	20
9	40

Table 13. Physical Circumstances for Dynamic Tests

Dynamic Test No.	Pressurization Rate, Qualitative	Test Geometry and Strand Configuration per Table 4
1VT	Slow	Twin strand differential; Type A
4VT	Slow	Dielectric transition window only
5VT	Slow	Dielectric transition window only
6VT	Slow	Twin strand differential; Type C
7VT	Slow	Twin strand differential; Type C
8VT	Fast	Twin strand differential; Type C
9VT	Fast	Twin strand differential; Type C
10VT	Slow	Single strand vs fixed ref.; Type C
11VT	Fast	Single strand vs fixed ref.; Type C
12VT	Fast	Dielectric transition window only
1TBT	Fast	Twin strand differential; Type C
2TBT	Slow	Twin strand differential; Type C

VT = Vibration Test

TBT = Transient Burning Test

Table 14. Pressurization Rate Parameters for Dynamic Tests

Dynamic Test Number	Flow Nzl. Throat Diameter (in.)	Initial Driver Ch. Pressure (psig)	Initial Test Ch. Pressure (psig)
1VT	0.05	6565	1514
4VT	0.05	7185	985
5VT	0.05	7218	1376
6VT	0.05	7127	1504
7VT	0.05	7207	1539
8VT	0.15	7295	1385
9VT	0.15	7370	1620
10VT	0.05	7383	1407
11VT	0.15	7577	1576
12VT	0.15	7380	1452
1TBT	0.15	7385	1660
2TBT	0.05	7290	1656

VT = Vibration Test

TBT = Transient Burning Test

Table 15. Digital Lowpass Cutoff Frequencies for Physical Quantities Relevant to Dynamic Tests

Dynamic Test Number	Digital Lowpass Cutoff Frequencies (Hz)				
	$\psi_m$	$p_2$	$A_{rel}$	$\psi_{th}$	$\psi_{sum}$
1VT	250	250	250	250	250
4VT	150	250	250	250	250
5VT	250	250	250	250	250
6VT	250	250	250	250	250
7VT	150	250	250	250	250
8VT	1500	1250	1500	1500	1500
9VT	1500	1250	1500	1500	1500
10VT	250	300	300	300	300
11VT	1000	1250	1500	1500	1500
12VT	500	1250	1500	1500	1500
1TBT	1250	1250	1250	N.A.	N.A.
2TBT	200	250	250	N.A.	N.A.

VT = Vibration Test

TBT = Transient Burning Test

APPENDIX C

GAS DYNAMIC MODEL

## GAS DYNAMIC MODEL

The simple gas dynamic model utilized in designing the combustion fixture is outlined below. Note that subscript "one" refers to the driver chamber and subscript "two" indicates the test chamber. The Heaviside unit function,  $H(z)$ , is used to write the governing equations so that they apply to flow both from and into the driver chamber. Also,  $H(z)$  is used in the consideration of the propellant ignition time and the time of flow onset from a chamber. The basic assumptions used in the model development are as follows:

1. The driver chamber is of constant volume
2. No heat loss occurs in either chamber or in the flow nozzle
3. Negligible velocities exist in both chambers
4. The propellant burns planarly within the waveguide in the test chamber
5. Two nonreacting gas species are present, nitrogen gas and propellant combustion products
6. Thermodynamic gas mixture properties are based upon mass averages
7. The Nobel-Abel equation of state is applicable in both chambers

The governing equations in the gas dynamic model are as follows:

conservation of mass:

$$\frac{d(m_1)}{dt} = WH(t - t_{FL})[H(p_2 - p_1) - H(p_1 - p_2)] \quad (C-1)$$

$$\frac{d(m_2)}{dt} = WH(t - t_{FL})[H(p_1 - p_2) - H(p_2 - p_1)] + \dot{m}_p H(t - t_{IG}) \quad (C-2)$$

conservation of energy:

$$\frac{d(m_1 e_1)}{dt} = WH(t - t_{FL})[h_2 H(p_2 - p_1) - h_1 H(p_1 - p_2)] \quad (C-3)$$

$$\frac{d(m_2 e_2)}{dt} = WH(t - t_{FL})[h_1 H(p_1 - p_2) - h_2 H(p_2 - p_1)] + \dot{m}_p E H(t - t_{IG}) \quad (C-4)$$

conservation of species mass:

$$\frac{d(m_{1,N_2})}{dt} = WH(t - t_{FL})[x_{2,N_2} H(p_2 - p_1) - x_{1,N_2} H(p_1 - p_2)] \quad (C-5)$$

$$\frac{d(m_{1,p})}{dt} = WH(t - t_{IG}) H(t - t_{FL})[x_{2,p} H(p_2 - p_1) - x_{1,p} H(p_1 - p_2)] \quad (C-6)$$

$$\frac{d(m_{2,N_2})}{dt} = WH(t - t_{FL})[x_{1,N_2} H(p_1 - p_2) - x_{2,N_2} H(p_2 - p_1)] \quad (C-7)$$

$$\frac{d(m_{2,p})}{dt} = \dot{m}_p H(t - t_{IG}) - WH(t - t_{IG})H(t - t_{FL}) [x_{2,p}H(p_2 - p_1) - x_{1,p}H(p_1 - p_2)] \quad (C-8)$$

test chamber volume change:

$$\frac{d(V_2)}{dt} = rA_p H(t - t_{IG}) \quad (C-9)$$

test propellant strand length change:

$$\frac{d(\ell_T)}{dt} = rH(t - t_{IG}) \quad (C-10)$$

In the above equations, the term  $W$  represents the mass rate of flow through the flow nozzle from either direction; it is always considered a positive quantity.

In the auxiliary equations given below, the index  $i$  can take on values 1 or 2 in order to identify parameters relevant to the driver and test chambers, respectively.

$$m_i = \rho_i V_i = m_{i,p} + m_{i,N_2} \quad (C-11)$$

$$e_i = \int_{T_{\text{ref}}}^{T_i} c_{v_i} dT \quad (\text{C-12})$$

$$x_{i,N_2} = \frac{m_{i,N_2}}{m_i} \quad (\text{C-13})$$

$$x_{i,p} = \frac{m_{i,p}}{m_i} \quad (\text{C-14})$$

$$c_{v_i} = x_{i,N_2} c_{v_{N_2}} + x_{i,p} c_{v_p} \quad (\text{C-15})$$

$$\bar{R}_i = x_{i,N_2} \bar{R}_{N_2} + x_{i,p} \bar{R}_p \quad (\text{C-16})$$

$$c_{v_{N_2}} = f_{N_2}(T) \quad (\text{C-17})$$

$$c_{v_p} = f_p(T) \quad (\text{C-18})$$

$$c_{p_i} = c_{v_i} + \bar{R}_i \quad (\text{C-19})$$

$$\gamma_i = \frac{c_{p_i}}{c_{v_i}} \quad (\text{C-20})$$

$$p_i = \frac{\bar{R}_i T_i}{\frac{1}{\rho_i} - \eta_o} \quad (\text{C-21})$$

$$E = \frac{nRT_0}{\gamma_0 - 1} = \frac{K_F}{\gamma_0 - 1} \quad (C-22)$$

$$h_i = e_i + \frac{p_i}{\rho_i} \quad (C-23)$$

$$r = Bp_2^2 \quad (C-24)$$

$$\dot{m}_p = rA_p \rho_p \quad (C-25)$$

In equation (C-22),  $nRT_0$  is equal to the "force" or the "force constant" of the propellant and  $E$  is equal effectively to the total energy available from a unit mass of propellant.<sup>(13)</sup> For M6 propellant the respective values of  $E$ ,  $\rho_p$ , and  $\eta_0$  are  $3.804 \times 10^6$  in.-lb/ibm,  $0.0571$  lbm/in.<sup>3</sup>, and  $29.92$  in.<sup>3</sup>/lbm.<sup>(14)</sup> For the temperature range of 540 to 9000°R, the constant volume specific heat for diatomic nitrogen was computed from published information.<sup>(15)</sup>

To determine properties relevant to propellant combustion products, a simple computer model was constructed for determining the thermodynamic properties of an equilibrium mixture of gases. The following species were assumed to be present in the combustion products: CO, CO<sub>2</sub>, H<sub>2</sub>O, OH, H, N<sub>2</sub>, NO, O<sub>2</sub>, O, N, and H<sub>2</sub>. For each species, a determination was made of the number of moles, mole fraction, mass, and mass fraction. The technique utilized in computing these quantities required the solution of eleven nonlinear, simultaneous algebraic equations and was highly analogous to the approach presented by Hill and Peterson.<sup>(16)</sup> Four equations resulted from the requirement of conservation of mass for each of the

elements carbon, nitrogen, oxygen, and hydrogen. The other seven required relations were based upon the seven independent equilibrium reactions which were selected for use in the calculation scheme. The temperature dependent equilibrium constants associated with these particular chemical reactions were taken from a tabulation by Hunt.<sup>(17)</sup> Specific heat data for the eleven gas species were taken from a NASA publication.<sup>(18)</sup> The mixture properties were based upon mass averages and were calculated for a variety of temperature and pressure combinations. At each thermodynamic state, the calculated mixture properties were the molecular weight, gas constant, constant pressure and constant volume specific heats, and the ratio of specific heats.

For the combustion products of M6 propellant at 500 atmospheres, the model yielded data which allowed the temperature dependent constant volume specific heat to be represented as

$$c_{v_p} = 0.26694 + 0.34656 \times 10^{-4}T - 0.33733 \times 10^{-8}T^2 \quad (C-26)$$

where  $T$  can range from 540 to 5400°R and  $c_{v_p}$  is in units of (BTU/lbm - °R). At the isochoric adiabatic flame temperature for M6 propellant ( $T_o = 4626^\circ\text{R}$ ), the model predicted a value for  $\gamma_o$  equal to 1.247. As based upon predictions from the equilibrium model, the average gas constant for the M6 propellant gases was 815.19 in.-lbf/lbm - °R.

In calculating the mass rate of flow through the nozzle, the expressions used for  $W$  were based upon derivations which required the use of the perfect gas law. This was done to preserve the simplicity of the model even though it does introduce an inconsistency since the Noble-Able equation of state is presumed to apply in the test and driver chambers. For the situation of non-choked flow, the relation utilized for  $W$  was

$$W = C_d Y \frac{A_t}{[1 - (d_t/D_h)^4]^{1/2}} [2 g_c \rho_h (p_h - p_q)]^{1/2} \quad (C-27)$$

where the expansion factor is given by

$$Y = \left[ r^{\frac{2}{\gamma}} \left( \frac{\gamma}{\gamma - 1} \right) \left( \frac{1 - r^{\frac{\gamma-1}{\gamma}}}{1 - r} \right) \left( \frac{1 - (d_t/D_h)^4}{1 - (d_t/D_h)^4 r^{\frac{2}{\gamma}}} \right) \right]^{1/2} \quad (C-28)$$

Equation (C-27) is the theoretical adiabatic relation for the mass rate of flow of an ideal compressible fluid across section  $A_t$ , but modified by a discharge coefficient.<sup>(19)</sup> Note that the subscripts "h" and "q" refer to the high and low pressure sides of the nozzle. In the non-choked situation,  $r = p_q/p_h$  is greater than the critical pressure ratio,  $r_{crit}$ . For choked or critical flow,  $r \leq r_{crit}$  and the expression used for calculating  $W$  was

$$W = C_d A_t \left[ 2 g_c p_h \rho_h r_{crit}^{\frac{2}{\gamma}} \left( \frac{\gamma}{\gamma - 1} \right) \left( 1 - r_{crit}^{\frac{\gamma-1}{\gamma}} \right) \right]^{1/2} \quad (C-29)$$

This equation, without the modifying discharge coefficient, yields the maximum theoretical mass rate of flow for the one-dimensional, steady, isentropic flow of a perfect gas.<sup>(20)</sup> When applying equations (C-27) and (C-29), the specific heat ratio is taken to be the value of  $\gamma$  relevant to the higher pressure chamber.

The actual flow nozzle was assumed to be comprised of a frictionless converging nozzle feeding a long duct of constant cross section where wall friction was important. In order to maintain the computationally simple aspects of the gas dynamic model, the practical effect of this friction was accounted for by reducing

the critical pressure ratio from the isentropic flow value and by slightly reducing the discharge coefficient from its typical value of 0.98 for nozzle.<sup>(21,22)</sup> Hence, for combustion fixture design purposes,  $r_{crit}$  was considered 0.49 and  $C_d$  was set at 0.93.

The fourth-order Runge-Kutta technique<sup>(23)</sup> was used to solve the ten simultaneous first-order ordinary differential equations which comprise the governing equations of the gas dynamic model. The transient solution began from a set of initial conditions for the dependent variables and continued until the end of a prescribed time interval. The immediate output of the transient solution was the time dependent values of the dependent variables; i.e., those quantities which appear in parentheses on the left-hand-side of equations (C-1) through (C-10). Further reduction to other parameters of interest was accomplished by the use of auxiliary equations (C-11) through (C-25). By invoking equation (5) in the Theoretical Model section, it was possible to construct another auxiliary expression which related the instantaneous length of the burning test propellant strand to the instantaneous actual phase angle change. This very useful relationship is given by

$$(\psi_{a,i} - \psi_a) = 2\beta_p(\ell_0 - \ell_T) \quad (C-30)$$

where  $\psi_{a,i}$  is the initial value of the actual phase angle.

APPENDIX D

FINITE ELEMENT ANALYSIS

## FINITE ELEMENT ANALYSIS

Presented in Figure 3 is a schematic of the structural idealization used to represent the dielectric material comprised of a single propellant strand in a waveguide and a contiguous section of the casting resin which filled the blind rectangular holes in the dielectric transition window. The total length of the combination of a virgin propellant strand (length 4.000 in.) and the mating section of casting resin (length 1.066 in.) was 5.066 in. This total length was divided into 50 segments. Hence, between interconnection nodes 1 through 51 there were 50 springs each having a spring constant given by  $EA/h = k_1$ . It was assumed that the casting resin had an elastic modulus and a Poisson's ratio which were equal to that of the propellant. In constructing the schematic of Figure 3, it was assumed that epoxy bonded the entire perimeter area of both the propellant strand and the casting resin section to the surrounding waveguide sidewalls. Thus, interconnection nodes 52 through 101 were fixed in space and connected by springs to moveable nodes 1 through 50. This aspect of the structural idealization was intended to simulate the restraining effect of the epoxy bond between the waveguide walls and the dielectric material. The technique by which the spring constant  $k_2$  was quantified is outlined below.

The cross sections of a propellant strand and a casting resin section were identical and rectangular. However, in order to keep the input to the finite element model computationally simple and to slant the analysis toward a less stiff system (i.e., a more conservative system), the cross sectional areas were considered circular and were constrained to have the same area as the rectangular waveguide cross sections. Spring constant  $k_2$  was determined by applying circular flat plate theory relevant to deflections small in comparison to plate thickness.

If a material obeys Hooke's law, the shearing stress  $\tau$  and shearing strain  $\gamma$  are related by<sup>(24)</sup>

$$\gamma = \frac{\tau}{G} \quad (D-1)$$

where  $G$  is the shear modulus,  $G = E/2(1 + \nu)$ . For small shearing strains, the following approximation can be written

$$\tan \gamma = \frac{dw}{dr} \cong \gamma = \frac{\tau}{G} \quad (D-2)$$

Define a spring constant given by

$$\bar{k} = \frac{(f_s)_{r=R_0}}{\bar{w}} \quad (D-3)$$

where  $(f_s)_{r=R_0}$  is the shear force at the edge of a circular flat plate of thickness  $h$  and radius  $R_0$ ;  $\bar{w}$  is the mean deflection. This mean deflection can be expressed as

$$\bar{w} = \frac{\int_A w \, dA}{\pi R_0^2} = \frac{2}{R_0^2} \int_0^{R_0} w \, r \, dr \quad (D-4)$$

By the use of equations (D-1) and (D-2) the following relation can be written

$$(f_s)_{r=R_0} = 2\pi R_0 h G \left( \frac{dw}{dr} \right)_{r=R_0} \quad (D-5)$$

The spring constant of equation (D-3) can now be expressed as

$$\bar{k} = \pi G h R_o \left[ \frac{\left( \frac{dw}{dr} \right)_{r=R_o}}{\int_0^{R_o} w r dr} \right] \quad (D-6)$$

where  $w$  represents the local deflection of the circular flat plate of thickness  $h$ . Assume that the plate is simply supported along its outer edge and that it is subjected to a load per unit area,  $q$ , distributed uniformly over its area. The expression<sup>(25)</sup> for the local deflection of such a plate is

$$w = \frac{q}{64D} (R_o^2 - r^2) \left( \frac{5+\nu}{1+\nu} R_o^2 - r^2 \right) + \frac{q h^2}{8D} \frac{(3+\nu)}{(1-\nu^2)} (R_o^2 - r^2) \quad (D-7)$$

where  $\nu$  is Poisson's ratio and  $D$  is the flexural rigidity given by  $D = E h^3 / 12(1 - \nu^2)$ . The second term on the right-hand-side of equation (D-7) represents the correction for shearing stresses and lateral pressure.

Substitution of equation (D-7) into equation (D-6) and subsequent evaluation of the resulting expression yields a spring constant. Assume that this spring constant can be used to represent the spring constant  $k_2$  shown in Figure 3. To compute the value of  $k_2$  relevant to a given plate material, values for  $E$ ,  $h$ ,  $\nu$ , and  $R_o$  are required. The elastic modulus for M6 propellant is 114,000 psi.<sup>(26)</sup> It was assumed that a Poisson's ratio of 0.45 was applicable to M6 propellant. The cross sectional area of the rectangular waveguide housing the dielectric material was 0.1186 in.<sup>2</sup>; hence, the radius of a circular cross section having the same area is 0.1943 in. Since the dielectric material was divided into 50 segments, the value for  $h$  was 0.10132 in. Based upon the above parameter values,  $k_2$  was computed to be  $3.6693 \times 10^5$  lbf/in.

The transient response analysis for the structural idealization of Figure 3 was achieved via use of a finite element model.<sup>(27)</sup> The time dependent loading was considered to be applied to the first interconnection node. In the model, initial conditions are specified with respect to an initial equilibrium configuration. Attention was focused on that output of the numerical solution which yielded the displacement, stress, and velocity of the first interconnection node. Although the model allows damping, no damping was considered because of the difficulty in quantitatively defining the mass proportional and/or stiffness proportional damping constants relevant to the structural idealization. Hence, only undamped transient numerical solutions were analyzed.

APPENDIX E

PHASE ANGLE DERIVATIVE RELATIONSHIPS

### PHASE ANGLE DERIVATIVE RELATIONSHIPS

After noting that  $A$ ,  $\alpha$ ,  $B_0$ , and  $\mu$  are constants while  $\psi_a$ ,  $\psi_m$ , and  $C$  are functions of time, take the time derivative of equation (16). Multiply the result by  $e^{-i\psi_a}$  and then equate the real and imaginary parts to get

$$\mu \dot{\psi}_a B_0 e^{\mu \psi_a} + C \dot{\psi}_m \sin(\psi_m - \psi_a) = \dot{C} \cos(\psi_m - \psi_a) \quad (\text{E-1})$$

$$\dot{\psi}_a B_0 e^{\mu \psi_a} - C \dot{\psi}_m \cos(\psi_m - \psi_a) = \dot{C} \sin(\psi_m - \psi_a) \quad (\text{E-2})$$

Dividing equation (E-2) by equation (E-1) and then multiplying each side of the resulting equation by  $\cos(\psi_m - \psi_a)$  yields

$$\dot{\psi}_a [B_0 e^{\mu \psi_a} \cos(\psi_m - \psi_a) - \mu B_0 e^{\mu \psi_a} \sin(\psi_m - \psi_a)] = C \dot{\psi}_m \quad (\text{E-3})$$

If after squaring equations (13) and (14) they are added together, the resulting expression becomes

$$B_0 e^{\mu \psi_a} \cos(\psi_m - \psi_a) = C - A \cos(\psi_m - \alpha) \quad (\text{E-4})$$

By eliminating  $C$  from equations (13-15), the following result can be written:

$$B_o e^{\mu \psi_a} \sin(\psi_m - \psi_a) = -A \sin(\psi_m - \alpha) \quad (\text{E-5})$$

Substituting equations (E-4) and (E-5) into equation (E-3) gives the desired result:

$$\dot{\psi}_a = \frac{\dot{\psi}_m}{1 - \frac{A}{C} \cos(\psi_m - \alpha) + \frac{\mu A}{C} \sin(\psi_m - \alpha)} \quad (\text{E-6})$$

APPENDIX F  
EQUIPMENT LIST

## EQUIPMENT LIST

In the following five lists the equipment relevant to the microwave experiments is identified.

A. Electronic components and signal conditioning devices as identified in Figure 13:

1. Sweep Oscillator (microwave source), Alfred Electronics, Model 650 main frame with Model 655AK oscillator plug-in.
2. Synchronizer, Frequency Engineering Laboratories, Model FEL 133A.
3. RF Power Meter, (monitor of microwave source output power), Hewlett-Packard, Model 431B.
4. Digital Frequency Meter (10 Hz resolution), Hewlett-Packard, Model 5248M main frame electronic counter with Model 5255A plug-in frequency converter.
5. Microwave Amplifier (TWT), Hewlett-Packard, Model 495A.
6. Harmonic Frequency Converter, Hewlett-Packard, Model 8411A.
7. Network Analyzer, Hewlett-Packard, Model 8410A.
8. Relative Gain Indicator, Hewlett-Packard, Model 8413A.
9. Amplifier (20 dB), Hewlett-Packard, Model 465A.

10. Filter (passive highpass on the 278 kHz test signal entering the phasemeter), in-house construction.
11. Phasemeter, Dranetz Engineering Laboratories, Inc.; Model 305C, option 103, Serial No. 5010958405; with Plug-in Model 305-PA-3002, Serial No. 4121407005.
12. Filter-Amplifier (16 lowpass settings), in-house construction.
13. A/D Data Acquisition System, in house construction.
  - a. Memory: three channels each with storage capability of 2048 12-bit words and one channel with storage capability of 2048 12 or 16-bit words; memory construction from 1024 word by one bit static random access memory elements; these Model 2102 RAM's were manufactured by Fairchild Semiconductor.
  - b. 12-bit channels: sample-and-hold amplifiers, Analog Devices, model SHA-5; A/D converter, Analog Devices, Model ADC12QU.
  - c. 15-bit channel: complete A/D conversion subsystem, Phoenix Data Inc., Model No. DAS 7215-001-04-02-1, Serial No. A6884.
14. Piezoelectric Quartz Pressure Transducers (two items), Kristal Instrument Corporation, Model 6202 with a thermoprotective plate impregnated with low viscosity oil.
15. Charge Amplifiers (two items), Kistler Instrument Corp., Model 503

16. Strip Chart Recorder, Techni-rite Electronics, Inc., Model TR-888 main frame with 4 Model TSC-810 signal conditioning plug-ins.
  17. Time Delay Sequencer, in-house construction.
  18. Capacitive Discharge Circuit, in-house construction.
  19. Audio Cassette Interface, in-house construction.
  20. Audio Cassette Tape Recorder, Superscope, Model CD-302A.
- B. Microwave circuitry components as shown in Figure 13; coaxial components have type N connectors while all other components have X-band waveguide flanges:
1. Ferrite Isolators, 9 items, Systron-Donner, Model DBG-480A.
  2. 3 dB Directional Couplers, 3 items, Systron-Donner, Model DBG-675-3 (2 items used in the reversed mode).
  3. Coaxial Hybrid Junction (used to equally divide the input power into two transmission lines), 1 item, Narda Microwave Corporation, Model 3035.
  4. 10 dB Directional Couplers, 3 items, Systron-Donner, Model DBG-675-10.
  5. 20 dB Coaxial Directional Coupler, 1 item, Narda Microwave Corporation, Model 3045C-20.
  6. 3 Port Circulator, 2 items, Systron-Donner, Model DBG-490.

7. Variable Attenuators (used in the main arms), 2 items, Systron-Donner, Model DBG-430.
  8. Variable Attenuators (used in cancellation loops), 2 items, Arra Inc., Model X520-40A.
  9. Variable Phase Shifter (used in main test arm), 1 item, Hewlett-Packard, Model X885A.
  10. Variable Phase Shifters (used in cancellation loops), 2 items, Systron-Donner, Model DBG-915-1.
  11. E-H Tuners. 2 items, Waveline Inc., Model 659.
- C. Electronic equipment not specifically shown in Figure 13 but still utilized during the performance of a test:
1. Digital Power Meter (used to check input power to the Harmonic Frequency Converter), Pacific Measurements, Model 1018A.
  2. RMS Voltmeter (used for noise measurements and to check initial test signal voltage amplitude to the phasemeter), Hewlett-Packard, Model 3400A.
  3. Oscilloscope (used for general trouble-shooting and noise measurements), Tektronix, Model 545A with Model 1A7A high-gain differential amplifier plug-in.
  4. Precision Voltage Source, in-house construction.
  5. Digital Multimeter, Hewlett-Packard, Model 3465A.

6. Digital Voltmeter, Hewlett-Packard, Model 3460B.

D. Major components of the pressurizing system shown in Figure 20:

1. Gas Booster Pump (up to 40,000 psi), American Instrument Company, Model 46-13475.
2. Pneumatically Operated Valves (three items), American Instrument Company, Model 44-19731.
3. Check Valves (two items), American Instrument Company, Model 44-16380.
4. Dial Pressure Gages (three items; used for monitoring pressure in booster pump and in combustion fixture chambers; Bourdon type), American Instrument Company, Model 47-18350.
5. Pressure Regulator, Victor Equipment Company, Model SR-200C.

E. Combustion fixture sealing components relevant to Figures 18 and 19:

1. Self-Sealing Electrical Feedthroughs (two items), American Instrument Company, Model 45-17582.
2. Rupture Disc Assembly (thrust nut was greatly modified before use), American Instrument Company,
  - a. Thrust nut, Model 1636-147-1
  - b. Thrust collar, Model 1620-090

c. Rupture disks (at a variety of failure pressures), Model 45-19290-1

3. Major End Cap Face Seals

a. Resilient metal c-seals (two items) Pressure Science Inc., Model 615A5X-0088-1.

b. Elastomeric back-up seals (two items), Parker Seal Company, Model 2-(362)N674-70.

4. Flow Nozzle Face Seal (elastomeric), Parker Seal Company, Model 2-(224)N674-70.

5. Explosive Valve Face Seal (resilient metal c-seal), Pressure Science Inc., Model 614A51-0050-1.

6. Dielectric Transition Window Face Seals

a. Larger resilient metal c-seal, Pressure Science Inc., Model 614A5X-0044-1.

b. Smaller resilient metal c-seal, Pressure Science Inc., Model 633A51-0025-1.

APPENDIX G  
DIGITAL SIGNAL ANALYSIS

## DIGITAL SIGNAL ANALYSIS

Digital signal analysis was performed on all data acquired by the A/D system. The purpose of this analysis was to eliminate unwanted high frequencies which carried little or no information and to produce an output set with highly reduced noise. The first operation done on a given discrete sample set was the computation of the spectrum which yielded the distributions over frequency of both the amplitude and the energy. To calculate these distributions, the fast Fourier transform (FFT) was utilized. This transformation is a very efficient algorithm for computing the *finite discrete Fourier transform (DFT)*.<sup>(38-40)</sup> For the FFT algorithm used with the experimental data, the number of samples which could be operated upon was constrained to be an integer power of 2.

Of course, the experimental data of interest did not always have precisely  $2^m$  samples in a set. However, the actual number of data samples in a time interval of interest was always just slightly more or somewhat less than a particular  $2^m$  value. Hence, for each physical quantity being analyzed, the most appropriate  $2^m$  number of discrete values was operated upon by the FFT algorithm. The resulting distortion in the spectral information was slight and did not compromise the judgment of where an acceptable digital lowpass cutoff frequency could be established for a given transient signal. It should be noted that all spectral analysis was done upon physically dimensioned discrete data which had been amplitude translated such that amplitude changes began from zero values.

The Fourier transform of any real function  $f(t)$  is

$$F(j\omega) = \int_{-\infty}^{\infty} f(t)e^{-j\omega t} dt \quad (G-1)$$

The DFT, denoted  $\bar{F}(j\omega)$ , can be defined using the zero-order approximation to  $F(j\omega)$ ; that is,

$$\bar{F}(j\omega) = \sum_{n=-\infty}^{\infty} f(nT)e^{-j\omega nT} \quad (\text{G-2})$$

where  $T$  is the sampling interval and also the interval of integration in the time domain. An alternate way of describing the evolution of the DFT is to note that the zero order approximation of  $F(j\omega)$  divided by  $T$  equals  $\bar{F}(j\omega)$ . Consequently,

$$T\bar{F}(j\omega) \cong F(j\omega) \quad (\text{G-3})$$

Any actual computation of the DFT must involve a finite summation of terms; hence, suppose there are  $N$  samples of  $f(t)$ . The DFT is periodic over  $\omega$  with period  $2\pi/T$ . Hence, by letting

$$\omega = \frac{2\pi m}{NT}; m = 0, 1, \dots, N-1 \quad (\text{G-4})$$

the usual formula for computing the independent values of the DFT becomes

$$F_m = F\left(j\frac{2\pi m}{NT}\right) = \sum_{n=0}^{N-1} f_n e^{-j(2\pi m n/N)}; m = 0, 1, \dots, N-1 \quad (\text{G-5})$$

where  $f(nT)$  has been written as  $f_n$ . Actually, only the values of  $\bar{F}_m$  for  $m = 0$  to  $N/2$  really need to be computed.

For each transient data signal, approximations were determined for  $|F(j\omega)|$  and  $|F(j\omega)|^2$ , the Fourier amplitude and energy spectrums, respectively. These approximations were  $T|\bar{F}(j\omega)|$  and  $T^2|\bar{F}(j\omega)|^2$ ; they required the computation of the DFT of a given sample set  $[f_n]$  acquired from the A/D system. It was, of course, assumed that the sampling interval  $T$  had been chosen so that essentially all of the spectral content of the waveform was contained below  $1/2T$  Hz, the Nyquist or folding frequency. The DFT amplitude was found from the quadrature of the real and imaginary parts; i.e.,

$$|\bar{F}_m| = \left( \left| \sum_{n=0}^{N-1} f_n \cos \frac{2\pi mn}{N} \right|^2 + \left| \sum_{n=0}^{N-1} f_n \sin \frac{2\pi mn}{N} \right|^2 \right)^{1/2} \quad (G-6)$$

where  $m$  needed only to vary from 0 to  $N/2$ .

Instead of utilizing  $T|\bar{F}(j\omega)|$  or  $T^2|\bar{F}(j\omega)|^2$  directly, two hybrid expressions were constructed and plotted as a function of frequency; the frequency range was  $\nu = 0$  to  $1/2T$  and the increment was  $\Delta\nu = 1/NT$ . The expressions for relative amplitude and accumulative energy are

$$A_m = 20 \log_{10} \left( \frac{|\bar{F}_m|}{|\bar{F}_{m \max}|} \right); \quad m = 0, 1, \dots, \frac{N}{2} \quad (G-7)$$

$$E_m = \frac{\sum_{m=0}^m |\bar{F}_m|^2}{\sum_{m=0}^{m=N/2} |\bar{F}_m|^2}; \quad m = 0, 1, \dots, \frac{N}{2} \quad (G-8)$$

In equation (G-7), the term  $|\bar{F}_{m \max}|$  is simply the maximum value of the DFT amplitude. Hence, the plot of  $A_m$  versus  $\nu$  showed the spectrum in decibels below the maximum  $|\bar{F}_m|$ . Values of  $E_m$  can range from 0 to 1 and they have significance only if essentially all the spectral content of the transient signal is contained below  $1/2T$  Hz. By analysis of the spectral information contained in the plots of  $A_m$  and  $E_m$  versus  $\nu$ , an appropriate digital lowpass cutoff frequency was established for each transient signal acquired by the A/D system. A cutoff frequency was chosen where  $A_m$  was sufficiently low and  $E_m$  sufficiently high. Generally, these threshold values were  $A_m = -40$  dB or less and  $E_m = 0.995$  or more.

Once a decision had been made on what frequencies in the signal to pass and which to reject, the given sample set  $\{f_m\}$  was passed through a lowpass, inphase nonrecursive digital filter which then created the output set  $\{g_m\}$ .<sup>(41)</sup> A nonrecursive filter is one in which the formula for  $g_m$  contains explicitly only values from the set  $\{f_m\}$ . A general form of the linear nonrecursive algorithm is

$$g_m = \sum_{n=-N}^N b_n f_{m-n} \quad (G-9)$$

where the limit  $N$  is finite to insure realization. Note that there are a total of  $2N + 1$  filter weights. Each coefficient  $b_n$  can be any real value including zero. The specific values of the  $b_n$ 's are dependent upon the desired real or complex transfer function defined in the frequency space. The counterpart or analog to the set of discrete smoothing weights  $\{b_n\}$  is the continuous weighting function  $b(t)$  which would be associated with continuous input and output functions; that is, by convolution

$$g(t) = \int_{-\infty}^{\infty} f(t - \tau)b(\tau)d\tau = \int_{-\infty}^{\infty} f(\tau)b(t - \tau)d\tau \quad (G-10)$$

The  $b_n$  can be evaluated directly from  $b(t)$  by noting that  $b_n \cong b(nT)T$  where equidistant samples have been assumed.

Assume that the transfer function  $H(\omega)$  is real and that it is symmetric with respect to  $\omega = 0$ ; i.e.,  $H(\omega) = H(-\omega)$ . The weighting function  $b(t)$  is

$$b(t) = \frac{1}{2\pi} \int_{-\infty}^{\infty} H(\omega) e^{j\omega t} d\omega = \frac{1}{2\pi} \int_{-\infty}^{\infty} H(\omega) e^{-j\omega t} d\omega \quad (\text{G-11})$$

This equation can be written in real form over the positive frequency space. The result is

$$b(t) = \frac{1}{\pi} \int_0^{\infty} H(\omega) \cos \omega t d\omega \quad (\text{G-12})$$

where  $b(t)$  is real and is symmetric with respect to  $t = 0$ ; i.e.,  $b(t) = b(-t)$ . If the time derivative of the output function is desired, then from equation (G-10)

$$g(t) = \frac{\partial [g(t)]}{\partial t} = \int_{-\infty}^{\infty} f(\tau) \frac{\partial}{\partial t} [b(t - \tau)] d\tau = \int_{-\infty}^{\infty} f(\tau) c(t - \tau) d\tau \quad (\text{G-13})$$

where  $c(t') = \partial/\partial t' [b(t')]$  when  $t' = t - \tau$ . By the use of equation (G-11),  $c(t)$  can be expressed as

$$c(t) = \frac{1}{2\pi} \int_{-\infty}^{\infty} j\omega H(\omega) e^{j\omega t} d\omega = \frac{1}{2\pi} \int_{-\infty}^{\infty} -j\omega H(\omega) e^{-j\omega t} d\omega \quad (\text{G-14})$$

Clearly,  $j\omega H(\omega)$  is the Fourier transform of  $c(t)$  while  $H(\omega)$  is the Fourier transform of  $b(t)$ . Rewriting equation (G-14) in real form over the positive frequency space yields

$$c(t) = \frac{1}{\pi} \int_0^{\infty} -\omega H(\omega) \sin \omega t d\omega \quad (\text{G-15})$$

where  $c(t)$  is a real function and is antisymmetric with respect to  $t = 0$ ; i.e.,  $c(-t) = -c(t)$ .

The specific form of the transfer function  $H(\omega)$  used in the digital signal analysis of the experimental data is shown in Figure 45. This transfer function gave a filter having unity gain and zero phase shift in the pass band with a first order roll-off between the pass ( $\omega \leq \omega_1$ ) and rejection ( $\omega \geq \omega_2$ ) bands. After the direct application of equations (G-12) and (G-15), the *smoothing* and derivative weighting functions for this particular  $H(\omega)$  were computed to be

$$b(t) = \frac{\cos \omega_1 t - \cos \omega_2 t}{\pi(\omega_2 - \omega_1)t^2} \quad (\text{G-16})$$

$$c(t) = \frac{\omega_2 t \sin \omega_2 t - \omega_1 t \sin \omega_1 t + 2 \cos \omega_2 t - 2 \cos \omega_1 t}{\pi(\omega_2 - \omega_1)t^3} \quad (\text{G-17})$$

The discrete weights needed in the algorithm represented by equation (G-9), come directly from equations (G-16) and (G-17). These discrete weights are

$$b_n^s = T b(nT) = \frac{\cos(2\pi f_1 nT) - \cos(2\pi f_2 nT)}{2\pi^2 n^2 T (f_2 - f_1)} \quad (\text{G-18})$$

$$b_n^d = Tc(nT) = \frac{f_2 \sin(2\pi f_2 nT) - f_1 \sin(2\pi f_1 nT)}{\pi T n^2 (f_2 - f_1)} - \frac{2b_n^s}{nT} \quad (G-19)$$

The superscripts "s" and "d" refer, respectively, to smoothing and derivative. Because of the symmetry of  $b_n^s$  and the antisymmetry of  $b_n^d$ , it was unnecessary to compute these coefficients for negative  $n$  values. The specific algorithm used to get the smoothed output was

$$g_m^s = \sum_{n=-N}^N b_n^s f_{m-n} ; b_{-n}^s = b_n^s ; b_0^s = T(f_2 + f_1) \quad (G-20)$$

To compute the derivatives of the output, the following algorithm was utilized

$$g_m^d = \sum_{n=-N}^N b_n^d f_{m-n} ; b_{-n}^d = -b_n^d ; b_0^d = 0 \quad (G-21)$$

The lowpass transfer function shown in Figure 45 is a Fourier transform associated directly with  $b(t)$  and indirectly with  $c(t)$ . For  $n$  in the interval  $[-N, N]$ , the discrete weights  $b_n^s$  and  $b_n^d$  are associated with a finite DFT which is a least-squares approximation to  $H(\omega)$ . With  $N$  finite, the goodness of fit between  $H(\omega)$  and  $\bar{H}(\omega)$  depends upon the sharpness of the roll-off after  $\omega_1$  together with  $N$ , the parameter which defines the number of weights. Central to this topic of error between the desired and the realized spectral window is the so-called Gibbs phenomenon which manifests itself as a fixed percentage overshoot and ripple before and after an approximated discontinuity.<sup>(42)</sup>

For a lowpass digital filter having a desired transfer function identical to that in Figure 45, Ormsby<sup>(43)</sup> discussed the mean square error  $e$  between  $\bar{H}(\omega)$  and  $H(\omega)$ . His empirical results for  $e < 0.006$  and  $e < 0.015$  were correlated with the following equation

$$e = \frac{0.012}{\lambda'_R N} \quad (\text{G-22})$$

where

$$\lambda'_R = k\lambda_R = k \left( \frac{\omega_2 - \omega_1}{\omega_s} \right) \quad (\text{G-23})$$

The sharpness of the roll-off after  $\omega_1$  is specified by  $\lambda_R$  and  $k$  is a constant greater than one which defines the size of the transition band in which the effective error is  $e$ . For example with  $k = 1.2$ ,  $\lambda = \omega/\omega_s$ , and  $\lambda_c = \omega_1/\omega_s$ , the maximum errors are less than  $e$  for  $\lambda < (\lambda_c - 0.1 \lambda_R)$  and  $\lambda > (\lambda_c + 1.1 \lambda_R)$ . If in equation (G-22) the value of  $N$  is made increasingly large, then a smaller  $\lambda'_R$  can exist for the desired maximum error or a smaller  $e$  can be gained for the same  $\lambda'_R$ .

The parameters which indicate the high accuracy or low error in the digital filtering conducted on the data from the steady-state burning tests are shown in Table 5. After the analysis of the spectral content of all the discrete physical data relevant to a given test, a single digital lowpass cutoff frequency was found to suffice for all transient signals. Each value of  $f_1$  in Table 5 represents such a frequency. In order to justify the choice of  $N = 200$  as shown in Table 5, consider the following argument. Let  $e = 0.006$  and  $N = 49$ , then from equation (G-22)  $\lambda'_R$  is found to be 0.0408. Since  $\lambda_R$  is 0.04,  $k$  will be 1.02. Clearly, by increasing  $N$

from 49 to 200 the error  $e$  will get smaller for the same  $\lambda'_R$ . Hence, by choosing  $N = 200$  the smoothed output  $g_m^s$  will have essentially no error. Also, by making  $N$  larger the derivative of the output  $g_m^d$  becomes a better approximation to the desired though not realizable case of  $N = \infty$ . It is important to note that for equal  $\lambda'_R$  the error in  $g_m^d$  is much more sensitive to  $N$  than is the error in  $g_m^s$ . Thus, when derivatives are to be calculated with the differentiating digital filter represented by equations (G-19) and (G-21), the value chosen for  $N$  should be larger than the number which would be satisfactory if only  $g_m^s$  were being computed. This is another reason why  $N$  was made 200 instead of only 49. For all steady-state burning tests, time derivatives were calculated by the digital nonrecursive differentiating filter.

Presented in Table 6 are the digital filter parameters relevant to all dynamic tests. Unlike the steady-state tests, no single lowpass cutoff frequency  $f_1$  was applied to all physical quantities of interest on a given dynamic test. Hence, no values  $f_1$  are indicated in Table 6. For the dynamic tests, these cutoff frequencies and the associated physical quantities are given in Table 15 which is discussed in Section 6.31 and not here. As indicated by the values of  $\lambda_R$  in Table 6, the roll-off after a cutoff frequency was sharper than that for a steady-state test. Consider the consequences of this fact. If  $k = 1.02$  as in the steady-state example, then  $\lambda'_R = 0.0102$  when  $\lambda_R = 0.010$ . When  $e = 0.006$  and  $\lambda'_R = 0.0102$  the value of  $N$  from equation (G-22) becomes 196. Obviously the use of  $N = 200$  gave very good results for the dynamic  $g_m^s$  although the filtered output was not quite as error free as that for the steady-state tests. A problem arose when the dynamic  $g_m^d$  was computed with  $N = 200$ . It was found that to get a high quality magnitude response from the differentiating nonrecursive algorithm, it was necessary to use values of  $N$  greater than 200. Such increases in the number of filter weights caused the computer costs to become prohibitive. One remedy to this problem would have been to use a differentiating digital filter with weighting coefficients different from those given by equation (G-19). There are many other differentiating filters and Kuo

and Kaiser<sup>(44)</sup> provide a comparison of the amplitude responses of several different designs. The solution which was implemented was to apply central differences to the already digitally filtered data. Thus, for all dynamic tests, time derivatives of any sample set were computed in this manner.

## BIBLIOGRAPHY

1. *Proceedings of the 4<sup>th</sup> ICRPG Combustion Conference*, "A Technique for Measurement of Solid Propellant Burning Rates During Rapid Pressure Transients," by S. V. Shelton (CPIA Publication No. 162, Vol. 1, Silver Spring, Maryland, December 1967), pp. 361-372.
2. A. Alkidas, A. Clary, G. Giles, and S. Shelton, *Measurement of Steady State and Transient Solid Propellant Burning Rates with Microwaves* (Final Report, Grant No. AFOSR-70-1934, Georgia Institute of Technology, Atlanta, Georgia, December 1973).
3. L. D. Strand, A. L. Shultz, and G. K. Reedy, *Determination of Solid Propellant Transient Regression Rates Using a Microwave Doppler Shift Technique* (Technical Report 32-1569, Jet Propulsion Laboratory, Pasadena, California, October 15, 1972).
4. L. D. Strand, A. L. Shultz, and G. K. Reedy, "Microwave Doppler Shift Technique for Determining Solid Propellant Transient Regression Rates," *J. of Spacecraft and Rockets*, Vol. 11, No. 2 (February 1974), pp. 75-83.
5. *AIAA 14<sup>th</sup> Aerospace Sciences Meeting*, Washington, D.C., January 26-28, 1976, "Feasibility Demonstration of a Variable Frequency Driver-Microwave Transient Regression Rate System," by L. D. Strand and R. P. McNamara, AIAA Paper No. 76-105, 9 p.
6. C. Price and A. Juhasz, *A Versatile User-Oriented Closed Bomb Data Reduction Program (CBRED)* (Technical Report No. 2018, Ballistic Research Laboratory, Aberdeen Proving Ground, Maryland, September 1977).
7. *Proceedings of the 11<sup>th</sup> JANNAF Combustion Meeting, Vol. 1*, "Ignition Transients and Pressurization in Closed Chambers," by L. H. Caveny and M. Summerfield (CPIA Publication No. 261, Silver Spring, Maryland, December 1974), pp. 433-457.
8. *Proceedings of the 14<sup>th</sup> JANNAF Combustion Meeting, Vol. 2*, "JANNAF Combustion Rate Workshop," by T. L. Boggs and C. Lenchitz (CPIA Publication No. 292, Silver Spring, Maryland, December 1977), pp. 253-261.

9. *Proceedings of the 12<sup>th</sup> JANNAF Combustion Meeting, Vol. 1*, "Numerical Solution of Three Solid Propellant Combustion Models During a Gun Pressure Transient," by D. E. Kooker and C. W. Nelson (CPIA Publication No. 273, Silver Spring, Maryland, December 1975), pp. 173-197.
10. C. W. Nelson, *Response of Three Types of Transient Combustion Models to Gun Pressurization* (Interim Memorandum Report No. 447, Ballistic Research Laboratory, Aberdeen Proving Ground, Maryland, October 1975).
11. C. W. Nelson, "Response of Three Types of Transient Combustion Models to Gun Pressurization," *Combustion and Flame*, 32, (1978), pp. 317-319.
12. *Sixteenth Symposium (International) On Combustion*, "Review of Dynamic Burning of Solid Propellants in Gun and Rocket Propulsion Systems," by K. K. Kuo and G. R. Coates (The Combustion Institute, Pittsburgh, Pennsylvania, 1977), pp. 1177-1192.
13. *Interior Ballistics of Guns* (AMC Pamphlet No. AMCP 706-150, United States Army Material Command, Washington, D.C., February 1965), pp. 1-15 to 1-16.
14. *Ibid.*, pp. 1-13 to 1-14.
15. G. J. Van Wylen and R. E. Sonntag, *Fundamentals of Classical Thermodynamics* (New York: Wiley and Sons, 1965), p. 601.
16. P. G. Hill and C. R. Peterson, *Mechanics and Thermodynamics of Propulsion* (Reading, Massachusetts: Addison-Wesley, 1965), pp. 28-37.
17. F. R. W. Hunt, ed., *Internal Ballistics* (London: His Majesty's Stationery Office, 1951), pp. 10-13 and p. 219.
18. B. J. McBride, S. Heibel, J. C. Ehlers, and S. Gordon, *Thermodynamic Properties to 6000°K for 210 Substances Involving the First 18 Elements*, NASA SP-3001 (National Aeronautics and Space Administration, Washington, D.C., 1963), pp. 308-326.
19. H. S. Bean, ed., *Fluid Meters* (Sixth edition; New York: The American Society of Mechanical Engineers, 1971), pp. 47-53.
20. *Ibid.*, pp. 66-68.

21. J. A. Owczarek, *Fundamentals of Gas Dynamics* (Scranton, Pennsylvania: International Textbook, 1964), pp. 223-236.
22. V. L. Streeter and E. B. Wylie, *Fluid Mechanics* (Sixth edition: New York: McGraw-Hill, 1975), pp. 469-470.
23. B. Carnahan, H. A. Luther, and J. O. Wilkes, *Applied Numerical Methods* (New York: Wiley and Sons, 1969), pp. 361-380.
24. S. Timoshenko, *Strength of Materials, Part 1, Elementary Theory and Problems* (Third edition; Princeton, New Jersey: D. Van Nostrand, 1958), pp. 57-61.
25. S. Timoshenko and S. Woinowsky-Krieger, *Theory of Plates and Shells* (Second edition; New York: McGraw-Hill, 1959), pp. 72-74.
26. P. J. Olenick, Jr., *Investigation of the 76mm/62 Caliber Mark 75 Gun Mount Malfunction* (NSWC/DL TR-3144, Naval Surface Weapons Center, Dahlgren Laboratory, Dahlgren, Virginia, October 1975) p. G-7.
27. J. N. Boone, *Transient Response Analysis of Coupled Elastic Rods with Applications to Projectile Dynamics* (NSWC/DL TR-3265, Naval Weapons Laboratory, Dahlgren, Virginia, January 1975).
28. S. Ramo, J. R. Whinnery, and T. VanDuzer, *Fields and Waves in Communication Electronics* (New York: Wiley and Sons, 1967), pp. 425-429.
29. M. I. Skolnik, *Introduction to Radar Systems* (New York: McGraw-Hill, 1962), pp. 72-86.
30. B. Carnahan and J. O. Wilkes, *Digital Computing and Numerical Methods* (New York: Wiley and Sons, 1973), pp. 266-267.
31. R. Hooke and T. A. Jeeves, "Direct Search of Numerical and Statistical Problems," *J. Assoc. Computer Machines*, Vol. 8 (1961), pp. 212-229.
32. G. S. G. Beveridge and R. S. Schechter, *Optimization: Theory and Practice* (New York: McGraw-Hill, 1970), pp. 383-389.
33. M. Sucher and J. Fox, eds., *Handbook of Microwave Measurements, Vol. 2* (Third edition; Polytechnic Institute of Brooklyn: Polytechnic Press, 1963), pp. 503-508.

34. "Standard Methods of Test for Complex Permittivity (Dielectric Constant) of Solid Electric Insulating Materials at Microwave Frequencies and Temperatures to 1650°C," ASTM Designation D 2520-70, *American National Standard C59.127-1970*, American National Standards Institute, pp. 2450-2468.
35. *Operating and Service Manual for the 415D Standing Wave Ratio Meter* (Palo Alto, California: Hewlett-Packard Company, 1962).
36. M. Schwartz, *Information Transmission, Modulation, and Noise* (second edition; New York: McGraw-Hill, 1970), pp. 410-421.
37. T. L. Boggs and B. T. Zinn, eds., *Progress in Astronautics and Aeronautics, Vol. 63, Experimental Diagnostics in Combustion of Solids*, "Feasibility of a Variable Frequency Driver-Microwave Transient Regression Rate Measurement System." by L. D. Strand and R. P. McNamara (New York: American Institute of Aeronautics and Astronautics, 1979) pp. 155-172.
38. S. D. Stearns, *Digital Signal Analysis* (Rochelle Park, New Jersey: Hayden Book Company, 1975), pp. 1-101.
39. W. T. Cochran, J. W. Cooley, et al., "What is the Fast Fourier Transform," *Proceedings of the IEEE*, Vol. 55, No. 10 (October 1967), pp. 1664-1674.
40. G. D. Bergland, "A Guided Tour of the Fast Fourier Transform," *IEEE Spectrum*, Vol. 6 (July 1969), pp. 41-52.
41. Stearns, op. cit., pp. 102-120.
42. B. Gold and C. M. Rader, *Digital Processing of Signals* (New York: McGraw-Hill, 1969), pp. 217-232.
43. J. F. A. Ormsby, "Design of Numerical Filters with Application to Missile Data Processing," *J. Assoc. Computer Machines*, Vol. 8, No. 3, (July 1961), pp. 440-466.
44. F. F. Kuo and J. F. Kaiser, eds., *System Analysis by Digital Computer* (New York: Wiley and Sons, 1966), pp. 228-243.

45. *Proceedings of the 13<sup>th</sup> JANNAF Combustion Meeting, Vol. 1*, "Burning Rates of Standard Army Propellants in Strand Burner and Closed Chamber Tests," by B. B. Grollman and C. W. Nelson (CPIA Publication 281, Silver Spring, Maryland, December 1976), pp. 21-43.
46. Olenick, Jr., op. cit., p. F-4.
47. "JANNAF Combustion Rate Workshop," (to be published in the *Proceedings of the 15<sup>th</sup> JANNAF Combustion Meeting*, Newport, Rhode Island, September 1978).
48. *Proceedings of the 13<sup>th</sup> JANNAF Combustion Meeting, Vol. 1*, "The Role of Ignition and Combustion in Gun Propulsion: A Survey of Developmental Efforts," by the Combustion Working Group Committee on Gun Propellant Ignition and Combustion (CPIA Publication No. 281, Silver Spring, Maryland, December 1976), pp. 315-339.
49. E. G. Plett and M. Summerfield, *Remarks on the Use of Microwaves for Measurement of Solid Propellant Burning Rates During Pressure Transients* (Princeton, New Jersey: Guggenheim Aerospace Propulsion Laboratories, Princeton University, September 15, 1970), preliminary draft for discussion, unpublished.
50. M. Summerfield and E. G. Plett, *Critique of Microwave Doppler Method for Measuring Instantaneous Burning Rates in Rapidly Changing Conditions* (Princeton, New Jersey: Guggenheim Aerospace Propulsion Laboratories, Princeton University, August 15, 1972), presented at the AFOSR Contractors Meeting in Chicago, August 15, 1972, unpublished.
51. R. B. Cole, *High Pressure Solid Propellant Combustion Studies Using a Closed Bomb* (Report No. S-68, Rohm and Haas Co., Redstone Arsenal Research Division, Huntsville, Alabama, August 1965).

**DISTRIBUTION**

Assistant Secretary of Defense (R&E)  
Department of the Navy  
Washington, DC 20301

Director of Defense Research and Engineering (OSD)  
Washington, DC 20301

Assistant Secretary of the Navy (R&D)  
Department of the Navy  
Washington, DC 20350

Chief of Naval Research  
Department of the Navy  
Arlington, VA 22217

Director of Naval Laboratories  
Department of the Navy  
Washington, DC 20360

Chief of Naval Operations  
Department of the Navy  
Washington, DC 20360

Chief of Naval Material  
Department of the Navy  
Washington, DC 20360

Commander  
Naval Sea Systems Command  
Washington, DC 20360  
Attn: SEA-06  
SEA-06R  
SEA-62CY  
SEA-62R (Blaine, Murrin)  
SEA-62Y  
SEA-621Y (Hawver)  
SEA-64

Commander  
Naval Air Systems Command  
Washington, DC 20360

**DISTRIBUTION (Continued)**

Commanding Officer  
Air Force Armament Test Laboratory  
Eglin AFB, FL 32542  
ATTN: O. K. Heiney  
Technical Library

Armaments Command  
Rock Island Arsenal  
Rock Island, IL 61200

Commanding General  
U.S. Army Material Command  
Washington, DC 20315

Commanding Officer  
Watervliet Arsenal  
Watervliet, NY 12189  
ATTN: Technical Library  
R. Hasenbein  
R. Gast  
P. M. Vottis

Commanding Officer  
Frankford Arsenal  
Bridge-Tacony Streets  
Philadelphia, PA 19137

Commanding Officer  
Picatinny Arsenal  
Dover, NY, 07801  
ATTN: Dr. Harry Fair  
J. Domen  
Dr. David Downs  
Dr. J. Picard  
C. Lenchitz

**DISTRIBUTION (Continued)**

Edward B. Fisher  
Calspan Corporation  
Buffalo, NY 14221

Joe Flanagan  
Rockwell International  
Space Division  
Downey, CA 90200

Proj. Warren Strahle  
Georgia Institute of Technology  
School of Aerospace Engineering  
Atlanta, GA 30332

Leon Strand  
Jet Propulsion Laboratory  
4800 Oak Grove Drive  
Pasadena, CA 91103

Vreg Yousefian  
Aerodyne Research, Inc.  
Bedford, MA 01730

Prof. Ben Zinn  
Georgia Institute of Technology  
School of Aerospace Engineering  
Atlanta, GA 30332

Commanding General  
Army Material and Mechanics Research Center  
Watertown, MA 02172

Commanding Officer  
U.S. Army Material Development and Readiness Command  
5001 Eisenhower Ave.  
Alexandria, VA 22304

Commanding Officer  
Army Research Office  
Arlington, VA 22207

**DISTRIBUTION (Continued)**

Commander  
Naval Ordnance Station  
Indian Head, MD 20640  
ATTN: S. E. Mitchell  
Technical Library

Commanding Officer  
Naval Ordnance Station  
Louisville, KY 40214

Superintendent  
U.S. Naval Academy  
Annapolis, MD 21402

Commandant  
Headquarters, U.S. Marine Corps  
Washington, DC 20380

Commanding General  
Marine Corps Development and Education Center  
Quantico, VA 22134  
ATTN: Head, Mid Range Branch  
Chief, Ground Operations Division

Superintendent  
Naval Postgraduate School  
Monterey, CA 93940

Dr. Robert L. Glick, P.E.  
Thiokol/Huntsville Division  
Huntsville, Alabama 35807

Dick Hessler  
Thiokol/Huntsville Division  
Redstone Arsenal, AL 35808

Bruce D. Hopkins  
Hercules, Inc.  
PO. Box 98  
Magna, UT 84044

DISTRIBUTION (Continued)

Dr. Bernard Iwanciov  
United Technologies Corporation  
1050 E. Arques Avenue  
Sunnyvale, CA 94088

Prof. Herman Krier  
University of Illinois at Urbana-Champaign  
Champaign, IL 61820

Prof. Kenneth K. Kuo  
Pennsylvania State University  
213 Engineering Unit E  
University Park, PA 16802

George Lo  
Palo Alto Research Laboratory  
3251 Hanover Street  
Palo Alto, CA 94304

Proj. J. R. Osborn  
Purdue University  
School of Mechanical Engineering  
West Lafayette, ID 47907

Prof. E. W. Price  
Georgia Institute of Technology  
School of Aerospace Engineering  
Atlanta, GA 30332

Dr. Robert S. Brown  
United Technologies Corporation  
1050 E. Arques Avenue  
Sunnyvale, CA 94088

Dr. Leonard H. Caveny  
Guggenheim Laboratories  
James Forrestal Campus  
Princeton, NJ 08540

**DISTRIBUTION (Continued)**

John E. Christian  
Hercules ABL  
P.O. Box 210  
Cumberland, MD 21502

Thomas W. Christian III  
Chemical Propulsion Infor. Agency  
Johns Hopkins Univ/APL  
Laurel, MD 20810

Wendell Christiansen  
Thiokol Corporation  
Wasatch Division  
P.O. Box 524  
Brigham City, UT 84302

Norm Cohen  
Jet Propulsion Laboratory  
4800 Oak Grove Drive  
Pasadena, CA 91103

James A. Condon  
Purdue University  
School of Mechanical Engineering  
West Lafayette, IN 47907

Dr. John DeRyke  
United Technologies Corporation  
1050 E. Arques Avenue  
Sunnyvale, CA 94088

Mike Ditore  
Aerojet Solid Propulsion Company  
Box 1168  
Sacramento, CA 95809

Kemper E. Eagle  
Atlantic Research Corporation  
7511 Wellington Road  
Gainesville, PA 22065

**DISTRIBUTION (Continued)**

**Director**  
Army Ballistics Research Laboratories  
Aberdeen Proving Ground, MD 21005  
ATTN: Dr. J. R. Ward  
P. M. Howe  
B. B. Grollman  
A. W. Horst  
A. Juhasz  
Dr. Tom Minor  
Dr. Ingo May  
C. W. Nelson  
W. Jackson  
J. J. Rocchio  
Dr. D. Kooker  
R. A. Wires  
T. L. Brosseau  
Technical Library

**Commanding Officer**  
Aberdeen Proving Ground  
Aberdeen, MD 21005

**Director**  
Advanced Research Projects Agency  
Department of Defense  
Washington, DC 20301

**Director**  
Naval Research Laboratory  
Washington, DC 20390

**Commander**  
Naval Weapons Center  
China Lake, CA 93555  
ATTN: D. Weathersby  
C. M. Anderson  
J. Pakulak  
T. L. Boggs

**DISTRIBUTION (Continued)**

Commanding Officer  
Army Research Office (Durham)  
Box CM, Duke Station  
Durham, NC 17706

Defense Technical Information Center  
Cameron Station  
Alexandria, VA 22314

(12)

Local:

E41

G

G02 (Soper)

G33 (Russell) (20)

R13 (Bernecker)

X210 (2)

X211 (2)